Alma Mater Studiorum - Università di Bologna

DOTTORATO DI RICERCA IN

MECCANICA E SCIENZE AVANZATE DELL'INGEGNERIA

Ciclo 35

**Settore Concorsuale:** 09/E4 - MISURE

**Settore Scientifico Disciplinare:** ING-IND/12 - MISURE MECCANICHE E TERMICHE

# QUALIFICATION OF OPTICAL FIBER SENSORS FOR THE STRUCTURAL HEALTH MONITORING OF AEROSPACE STRUCTURES

**Presentata da:** Francesco Falcetelli

**Coordinatore Dottorato**

Lorenzo Donati

**Supervisore**

Raffaella Di Sante

**Co-supervisore**

Lorenzo Donati

**Esame finale anno 2023**

*To Giulia and my Parents*

# Acknowledgements

If I had to compare the Ph.D. journey with a sport, it would be, without any doubt, a marathon. You have to run fast enough to achieve your goals while keeping in mind that you can't exceed your pace for too long to finish the race. Now, while I'm writing, I see the finish line, and I'm making the last sprint.

During my Ph.D., my feelings constantly oscillated from deep desperation to immeasurable happiness, like a pendulum. The first lesson that I've learned is that you can't push the pendulum in the right direction alone, or at least I couldn't. But I was lucky. I have always been surrounded by amazing people helping me to find the right motivation and never give up.

These words are for them, to the people who turned my insecurity and anxiety into the strongest mettle, which is now my best quality.

*My first thoughts are for my fiancée Giulia and my parents Chimena and Rolando. Without You, I would not even be able to start this Ph.D. I love you.*

*My deepest gratitude is to my supervisor and mentor, Raffaella. You gave me the possibility to start this journey and always believed in me, even when other people wouldn't have.*

*I'm thankful to my co-supervisor, Lorenzo Donati, and also to Prof. Enrico Troiani for his unconditional support during these years.*

*Thank you, Dimitrios Zarouchas. You trusted me even before knowing me. You never acted like a boss and made me feel at home in the Structural Integrity & Composites Group at the Faculty of Aerospace Engineering of TU Delft. I will never forget the dynamic environment full of bright and kind people.*

*Special thanks to Nan for your precious suggestions. You always found the time to teach me what I didn't know, even when there was no time. You made me a better researcher and person.*

*A special dedication is to Prof. Marcias Martinez, who was always available to discuss with me in the tough moments. His suggestions from the other side of the Atlantic Ocean helped me find the right path more than once.*

*Thank you to Demetrio, the best labmate you can find. We spent countless hours in the lab. I often thought all the experiments were too long and just impossible to complete, but we always supported each other and made it.*

*My personal Delft crew is unforgettable and, for sure, one of my best achievements in this*

*Ph.D. journey. Thank you, Gioele, Davide, Matteo, and Daniele for all the adventures in the Netherlands.*

*When I returned home, I also realized why I love my country. Thanks to all my Ph.D. student colleagues at the University of Bologna, we shared an amazing journey. Special thanks to Antonio; your friendship is priceless to me.*

*I also want to thank my old high school friends Francesco, Alessandro, and Lorenzo for supporting me during these years. We never lost over time despite the distance.*

*I would like to thank many others, but this Ph.D. thesis must start at some point! I guess this is the curse of the luckiest man, having too many friends.*

# Abstract

In recent years, composite materials have revolutionized the design of many structures. Their superior mechanical properties and light weight make composites convenient over traditional metal structures for many applications. However, composite materials are susceptible to complex and challenging to predict damage behaviors due to their anisotropy nature. Therefore, structural Health Monitoring (SHM) can be a valuable tool to assess the damage and understand the physics underneath. Distributed Optical Fiber Sensors (DOFS) can be used to monitor several types of damage in composites. However, their implementation outside academia is still unsatisfactory. One of the hindrances is the lack of a rigorous methodology for uncertainty quantification, which is essential for the performance assessment of the monitoring system. The concept of Probability of Detection (POD) must function as the guiding light in this process. However, precautions must be taken since this tool was established for Non-Destructive Evaluation (NDE) rather than Structural Health Monitoring (SHM). In addition, although DOFS have been the object of numerous studies, a well-established POD methodology for their performance assessment is still missing. This thesis aims to develop a methodology to produce POD curves for DOFS in composite materials. The problem is analyzed considering several critical points, such as the strain transfer characterizing the DOFS and the development of an experimental and model-assisted methodology to understand the parameters that affect the DOFS performance.

# Contents

# List of Figures

# List of Tables

# List of Symbols

| **Symbol** | **Description** | **Unit** |
|---|---|---|
| $\alpha$ | Thermal expansion coefficient | $^{\circ}\mathrm{C}^{-1}$ |
| $\mathbf{1}_{\boldsymbol{N}}$ | Vector of length $N$ of ones | $\cdots$ |
| $\boldsymbol{x'}$ | Translated spatial domain vector | mm |
| $\boldsymbol{x}$ | Spatial domain vector | mm |
| $\Delta\lambda_B$ | Bragg's wavelength shift | nm |
| $\Delta\lambda$ | Wavelength shift | nm |
| $\Delta\nu$ | Frequency shift | GHz |
| $\Delta F$ | Frequency range | Hz |
| $\Delta x$ | Spatial resolution | mm |
| $\Delta X$ | Interrogator resolution | mm |
| $\Delta z_{min}$ | Maximum theoretical spatial resolution for OFDR systems | s |
| $\gamma$ | Sweep rate of the tunable laser source | $\mathrm{s}^{-2}$ |
| $\kappa$ | Dielectric constant | 1 |
| $\lambda_B$ | Bragg's wavelength | nm |
| $\lambda$ | Wavelength of light | nm |
| $\Lambda$ | Grating period $\Lambda$ | nm |
| $\nu$ | Poisson's ratio | 1 |
| $\omega\left(t\right)$ | Instantaneous angular frequency | $\mathrm{rad\,s^{-1}}$ |
| $\omega_b$ | Angular beat frequency | $\mathrm{rad\,s^{-1}}$ |
| $\phi\left(t\right)$ | Time-varying phase | rad |
| $\Pi_i$ | Interrogator window function | mm |
| $\rho_e$ | Effective photo-elastic constant | 1 |
| $\rho$ | Density | $\mathrm{kg\,m^{-3}}$ |
| $\tau$ | Propagation delay | s |
| $\theta\left(t\right)$ | Random phase fluctuations | rad |
| $\xi$ | Thermo-optic coefficient | $^{\circ}\mathrm{C}^{-1}$ |
| $E_0$ | Optical field amplitude | $\mathrm{V\,m^{-1}}$ |
| $E_i$ | Incident optical field | $\mathrm{V\,m^{-1}}$ |
| $E_s$ | Backscattered optical field | $\mathrm{V\,m^{-1}}$ |
| $f_0$ | Initial frequency | Hz |
| $f_b$ | Beat frequency | Hz |
| $f$ | Frequency | Hz |
| $j$ | Imaginary unit | 1 |
| $K_\varepsilon$ | Strain-related constant in Bragg's wavelength shift equation | $\mathrm{nm\,\mu\varepsilon^{-1}}$ |

| | | |
|---|---|---|
| $K_T$ | Temperature-related constant in Bragg's wavelength shift equation | $\mathrm{nm\,°C^{-1}}$ |
| $n_{eff}$ | Effective refractive index | 1 |
| $p_{ij}$ | Pockel's coefficient | 1 |
| $p$ | Pressure | Pa |
| $R$ | Reflectivity of the fiber under test | 1 |
| $s$ | Entropy | $\mathrm{J\,K^{-1}}$ |
| $T_s$ | Sweep time | s |
| $T$ | Temperature | K |
| $t$ | Time | s |

## Mechanical Properties

| **Symbol** | **Description** | **Unit** |
|---|---|---|
| $\boldsymbol{Z}$ | Strain noise vector | $\mu\varepsilon$ |
| $\Delta a_m$ | Average delamination length increment | mm |
| $\Delta a$ | Delamination length increment | mm |
| $\delta$ | Displacement at the load point | mm |
| $\epsilon_P$ | Load error | N |
| $\Gamma$ | Mechanical transfer function | $\mathrm{mm^{-1}}$ |
| $\mu_E$ | Mean of the Young's modulus along the x-axis | MPa |
| $\mu_k$ | Mean of the shear lag constant | $\mathrm{mm^{-1}}$ |
| $\mu_w$ | Average specimen width | mm |
| $\sigma_a$ | Random delamination length increment standard deviation | mm |
| $\sigma_E$ | Standard deviation of the Young's modulus along the x-axis | MPa |
| $\sigma_k$ | Standard deviation of the shear lag constant | $\mathrm{mm^{-1}}$ |
| $\sigma_p$ | Load standard deviation | N |
| $\sigma_w$ | Standard deviation of the specimen width | mm |
| $\sigma_x$ | Stress along the x-axis | MPa |
| $\sigma_z$ | Strain noise standard deviation | $\mu\varepsilon$ |
| $\varepsilon_a$ | Random delamination length increment | mm |
| $\varepsilon_m$ | Strain value of the host structure | $\mu\varepsilon$ |
| $\varepsilon_x$ | Strain along the x-axis | $\mu\varepsilon$ |
| $\varepsilon_{mt}$ | Measured strain profile (theoretical) | $\mu\varepsilon$ |
| $\varepsilon_m$ | Measured strain profile | $\mu\varepsilon$ |
| $\varepsilon$ | Longitudinal strain | $\mu\varepsilon$ |
| $a_0$ | Initial crack length | mm |
| $a_f$ | Final crack length | mm |
| $a_{true}$ | True crack length | mm |
| $C$ | Compliance | $\mathrm{mm\,N^{-1}}$ |
| $E_x$ | Young's modulus along the x-axis | MPa |
| $h$ | Specimen half height | mm |
| $I_z$ | Moment of inertia about the z-axis | $\mathrm{mm^4}$ |
| $k$ | Shear lag constant | $\mathrm{mm^{-1}}$ |

| | | |
|---|---|---|
| $L$ | Length of the spatial domain | mm |
| $M_z$ | Moment about the z-axis | N m |
| $n_c$ | number of cracks | 1 |
| $P$ | Load | N |
| $R$ | Loading ratio | 1 |
| $w$ | Specimen width | mm |

## Statistics

| **Symbol** | **Description** | **Unit** |
|---|---|---|
| $\alpha$ | Significance level | $\cdots$ |
| $\Delta$ | $a_{90/95} - a_{90}$ | mm |
| $\epsilon_{ht}$ | Hot-touch error | mm |
| $\hat{a}_{th}$ | Threshold value of the damage index | $\mu\epsilon$ |
| $\hat{a}$ | Measurement output | $\cdots$ |
| $\sigma_{ht}$ | Hot-touch error standard deviation | mm |
| $A^2$ | Anderson-Darling statistics | $\cdots$ |
| $a_{90}$ | Crack length with 90% probability of detection | mm |
| $a_{90/95}$ | Crack length with 90% probability of detection (confidence level of 95%) | mm |
| $a$ | Crack length | mm |
| $H_0$ | Null hypothesis | $\cdots$ |
| $K$ | Tolerance factor | 1 |
| $n_v$ | Number of virtual specimens | 1 |
| $n$ | Number of specimens | 1 |
| $r^2$ | Coefficient of Determination | 1 |
| $s$ | Standard deviation of the lengths at detection | mm |

# List of Abbreviations

## Damage

**BVID** Barely Visible Impact Damage, 47

**KDL** Known Damage Location, 12

**ODSCC** axial Outside Diameter Stress Corrosion Cracks, 45

**UDL** Unknown Damage Location, 12

## Machine Learning

**CNN** Convolutional Neural Networks, 48

**MC** Monte-Carlo, 46

**MCMC** Markov Chain Monte Carlo, 46

## Material

**Al** Aluminum, 45

**AUSS** AUstenitic Stainless-Steel, 46

**CFRP** Carbon Fiber-Reinforced Polymer, 3

## Statistics

**AEL** Absolute Error of Localization, 37

**CE** Characterization Error, 41

**DI** Damage Index, 97

**LaD** Length at Detection, 5

**LMM** Linear Mixed-effect Model, 25

**LOC** Localizer Operating Characteristic, 37

**LUS** safety Limit against Under Sizing, 40

**M-POD** Multivariate Probability of Detection, 13

**MAPOD** Model-Assisted Probability of Detection, 5

**MAPOD - XFN** MAPOD - Transfer Function, 33

**MAPOD-FMA** MAPOD - Full Model-Assisted, 33

**MAPOL** Model-Assisted Probability of Localization, 38

**MLE** Maximum-Likelihood Estimation, 16

**NLA** Normalized Localization Accuracy, 36

**NPP** Negative Predicted Probability, 14

**NPV** Negative Predictive Value, 14

**NQA** Normalized Quantification Accuracy, 41

**OLS** Ordinary Least Squares, 16

**OSTI** One-Sided Tolerance Interval, 27

**PDL** Probability of Damage Location, 48

**PFA** Probability of False Alarm, 4

**PFP** Probability of False Positive, 14

**POD** Probability of Detection, 4

**POL** Probability of Localization, 37

**POS** Probability of Sizing, 40

**PPP** Positive Predicted Probability, 14

**PPV** Positive Predictive Value, 14

**PTN** Probability of true negative, 14

**REM** Random-Effects Model, 5

**RMSE** Root Mean Square Error, 45

**ROC** Receiver Operating Characteristic, 4

**SNR** Signal-to-Noise Ratio, 106

# Research Field

**A-SHM** Automatic SHM, 12

**NDE** Non-Destructive Evaluation, 4

**NDI** Non-Destructive Inspection/Investigation, 9

**NDT** Non-Destructive Testing, 9

**QNDE** Quantitative Non-Destructive Evaluation, 10

**S-SHM** Scheduled SHM, 12

**SHM** Structural Health Monitoring, 3

# Sensing

**Φ-OTDR** Phase-sensitive optical time-domain reflectometry, 54

**AE** Acoustic Emission, 5

**AUT** Automated Ultrasonic Testing, 40

**CNT** Carbon Nanotube, 5

**CVM** Comparative Vacuum Monitoring, 5

**DOFS** Distributed Optical Fiber Sensor, 4

**ECT** Eddy Current Testing, 40

**FBG** Fiber Bragg Grating, 5

**FUT** Fiber Under Test, 55

**GIM-OFS** Graded-Index Multimode Optical Fiber Sensors, 87

**GLW** Guided Lamb Waves, 5

**IRT** InfraRed Thermography, 45

**LITPI** Lock-in Thermographic Phase Imaging inspection, 46

**LPG** Long Period Grating, 50

**OBR 4413** Optical Backscatter Reflectometer™ Model 4413, 54

**ODiSI-B** Optical Distributed Sensor Interrogator - Model B, 54

**OFDR** Optical frequency-domain reflectometry, 6

**OFS** Optical Fiber Sensor, 3

**OLCR** Optical low-coherence reflectometry, 54

**OTDR** Optical time-domain reflectometry, 54

**P-OTDR** Polarization-sensitive optical time-domain reflectometry, 54

**PT** optical Pulsed Thermography, 45

**PZT** Lead Zirconate Titanate, 45

**SG** Strain Gauge, 47

**SISM-OFS** Step Index Single-Mode Optical Fiber Sensors, 87

**SPA** Sampling Phased Array, 46

**SWI** Swept-wavelength Interferometry, 54

**TLS** Tunable Laser Source, 55

**TOFD** Time-of-Flight Diffraction, 40

**UPA** Ultrasonic Phased Array, 46

**UT** Ultrasonic Testing, 45

**VT** Vibrothermography, 46

## Other

**ASIP** Aircraft Structural Integrity Programs, 13

**ASM** American Society of Metals, 15

**BC** Boundary Condition, 64

**CASE** Cognitive Architecture for State Exploitation, 13

**CBA** Cost–Benefit Analysis, 11

**CDF** Cumulative Distribution Function, 37

**DCB** Double Cantilever Beam, 6

**EDM** Electrical Discharge Machined, 45

**EOCs** Environmental and Operational Conditions, 4

**FEM** Finite Element Method, 46

**FMECA** Failure Mode, Effects, and Criticality Analysis, 11

**GLS** Generalized Linear Model, 16

**MAPRA** Model-Assisted Probabilistic Reliability Assessment, 13

**OSP** Optimal Sensor Placement, 22

**PULSe** Pervasive Ubiquitous Lightwave Sensor, 65

**SRQ** Scientific Research Question, 5

**SRSQ** Scientific Research Sub-Question, 5

**TRL** Technology Readiness Level, 11

**USAF** United States Air Force, 15

# Part I

# State of the art

# Chapter 1

# Introduction

> *If a cluttered desk is a sign of a cluttered mind, of what, then, is an empty desk a sign?*
>
> *Albert Einstein*

Over the last decades, composite laminates have become the predominant structural material in various engineering applications. Nowadays, the quest to develop safer and lighter structures still fosters the scientific community to investigate different damage mechanisms in composite materials and their reciprocal interaction. However, despite the impressive amount of research, open questions are still present, and the understanding of the physics behind failure modes in composites is limited [1]. Moreover, composite structures are particularly susceptible to flaws arising from the manufacturing process and service and exhibit complex failure modes as opposed to metals. Among them, delamination constitutes one of the most common damage mechanisms and can also occur in adhesive bonds [2]. Using large safety factors mitigates the risks of catastrophic structural failure but leads to heavier designs and might not be deemed sufficient to guarantee safety.

Consequently, delamination growth represents a severe threat to structural integrity in Carbon Fiber-Reinforced Polymer (CFRP) structures, and it becomes necessary to implement Structural Health Monitoring (SHM) strategies. SHM can provide essential information about delamination existence, location, and size. Moreover, it can also deepen the understanding of other correlated damage mechanisms and thus promote the introduction of innovative composite materials and structures [3]. SHM offers a wide range of techniques, each with its strengths and weaknesses depending on the application.

Among them, Optical Fiber Sensor (OFS) provide numerous advantages over traditional strain sensing techniques. For example, they are intrinsically immune to electromagnetic interference; they have large bandwidth, which enables multiplexing solutions; and can survive harsh Environmental and Operational Conditions (EOCs) if protected with appropriate coatings and cable sheaths. Alj et al. provide further details about the durability of OFS [4]. Moreover, their lightweight and small size allow them to be embedded in composites [5] as well as 3D printed structures [6], and they have recently been shown to be a viable alternative to accelerometers for modal analysis [7]. Recent advances in optical fiber technology fostered the use of Distributed Optical Fiber Sensor (DOFS) based on Raman, Brillouin [8], and Rayleigh backscattering. DOFS based on Rayleigh backscattering are particularly promising for monitoring damage, such as delamination growth, in composites since they provide millimeter resolution along the fiber length within several meters of range [9].

However, assessing the damage detection performance of optical fibers is not a straightforward process. The OFS datasheet specifies the geometrical, mechanical, and optical properties. On the other hand, the interrogator datasheet provides the resolution, wavelength range, wavelength stability, maximum sensor length, measurement uncertainty, and sampling rate. Nevertheless, these metrics do not directly assess strain-based damage detection performance since *damage* is not a physical quantity that can be directly measured. Indeed, Axiom IVa of SHM states that sensors cannot measure *damage* and that a feature extraction process is needed to obtain damage-related information [10]. For example, considering delamination monitoring, the detection performance is expected to change depending on the loading conditions because they affect the damage-induced strain in the structure. In addition, depending on the strain transfer occurring from the structure to the fiber core [11], DOFS may exhibit different detection performances. The current literature lacks well-established methodologies for certification and performance evaluation for damage detection, preventing the adoption of this technology in many applications.

The performance of Non-Destructive Evaluation (NDE) methods, widely accepted in many industries (aerospace, automotive, oil and gas, medical, and marine, to name a few), is evaluated following the guidelines provided in the MIL-HKBK-1823A [12]. First, damage detection performance is quantified using Probability of Detection (POD) curves and Probability of False Alarm (PFA). Furthermore, varying the threshold value makes it possible to evaluate the POD against the PFA and obtain the so-called Receiver Operating Characteristic (ROC) curve [13], [14].

It is legitimate to ask whether one can apply these NDE reliability metrics to SHM. The naive application of POD curves in SHM would lead to inconsistent results. One of the most critical differences between NDE and SHM is their variability sources. The human factor represents the highest variability contribution in NDE, whereas SHM is affected by both temporal and spatial sources of variability. Moreover, SHM is typically characterized by repeated measurements over time, implying that the independent measurement assumption used in NDE does not hold [15].

Meeker et al. reviewed and proposed statistical methods for SHM [16], extending the theory described in the MIL-HKBK-1823A [12]. The authors demonstrate that the Length at Detection (LaD) [17], and the Random-Effects Model (REM) [18], are valid statistical methods for handling SHM data. However, in both cases, the lack of data often hinders their applications since it is challenging to manufacture and test many structures equipped with identical sensing systems. Model-Assisted Probability of Detection (MAPOD) curves can reduce the amount of requested experimental data. They allow the modeling of many types of variability sources, but the computational cost can be prohibitive due to the *curse of dimensionality*. Surrogate modeling can mitigate this problem and is already available in software such as CIVA [19], [20].

The analysis of the literature (see Chapter 2) shows that in SHM, POD curves were mainly applied to Guided Lamb Waves (GLW) [14], [15], [21]–[28] and occasionally to other techniques such as Comparative Vacuum Monitoring (CVM) [17], [29], Acoustic Emission (AE) [30], [31], and Carbon Nanotube (CNT) [18]. Table 2.A.3 highlights that only a few POD studies on OFS are present, and no POD studies on DOFS are available. Grooteman developed a numerical model of a three-stringer thermoplastic composite panel installed with Fiber Bragg Grating (FBG) sensors and computed the frequency shift in the eigenmodes. Then, using the modal strain energy as a damage indicator, they generated a POD curve using the hit/miss approach [32]. Sbarufatti et al. developed POD curves to quantify the performance of FBGs bonded onto an aluminum stiffened panel in terms of minimum detectable crack length [33]. In this work, the authors compared the confidence interval for a population proportion method [34] with the one-sided tolerance interval for a normal distribution [35].

## 1.1 Scientific Gap and Research Questions

To the best of the author's knowledge, no study presents a rigorous methodology for qualifying DOFS in different scenarios using POD curves. Moreover, MAPOD approaches have never been applied to qualify DOFS. Finally, nobody analyzed how the strain transfer properties of DOFS affect POD curves.

Therefore, the Scientific Research Question (SRQ) being addressed in this Ph.D. research project is:

SRQ *"Is it possible to develop a rigorous methodology to qualify the detection performance of DOFS in composite laminates?"*

This main question will be analyzed focusing on four Scientific Research Sub-Questions (SRSQs):

SRSQ1 *"Which is the most appropriate statistical method to develop POD curves in SHM for DOFS?"*

SRSQ2 *"Is it possible to develop a novel strain transfer model to understand its underlying mechanism and unfold its critical parameters?"*

SRSQ3 *"is it possible to conduct an experimental POD study for DOFSs in composite laminates?"*

SRSQ4 *"Is it possible to develop a MAPOD framework for DOFSs?"*

## 1.2 Thesis Outline

The thesis is structured in two main parts: Part I analyses the state of the art, and Part II presents the main scientific contributions. Specifically, the thesis is structured as follows:

**Part I**

Chapter 1 introduces the research project and the main SRQ.

Chapter 2 provides a systematic literature review of statistical methods to assess the reliability of SHM systems, aiming to answer SRSQ1. At the end of the chapter, Appendix § 2.A condenses the most significant studies. The state of art analysis sheds some light on the scientific gap, thus highlighting the motivation behind this thesis.

Chapter 3 provides a general introduction to OFS and specifically DOFS based on Optical frequency-domain reflectometry (OFDR). At the end of the chapter, § 3.A and § 3.B show a glimpse of potential alternative applications of OFSs.

**Part II**

Chapter 4 develops a novel analytical model, validated through numerical simulations and experiments, to analyze the strain transfer mechanism in DOFS, thus answering SRSQ2.

Chapter 5 presents an experimental methodology to assess the performance of DOFS to detect mode I delamination in Double Cantilever Beam (DCB) specimens under static and fatigue loading, answering SRSQ3. The chapter concludes with Appendix § 5.A, showing a correlated research activity developed with the same experimental data.

Chapter 6 focuses on SRSQ4, developing a MAPOD framework for DOFS taking as a case study the experiments presented in Chapter 5.

Chapter 7 Contains the answer to the main SRQ. It retraces the main stages and achievements of the thesis and suggests potential future research activities.

## 1.3 Graphical Abstract

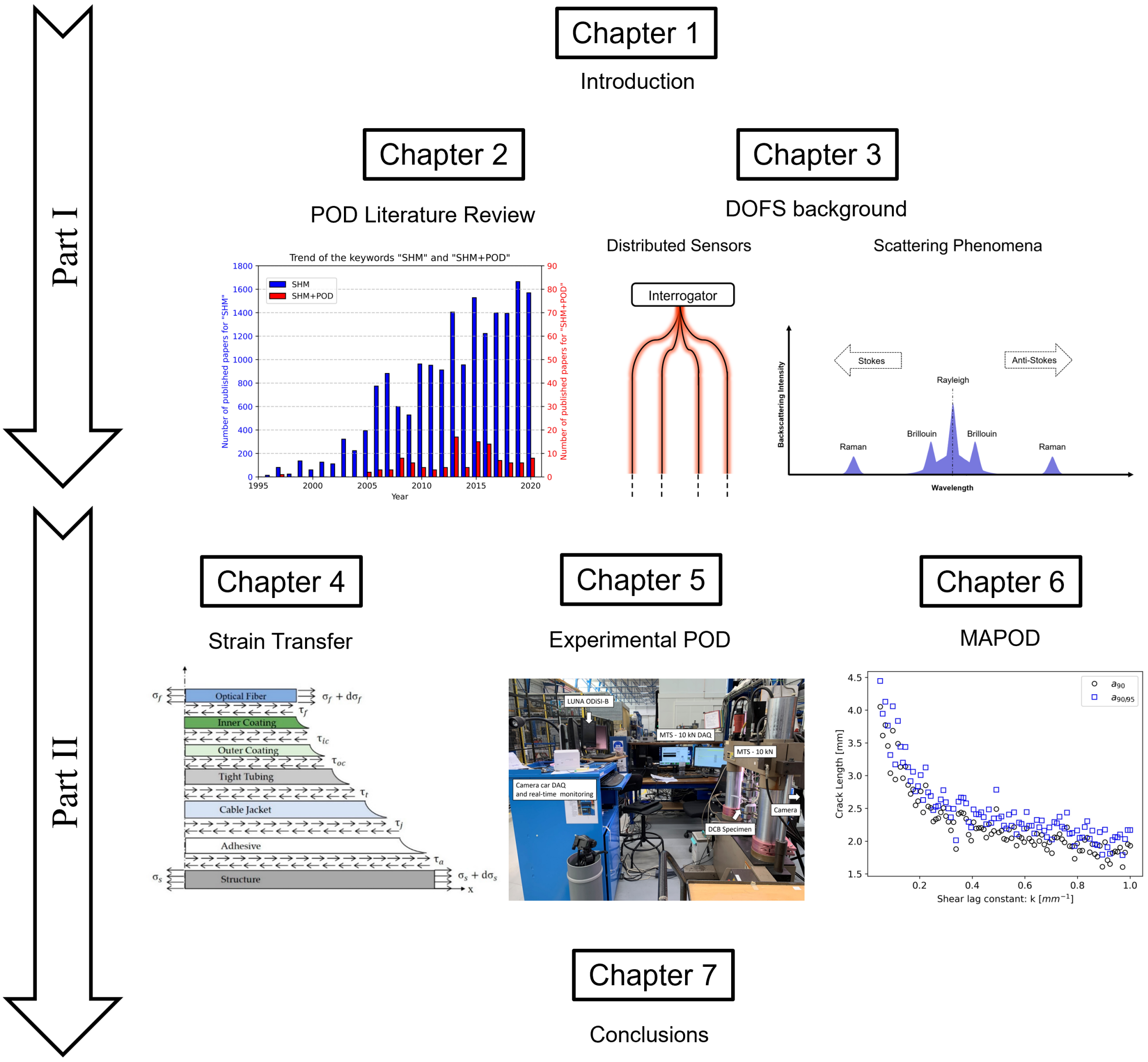

**Figure 1.1:** Graphical abstract of the research.

# Chapter 2

# Probability of detection, localization, and sizing: The evolution of reliability metrics in Structural Health Monitoring

> *Nothing in life is to be feared, it is only to be understood. Now is the time to understand more, so that we may fear less.*
>
> *Marie Curie*

## 2.1 Introduction

**Non-Destructive Evaluation** According to the American Society of Non-destructive Testing (ASNT), Non-Destructive Evaluation (NDE) can be defined as the examination of an object with technology that does not affect the object's future usefulness [36]. The term *evaluation* may be sometimes substituted by *testing*, *inspection*, *investigation*, and *examination*, giving rise to other similar acronyms such as Non-Destructive Testing (NDT) and Non-Destructive Inspection/Investigation (NDI). In practice, all of them express the same engineering discipline. Hellier suggests that a proper definition for NDE could be "a process that does not result in any damage or change the material or part under to examination and through which the presence of conditions or discontinuities can be detected or measured, then evaluated" [37]. Other definitions are also available, such as the one given by the British Institute of NDT: “Non-Destructive Testing (NDT) is the branch of engineering concerned with all methods of detecting and evaluating flaws in materials” [38]. According to Achenbach, NDE was initially thought as an extension of NDI, in the sense that the latter is limited to the damage detection whereas the former should be able to perform also damage characterization [39]. The interest in NDE increased significantly after the famous Aloha accident in 1988 followed one year later by the DC-10 crash in an emergency landing in the Sioux City airport [39]. Since that time, NDE is a continuously evolving field, and increasingly more importance is given to the development of methodologies to quantify the reliability and the performance of the various NDE systems. The increasing complexity of the systems to be monitored and the need of certifying the effectiveness of a given measuring technique fostered the development of statistical tools to evaluate the performance of NDE systems. In general, the main objective of a NDE technique is to determine whether a certain damage is present in the structure under test. However, the natural subsequent step is to develop techniques not only capable to detect a certain flaw, but also to quantify it in terms of size, shape and location [40]. In this case, the term Quantitative Non-Destructive Evaluation (QNDE) is considered more appropriate. Achenbach states that QNDE has become a veritable engineering subject including, not only damage detection and characterization, but also detailed analysis regarding the system validation and its performance reliability [41]. The same author highlights the importance of building a measurement model. Indeed, it can be useful to interpret the experimental data and it might be able to provide numerical results, essential to optimize the testing configuration [42]. From a certain point of view QNDE is the precursor of SHM and its comprehension is important to understand SHM.

**Structural Health Monitoring** The concept of inspection is fundamentally different from the concept of monitoring according to Derriso et al. in three main aspects: the evaluation frequency, the use of previous system outcomes, and the decision range which is possible exploiting the evaluation process results [43]. Therefore, while inspections are conceived to provide a go/no go evaluation related to the health of a structural component, monitoring offers the possibility to take multiple actions thanks to the higher amount of available information.

Farrar and Worden defined SHM as the process of implementing a damage identification strategy for aerospace, civil and mechanical engineering infrastructure [44]. Other definitions are available in the literature [35], [45]–[47], all have the common goal of switching from the current scheduled maintenance philosophy to a condition-based maintenance approach.

Condition-based maintenance empowered by SHM can reduce maintenance costs, inspection time [48] and downtime [45]. The reduced labor requirement of SHM can lead to an increase in safety [39], [45] compared to manual inspections, not only for the personnel, but also for the structure itself which may be accidentally damaged during inspections [49]. For difficult-to-reach area, SHM offers the possibility to overcome the accessibility limitations by permanently installed sensors [50]. The military industry sees SHM as an opportunity to increase the combat asset readiness [10]. The examples of other benefits of SHM are the early detection of damage during normal operational conditions and a drastic decrease of the human factor [48].

In the recent years, the usage of composites has been increasing. However, the complexity of such materials and the presence of a multitude of different possible damage mechanisms still force engineers to use a conservative design approach [47]. The availability of online monitoring data provided by the SHM may enhance the understanding of the new materials and thus leave room to more innovative and closer-to-the-limit design. The reduction of structural design margins can lead to lighter structures. If the structural weight reduction is higher than the additional weight of the monitoring system (sensors, cables, and electronics), lower fuel consumption thus lower $CO_2$ emissions as well as wider design range are expected [45].

A Sandia National Labs report written by Roach in 2011 stated that the Technology Readiness Level (TRL) of SHM systems did not go beyond TRL 8 and the majority were concentrated at TRL 4 [51]. In 2013 Seaver et al. [52] presented a classification of different sensing technologies based on their TRL. At that time, the TRL was ranging from 3 to 9 depending on the specific application. In recent years, several technologies based on ultrasonic permanently installed sensors such as guided wave monitoring and point thickness measurements became commercially successful [53]. However, there are still barriers preventing a complete transition toward SHM. In 2018 Cawley addressed the main reasons of this unsatisfying rate of transition from NDE towards practical applications of SHM [53]. The lack of specific techniques for performance validation, regarding both damage detection and its corresponding false call rate, was identified as a critical point preventing the widespread of SHM. The need of performance validation was also outlined in a recent publication of the same author [54]. The MIL-HKBK-1823A [12] allows the assessment of NDE methods exploiting the concept of POD curves. However, there is a lack of specific guidelines and procedures to evaluate the system monitoring capabilities in the field of SHM [49].

The awareness in the SHM community about the topic of POD curves is still limited. Figure 2.1 shows the number of publications with the keywords *SHM* and *SHM+POD* since 1995. Despite increasing attention to SHM, only few studies were related to POD curves.

The establishment of common certification criteria is fundamental to the application of SHM technologies [55]–[59], and has the potential of improving the design of the system itself [60]. According to Aldrin et al. the qualification of SHM technologies should be based on already present guidelines [61], such as: Cost–Benefit Analysis (CBA) [62], materials and structure certification, NDE metrics (i.e., POD curves)[12], and procedures for performing a Failure Mode, Effects, and Criticality Analysis (FMECA) [63]. In 2011 Aldrin et at. Formulated a protocol [64], mainly based on the already exist-

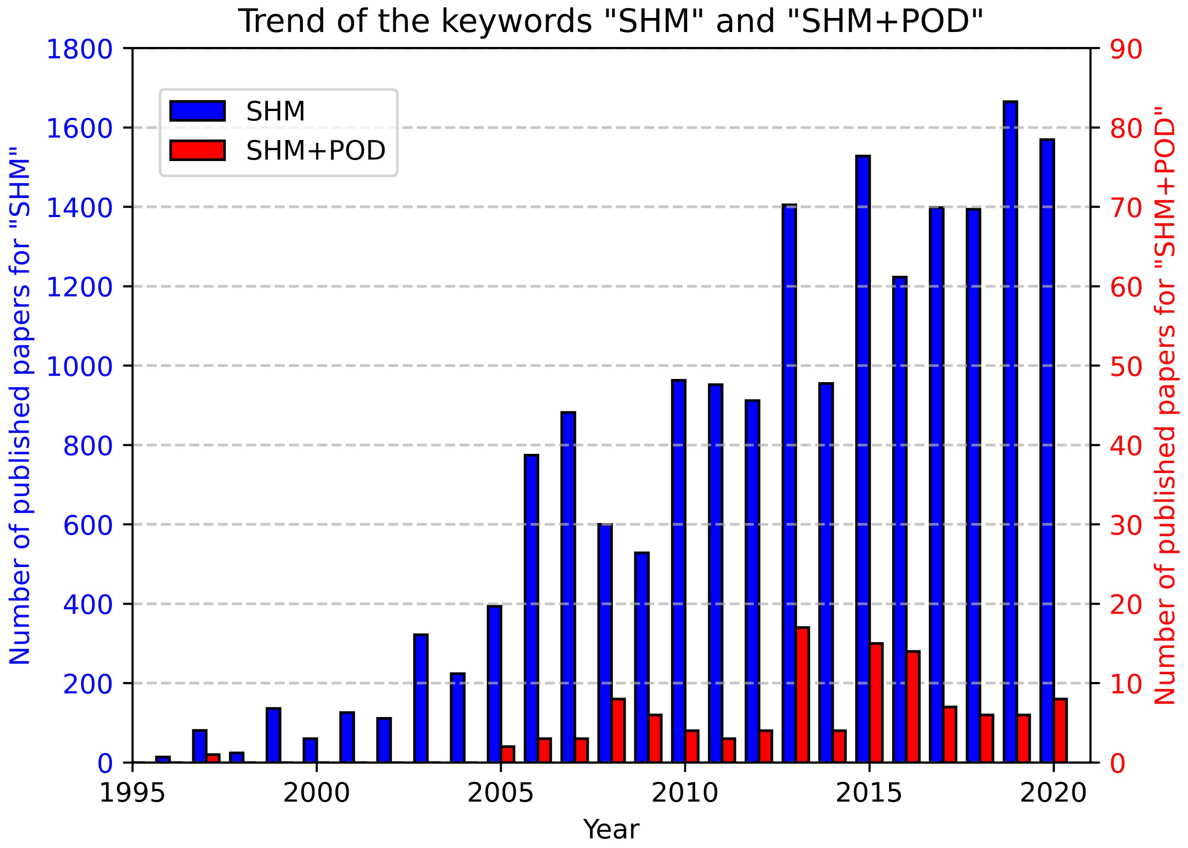

**Figure 2.1:** Trend of the keywords *SHM* and *SHM+POD* analyzing the publications selected from Web of Science Core Collection (May 2021).

ing MIL-HKBK-1823A [12]. One year later, this protocol was applied to a real case study, with promising results [56]. Kessler examined three validation standards [65]–[67], already utilized in the aeronautical sector, in an attempt of identifying potential relationships with SHM applications [68].

The scientific question arising from these preliminary considerations is when it is possible to apply standard POD curves for SHM systems. SHM systems can be classified in four categories [69]. First, it is possible to distinguish Scheduled SHM (S-SHM) systems, from Automatic SHM (A-SHM) [35]. In this case the classification is done according to the way sensor data are collected, scheduled time intervals in the former and continuously in the latter. Second, the damage location can be known KDL or unknown UDL, providing another criterion to further classify an SHM system. According to Janapati et al., only the KDL S-SHM could be evaluated using the standard tools of NDE methods such as POD curves [69]. However, the employment of A-SHM has an increasing trend in the SHM community and it is important to being capable of deriving POD curves even for such cases.

Another fundamental aspect is the need of additional metrics to evaluate the reliability of the system also in terms of damage localization and characterization [56], [57],

[61], [64]. The Model-Assisted Probabilistic Reliability Assessment (MAPRA) methodology follows this line of reasoning [57]. Kabban and Derriso state that, in the perspective of developing a statistical framework for the certification of SHM systems, the system accuracy and reliability should be assessed with respect to three main points: (i) the capability to determine the presence of the damage (detection problem already common in NDE), (ii) the ability to assess the extent, and (iii) the location of the damage [60]. These additional metrics would find their natural allocation within the paradigm of the SHM phases (detection, localization, assessment, prognosis), initially proposed by Rytter in 1993 [70], and successively chosen as a reference in the field [10], [69], [71].

It is interesting to conclude the introduction topic of SHM reliability evaluation with a philosophical question. Could it be necessary to rethink the current regulations and develop new reliability metrics better suited for the advancement of SHM technology? Derriso et at. conceptualized the Cognitive Architecture for State Exploitation (CASE), which resembles the human cognitive behavior and aims to exploit the full potential of a SHM technology, making use of its higher levels (i.e., health management of the full system)[43][72]. Despite the CASE approach demonstrated to be more effective in terms of down time costs with respect the Aircraft Structural Integrity Programs (ASIP) philosophy [73], its full potential cannot be exploited because many of its functionalities should be removed to fulfill the guidelines given in the MIL-HDBK-1823A.

The purpose of this chapter is to provide a systematic review of the existing reliability methods in SHM, highlighting the current challenges and areas where further investigation is required. Most of the attempts to quantify the reliability of SHM systems stem from regulations already present in the NDE field. Therefore, it is important to understand the existing guidelines and the basis to transfer the same concept toward SHM.

Chapter 2 is organized as follows:

§ 2.2 reviews the statistics behind the POD development in NDE.

§ 2.3 examines the variability sources in SHM and their spatial and temporal implications.

§ 2.4 reviews different statistical models to produce POD curves in SHM.

§ 2.5 introduces the concept of Multivariate Probability of Detection (M-POD) using model-assisted methods and metamodels.

§ 2.6 discusses a series of localization and sizing metrics used in SHM.

§ 2.7 summarizes the main findings of the literature review, examining current challenges and areas where further investigation is required.

§ 2.A summarizes in Table 2.A.3 the most relevant case studies analyzed in this literature review.

## 2.2 Reliability assessment in non-destructive evaluation

### 2.2.1 The detection problem

Table 2.1 shows the four possible system outcomes for a detection problem [60], [74].

**Table 2.1:** Possible system outcomes combination in a detection problem.

| | Presence of damage | Absence of damage |
|---|---|---|
| Detection | True positive (TP)<br>Probability of Detection (POD) | False positive (FP)<br>Probability of False Alarm (PFA) |
| No detection | False negative (FN)<br>Probability of false negative (PFN) | True negative (TN)<br>Probability of true negative (PTN) |

The POD is also often referred to as Positive Predicted Probability (PPP) [74], whereas the PFA is sometimes simply called Probability of False Positive (PFP) [60]. In the same manner, the Probability of true negative (PTN) can be named Negative Predicted Probability (NPP) [74]. Summing the probability values of each columns in Table 2.1 always returns the value of one as a direct consequence of set theory [60], [74], [75]. Exploiting Bayesian conditional probability, it is possible to introduce the concepts of *sensitivity* and *specificity*. Calling $P(AD)$ the probability for the structure to be to be healthy (absence of damage), $P(PD)$ the probability for the structure to be not healthy (presence of damage), $P(Det)$ the probability of the system to report a detection, $P(NoDet)$ the probability of the system to do not report a detection, one has:

$$POD = P(Det|PD) = sensitivity \tag{2.1}$$

$$PFA = 1 - P(NoDet|AD) = 1 - specificity \tag{2.2}$$

The POD and PFA are useful in the design phase and to assess the reliability of the measuring system. On the other hand, under operational conditions it can be useful to refer to the other two probabilities: the Positive and Negative Predictive Values (PPV) and (NPV) [60]. The engineer can use the PPV and the NPV to determine the conditional probability that a certain damage is present given that it was detected, which is crucial to take the right choice in terms of maintenance.

$$PPV = P\left(PD|Det\right) = \frac{P\left(Det|PD\right) \cdot P(PD)}{P\left(Det\right)} = \frac{POD \cdot P(PD)}{POD \cdot P\left(PD\right) + PFA \cdot P\left(AD\right)} \tag{2.3}$$

$$NPV = P\left(AD|NoDet\right) = \frac{P\left(NoDet|AD\right) \cdot P(AD)}{P\left(NoDet\right)} = \frac{(1 - PFA) \cdot P(AD)}{(1 - PFA) \cdot (AD) + (1 - POD) \cdot P(PD)} \tag{2.4}$$

The comparison of Equation 2.1 and Equation 2.2 with Equation 2.3 and Equation 2.4 shows that while POD and PFA depends only on the inspection methodology, the PPV, and the NPV depend also on the prevalence. The prevalence is the likelihood of structural damage being present. In a low-prevalence scenario, the PPV can be relatively low even if the POD is high.[60], [76].

### 2.2.2 General considerations on probability of detection curves

Several POD definitions are available in the literature [41], [77], [78]. The NDE reliability studies of Berens, published in the American Society of Metals (ASM) in 1989 [79], provide a first guide on utilizing POD curves. Today, the MIL-HKBK-1823A (Appendix G) [12] contains a detailed description of the process for determining a POD. Using PODs, researchers can compare the effectiveness of various monitoring techniques [80] and calculate the sensitivity and reliability of the inspection process. [81].

Within the ASIP, the United States Air Force (USAF) uses POD curves to evaluate the reliability of numerous NDE techniques [82]. The POD curve can be used in the aerospace industry to conduct risk analyses, plan inspections, predict the remaining useful life of a specific component, and establish acceptance/rejection criteria [83]. POD are also gaining popularity in sectors like the nuclear industry, where they were previously less common [84].

It is essential to have enough data available for a POD study [85]. A good rule of thumb would be to use at least 40 data points [12], [16]. When determining the ideal sample size for a POD study, Annis et al. experienced that beyond $60$ samples, the improvement to the confidence bounds became less significant [86]. The paper by Gandossi and Annis contains additional details [87]. The POD model type also affects the minimum number of samples. For example, a minimum of $60$ samples are required when using logistic models in order to prevent instability [88]. A statistical method for planning a POD study that introduces a dimensionless standardized flaw-size variable is presented in Koh and Meeker [89]. Nevertheless, because it is frequently impractical to produce a statistically significant number of specimens, a considerable amount of effort has been put into developing methods that can reduce the necessary data.

### 2.2.3 Binary (Hit/Miss) data

The first technique for calculating a POD was historically based on the ratio between the number of defects found ($n$), typically cracks, and the total number of defects inspected in the structure ($N$) [12]. A trade-off between the crack length and POD resolution is implied by this method. As a result, new methodologies were created to address these statistical weaknesses. The system only offers qualitative information regarding the presence or absence of damage when dealing with hit/miss data [74]. Generalized Linear Models (GLSs) serve as the foundation for the supporting statistical models. The idea is to use continuous functions bounded in the range $[0, 1]$ like the logit, probit, cloglog, and loglog functions [12] and compute the model parameters using the maximum likelihood criterion [90]. The following references provide more information on POD for hit/miss data as well as the specific statistical techniques used to calculate the corresponding lower confidence bounds [91]–[98].

### 2.2.4 â versus a method

The most widely used technique for determining POD in the NDE field is the $\hat{a}$ *vs.* $a$ analysis. The measurement output is symbolized by $\hat{a}$, and the damage size (i.e., crack length) that caused that measurement signal is represented by the $a$ parameter [12].

#### From regression to probability of detection curve

Ordinary Least Squares (OLS) linear regression is frequently used in engineering. Nevertheless, the OLS would deliver non-conservative results when working with censored data. In these circumstances, other methods, like the Maximum-Likelihood Estimation (MLE), must be employed. However, the result of the MLE method and OLS regression analysis match without censored data [99]. In both situations, if six criteria are met [88], [100], the models' consistency holds.

(C1) The model must reflect the data.

(C2) There must be a continuous and observable response.

(C3) The parameters' linearity needs to be satisfied.

(C4) Homoskedasticity. The variance is uniform about the regression line.

(C5) There must be no spatial or temporal correlation between the observations.

(C6) The errors must be normally distributed.

Finding the appropriate $\hat{a}$ *vs.* $a$ plot is essential in the regression analysis. There are four possible pairings [101]:

(i) $\hat{a}$ vs. $a$.

(ii) $\hat{a}$ vs. $\log a$.

(iii) $\log(\hat{a})$ vs. $a$.

(iv) $\log(\hat{a})$ vs. $\log a$.

Plotting each of the four potential graphs and selecting the one with the best fit is a good practice [88]. The following regression equation describes how the two variables are related to one another when taking into account the $\hat{a}$ *vs.* $a$ case (the same process can be applied to the other three cases as well).

$$\hat{a} = \beta_0 + \beta_1 a + \varepsilon \tag{2.5}$$

Where $\beta_0$ and $\beta_1$ stand for the model's regression coefficients, and $\varepsilon \sim N(0, \tau)$ is the corresponding error term that is normally distributed with zero mean and standard deviation of $\tau$ [12], [15], [16], [80]. The expected value for a is:

$$E(\hat{a}) = \hat{y} = \hat{\beta}_0 + \hat{\beta}_1 a \tag{2.6}$$

Where $E$ stands for the expectation operator and $\hat{\beta}_0$, $\hat{\beta}_1$ are the estimates for the model parameters since the true values of the parameters $\beta_0$ and $\beta_1$ are unknown. The POD curve, whose value corresponds to the shaded area in Figure 2.2, is derived after calculating the regression model parameters.

$$POD(a) = P(\hat{a} > \hat{a_{th}}) = 1 - P(\hat{a} < \hat{a_{th}}) = 1 - \Phi_{Norm}(z) \tag{2.7}$$

In Equation 2.7, $\hat{a}_{th}$ is an arbitrarily imposed threshold value that the engineer chooses. Equation 2.8 gives the value of $z$:

$$z = \frac{\hat{a}_{th} - \hat{y}}{\tau} = \frac{\hat{a}_{th} - (\hat{\beta}_0 + \hat{\beta}_1 a)}{\tau} \tag{2.8}$$

Equation 2.9 provides a different way to express the POD:

$$POD(a) = \Phi_{Norm}\left(\frac{a - \hat{\mu}}{\hat{\sigma}}\right) \tag{2.9}$$

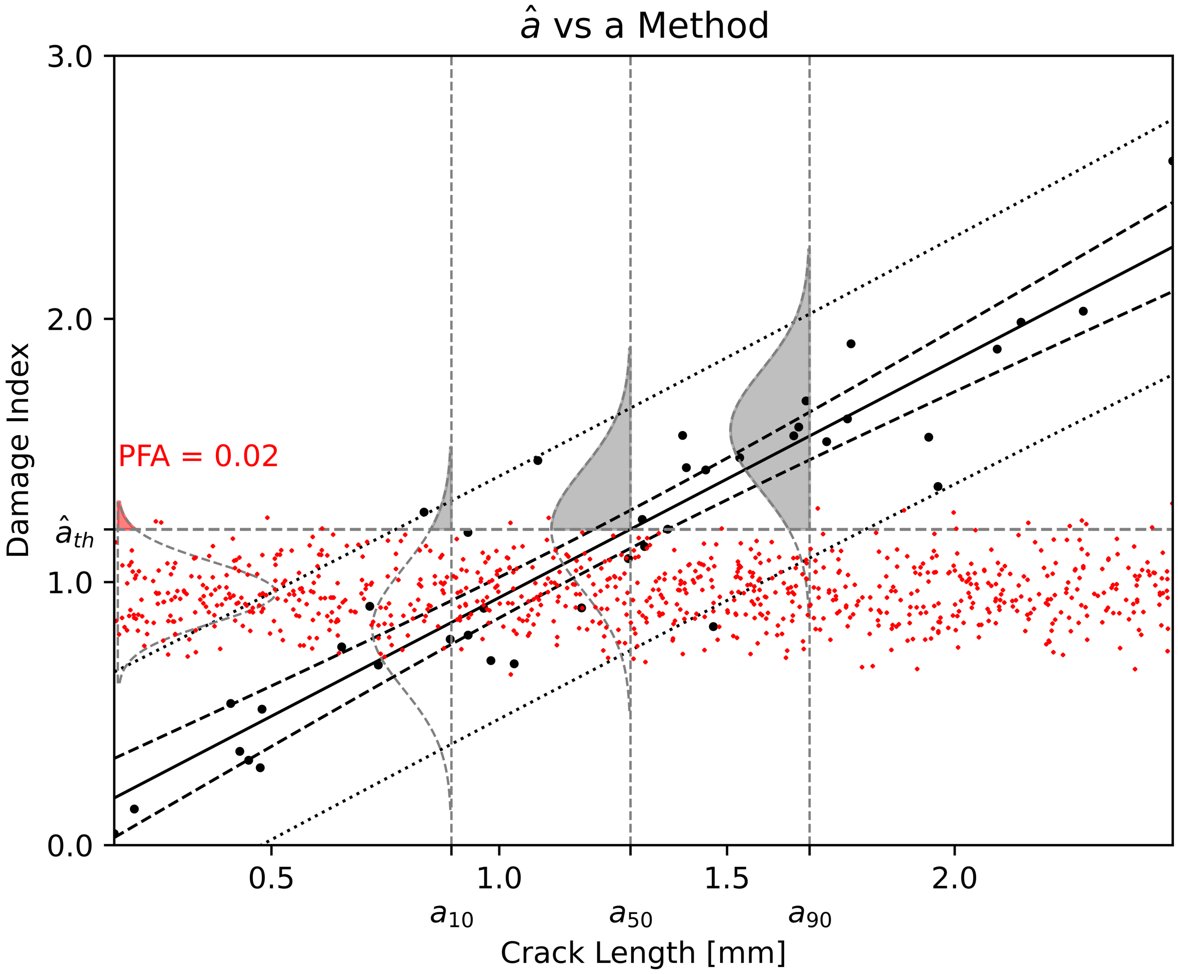

**Figure 2.2:** The solid line represents the expected value for $\hat{a}$, the $95\%$ Wald confidence bounds are shown with dashed lines, and the prediction intervals are plotted with dotted lines. Red dots represent Gaussian noise. Finally, the POD is represented by the grey-shaded portions of the Gaussian curves.

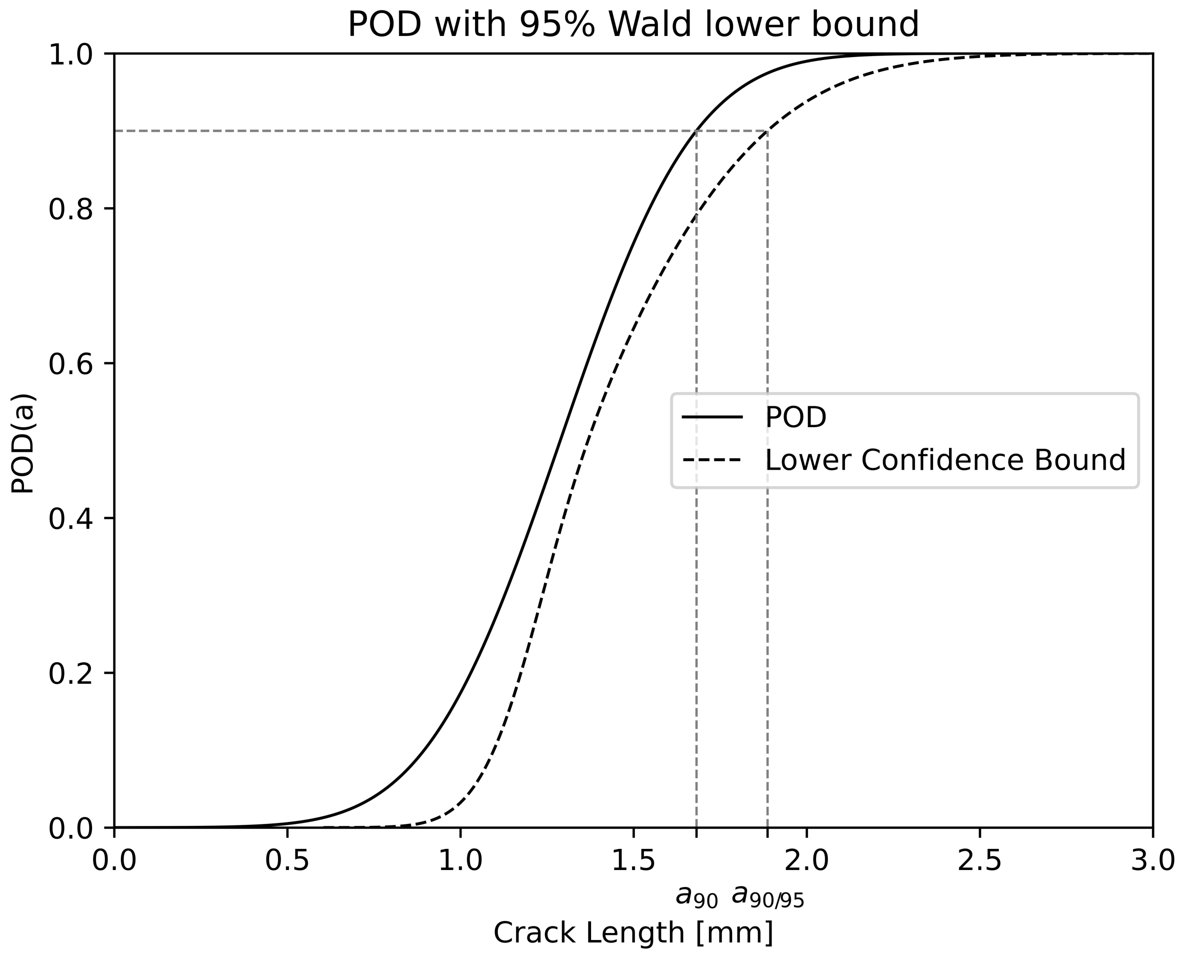

**Figure 2.3:** The POD curve is shown with a solid line, whereas the dashed line represents its lower $95\%$ Wald confidence bound obtained with the Delta method.

.

Equation 2.10 provides the location and shape parameters, $\hat{\mu}$ and $\hat{\sigma}$, respectively:

$$\hat{\mu} = \frac{\hat{a}_{th} - \hat{\beta}_0}{\hat{\beta}_1}; \quad \hat{\sigma} = \frac{\hat{\tau}}{\hat{\beta}_1} \tag{2.10}$$

The estimated crack lengths at which the POD and its corresponding $95\%$ lower bound equal $90\%$ are called $a_{90}$ and $a_{90/95}$, respectively (see Figure 2.3).

### Choosing the right threshold

The detection threshold affects every POD. Therefore, the POD curve would inevitably be improved by arbitrarily lowering $\hat{a}_{th}$ but at the expense of raising the PFA [83]. As a result, the POD of various inspection methodologies can be compared if and only if their PFA is the same [16]. The PFA is calculated using Equation 2.11:

$$PFA(a) = P(\hat{a}_{noise} > \hat{a}_{th}) \tag{2.11}$$

The best threshold ($\hat{a}_{th}$) could be chosen using the so-called ROC graph [102]–[104]. A thorough explanation of the ROC curve and how it is typically used to evaluate classifier performance can be found in Fawcett's papers [13], [105]. The POD obtained with the $\hat{a}$ *vs.* $a$ method depends on the PFA and the flaw dimensions. As a result, a family of ROC curves can be obtained by choosing various flaw sizes [106]. However, there are additional methods for choosing the best decision threshold. According to the MIL-HKBK-1823A, Plotting $a_{90}$, $a_{90/95}$, and the PFA against $\hat{a}_{th}$ allows for the best POD and PFA trade-off [12], [88].

**Probability of detection curve bounds**

Confidence intervals convey the statistical uncertainty brought on by the scarcity of available data [83]. It is possible to divide the computation of the POD lower bound into two steps. First, the Wald method is used to compute the confidence and prediction intervals (the latter differs from the former because it also considers the uncertainty of the observations around the expected mean). Second, these confidence intervals are transferred to the POD curve using a technique known as the Delta Method. The Delta method allows for the computation of the confidence bounds of non-linear functions [107] and can be thought of as a method for estimating the moments of random variable functions [108]. The MIL-HDBK-1823A contains further information on the mathematical foundations of the Wald and Delta methods [12].

## 2.3 Variability sources in structural health monitoring

### 2.3.1 A comparisoon with NDE

It is crucial to record all potential sources of variability in a POD study. Inaccurate estimates of the POD curve can result from incomplete variability considerations [83]. Variability is related to the inherent stochasticity of the phenomenon under investigation. [16]. As a result, adding more data would reduce the confidence bounds rather than the variability. Li et al. suggested using the $0.05$ POD quantile estimate for accounting for the inherent population variability and then calculated its lower confidence bound to account for the uncertainty affecting the model parameters [109]. When an engineer wants to consider the worst-case scenario, referring to a small quantile of the POD curve may be a better option [110].

One potential source of variability in NDE is the actual morphology of the cracks [111], [112]. Because of the instrument manufacturing process, some variability may be associated with the sensing device. The signal output of a particular measuring technique may change depending on environmental factors like temperature and humidity

[16]. Eventually, among all the sources of variability, the human factor contribution in NDE systems is frequently thought to be the highest [113], [114].

In locations where typical NDE inspection is impractical because of complex geometries and accessibility issues, the SHM system can typically acquire data automatically [50]. However, it is not entirely accurate to say that SHM systems are not subject to human variability. The installation phase of the sensing apparatus is, in effect, a source of human-related variability [113].

All the variability sources of NDE methods are generally carried over into structural health monitoring. Examples of variability sources impacting NDE and SHM systems include the manufacturing process (sensors, interrogators, test structures, etc.) and damage morphology [16], [112].

A POD study in SHM should also take into account additional factors. For example, permanently installed sensors in SHM are prone to degradation over time, affecting the POD curve [99], [115]. Depending on the technique, degradation may affect the sensor/structure coupling through adhesives, welds, or dry couplings. In addition, changes in the structure as a result of maintenance procedures can also impact the monitoring performance.

Environmental and Operational Conditions (EOCs), such as temperature, moisture, pressure, and chemical loading, can potentially be detrimental in SHM [116]–[118].

In addition, the loading condition of the structure, which is subject to change over time (take-off, cruising, maneuvers, and landing), represents another source of variability.

Another point to ponder in SHM is the reciprocal position of sensors and damage. Because sensor location is a significant source of variability, it is essential to evaluate how the POD curves of SHM systems relate to the location of defects [28], [69], [99].

Furthermore, the on-board SHM device may cause changes in the recorded signal response [16]. For instance, self-powered sensors can transmit the monitoring data with a wireless connection to an on-board memory storage device. In such a case, Mandache et al. suggest that electromagnetic interference with avionics is a potential source of variabilities [119].

In conclusion, while the human factor is the principal source of variability in NDE, it is possible to separate the variability sources into spatial (location uncertainty) [21], [28], [69], [99], and temporal (environmental effects, [26], [113], [114] aspects in SHM.

Table 2.2 outlines the most significant differences between NDE and SHM in terms of variability sources.

**Table 2.2:** Variability Sources: NDE vs. SHM.

| | Variability Sources | NDE | SHM |
|---|---|---|---|
| Aging | Sensor degradation | N | Y |
| | Coupling degradation | N | Y |
| Damage-related | Damage morphology | YY | YY |
| | Reciprocal sensor/Flaw location | N | YY |
| EOCs | Loading conditions (stress/strain) | N | YY |
| | Chemical loading | Y | YY |
| | Humidity | Y | YY |
| | Pressure | Y | YY |
| | Temperature | Y | YY |
| Human factor | Data interpretation | Y | Y |
| | Measurement procedure | YY | N |
| | Installation process | Y | Y |
| Manufacturing process | Damage morphology | Y | Y |
| | Reciprocal sensor/Flaw location | Y | Y |
| Data communication and storage | Damage morphology | Y | Y |
| | Reciprocal sensor/Flaw location | N | Y |

Variability source not present → N; Variability source present → Y; Dominant source of variability → YY.

### 2.3.2 Spatial aspects of probability of detection

#### Optimal sensor placement using probability of detection

Numerous authors have investigated spatial variability sources in SHM [21], [23], [120]. Often, the impact of the damage location on POD curves results in an Optimal Sensor Placement (OSP) problem [21]. In fact, POD curves in SHM systems may be used not only to quantify system performance but also to design the SHM system itself, choosing the best sensor location. Tan and Zhang recently summarized the main developments in the OSP field in a review article [121]. The research by Flynn and Todd, who were among the first to use the ideas of POD and PFA to develop a framework for OSP, is an essential reference [122]. Azarbayejani et al. maximized POD curves to perform OSP [123]. Markmiller and Chang, in a study concerning the structural dynamic response after an impact, leveraged POD curves as a design constraint to perform OSP [124]. Mallardo et al. exploited POD curves to analyze the performance of an artificial neural network for the localization of impacts in a composite plate and a composite stiffened panel. The OSP was selected to maximize the POD curves associated with various sensor combinations [125], [126]. Yan et al. estimated the best sensor configurations using a model-assisted POD approach [127]. By utilizing POD curves, Chen et al. identified the ideal Lamb waves driving frequency for spotting the emergence of a fatigue crack in a metallic specimen [128]. To determine the best optical fiber layout in a stiffened composite panel, Grooteman used POD as an objective function [32]. In a Guided Lamb Waves (GLW) study, Tabjula et al. employed outlier analysis to reduce the number of sensing points and POD to measure system performance [129].

### Specimens versus test structures

A POD study is conducted using multiple samples in NDE. Analogously, one should use multiple identical structures in SHM. However, this complicates applying an already costly procedure since this requires a series of identical sensing systems. Müller et al. demonstrated that this is not attainable in real applications and is only theoretically possible because of the variability involved in the manufacturing process and sensor installation [113]. Therefore, the POD curve will apply only to that specific structure and sensing network configuration utilized to perform the POD study. In a US patent related to Acellent Technologies, Liu and Chang suggest simulating damage by bonding stiff metal or damping patches into the structure to build a POD database for a large structure [130]. However, the authors also noted that this could be a limiting factor since a database built with real flaws is expected to produce more accurate results. The introduction of real damages implies that the damaged structure might not be reusable, which increases the time and cost. Implementing real defects increases the time and costs because the damaged structure becomes unusable for future tests.

### Decision threshold for structural health monitoring systems

Data related to damaged structures might not always be available, or if it is, it might not be statistically relevant. In such circumstances, one could use unsupervised learning algorithms, which are capable of selecting the most appropriate threshold [10]. The literature in the area of novelty detection contains a wide range of techniques. Some methodologies, like *outlier analysis*, demand the feature vector to be normally distributed [131]. Other methods, like *extreme value statistics* [132], can determine the best threshold value without using the normality assumption. Markou and Singh outlined the essential statistical [133] and neural network-based [134] approaches. Cobb et al. advise using a hit/miss strategy for SHM systems due to these additional difficulties in establishing a suitable threshold [135]. Monaco et al. suggest a method based on a statistical noise analysis to assess the threshold of an SHM GLW problem [74]. The Kolmogorov-Smirnov test is employed in their study to reject the null hypothesis (the experimental data did not follow a Gaussian distribution). Memmolo et al. employed the same method for choosing the most appropriate threshold using a tomography technique based on GLW to optimize the damage detection problem in a composite plate [136]. In Yue et al.'s study [137], the authors used outlier analysis to detect multiple barely visible impact damage (BVID) in large composite aircraft panels. For this purpose, a pristine reference database was generated using coupons and mono-stringer panels varying the temperature over a wide range.

### 2.3.3 Temporal aspects of probability of detection

Temporal aspects in a POD study can be tackled using Sequential Data Analysis (SDA). SDA allows dealing with slowly evolving spurious signal variations due to EOCs, defect morphology, sensors drift, and other kinds of variability sources.

#### Sequential data analysis

EOCs represent the principal source of variability in SHM, as shown in Table 2.2. Therefore, it is vital to consider how they might impact the performance of the SHM system. In NDE, measurements for specific damage at various EOCs are possible, but it is impossible to accomplish the same in SHM. The entire history of the EOCs has an impact on the SHM detection results. Additionally, this is combined with damage evolution, necessitating the study of a massive number of structures.

Temperature, for example, has been reported to be the dominant effect among EOCs in ultrasonics SHM studies [118], [138]–[140]. The Baseline Signal Stretch (BSS) and the Optimal Baseline Selection (OBS) are the two primary methods for temperature compensation (BSS). The OBS methodology is well described in the Lu and Michaels paper [141]. The BSS methodology is employed in many studies, including Croxford et al. [142], Michaels [143], Clarke et al. [140] and Harley and Moura [144]. For adequate temperature compensation of significant temperature variations (up to 70°C) [145], and anisotropic materials [146], data-driven methods have recently been developed.

Liu et al. presented a hybrid procedure to deal with the slowly evolving spurious signal changes caused by EOCs [26]. They observed the signal response of a pipe monitoring system structure under various EOCs in the pristine case. The signal change due to damage was then artificially superimposed onto the undamaged signal. The authors used a BSS algorithm for temperature compensation. Finally, they compared the results obtained with the baseline subtraction, Singular Value Decomposition (SVD), and Independent Component Analysis (ICA) damage feature extraction techniques. The ICA method was the most effective at creating trustworthy ROC curves.

Mariani and Cawley recently reviewed other temperature compensation methods [24]. One of them is the location-specific temperature compensation (LSTC), which demonstrated promising results for torsional guided wave signals in pipe monitoring, leading to a patent [147][148][149]. Mariani and Cawley also presented a change detection algorithm based on the Generalized Likelihood Ratio (GLR)[150] and investigated the damage detection performance using data obtained with the LSTC or OBS methods [24]. Their approach demonstrated to be sensitive to changes from the undamaged condition. Nonetheless, the methodology is only applicable if there is no sensor drift, being one of the essential hypotheses of the change detection algorithm. To address the sensor drift issue, Mariani et al. proposed a novel methodology, using as a case study a thick copper block specimen [151]. They reduced the impact of PZT sensor drifts, taking advantage of the back wall echo ratio. In a recent article, causal dilated convolutional neural networks were employed to account for sensor drift and EOCs [22]. This last approach, which stems from WaveNet (a deep neural network for audio waveforms) [152], showed superior performance compared to the OBS and BSS methods.

## 2.4 Probability of detection for structural health monitoring

It is frequently claimed that the primary distinction between NDE and SHM in terms of POD curves is that subsequent inspections are independent in the former and correlated in the latter. This assertion is not entirely accurate. It would be more appropriate to say that the degree of statistical independence within repeated measurements is more significant in NDE than in SHM. Only random events possess the property of statistical independence, to be exact.

For instance, Forsyth simulated the effect of performing repeated liquid penetrant and eddy cuurent testing inspections showing that the assumption of *full independence* does not hold [81].

It follows a fortiori that the independence hypothesis also does not hold in SHM, where the monitoring systems can record continuous data streams from the structure. This temporal correlation within subsequent measurements prevents conventional statistical techniques from producing POD curves and represents one of the biggest challenges thwarting the widespread adoption of SHM [72].

Shook et al. formulated a mathematical model to obtain POD curves for repeated dependent data [153]. Eliminating some information might be a strategy to preserve data independence. Nonetheless, this solution would compromise the overall performance of the SHM system [15]. Therefore, several researchers conducted studies aiming to generalize the construction of POD curves in SHM [16].

This section presents three POD methods conceived for SHM:

1. The Length at Detection (LaD) method;

2. The Linear Mixed-effect Model (LMM);

3. The Random-Effects Model (REM).

### 2.4.1 The length at detection method

The LaD method was used by Roach et al. in 2007 [154], and Roach in 2009 [17], to investigate the effectiveness of Comparative Vacuum Monitoring (CVM) in specimens made of steel and aluminum. Sbarufatti et al. [33], [155] used Fiber Bragg Grating (FBG) sensors to monitor fatigue cracks on the tail boom stringers and fuselage panels of a helicopter. They also developed a model-assisted framework and applied the LaD method to estimate the detection performance of the system.

The LaD method removes the correlation of repeated data considering only the measurement when the crack, or more in general damage, is first noticed [16]. Detection is made when the system returns a signal exceeding a user-defined threshold. Each crack/sensor pair provides a length at detection. Therefore, the final result is a population of lengths at detection with a specific statistical distribution. The cumulative function of this distribution represents the corresponding POD [156]. Determining which is the correct probability distribution to utilize is not straightforward. If the crack population exhibits a Gaussian distribution, then:

$$POD(a) = P(X < a) = \Phi_{Norm}\left(\frac{a - \bar{x}}{s}\right) \tag{2.12}$$

Likewise, if the crack population fits a lognormal distribution, Equation 2.12 is replaced by Equation 2.13:

$$POD(a) = P(X < a) = \Phi_{Norm}\left(\frac{\ln a - \bar{x}}{s}\right) \tag{2.13}$$

The sample mean and standard deviation are represented, respectively, by the variables $\bar{x}$ and $s$. The hypothesis that the crack population at detection follows a normal or lognormal distribution is not straightforward to verify and can limit the application of this method. The use of the notorious Anderson-Darling test is one option [157]. If the p-value returned by the test is less than 0.05, which stands for the selected significance level, the assumption made on the statistical distribution (normal or lognormal) is rejected [156].

Another helpful tool for testing the assumptions above is a probability plot. First, the distribution obtained in the experiments is plotted against the theoretical normal (or lognormal) distribution. Then, the population follows the theoretical probability distribution if the plot is a straight line. Even for other types of statistical distributions, such as the largest extreme value and Fréchet distribution and the smallest extreme value and Weibull distribution, the LaD methodology still holds [16]. Meeker et al. provide more details about these distributions in Appendix C of their book [158].

The LaD method working principle is simulated and visualized using synthetic data in Figure 2.4.

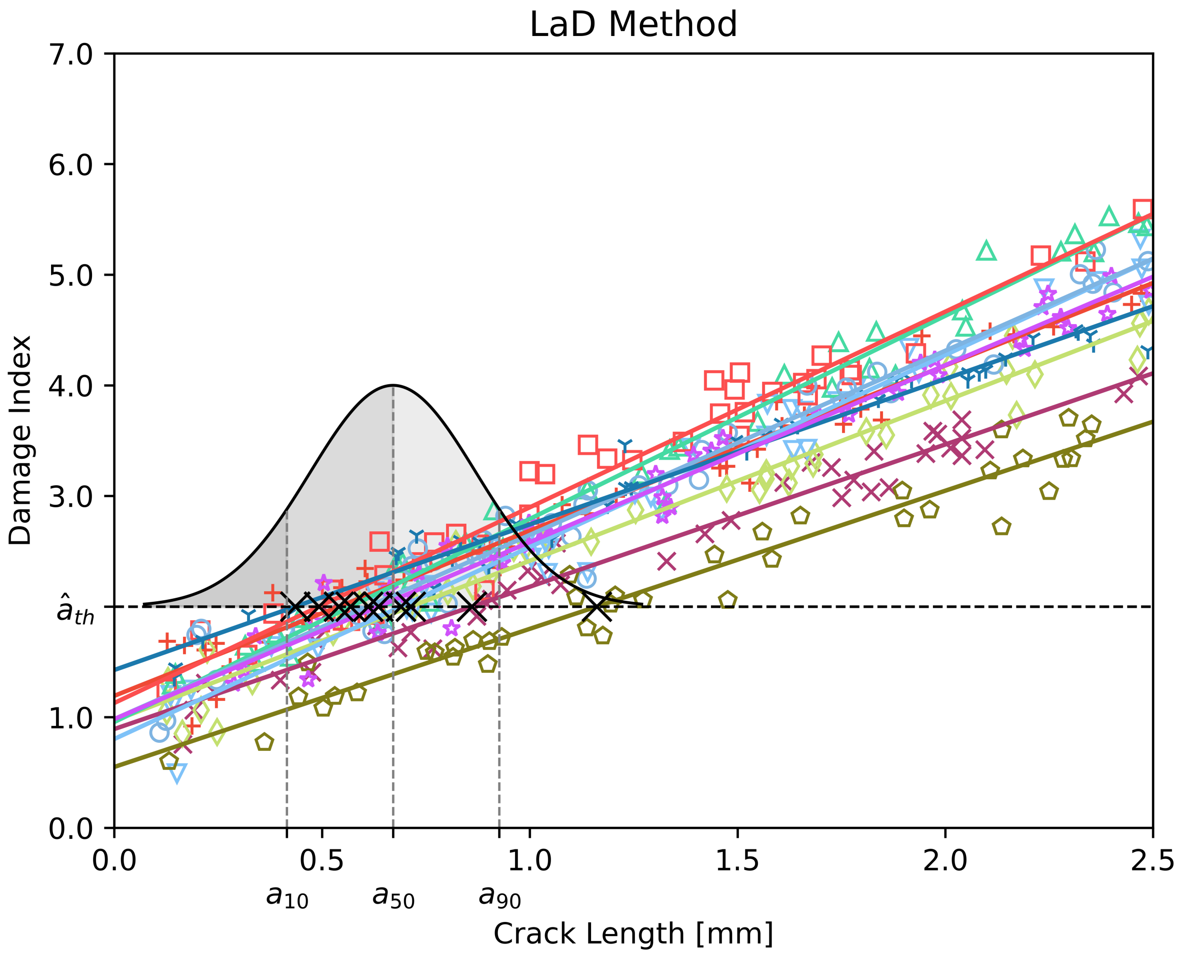

**Figure 2.4:** LaD method was used with 10 samples (shown by different markers); there are 40 measurements on each specimen.

Statistical techniques based on the non-central t distribution [16], [158], or the One-Sided Tolerance Interval (OSTI) method, are used to obtain the confidence bound. Roach was the first to suggest this method for the CVM-based detection of fatigue cracks. It offers an estimate for the upper bound, depending on the detection (usually set at $90\%$) and confidence (typically equal to $95\%$) levels [49]. It has been reported that the OSTI approach can provide consistent results even with less than ten data points [159]. Employing the same nomenclature used by Roach [17], Equation 2.14 returns the upper bound for the tolerance interval:

$$T = \bar{x} + K_{n,\gamma,\alpha} \cdot s \tag{2.14}$$

The tolerance interval is denoted by $T$, while $\bar{x}$ and $s$ represent the mean and standard deviation of the detection lengths, respectively. The probability factor, $K$, depends on three parameters: (i) the sample size $n$, (ii) the confidence level $\gamma$, and (iii) the detection level $\alpha$ [160]. Specific tables available in the literature provide the value of K; for example, see the work of Meeker, Hahn, and Escobar [158] or Krishnamoorthy and Mathew [161]. As the sample size decreases, the probability factor increases, thus introducing a penalty for the low number of data points [49]. High confidence levels also increase the value of $K$, which is expected. Eventually, the detection level $\alpha$ is also positively correlated to $K$ since higher detection levels must translate into longer crack lengths.

### 2.4.2 Linear mixed-effect model

OLS or MLE cannot be applied for time-dependent data because the observations are correlated [100]. Generalized least square models, which Aitken first studied in 1936 [162], can handle such time dependency [15]. Another possibility is to employ a linear mixed-effect model (LMM). This method goes beyond traditional linear models and is appropriate for time-dependent datasets. The acronym LMM tells that the *model* is *linear* and contains a *mixed effect*. The mixed effect consists of a *random effect*, which could be the intercept or the slope, and a *fixed effect* that expresses the expected data pattern. In 2015, Kabban et al. proposed to use the LMM model to generalize the traditional $\hat{a}$ vs. $a$ approach for time-dependent data with a random intercept for each experimental unit (EU). [15].

Equation 2.15 gives a mathematical description of the LMM model:

$$\begin{gathered} \hat{a}_{ij} = \beta_0 + \beta_{0i} + \beta_1 a_{ij} + \varepsilon_{ij} \\ i = 1, ..., n; \quad j = 1, ..., m \end{gathered} \tag{2.15}$$

The term $\hat{a}_{ij}$ refers to the $j^{th}$ measurement from the $i^{th}$ EU, whereas $a_{ij}$ denotes the real crack length. The symbols $\beta_0$ and $\beta_1$ represent the two fixed regression coefficients. Finally, the random intercept and the error term are expressed in Equation 2.16:

$$\beta_{0i} \sim \mathcal{N}(0, \omega^2); \quad \varepsilon_{ij} \sim \mathcal{N}(0, \tau^2) \tag{2.16}$$

Where $\mathcal{N}$ denotes the normal probability distribution, and $\omega^2$ and $\tau^2$ are the random intercept and error term variances, respectively. From a statistical perspective, this differs significantly from the conventional model shown in Equation 2.5. In Equation 2.15, the response depends on the error and the random effect variances, implying that measurements taken from the same EU are correlated and that measurements from different EUs are independent. The marginal model, which returns an expected value by averaging all the random effects, can be used to derive the parameter estimates.

### 2.4.3 Random effects model

This model, also known as the Repeated Measures Random Effects Model (REM$^2$)[18], is a generalization of the $\hat{a}$ vs. $a$ method presented in the MIL-HKBK-1823A [12]. Additionally, it advances the LMM model proposed by Kabban et al.[15] because it supports random intercepts and random slopes. Therefore, the set of fitted responses of each crack-sensor pair would produce a series of lines, each with a different slope and intercept. Consequently, the technique calculates the joint distribution of these parameters [16]. The REM$^2$ is described by Equation 2.17:

$$\begin{gathered} \hat{a}_{ij} = \beta_{0i} + \beta_{1i}(a - \bar{a}) + \varepsilon_{ij} \\ i = 1, ..., n; \quad j = 1, ..., m \end{gathered} \tag{2.17}$$

The term $\hat{a}_{ij}$ stands for the $j^{th}$ measurement response of the $i^{th}$ crack-sensor combination. For instance, $\hat{a}_{ij}$ could be a scalar value expressing a user-defined damage index. The regression coefficients $\beta_{0i}$ and $\beta_{1i}$ replace $\beta_0$ and $\beta_1$, which were used in the classic $\hat{a}$ vs. $a$ method. Likewise, also the error term, $\varepsilon_{ij}$ now differs for each crack-sensor pair. Finally, it should be highlighted that in the REM$^2$ the slope coefficient, $\beta_{1i}$, multiplies the crack length $a_{ij}$ subtracted by the sample mean of the crack lengths, $\bar{a}$.

Equation 2.18 provides the POD expression:

$$POD(a) = P(a > a_{th}) = 1 - \Phi_{Norm}(z) \tag{2.18}$$

Where $a_{th}$ is the detection threshold defined by the engineer. Equation 2.19 shows the expression of $z$:

$$z = \frac{a_{th} - [\mu_{\beta_0} + \mu_{\beta_1}(a - \bar{a})]}{\left[\sigma_{\beta_0}^2 + (a - \bar{a})^2 \sigma_{\beta_1}^2 + 2(a - \bar{a})\sigma_{\beta_0}\sigma_{\beta_1}\rho + \sigma_{\varepsilon}^2\right]^{\frac{1}{2}}} \tag{2.19}$$

Where $\mu_{\beta_0}$, $\mu_{\beta_1}$ and $\sigma_{\beta_0}$, $\sigma_{\beta_1}$ represent the mean and the standard deviation of the intercepts and slopes evaluated at the crack size equal to $\bar{a}$, respectively.

Similarly, the standard deviations of the intercepts (estimated at the crack size equal to $\bar{a}$) is denoted with $\sigma_{\varepsilon}$. Lastly, the value of $\rho$ reflects the correlation between the slopes and intercepts. In Figure 2.5 the REM$^2$ is applied to a synthetic dataset.

The MLE can be used to compute the POD lower bound. Nevertheless, Meeker et al. show how Bayesian methods with weekly informative priors can also be employed to obtain the lower bound [16].

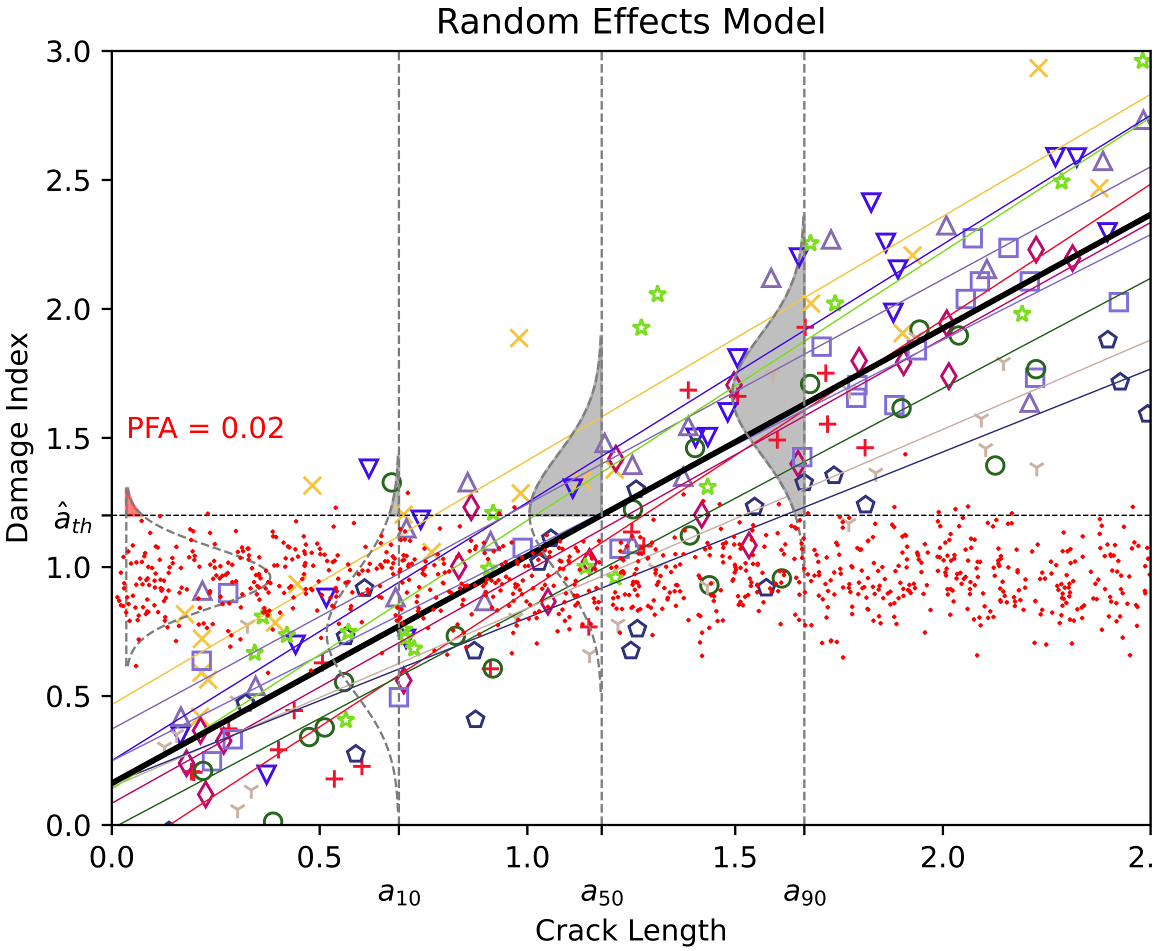

**Figure 2.5:** REM$^2$ method was applied to 10 specimens, each one with 20 measurements. The red dots indicate measurements due to noise.

### 2.4.4 Comparison between length at detection and random effects model methods

This section discusses the main distinctions between the LaD and the REM$^2$ methods. However, since the REM method generalizes the LMM approach, this analysis does not consider the latter.

LaD and REM models provide two statistical techniques for assessing POD curves in SHM. For example, the LaD method was used to assess the reliability of CVM in aerospace structures. Within the Federal Aviation Administration's (FAA) research program in SHM, which was launched in 2011, the principal original equipment manufacturers (OEMs) and airline operators like Boeing and Delta have recently begun to accept the use of this strategy in the United States [163]. However, the LaD approach does not fully utilize the potential of the particular SHM application because it ignores some information. Additionally, it necessitates assuming a specific crack length at detection distribution, which is not always simple to verify. The REM$^2$, on the other hand, makes use of the entire dataset, which also suggests that the model is more resistant to deviations from the model hypotheses. Furthermore, its compatibility with a model-assisted approach, which is even more significant, makes it very appealing for upcoming applications. O'Connor conducted a study to quantify the differences between these two statistical approaches [164]. Compared to the REM$^2$, the LaD method appeared more appropriate when few observations were available (less than 10) due to the impossibility of fitting a 5-parameter REM$^2$. However, it also emerged that with the LaD method, it is challenging to verify the use of a specific distribution (normal or lognormal). Consequently, since the LaD requires less computational effort, it might be preferred in some engineering applications. O'Connor calculated $a_{90}$ for various datasets and used it as a benchmark. When the normal distribution approximation of the crossing lengths was inappropriate, the LaD overestimated the $a_{90}$ [164]. Nevertheless, this error could be tolerated from an engineering standpoint because it goes toward a conservative prediction. Except for cases where the $\sigma_{\beta_1}$ value was high, the results from the two methods were comparable. Usually, the parameter used to describe the damage in the LaD and REM models is the crack length. However, more variables could impact the signal response in real applications, so it could be more appropriate to consider a vector rather than a scalar value. In such a case, the current formulation of the models should be generalized to handle a *damage vector*.

Previous literature tended to ignore data dependency, but current research shows that this is not the best course of action. Although these statistical techniques are still relatively new to the SHM field, they have already been used in several case studies. LaD and REM approaches were recently adopted by Kessler et al. to derive POD curves [18]. The authors employed the 4-point bend test to determine crack growth from an Electrical Discharge Machined (EDM) notch on aluminum bars. With the help of a carbon nanotube (CNT) sensor, which has much potential for aerospace applications, they kept track of crack propagation [165]. Using Meeker's methodology [16], a recent study used a Bayesian approach to derive POD curves for various case studies [166]. The relationship between the damage index and the damage size was nonlinear, which is common in most SHM systems based on ultrasound techniques. However, the authors recovered linearity by applying a logit transformation to the damage index.

## 2.5 Multivariate probability of detection

One parameter might not be enough to describe the defect characteristics accurately. Therefore, Bode et al. created POD curves based on defect size and percent corrosion to assess the corrosion in aircraft structures [167]. Lee et al. developed a M-POD surface based on a multivariate log-logistic regression model based on hit/miss detection. They considered the length and depth of a defect as parameters in an ECT application [168]. In another ECT study, Hoppe extended the traditional $\hat{a}$ vs. $a$ method to develop a M-POD as a function of crack length and depth [169]. In a study similar to Hoppe's earlier research, Aldrin et al. in 2012 concluded that including both the crack depth and the length reduced model uncertainty by about $20\%$ [170]. The same authors used VIC-3D©, a physics-based model, to account for several parameters, thereby decreasing the variability and sample requirements. Another case study on the ECT of fastener sites for fatigue cracks [171] showed that the calibrated physic-based model outperformed the traditional $\hat{a}$ vs. $a$ method because it considered more parameters than just the crack length [172]. A M-POD approach was used by Pavlović et al. for an ultrasonic examination of a cast iron component [173]. This method made it possible to compute many POD curves as a function of a chosen variable while keeping the values of the other parameters constant. Yusa and Knopp remarked that the M-POD in Pavlović et al. relies on 12 coefficients which are not easy to compute, and stated that it is unlikely to have a uniform variance [174]. For this reason, they proposed a multi-parameter strategy where, in contrast, the variance depends on the parameters rather than being constant. In a different study, Gao et al. describe the response of a vibrothermography test as a function of vibration amplitude, pulse length, trigger force, and crack length using a linear mixed effect model [175].

M-POD studies on SHM systems, characterized by permanently mounted sensors, have only recently been studied. Due to their mathematical framework, which offers the possibility of incorporating the additional variability sources present in SHM systems, M-POD models are particularly appealing. However, using a model-assisted approach appears to be inevitable for implementing M-POD into real SHM applications.

### 2.5.1 Model-assisted probability of detection

MAPOD curves are based on NDE, but they can be leveraged for SHM studies [16]. The Pacific Northwest report, written by Meyer et al. in 2014, contains a thorough analysis of MAPOD studies [176]. Thompson pioneered this field of study by leading the MAPOD Working Group at Iowa State University from 2003 to 2010 [177].

One of the purposes of a MAPOD study is to collect data using a physics-based model, thus reducing the amount of experimental data necessary to produce a trustworthy POD [178]. There are two main MAPOD methodologies [83], [178]:

- the MAPOD - Transfer Function (MAPOD - XFN) approach;
- the MAPOD - Full Model-Assisted (MAPOD-FMA) approach.

**MAPOD - Transfer Function approach** The MAPOD - XFN takes advantage of the relationship between the output signal of natural and artificially produced flaws, which are easier and less expensive to produce [179]. Utilizing the MAPOD - XFN approach, one can start from an existing empirical POD curve for a specific technique and transfer these results to another comparable configuration. Then, a physical model or particular laboratory tests may be used to compute the underlying transfer function [180].

**MAPOD - Full Model-Assisted approach** The MAPOD-FMA approach attempts to capture all the variability sources and combines the data collected from physics-based models with empirical knowledge, such as experimental noise, to predict the signal strength of a specific NDE/SHM technique as a function of various parameters and flaw properties [180], [181]. The MAPOD-FMA approach was initially used for ultrasonic testing methods, but the approach can be considered general and applied to other sensing techniques [83].

Thompson showed that the MAPOD - XFN and MAPOD-FMA strategies are two sides of the same coin [180]. A protocol for a unified approach to MAPOD was issued in 2008 [178], and it was later incorporated in the MIL-HKBK-1823A [12].

Gianneo et al. employed the MAPOD approach in a study about GLW propagating in a lightweight material [28], [117], using the work of Pavlović et al. [173] as a reference. The authors developed a M-POD curve, referred to in the paper as the *master* POD. Then, they obtained a series of *classic* POD curves as a function of single parameters, such as the angle with respect to the PZT sensors, the Lamb wave mode ($A_0$ or $S_0$), and the defect size. The other parameters, however, were regarded as random variables.

When using numerical models, the *known unknowns* significantly impact how well they capture all the sources of variability [182]. Previous knowledge about the critical variables is essential to implement them into the numerical models and to obtain the correct variability information from the experiments. Memmolo et al., for instance, chose to employ a MAPOD strategy for a GLW-based technique [183]. They incorporated variability by superimposing random noise to the FEM model output and randomly varying the damage-related parameters, such as the morphology and the position in the structure. Tschoke et al. investigated the viability of MAPOD to produce POD maps in a CFRP automotive component and obtained encouraging results [23]. Given that the damage location is considered an additional parameter, this can be regarded as an M-POD. Similarly, Leung and Corcoran assessed the POD spatial distribution and combined it with the probability of defect location [21].

### 2.5.2 Metamodels

The computational burden generally increases with the number of variability-related parameters considered in the M-POD. Indeed, high-dimensional problems can be time-consuming processes because of the *curse of dimensionality*. As a result, researchers have been using metamodels to reduce the computational load in the last few years. Metamodels, also known as surrogate models, are essentially simplified versions of the original model based on physics [19]. For instance, the software CIVA [20], [184], enables the use of metamodels for MAPOD studies in NDE and SHM applications. Additionally, it is possible to use surrogate models for other tasks like sensitivity analysis, Sobol index evaluation, or the creation of non-parametric POD curves [19], [185].

Miorelli et al. developed database and metamodels generation schemes such as the Output Space Filling Criterion and the Support Vector Regression algorithm (all the analyses were conducted using CIVA) [186]. Engineers frequently make assumptions about the probability distributions of the variability source variables. These hypotheses are challenging to confirm, and numerous simulations are needed to analyze all the potential parameter combinations. Traditional physics-based models result in prohibitive computational costs for real-world applications. A method for creating beams of POD curves and determining confidence bounds was created by Dominguez et al. [187]. They created a database in order to use a surrogate model. Although the process for database creation is computationally expensive, it quickly becomes convenient as POD beams need to be produced.

### 2.5.3 Bayesian methods

Another helpful tool for handling this large amount of requested data is Bayesian statistics [188]. It offers a mathematical framework for making inferences and decisions exploiting prior knowledge [189]. In the SHM context, the prior refers to the amount and nature of the structural damage. Then, when new experimental evidence becomes available, the prior belief can be updated. Although Bayesian statistics offers an interesting perspective for tackling many SHM case studies, it was not often considered in the past. The reason is that, from a computational standpoint, this approach can be very time-consuming. However, recent developments in high-speed computing have easily made it possible to apply the Markow Chain and Monte Carlo techniques. The likelihood needed in the renowned Bayes' formula can be derived using these algorithms in conjunction with physics-based models. Even if the prior is unavailable or brings poor information, applying this approach simply by considering a uniform distribution of the prior is still possible. In this way, the posterior relies only on likelihood and is unaffected by the prior belief. The likelihood could be calculated experimentally or by using data from physics-based models [190]. To the best of the author's knowledge, few studies of SHM reliability have used Bayesian statistics, despite the fact that it has already been used in the field of NDE to create POD curves [191]–[194]. Contrary to conventional methods, where the only information taken into account is whether or not a specific threshold is exceeded, the Bayesian approach has the advantage of utilizing the complete response of the measuring system [195]. Consequently, this is a promising area of study for SHM that needs further research.

### 2.5.4 Fusion of probability of detection curves

Various sensor-damage combinations are present in a SHM system. Additionally, various sensor types may coexist in the same structure to offer supplementary information. As a result, different POD curves for the same structure will be generated, each associated with a particular measuring method. Ameyaw et al. used POD curves to detect and isolate faults in vibration-based systems (FDI) [101], [196], [197]. Different POD curves were generated depending on the type of sensor, its position, and the location of the damage. It is rational to devise a method for combining several POD curves related to various sensors and obtain a unique POD curve representative of the whole system. Instead of combining all the POD curves into a single one, Ameyaw et al. presented a method in which many belief values are computed using the Bayesian Combination Rule (BCR) [101], [196], [197]. All possible sensor combinations are taken into account in this method. It is possible to derive a corresponding number of belief curves as a function of the damage size by applying the BCR to each potential detection/missed-detection combination.

Fusing the curves, however, is frequently undesirable because it dilutes the available information. Applying sensor fusion at a lower level would be more appropriate. For example, one could create a single POD curve using a single damage index obtained by combining features from various sensors. Since numerous fusion algorithms are described in the literature [10], [198]–[200], it stands to reason that more than one approach might be used.

## 2.6 Localization and Sizing metrics

### 2.6.1 Probability of Localization

This section examines the most significant advancements made to quantify localization performance. Localization represents the second phase in the SHM paradigm only in the systems with an *unknown damage location* (UDL). Indeed, monitoring a *known damage location* (KDL), sometimes called hot-spot monitoring, does not require any localization because the damage position is, by definition, known. Hot-spot monitoring should not be confused with NDE. Even if the damage location is known in both situations, SHM KDL cases cannot be treated with traditional NDE techniques due to the data correlation issues covered in § 2.3 and § 2.4.
However, SHM systems with a KDL are rare for two main reasons:

(i) it can be difficult to identify the exact locations where damage is most likely to occur;

(ii) unexpected events like impacts or unknown failure mechanisms are always possible (especially in composites).

Therefore, additional metrics are needed to have acceptable reliability standards for localization. Aldrin et al. assert that such a metric should include an error in the estimate and the associated confidence bounds [61]. They provide as an example the so-called Normalized Localization Accuracy (NLA):

$$NLA = \sqrt{\frac{1}{N_p}\sum_{i=1}^{N_p}\left(\frac{\varepsilon_i^p}{p_i'}\right)^2} \tag{2.20}$$

In Equation 2.20, $N_p$ is the error of the i$^{\text{th}}$ estimation, $\varepsilon_i^p$, related to the location, $p$. The variable $p'$ represents a normalizing length factor. The confidence bounds around the damage location estimate are then calculated using the NLA (with a specified confidence level, for example, $95\%$). Using broadband piezoelectric sensors, Gagar et al. studied the location accuracy of Hsu-Nielson and fatigue crack AE sources. They plotted the cumulative frequency of the location error as a measureand against the error, and used this metric to assess the location performance of the system. [201]. In the field of Guided-Wave (GW) propagation, Flynn et al. proposed a novel damage localization algorithm in 2011, based on the Rayleigh Maximum-Likelihood Estimate (RMLE) [202].

The authors highlighted the need for a statistical tool to assess how well their algorithm performed in comparison to other state-of-the-art approaches. The peak sharpness in the proximity of the damage location in an image cannot be considered a reliable metric. For example, if the performance index $I$ is a function of a certain feature matrix $V$, one can fictitiously suppress the noise by simply redefining $I = f(V)$ as $I' = \exp f(V)$. However, the underlying information remains unchanged. For these reasons, Flynn et al. proposed two methods.

The first methodology consisted in producing a density map of the localization probability density function (LPDF). This method offers insightful information about localization performance but can be considered a qualitative approach. Therefore, since SHM requires quantitative metrics in order to make decisions, it is not appropriate.

Similarly to ROC curves, Flynn et al. developed the Localizer Operating Characteristic (LOC) curve, whose points represent an estimate of the probability of predicting the location of damage inside a certain area surrounding the true location [202]. Therefore, each damage location will display its own LOC, and the overall algorithm performance is evaluated by averaging multiple LOCs.

Mallardo et al. used a genetic algorithm (GA) to solve an OSP problem for impact localization in smart composite panels [126]. The authors evaluated the probability density function of locating damage within a certain distance from the true location for every sensor combination. Then, the corresponding Cumulative Distribution Function (CDF) was used as a reliability metric to assess the localization performance of the system. Moriot et al., leveraging the LOC and CDF concepts, created a Probability of Localization (POL) curve, defined as the probability of locating the damage within a tolerance radius equal to $\epsilon$ [27], [203]. Equation 2.21 illustrates the POL mathematical formulation as a function of $\epsilon$:

$$POL(\epsilon) = \frac{1}{K} \sum_{j=1}^{K} H\left(\epsilon - AEL_j\right) \tag{2.21}$$

Where $K$ stands for the number of experiments and the Absolute Error of Localization (AEL), defined by Equation 2.22, is the Euclidean distance between the computed $(\hat{x}_a, \hat{y}_a)$ and the true $(x_a, y_a)$ location of the flaw.

$$AEL = \sqrt{\left(\hat{x}_a - x_a\right)^2 + \left(\hat{y}_a - y_a\right)^2} \tag{2.22}$$

The symbol $H$ denotes the Heaviside-step function. Therefore, only the cases where $\epsilon > AEL_j$ are counted, which means considering only the computed locations that fall inside a circle with radius $\epsilon$ and center the point of coordinates $(x_a, y_a)$. Figure 2.6 shows an example of the application of such methodology using synthetic data:

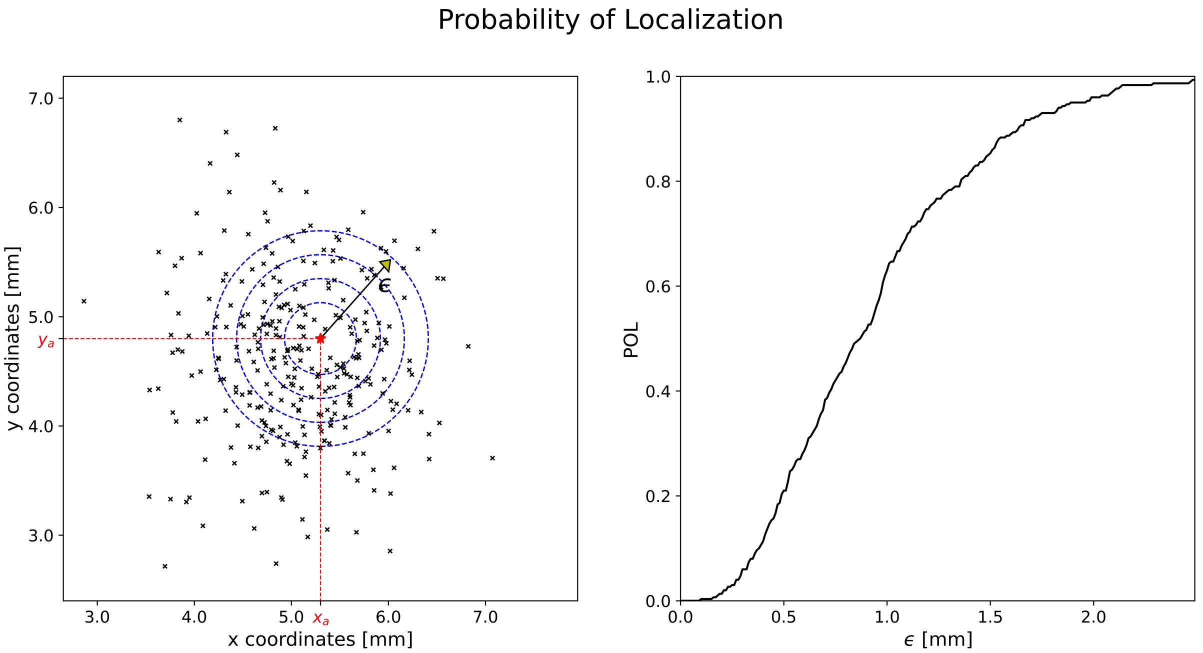

**Figure 2.6:** POL was calculated using the definition of Moriot et al. [27]

The same authors also developed the idea of Model-Assisted Probability of Localization (MAPOL), which serves as a tool for creating synthetic data and, thus, POL curves. Despite the fact that this methodology represents a step forward to deriving a reliable localization metric, similarly to POD curves, it has the drawback of having meaningless confidence bounds because the POL is not the result of any regression operation. This approach is inappropriate for applications where decisions are made in accordance with an acceptable risk due to its inability to evaluate uncertainty.

Yue and Aliabadi investigated a hierarchical method for assessing the reliability of GLW systems [25]. The third level of the methodology focuses on damage localization and evaluates its performance through the concepts of *trueness* and *precision*. [204], [205]. The *trueness* represents the systematic error, and its definition (Equation 2.23) is similar to the AEL:

$$Trueness = \sqrt{(\bar{x} - x_d)^2 + (\bar{y} - y_d)^2} \tag{2.23}$$

Where $(x_d, y_d)$ and $(\bar{x}, \bar{y})$ are the coordinates of the true location and the mean of several location estimates, respectively.

On the other hand, *precision* is related to random error and is defined by Equation 2.24 [25]:

$$Precision = \pi ab\sqrt{\chi^2_{2,95\%}} \tag{2.24}$$

The precision can also be interpreted as the area of the ellipse given by Equation 2.25:

$$\frac{(x-\bar{x})^2}{a^2}+\frac{(y-\bar{y})^2}{b^2}=\chi^2_{2,95\%} \tag{2.25}$$

Where $a$ and $b$ are the smallest and highest eigenvalues of the covariance matrix (related to the location estimates) and $\chi^2_{2,95\%}$, stands for a two-degree of freedom chi-square distribution at the $95\%$ of confidence. Figure 2.7 illustrates how this method applies to a synthetic dataset.

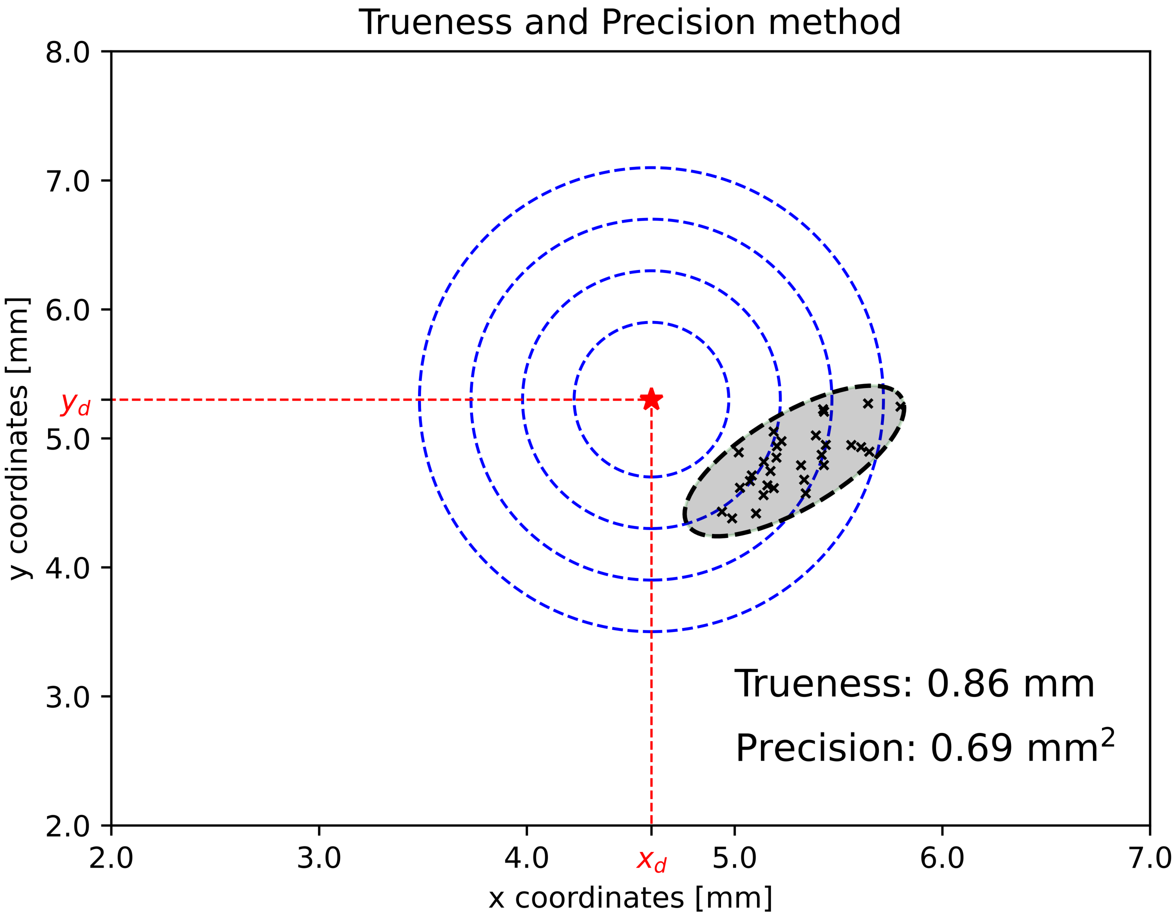

**Figure 2.7:** Location accuracy estimation using the concepts of trueness and precision (Yue and Aliabadi [25])

The same authors created a probabilistic framework based on Bayes' law to quantify the probability of correctly locating the damage inside a chosen area [25].

A different approach was proposed by Leung and Corcoran and is based on the concept of Probability of Damage Location (PDL) maps [21].

$$PDL(i)=\frac{P_f(i)}{\sum_{k=1}^{n}P_f(k)} \tag{2.26}$$

The numerator in Equation 2.26, $P_f(i)$, defines the probability of the damage being present at the $i^{th}$ location. The denominator comprises the sum of all the $P_f$ computed among the $n$ number of discretized locations considered in the analysis.

The literature shows an increasing interest in developing many different localization metrics. Therefore, much effort should be put into defining a common methodology to pave the way for an accepted standard in the future.

### 2.6.2 Probability of Sizing

In SHM, the third step aims to characterize the previously detected and located damage. The definition of damage characterization or identification can be difficult to formalize. Depending on the particular application, it might be necessary to categorize the various damage shapes or damage types or to quantify the damage size. Consider a composite material as an example. Classifying matrix cracking, delamination, fiber breakage, and fiber pull-out is just as critical as assessing the size of the damage.

The Probability of Sizing (POS) can be thought of as the probability that damage or defect will be correctly sized. In other words, it refers to how accurately a defect size is estimated [206]. There have already been prior attempts to assess the sizing accuracy of a specific measurement technique [207]. For instance, researchers evaluate the sizing performance in Automated Ultrasonic Testing (AUT) using the so-called safety Limit against Under Sizing (LUS). The LUS, also called the 95% LUS, is a metric representing the lower 95% uncertainty bound of the linear regression model, where the true damage size (typically assessed using destructive testing) is plotted against the estimated value provided by AUT [208][209].

According to Annis et al., using the LUS metric should be done with extreme caution. Indeed, the LUS underlying assumptions (linearity of the response and homoscedasticity of the variance) might not be true [100]. Some authors, similarly to the $\hat{a}$ vs. $a$ method, perform a linear regression of the measured versus true damage sizes [210]–[213]. Lee et al., for example, assessed the reliability of sizing for axial outside diameter stress corrosion cracks in steam generator tubes [168]. They computed the coefficient of determination $r^2$ of the linear regression between the measured size, estimated with Eddy Current Testing (ECT) and the real size, evaluated with destructive testing. The sizing performance of the ECT technique is then estimated using the $r^2$ score as a reference. In order to estimate the flaw sizes using ultrasonic methods, Ginzel et al. [214] revisited the equations introduced by Ermolov in 1972 [215]. The authors noted that sizing accuracy depends on many parameters, including the measuring technique, material, structure layout, and defect orientation. Nath et al. suggested using POD and POS curves to evaluate the reliability of the Time-of-Flight Diffraction (TOFD) inspection method [210], [211], [216]. POS curves were generated similarly to POD curves using the $\hat{a}$ vs. $a$ method, replacing the $\hat{a}$ value with the measured defect size. The threshold was then arbitrarily set to a specific value or equal to the maximum difference between the measured flaw size (in this case, the depth) and the real flaw size.

This approach is fallacious and not in compliance with the POS definition [206]. In fact, rather than representing the probability of correctly sizing a defect, these curves represent the probability that the estimated defect size will exceed an arbitrarily chosen size.

An alternative approach consists in determining the probability density function of the damage size once detection is made [217], [218]. This also allows the computation of an upper bound on the size.

Maintaining the same philosophy used for the localization problem, according to Aldrin et al., the evaluation of sizing performance should consist of a bias error in the estimate and the corresponding confidence bound. Thus, the authors introduced the so-called Normalized Quantification Accuracy (NQA), whose expression is equivalent to the NLA but related to sizing [61].

In 2014, Aldrin et al. attempted to provide a more rigorous definition for both sizing and localization metrics. They proposed the Characterization Error (CE), which is the difference between the estimated damage feature (location, size, depth, width), $\hat{a}$, and the actual damage state, $a$ [82]. The CE follows the mathematical framework of the MIL-HKBK-1823A. Nevertheless, the authors apprise that the process is more complex than conventional POD studies and requires the application of both engineering and statistical expertise. One should pose particular attention to low signal-to-noise ratios, measurements taken close to the saturation level, poorly posed inversion problems, and failure mechanisms independent of defect size because they could all contribute to inadequate characterization results [219].

To the best of the author's knowledge, no specific case studies have attempted to develop a sizing metric for SHM systems, even though damage characterization represents the third fundamental level of SHM [70].

## 2.7 Discussion and perspectives

Until now, Chapter 2 described the evolution of POD and considered the development of localization and sizing metrics. This section summarizes the most relevant case studies (see Table 2.A.3 in § 2.A) and examines future perspectives on SHM reliability.

The *Field* column of Table 2.A.3 confirms the growth of the SHM field, showing a progressive transition from NDE toward SHM studies.

The *Metric* column reveals that the majority of studies focus on POD curves, with only a small number considering localization and sizing metrics. Metrics for localization and sizing still exhibit significant heterogeneity, and there are no widely recognized standards. Furthermore, given the hierarchical nature of SHM systems, the relationship between detection, location, and sizing metrics needs to be examined.

Sequential data analysis represents a valid tool to handle serially correlated time series data due to varying EOCs, defect morphology, and sensor drift.

The LaD, LMM, and REM are valid statistical methodologies for the SHM field. The LaD is a relatively simple approach. On the other hand, the LMM and the REM utilize data more efficiently but require a thorough understanding of advanced statistical tools.

M-POD curves depend on several parameters and often require numerical models to be computed. Therefore, the MAPOD approach is fundamental for the derivation of M-POD curves. Being able to capture all the sources of variability is the most significant challenge. Due to the *curse of dimensionality*, the computational cost increases exponentially with the number of parameters considered in the analysis. Metamodels are promising tools for addressing this challenge because they can reduce the computational effort of many orders of magnitudes, enabling the generation of beams of POD curves.

In the presence of multiple sensing systems, POD fusion methodologies can be considered. Since this subject is still in its early stages, it is unclear whether or not it is convenient to combine various POD curves because this operation might dilute the information available. Nevertheless, fusing different sensor information at a lower level could lead to more effective damage indices and accordingly improve POD curves.

Since all POD approaches for SHM originate from the $\hat{a}$ vs. $a$ method, there are no methodologies for handling repeated time-dependent hit/miss data in the literature. Hit/miss data that are present in SHM are incorrectly processed using traditional NDE methodologies. Therefore, more research on this subject is necessary.

All of the sensing methods applied in reliability assessment studies are displayed in the *Sensing* column. Although many measurement methods have been employed, some are surprisingly uncommon. For instance, despite the fact that AE [1] and DOFS [5] have emerged as promising technologies in the field of SHM, reliability POD studies on these techniques are still lacking.

One of the main obstacles to the validation and certification of SHM systems is the absence of clear reliability metrics. The *Objective* column emphasizes that while many studies have attempted to evaluate the performance of a given system, very few have concentrated on the creation of new reliability metrics. This disparity indicates that additional effort should be put forth into the development of widely accepted protocols to assess SHM systems in terms of detection, localization, and sizing.

In principle, SHM POD studies should consider real representative structures. However, the *Material and Structure* column of Table 2.A.3 shows that the majority of the reviewed literature develops POD curves using simplified structure components or even specimens (as is typically done in NDE).

Using numerical models could be the only solution to conciliate the need to replicate a test structure as closely as possible to reality, thus capturing all the sources of variability, with the need for many structures to obtain a statistically relevant sample. According to the *Numerical Analysis* column, an increasing number of SHM studies are using numerical models to generate POD curves. However, since the model might not capture or accurately represent the real structure, it is challenging to replace experimental data completely. The most promising strategy seems to be a hybrid approach using numerical simulations and experiments [26]. These two types of data could be combined using Bayesian statistics. To the best of the author's knowledge, this has only been done for NDE POD studies. Further research should be conducted on this topic for SHM systems as well since the amount of data is even more considerable.

In Table 2.A.3, the column *Damage and its Estimation* highlights that POD curves are a function of the estimated damage size rather than the true damage size. Therefore, it is implicitly assumed that the measurement method used to address the true damage size is much more accurate than the value given by the SHM system. However, in many cases, this hypothesis is impossible to prove. Therefore, the implementation of the uncertainty related to the true damage estimation in POD curves should be studied.

The following remarks summarize the key points of the literature review:

- The SHM field is growing faster than the development of its reliability metrics. Further research is needed to develop statistical methods capable of quantifying the performance of SHM systems.

- In SHM, using standard NDE methods for POD curves is not possible.

- POD curves are typically developed under the assumption that there is no uncertainty in the true damage estimation. Unfortunately, this hypothesis is often hard to verify.

- Sequential data analysis can handle sensor drift and SHM systems under varying EOCs. It is a promising area of study that deserves more investigation.

- The LaD and REM are two statistical models that can generate POD in the presence of spatial/time-correlated data, but their use in the SHM literature is still limited to few studies.

- The use of MAPOD curves is crucial in M-POD curves studies, which allows for the inclusion of multiple parameters. However, due to the *curse of dimensionality*, the computational cost increases exponentially with the number of parameters. Metamodels are a valid solution to alleviate the problem.

- POD and ROC curves may improve by fusing data from various sensor sources.

- The main challenge for obtaining accurate numerical models and experiments is to capture every source of variability.
- Experimental and numerical data can be combined using Bayesian statistics. This approach is promising for POD studies in SHM.
- Even though recent studies have developed metrics for localization and sizing, widely and commonly accepted standards are still missing. Further research is needed to develop a protocol that can integrate these scattered efforts, using statistical tools capable of generating confidence intervals.

## 2.A Appendix: Literature review summary

Table 2.A.3 summarizes the most significant studies analyzed in Chapter 2. On the next page, Table 2.A.3 is shown using a landscape format to provide a better visual interpretation.

**Table 2.A.3:** Case studies in NDE and SHM reliability and performance quantification assessment

| Field | Metric | Sensing | Objective | Material and structure | Damage and its estimation | Numerical analysis | Ref. | Year |
|---|---|---|---|---|---|---|---|---|
| SHM | POD (LaD) | CVM | Reliability assessment of CVM | Thin Al specimen and thick steel specimen | Fatigue Cracks (initial crack lengths known from manufacturing and crack growth assessment from known initial distance between the crack and the CVM sensor) | No | [17] | 2009 |
| NDE | MAPOD-FMA | ECT | Sensitivity analysis of MAPOD-FMA related to the model factors | Two-layer Al structure | Cracks around titanium fastener holes | VIC-3D®, Monte-Carlo simulations | [171] | 2009 |
| NDE | POD (hit/miss) | IRT | Reliability assessment of IRT | CFRP specimen | Impacts (dimension estimated with C-Scan UT) | No | [220] | 2010 |
| NDE | POD ($\hat{a}$ vs. $a$); POS (different from def. given in [206]) | TOFD | Reliability assessment of TOFD | Al specimen | EDM vertical slits (dimension known from manufacturing process) | No | [210] | 2010 |
| NDE | M-POD (hit/miss multivariate log-logistic regression) $r^2$ and RMSE (true size vs. measured size) | ECT | Reliability assessment of ECT | Top of tube sheet in steam generator tubes | ODSCC (dimension estimated from destructive testing) | No | [168] | 2010 |
| NDE | M-POD ($\hat{a}$ vs. $a$ generalization) | ECT | Extend traditional $\hat{a}$ vs. $a$ POD for ECT to M-POD | 5 different sets of flat plate specimens of different materials | Cracks (dimension estimation not specified) | No | [169] | 2010 |
| SHM | POD and PFA maps | Piezoelectric patches | Define a methodology for OSP | Different shaped plates | Defect is modeled as a symmetric scatterer | Modeling of the wave propagation | [122] | 2010 |
| SHM | POD as a function of the number of sensors | PZT | OSP for impact detection | CFRP stiffened panel | Impacts were simulated applying the load in 281 points | Abaqus model of the structure | [124] | 2010 |
| NDE | POD ($\hat{a}$ vs. $a$) (hit/miss) | PT | Reliability assessment of PT using several post-processing techniques | CFRP panel | Teflon insertions at various depths simulating delamination (hypothesis: delamination area = teflon insertions area) | No | [221] | 2012 |

*Continued on next page*

Table 2.A.3 – *Continued from previous page*

| Field | Metric | Sensing | Objective | Material and structure | Damage and its estimation | Numerical analysis | Ref. | Year |
|---|---|---|---|---|---|---|---|---|
| NDE | MAPOD ($\hat{a}$ vs. $a$) | ECT | Demonstration of MAPOD methodology for ECT | Ti-6Al-4V specimens | Fatigue cracks and EDM notches | VIC-3D®, surrogate model | [56] | 2012 |
| SHM | POD (hit/miss) | OFS | Reliability assessment of OFS | Modeled thermoplastic affordable primary aircraft structure stiffened panel | Several damage types were simulated numerically | Only FEM simulations were used for the entire study | [32] | 2012 |
| NDE | POD ($\hat{a}$ vs. $a$) | UPA, SPA | Reliability assessment of UPA and SPA | AUSS specimen, ferritic specimen, dissimilar metal welds, cladded specimen | Inter-granular stress corrosion cracking or Fatigue cracks, EDM notches, welding irregularities. (Dimension assessed with surface crack testing, radiography, creation of microsections) | No | [222] | 2013 |
| NDE | M-POD | ECT | Use of bayesian methods to evaluate M-POD and POD with physic-based models | See ref. [56], [171] | [56], [171] | MC, MCMC | [172] | 2013 |
| NDE | M-POD (mixed effect model) | VT | Find the best VT setting and development of POD for similar applications | Aircraft engine turbine blade (material is not specified, probably is a superalloy) | Cracks (dimension assessment using acetate replication) | No | [175] | 2014 |
| SHM | POD (LMM) | AE with PZT | Development of POD method for SHM (independence hypothesis is removed) | Wing attachment lug (material is not specified, probably is Al) | Fatigue cracks (fatigue cycling paused every 1000 cycles to collect PZT data and to record visual crack length information) | Simulated dataset is used | [15] | 2015 |
| NDE | POD ($\hat{a}$ vs. $a$) | LITPI | Reliability assessment of LITPI | CFRP specimen | Flat-Bottom holes (dimension known from manufacturing | No | [223] | 2015 |
| SHM | POD (hit/miss) | Nodes in the numerical model | Reliability assessment of GLW based tomography | CFRP plate | Damage is simulated via local stiffness degradation in the FEM model | FEM using Abaqus | [183] | 2016 |
| SHM | MAPOD (OSTI) | FBG | Reliability assessment of FBG network | Fuselage panels of a helicopter | Fatigue cracks visually identified and measured with a caliper about 100000 cycles after artificial notch creation | FEM | [33] | 2017 |

*Continued on next page*

Table 2.A.3 – *Continued from previous page*

| Field | Metric | Sensing | Objective | Material and structure | Damage and its estimation | Numerical analysis | Ref. | Year |
|---|---|---|---|---|---|---|---|---|
| SHM | POD ($\hat{a}$ vs. $a$); POL | GLW with PZT | Reliability assessment of GLW imaging techniques | Al6061-T6 plate | Viscoelastic disc loaded with a mass of 500 g | MAPOD and MAPOL are produced using COMSOL | [27] | 2017 |
| SHM | M-POD | GLW with PZT | Reliability assessment of M-POD for GLW | Al plates | Artificial slot was realized by a blade cut (dimension known from manufacturing) | FEM (Abaqus) | [28] | 2017 |
| SHM | ROC | GLW with PZT | Development of a reliability assessment methodology under varying EOCs | Pipe specimen | Growing corrosion is represented by the constant growth rate of the cross-sectional area loss. (Damage is synthetically added to the received signal) | FEM | [26] | 2017 |
| SHM | POD (OSTI) | CVM | Reliability assessment of CVM | Metal specimen | Fatigue cracks | No | [29] | 2018 |
| SHM | POD (LaD, REM) | CNT | Reliability assessment of CNT | Al-Li alloy specimen | Fatigue cracks initiated from EDM notches. Image was captured every 1000 cycles to capture the crack extending) | FEM to simulate CNT resistance as a function of the crack length | [18] | 2019 |
| SHM | POD ($\hat{a}$ vs. $a$) and POD fusion | Accelerometers, laser sensors, SG sensors | Extend the use of POD to the field of fault detection and isolation | Steel beam | Additive masses in a vibration-based test (modal hammer excitation) | No | [101] | 2019 |
| SHM | POD (LaD, REM) | See ref. [17], [18], [29], [50], [165] | Development of POD methods for SHM (independence hypothesis is removed) | See ref. [17], [18], [29], [50], [165] | See ref. [17], [18], [29], [50], [165] | See ref. [17], [18], [29], [50], [165] | [16] | 2019 |
| SHM | POD (hit/miss); Trueness and Precision | GLW with PZT | Development of a hierarchical approach for reliability assessment of GLW-SHM systems | Simple flat panels, panels with 4 CFRP Ω stiffeners and 3 Al stringers | BVID produced by low-velocity weight-Drop impacts. BVID assessment using C-Scan | No | [25] | 2020 |
| SHM | ROC | GLW with Guided Ultrasonics Ltd. gPIMS sensor ring [148] | Development of a change detection algorithm for SHM under varying EOCs | 5 m long, 8-in schedule 40 pipe | Damage was simulated by adding to the experimental signals the reflection expected from a defect. Further details in Heinlein et al [224] | FEM | [24] | 2020 |

*Continued on next page*

Table 2.A.3 – *Continued from previous page*

| Field | Metric | Sensing | Objective | Material and structure | Damage and its estimation | Numerical analysis | Ref. | Year |
|---|---|---|---|---|---|---|---|---|
| SHM | MAPOD ($\hat{a}$ vs. $a$) | GLW with PZT | A POD map is used to study the effect of damage position on system reliability | Automotive component made of CFRP | Each delamination was modeled as a local change in stiffness | Elastodynamic finite integration. Technique was used to model Lamb waves | [23] | 2021 |
| SHM | MAPOD (as implemented in CIVA [19], [225], POD and PDL maps | bulk-wave ultrasonic sensor and a potential-drop sensor | Develop a probabilistic framework for the reliability assessment permanently installed sensors | Rectangular beam undergoing three-point and four-point fatigue bending | Square defects with side length between 2 mm and 8 mm | FEM (Abaqus and COMSOL) | [21] | 2021 |
| SHM | ROC | GLW with PZT | Causal dilated CNN for automatic inspection of ultrasonic signals | 500 × 500 × 5 mm steel plate | Through-thickness hole was introduced at the desired location by removing elements in the numerical model | FEM (Pogo [226]) | [22] | 2021 |

# Chapter 3

# Optical Fiber Sensors

> *Music is the arithmetic of sounds*
> *as optics is the geometry of light*
>
> *Claude Debussy*

In recent years, Optical Fiber Sensors (OFSs) have spread throughout the scientific community and the industry for their beneficial sensing capabilities in several applications. Some advantages of using OFSs over traditional sensing techniques include their large bandwidth (allowing the transmission of a large amount of information in the same physical line), small size and light weight, immunity to electromagnetic interference (due to their dielectric nature), and durability [5], [227].
The taxonomy of OFSs can be based on their operating principle: interferometric, grating-based, and scattering-based.

## 3.1 Interferometric OFSs

An interferometric OFS takes advantage of the interference between two light waves propagating through different optical fiber paths [228]. There are a variety of possible fiber optic interferometer configurations, such as the Mach-Zehnder, Michelson, Fabry-Perot, and Sagnac. In all cases, a light beam must be split and then recombined, and the measurand must be capable of affecting the optical properties on one of the two optical paths. Analyzing the change in the optical phase, it is then possible to accurately determine the variation in the corresponding physical quantity [5].

A completed and detailed description of their working principle is outside the scope of this thesis. Nevertheless, it is possible to conclude that the major benefit of using interferometric OFS is their high resolution. In contrast, the major drawback from an SHM perspective is their limited multiplexing capabilities, and it is possible to consider them as single-point sensors (see left-hand side of Figure 3.1).

## 3.2 Grating-based OFSs

Grating-based OFSs, can also be regarded as single-point sensors. However, unlike interferometric OFSs, they are suitable to be multiplexed, allowing for quasi-distributed sensing. Indeed, it is possible to interrogate multiple channels, each one with an array of several inscribed gratings (see right-hand side of Figure 3.1). Depending on the characteristics of its grating period ($\Lambda$), a grating-based OFS can be further classified as a uniform Fiber Bragg Grating (FBG), tilted FBG, chirped FBG, or Long Period Grating (LPG) [5], [229].

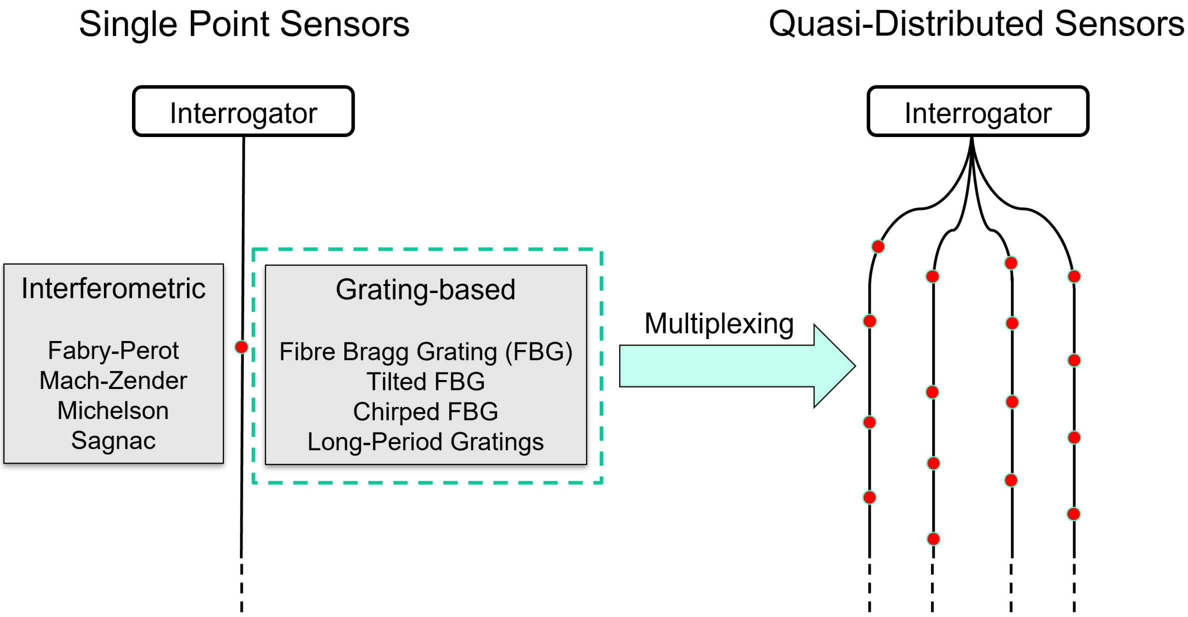

**Figure 3.1:** Interferometric and grating-based OFSs classification.

Chapter 3 would be too long to review all these grating-based OFSs. Therefore, hereafter it is only provided a brief introduction to uniform FBGs. As will be shown later in § 3.3, it is possible to transfer some concepts valid for uniform FBGs to distributed sensing based on Rayleigh backscattering, which is the experimental technique used in .

### 3.2.1 Uniform Fiber Bragg Gratings

The history of FBGs dates to 1978, when Hill et al. observed the index of refraction changes in germanium-doped silicate fibers [230]. In 1989, Meltz and coworkers made a breakthrough in the field, proposing a new methodology to generate FBGs using coherent UV radiation [231]. Since then, FBGs fabrication technology has attracted the interest of many researchers [232], and there is a wealth of literature describing its evolution [233]–[235].

Figure 3.2 summarizes the FBG working principle. The grating visible at the center of the fiber can be regarded as a periodic refractive index modulation. Although the refractive index variation is oftentimes illustrated as a square waveform, its shape is better represented by a sinusoidal function [235]. Uniform FBGs (i.e. having constant index modulation and grating period) show undesired sidelobes in the reflected spectrum, which can be reduced through proper apodization profiles of the refractive index [236]–[238]. Monotonically varying the grating period will lead to chirped FBGs [239], whereas tilting the grating planes from their original orthogonal direction with respect to the longitudinal axis of the fiber will produce a tilted FBG [240].

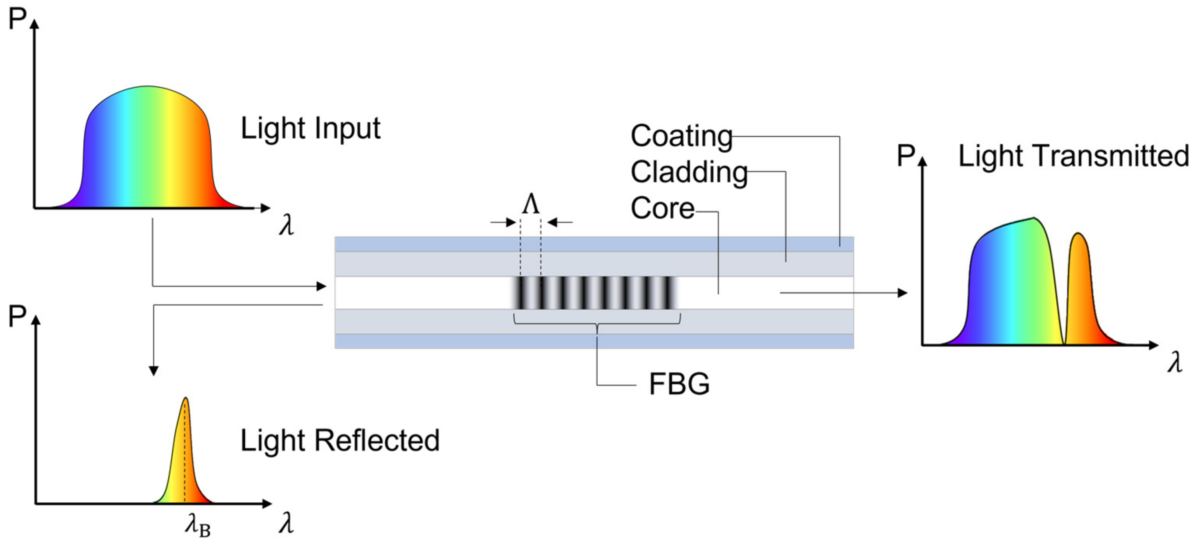

**Figure 3.2:** FBG working principle. In the transmitted spectrum, it is missing the power ($P$) associated with the Bragg's wavelength, which can be measured in the reflected spectrum.

### Mathematical description

According to the Bragg's law, when a broadband incident optical field illuminates an FBG, which can be regarded as the periodical effective refractive index ($n_{eff}$) variation of period $\Lambda$, only the Bragg's wavelength ($\lambda_B$) is reflected, leading to Equation 3.1 [241]:

$$\lambda_B = 2n_{eff}\Lambda \tag{3.1}$$

When the FBG is subjected to longitudinal strain ($\varepsilon$), its period changes, which in turn produces a Bragg's wavelength shift ($\Delta\lambda_B$) [242]:

$$\frac{\Delta\lambda_B}{\lambda_B} = (1 - \rho_\varepsilon)\,\varepsilon \tag{3.2}$$

Where $\rho_e$ represents the effective photo-elastic constant and can be expressed as a function of the Poisson's ratio ($\nu$) and Pockel's coefficients ($p_{ij}$) of the stress-optic tensor:

$$\rho_e = \frac{n_{eff}^2}{2}\left[p_{12} - \nu\left(p_{11} + p_{12}\right)\right] \tag{3.3}$$

For FBGs written in standard optical fibers with a Bragg's wavelength of $1550\,\mathrm{nm}$, the expected sensitivity value is $1.2\,\mathrm{pm}\,\mu\varepsilon^{-1}$ [243]. Another fundamental figure of merit is the detection limit, which can vary according to the interrogation technique. The interested reader can find typical detection limits values in the work of Campanella et al. [244]. The effect of temperature can be estimated by differentiating Equation 3.1 as follows:

$$\Delta\lambda_B = 2\left(n_{eff}\frac{\partial\Lambda}{\partial T} + \Lambda\frac{\partial n_{eff}}{\partial T}\right)\Delta T \tag{3.4}$$

Equation 3.4 can be reshaped as [234], [245]:

$$\Delta\lambda_B = \lambda_B\left(\alpha + \frac{1}{n_{eff}}\frac{\partial n_{eff}}{\partial T}\right)\Delta T = \lambda_B\xi\Delta T \tag{3.5}$$

Where $\alpha$ is the thermal expansion coefficient of the optical fiber (e.g., silica), which summed to the thermally induced effective refractive index change, leads to the thermo-optic coefficient $\xi$. For a germanium-doped silica optical fiber, the effect of temperature on the wavelength shift is mainly dominated by the consequent change in the refractive index, which is approximately equal to $8.6 \times 10^{-6}\,{}^{\circ}\mathrm{C}^{-1}$, rather than the inherent thermal expansion of the optical fiber, since $\alpha$ is approximately $5.5 \times 10^{-7}\,{}^{\circ}\mathrm{C}^{-1}$ for silica. Applying these values to Equation 3.5, with a Bragg's wavelength of $1550\,\mathrm{nm}$, it is possible to compute the sensor sensitivity with respect to the temperature, which happens to be approximately $14\,\mathrm{pm}\,{}^{\circ}\mathrm{C}^{-1}$.

If both strain and temperature effects are present simultaneously and assuming independency between the strain and the thermal response, which holds for small perturbations [242], the change of the Bragg's wavelength can be expressed using Equation 3.6 [243], [246]:

$$\Delta\lambda_B = K_\varepsilon\Delta\varepsilon + K_T\Delta T \tag{3.6}$$

Where $K_\varepsilon$ and $K_T$ are the strain- and temperature-related constants whose values can be computed experimentally.

## 3.3 Scattering-based Optical Fiber Sensors

Scattering-based OFSs are often referred to as Distributed Optical Fiber Sensors (DOFSs) due to their ability to provide information along the whole fiber length (see left-hand side of Figure 3.3). There are three main mechanisms of light scattering, namely Rayleigh, Brillouin, and Raman (see right-hand side of Figure 3.3).

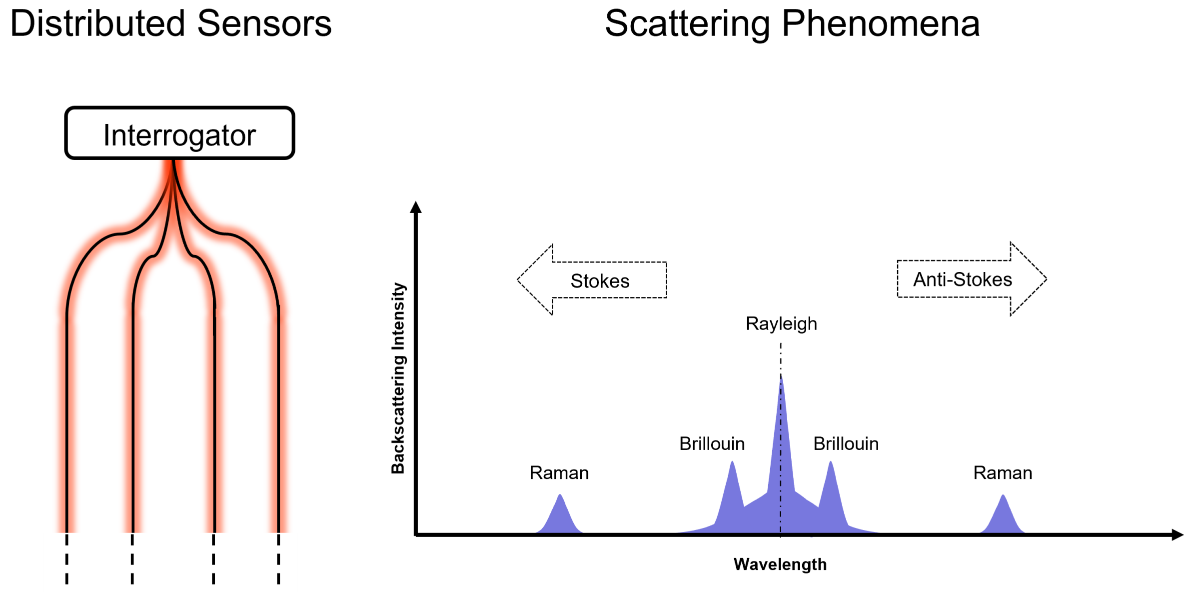

**Figure 3.3:** Distributed OFSs classification according to scattering phenomena (adapted from [247])

Rayleigh scattering originates from light interacting with non-propagating refractive index fluctuations. It is also called *elastic* scattering because the incident photons are scattered with a negligible energy loss, thus without any frequency shift. If the energy of the incoming photon differs from that of the scattered photon, the scattering is called *inelastic*. The corresponding frequency shift is called Stokes or anti-Stokes components, depending on whether the scattered light has a frequency lower or greater than the incident light. Brillouin and Raman scattering are examples of inelastic scattering.

Brillouin scattering is an inelastic process resulting from the interaction between a light wave signal with propagating acoustic waves in the optical fiber [5]. These acoustic waves are often referred to as phonons and can be considered refractive index perturbations traveling along the optical fiber. The photon-phonon interaction produces Brillouin scattering characterized by a certain frequency shift, similar to the Doppler shift resulting from light interacting with a diffraction grating traveling at the speed of sound [247], [248].

Raman scattering is an inelastic interaction induced by light interacting with molecular vibrations. The negligible cross-sensitivity to pressure and strain perturbations makes Raman scattering ideally suited for temperature measurements.

In § 3.3.1, an in-depth analysis of Rayleigh scattering is carried out since it is the physical phenomenon exploited by the interrogator unit used in the experimental activity of this thesis.

### 3.3.1 DOFSs based on Rayleigh Backscattering

As previously stated, Rayleigh scattering is an elastic scattering originating from light interacting with non-propagating refractive index fluctuations. In optical fibers, Rayleigh scattering represents one of the main causes of the power loss mechanism (together with material absorption). Moreover, the losses are particularly accentuated at short wavelengths since the intensity of scattered light is proportional to $\lambda^{-4}$.

In a perfectly homogeneous medium, these refractive index fluctuations would be generated by thermally related non-propagating entropy fluctuations according to the following Equation 3.7 [247]:

$$\Delta\kappa = \left(\frac{\partial\kappa}{\partial\rho}\right)_T \left(\frac{\partial\rho}{\partial s}\right)_p \Delta s \tag{3.7}$$

Where $\kappa$ is the dielectric constant, $\rho$ is the material density, and $s$ is the entropy. The subscripts $T$ and $p$ denote isothermal and isobaric variations conditions, respectively. The dielectric constant is then related to the refractive index with the following well-known equation:

$$\kappa = n^2 \tag{3.8}$$

However, since optical fibers are not perfectly homogeneous media, Rayleigh scattering is mainly dominated by refractive index fluctuations caused by density variations frozen into the fused silica during the manufacturing process [249].

Distributed fiber sensing based on Rayleigh backscattering can be achieved through different approaches, such as Optical time-domain reflectometry (OTDR), Phase-sensitive optical time-domain reflectometry ($\Phi$-OTDR), Polarization-sensitive optical time-domain reflectometry (P-OTDR), Optical frequency-domain reflectometry (OFDR), and Optical low-coherence reflectometry (OLCR).

A comprehensive description of all these technologies is outside the scope of this thesis; the interested reader can find further insights in the review article of Lu et al. [247]. The following section (§ 3.3.2) focuses on OFDR, the underlying working principle of the Optical Backscatter Reflectometer™ Model 4413 (OBR 4413) (see Chapter 4), and Optical Distributed Sensor Interrogator - Model B (ODiSI-B) interrogators (see Chapter 5).

### 3.3.2 Optical frequency-domain reflectometry

OFDR, often referred to as Swept-wavelength Interferometry (SWI) [9], is particularly attractive among the various distributed sensing technologies due to its ability to achieve high spatial resolution with a large dynamic range [250].

The first use of OFDR dates back to the work of Eickhoff et al. in 1981 [251]. Then, in 1998, Froggat et al. presented a method to achieve high-spatial resolution measurements exploiting Rayleigh backscattering [252].

As shown in the left-hand side of Figure 3.4, in SWI, a Tunable Laser Source (TLS) is used to sweep a continuous wave light source through a certain frequency range ($\Delta F$). The light beam is then split into two paths, corresponding to the two arms of a Mach-Zender interferometer. In the measurement arm, it is placed another 50/50 coupler which further splits the light allowing the interrogation of the Fiber Under Test (FUT). Then the backscattered light from the FUT is recombined with the reference field through another 50/50 coupler [253]. A more detailed description can be found in the study of Soller et al. [254].

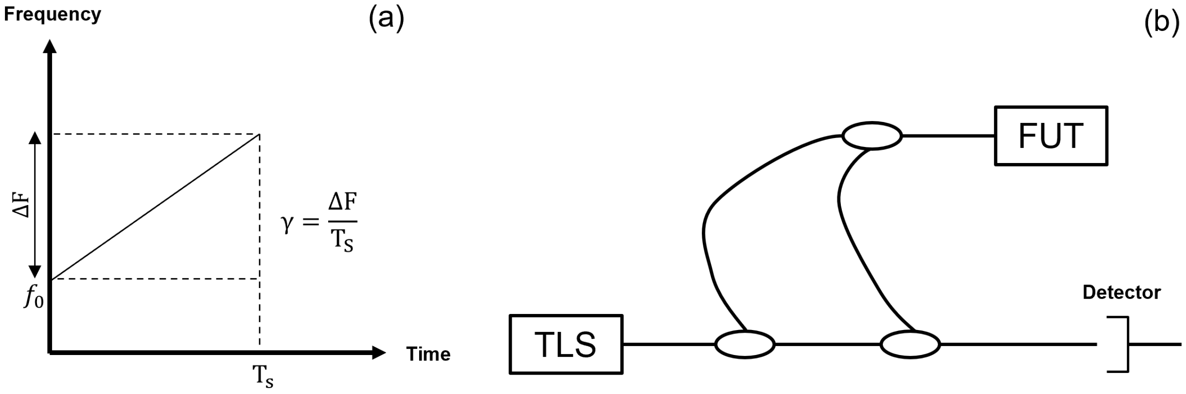

**Figure 3.4:** (a) schematic of TLS sweep frequency, and (b) OFDR interrogator architecture (adapted from [255])

According to Ahn et al. [256], the incident optical field ($E_i$) of a frequency-sweep laser source can be written as:

$$E_i(t) = E_0 \exp\{j\phi(t)\} \tag{3.9}$$

Where $E_0$ is the optical field amplitude, $j$ is the imaginary unit ($j^2 = -1$), and $\phi(t)$ is the time-varying phase. By definition, the instantaneous optical angular frequency ($\omega(t)$) can be written as the derivative with respect to time $\phi(t)$ as defined by Equation 3.10:

$$\omega(t) = \frac{\mathrm{d}\phi(t)}{\mathrm{d}t} \tag{3.10}$$

The frequency ($f$) of a TLS can be described as a function of time ($t$) as outlined by Equation 3.11:

$$f(t) = f_0 + \gamma t \tag{3.11}$$

Where $f_0$ represents the initial frequency and $\gamma$ is the sweep rate of the TLS. Then it is possible to write $\omega\left(t\right)$ for a TLS as:

$$\omega\left(t\right)=2\pi f=2\pi\left(f_0+\gamma t\right) \tag{3.12}$$

Implementing the definition of $\omega\left(t\right)$ given in Equation 3.12 into Equation 3.10, it is possible to compute $\phi\left(t\right)$ as a funciton of $\omega\left(t\right)$:

$$\phi\left(t\right)=\int_0^t\omega\left(t\right)\,dt=2\pi f_0 t+\pi\gamma t^2 \tag{3.13}$$

In real applications, the TLS would be affected by random phase fluctuations ($\theta\left(t\right)$) due to noise. Hence, Equation 3.13 can be rewritten as:

$$\phi\left(t\right)=2\pi f_0 t+\pi\gamma t^2+\theta\left(t\right) \tag{3.14}$$

Therefore, the electric field can be expressed combining Equation 3.9 and Equation 3.14:

$$E_i\left(t\right)=E_0\exp\{j\left[2\pi f_0 t+\pi\gamma t^2+\theta\left(t\right)\right]\} \tag{3.15}$$

On the other hand, the backscattered electric field ($E_s$) with a certain propagation delay $\tau$ would be equal to:

$$E_s\left(t-\tau\right)=\sqrt{R}E_0\exp\left\{j\left[2\pi f_0\left(t-\tau\right)+\pi\gamma\left(t-\tau\right)^2+\theta\left(t-\tau\right)\right]\right\} \tag{3.16}$$

Where $R$ represents the reflectivity of the fiber under test. The interference between $E_i$ and $E_s$ produces a beating signal with intensity ($I(t)$) equal to:

$$I\left(t\right)=E_0^2+RE_0^2+2\sqrt{R}\cos\left\{2\pi\left[f_o\tau+\gamma\tau t+\frac{1}{2}\gamma\tau^2+\theta\left(t\right)-\theta\left(t-\tau\right)\right]\right\} \tag{3.17}$$

Introducing the beat frequency ($f_b$):

$$f_b=\gamma\tau \tag{3.18}$$

It is possible to derive the angular beat frequency ($\omega_b$) as:

$$\omega_b=2\pi\gamma\tau \tag{3.19}$$

Hence, exploiting the definition of $\omega_b$ it is possible to write Equation 3.17 as given by Equation 3.20:

$$I\left(t\right)=E_0^2+RE_0^2+2\sqrt{R}\cos\left[\omega_0\tau+\omega_b t-\frac{1}{2}\omega_b\tau+\theta\left(t\right)-\theta\left(t-\tau\right)\right] \tag{3.20}$$

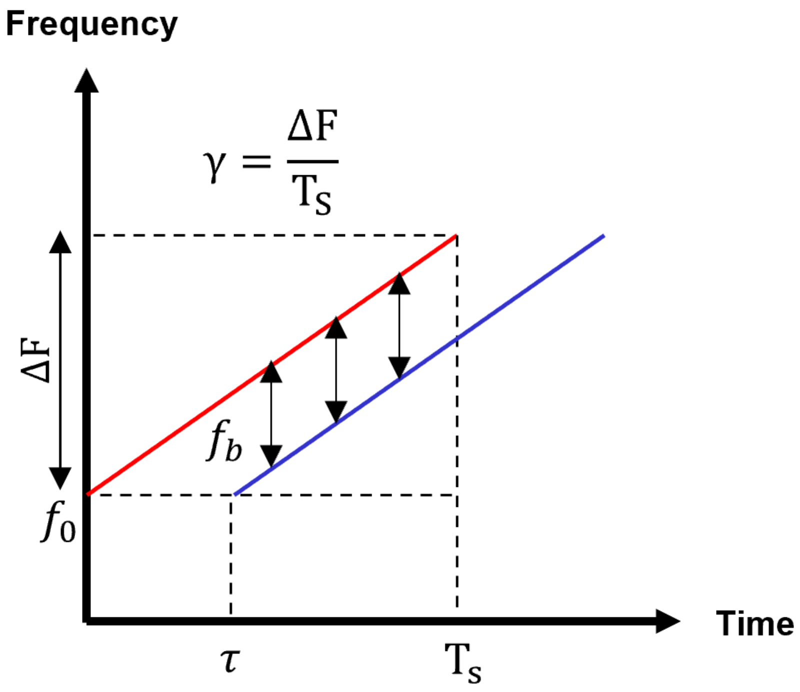

**Figure 3.5:** Schematic of beat frequency ($f_b$) due to interference between $E_i$ and $E_s$.

The third term in Equation 3.20 is called *interference* term and contains beat frequency ($f_b$) information. Analyzing the signal in the frequency domain through the Fourier transform makes it possible to compute $f_b$ for a single, localized reflection. However, the interrogator analyzes the backscatter contributions of all the points along the fiber. The interference pattern due to Rayleigh backscattering results in a repeatable *fingerprint* [253]. The result is the equivalent of having a weak FBG distributed along the fiber. Indeed, the math describing the expected wavelength shift ($\Delta\lambda$), or frequency shift ($\Delta\nu$), due to strain and temperature perturbations is also similar to the one used for FBGs [9]. Therefore, Equation 3.6 adapted to OFDR assumes the form of:

$$\frac{\Delta\lambda}{\lambda} = -\frac{\Delta\nu}{\nu} = K_\varepsilon \Delta\varepsilon + K_T \Delta T \tag{3.21}$$

Referring to Figure 3.5, it is also possible to derive the maximum theoretical spatial resolution for OFDR systems ($\Delta z_{min}$) of the interrogation system considering that the beat signal has a duration that is limited by the sweep time ($T_s$) [257]:

$$\Delta z_{min} = \frac{1}{T_s} \frac{c}{2n\gamma} = \frac{c}{2n\Delta F} \tag{3.22}$$

## 3.A Appendix: Strain Modal Testing with Fiber Bragg Gratings for Automotive Applications

This research activity aims to assess the capability of FBGs to perform strain modal analysis on composite structures. The study shows that FBGs and accelerometers have comparable performance. Further research would be devoted to developing a POD methodology for strain modal testing using FBGs.

The main contents of this correlated research activity can be found in the following publication:

**F. Falcetelli**, A. Martini, R. Di Sante, and M. Troncossi, "Strain Modal Testing with Fiber Bragg Gratings for Automotive Applications," *Sensors*, 2022. https://doi.org/10.3390/s22030946

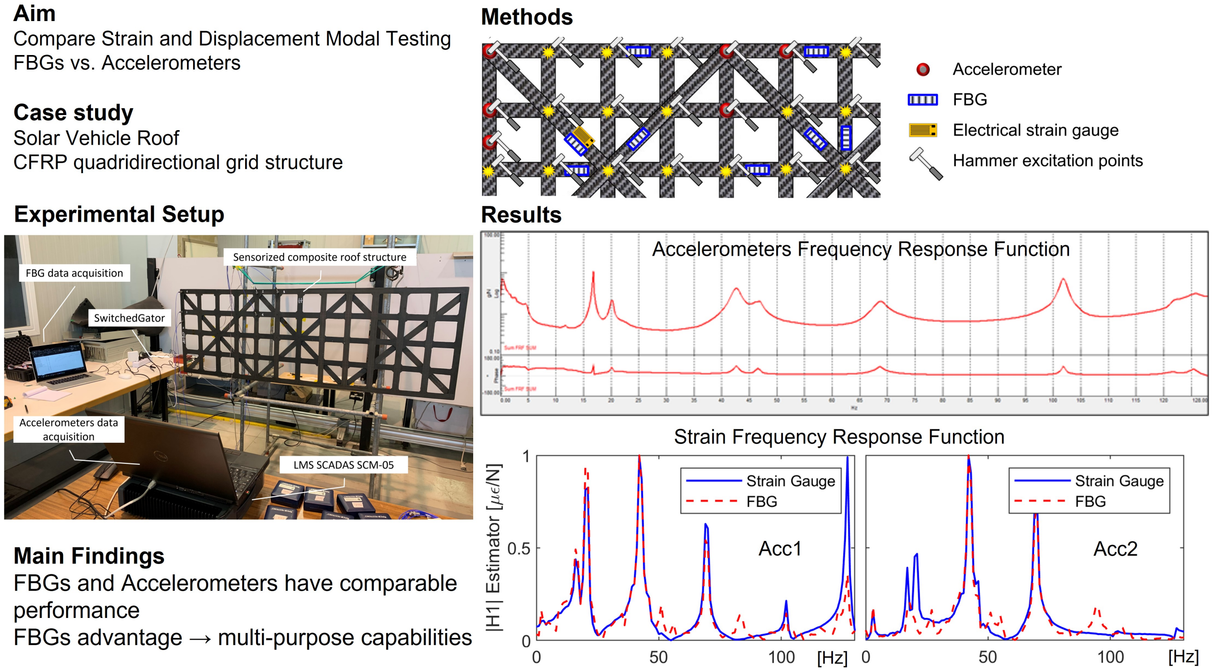

**Aim**
Compare Strain and Displacement Modal Testing
FBGs vs. Accelerometers

**Case study**
Solar Vehicle Roof
CFRP quadridirectional grid structure

**Experimental Setup**

**Methods**

**Results**

**Main Findings**
FBGs and Accelerometers have comparable performance
FBGs advantage → multi-purpose capabilities

**Figure 3.A.6:** Graphical abstract of the research.

## 3.B Appendix: Strategies for Embedding Optical Fiber Sensors in Additive Manufacturing Structures

This research discusses current embedding strategies for OFSs in structures produced with the fused deposition modeling technique. A novel methodology to embed OFSs is introduced and then tested. The research also provides a strain transfer study for DOFSs embedded in 3D-printed structures. The main contents of this correlated research activity can be found in the following publication:

**F. Falcetelli**, R. Di Sante and E. Troiani, "Strategies for Embedding Optical Fiber Sensors in Additive Manufacturing Structures," *European Workshop on Structural Health Monitoring. EWSHM 2020 - Lecture Notes in Civil Engineering*, 2020. https://doi.org/10.1007/978-3-030-64908-1_34

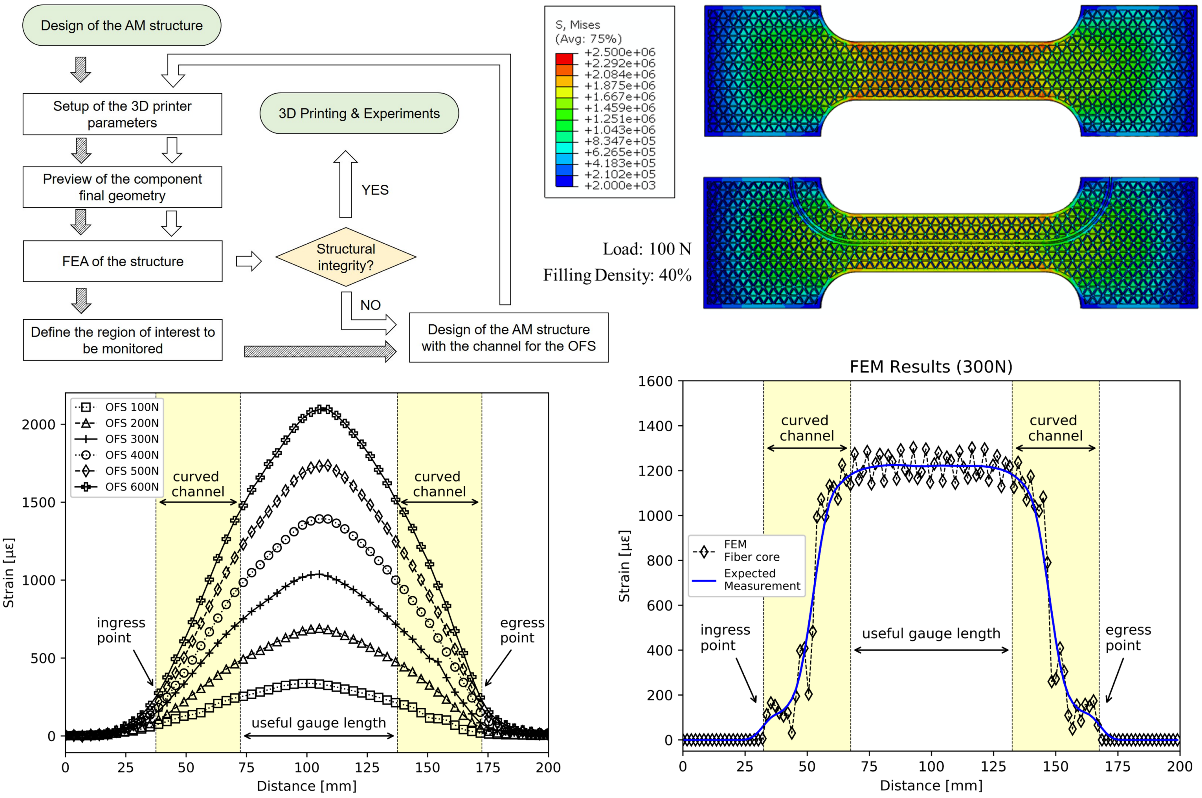

**Figure 3.B.1:** Graphical abstract of the research

# Part II

# Scientific contributions

# Chapter 4

# Strain Transfer in OFS

> *It doesn't matter how beautiful your theory is, it doesn't matter how smart you are. If it doesn't agree with experiment, it's wrong.*
>
> *Richard Feynman*

## 4.1 Introduction

Optical fibers must survive harsh environmental conditions for several in-situ monitoring applications [8], [258], [259]. In these cases, the addition of multiple coatings is useful to prevent possible damage or breakage of the optical fiber. On the other hand, protective layers usually cause a discrepancy between the strain profile of the structure and the fiber core. Therefore, the analysis of the strain transfer mechanism, from the structure to the external fiber coatings and eventually to the fiber core, aims to obtain an accurate prediction of the measured strain. This capability becomes fundamental to appropriately analyzing the damage-induced strain.

As will be shown in Chapter 5, the damage detection performance of SHM systems based on OFSs can be dominated by their strain transfer properties.

The accuracy of the strain transfer model depends on the uncertainty associated with its parameters. In this regard, Chapter 6 illustrates how the uncertainty in the shear lag constant ($k$), the key parameter in the proposed strain transfer model (see Equation 4.15), becomes of paramount importance for developing MAPOD curves.

The initial studies on the strain transfer mechanism focused on OFSs embedded in composite or concrete structures. In [260], Cox introduced the shear lag theory, establishing the fundamentals for the development of future strain transfer models. Subsequently, Claus et al., discussed the behavior of embedded optical fibers during the life cycle of structural components, highlighting the role of the fiber coating in the strain transfer process [261]. Nanni et al., investigated the use of optical fibers for in situ monitoring of concrete structures and demonstrated that the embedding direction (with respect to the applied load) influences the performance of the sensor [262]. Pak studied the strain transfer efficiency of an optical fiber embedded in a host matrix, demonstrating that the strain transfer is maximized when the shear modulus of the coating equals the geometric mean value of the shear moduli of the matrix and fiber [263]. Ansari and Libo developed a complete strain transfer model for an embedded optical fiber with three layers: the fiber core, coating and host structure [264]. They introduced for the first time the shear lag parameter, which condenses the mechanical and geometrical properties of the system. Their model became a reference in the field but was also discussed by other authors for the use of inadequate Boundary Conditions (BCs), i.e., the complete strain transfer at the fiber midpoint. Li et al., derived an analytical model to predict the strain transfer related to FBG sensors [265]. The authors demonstrated that the strain at the fiber midpoint does not necessarily match the strain value present in the host material. The BCs were applied at the two ends of the fiber assuming that the normal strain in the fiber core is null. In a subsequent study [266], the same authors proposed a refined strain transfer model considering also the mutual interaction between the fiber and the host material. The shear lag constant was redefined without changing the governing equations and the BCs. The study carried out by LeBlanc et al., analyzed the effect of strain gradients on the reflected spectra in FBG sensors [267]. The strain gradients arise due to the strain transfer phenomenon, causing the peak broadening of the reflected spectrum and affecting the spatial resolution. When FBGs are embedded in composite laminates or bonded at high temperatures, transverse stress fields are likely to be present [268]. This condition can lead to peak splitting effects in the reflected spectra, because of the strain-induced birefringence in the optical fiber. These effects should be taken into account in the strain transfer analysis to avoid misinterpretation of the results. Recently, Wang and Xiang studied the behavior of optical fibers embedded in asphalt pavements, making use of the Goodman's hypothesis to model the interfacial shear stresses [269].

Despite the increasing interest in embedded optical fiber sensors configurations, surface-bonded optical fiber sensors still represent a viable solution for many applications. In this case, the strain transfer model from the structure to the fiber core is asymmetric and the complexity of the analysis increases [270]. Wan et al., made a first parametric analysis of the strain transfer for surface-bonded OFSs studying the influence of the side width, bonding length, bottom and top thickness of the adhesive [271]. They used the analytical model for embedded optical fiber developed by Li et al. [265], and analyzed its range of validity for the surface-bonded configuration. The complexity of the geometrical layout forced the authors to rely on FEM simulations to determine the shear lag characteristics. Subsequently, Li et al., studied the strain transmission of a surface-bonded FBG sensor [272]. In their work, they derived the strain distribution not only for the FBG sensor but also for the substrate structure, emphasizing their mutual interaction. Her and Huang modeled a segment of a surface-bonded OFS with a more complex structure [273]. Their model consisted of four different layers, i.e., fiber core, coating, adhesive and substrate structure, including the possibility of a gap in the adhesive. Feng et al., investigated the strain transfer phenomenon for crack detection purposes using DOFSs [274]. Billon et al., developed a qualification methodology for DOFSs [275]. Unlike previous analytical models, they used a hybrid approach based on the derivation of a mechanical transfer function which is not known a priori and must be computed with the aid of FEM simulations. They also highlighted the importance of considering the interrogator resolution in the strain transfer analysis for crack detection.

Despite the number of available studies, the research is still limited to rather simple configurations. The cited models for surface-bonded OFSs consider a maximum of four layers. Moreover, in all the considered analytical models the strain at the ends of the bonding length is considered null. This configuration is not truly representative of real experimental setups. In fact, the deformation in the fiber structure does not decrease dramatically to zero. This discrepancy has implications for the BCs applied at the fiber ends and, therefore, may alter the prediction of the strain transfer profile.

In this study a novel strain transfer model is investigated. Seven layers were considered in the analysis, i.e., structure, adhesive, cable jacket, tight tubing, outer and inner coatings and fiber core, in order to provide a through representation of the largest number of possible fiber cable designs. The sensing cable was extended beyond the ends of the bonding length to reproduce the experimental setup more accurately. The model was validated both numerically and experimentally using DOFSs, using two cable prototypes developed within the European Horizon 2020 project Pervasive Ubiquitous Lightwave Sensor (PULSe) [276]. The general aim of PULSe is to develop a cost-effective Brillouin distribute sensing solution based on a synergy of innovative interrogator equipment (exploiting coding techniques [277] and ring lasers schemes [278]), strain sensing cable, data processing software, and open-access market take-up support tools.

In principle, the novel methodology can be applied to any type of optical fiber sensor. Nevertheless, the use of distributed sensors for the validation phase presents some advantages. Distributed sensing offers the possibility to validate the predicted strain transfer along the whole fiber with high resolution. This is particularly critical when dealing with high strain gradients, as is the case of bonded segments. For this reason, it was decided to validate the analytical model with DOFS cables. Finally, the results are presented and discussed to assess the performance of the novel analytical

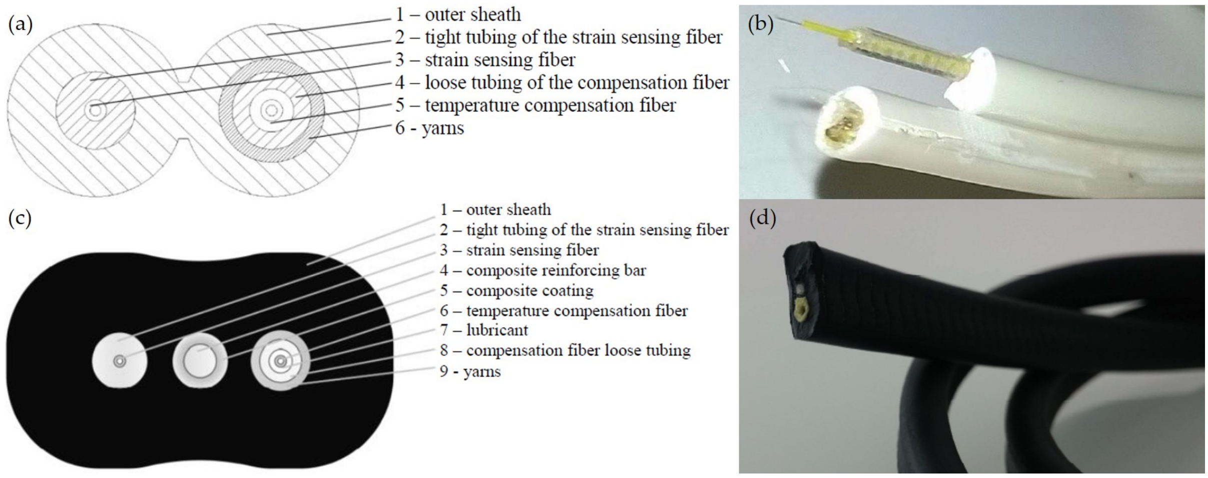

**Figure 4.2.1:** First cable prototype conceptual layout (a) and manufacturing design (b). Second cable prototype conceptual layout (c) and manufacturing design (d).

model for different bonding lengths, load levels, and cable geometries.

## 4.2 Materials and Methods

The two fiber sensing cables considered in this study are reported in Figure 4.2.1. Both strain sensors are characterized by a multi-layered structure.

They are equipped with an additional sensing fiber that allows for the compensation of temperature effects. The outer sheath protects the fiber against environmental agents. The intermediate tight tubing ensures further protection and optimizes the mechanical coupling between the fiber and the outer layers. The mechanical decoupling of the temperature-sensing fiber from the jacket is obtained by the insertion of aramid Kevlar® yarns and a lubricant. The high modulus Kevlar® yarns attenuate the deformations in the vicinities of the temperature compensation fiber, whereas the silicon lubricant significantly reduces the friction coefficient between the fiber and the outer layer. The composite reinforcing bar, which is only present in the second cable prototype, is added to avoid severe bending and thus possible breakage of the fiber. On the other hand, due to its coating and the silicon lubricant, it is mechanically decoupled from the outer sheath. This design feature prevents the reinforcing bar to bear a significant amount of axial load instead of the fiber core, which would result in a delay of the strain transfer mechanism. In both cables, the sensing fiber (Corning® SMF-28e+® LL) has a dual-layer coating system made of a primary (or inner) coating and secondary (or outer) coating. The material properties and the geometrical dimensions of the two cables are summarized in Table 4.2.1 and Table 4.2.2.

The strain transfer phenomenon was studied by bonding the two optical cables on the surface of an aluminum specimen with the material and geometrical properties reported in Table 4.2.3.

**Table 4.2.1:** Material properties and geometrical dimensions of the first sensing cable.

| Cable 1 | Optical Fiber | Inner Coating | Outer Coating | Tight Tubing | Cable Jacket | Adhesive |
|---|---|---|---|---|---|---|
| Material | Silica | "Soft" Acrylate | "Stiff" Acrylate | Polyamide | LDPE | Epoxy |
| Young's Modulus [GPa] | 21.7 | $1.30 \cdot 10^{-3}$ | 1.55 | 2.5 | 0.2 | 1.72 |
| Shear Modulus [GPa] | 8.89 | $4.36 \cdot 10^{-4}$ | 0.54 | 0.9 | 0.07 | 0.65 |
| Outer Radius [µm] | 62.5 | 95 | 125 | 450 | 1200 | n/a |

**Table 4.2.2:** Material properties and geometrical dimensions of the second sensing cable.

| Cable 1 | Optical Fiber | Inner Coating | Outer Coating | Tight Tubing | Cable Jacket | Adhesive |
|---|---|---|---|---|---|---|
| Material | Silica | "Soft" Acrylate | "Stiff" Acrylate | LDPE | EPDM | Epoxy |
| Young's Modulus [GPa] | 21.7 | $1.30 \cdot 10^{-3}$ | 1.55 | 0.2 | $7.8 \cdot 10^{-3}$ | 1.72 |
| Shear Modulus [GPa] | 8.89 | $4.36 \cdot 10^{-4}$ | 0.54 | 0.07 | $2.7 \cdot 10^{-3}$ | 0.65 |
| Outer Radius [µm] | 62.5 | 95 | 125 | 450 | 1800 | n/a |

The methodology adopted in this study consists of:

1. Development of the analytical model of the two sensing cables.
2. Development of the experimental setup and testing.
3. Numerical modeling of the experimental setup.

### 4.2.1 Analytical Model

The basic analytical model for the two sensing cables is in line with the traditional strain transfer models developed for bare surface-bonded optical fibers. However, in the present case some additional assumptions are considered and different BCs are applied. The model is developed under the following assumptions:

(A1) All the materials involved in the analysis behave as linear elastic materials and there is perfect bonding at all the layer interfaces.

(A2) It is assumed that the fiber core and the cladding behave as a unique homogeneus material which is referred to as "optical fiber".

(A3) The optical fiber coatings, the corresponding tight tubing, the cable jacket, and the adhesive carry only shear stresses. Indeed, the Young moduli of these cable components are at least one or two orders of magnitude smaller than those of the optical fiber and the specimen.

**Table 4.2.3:** Material properties and geometrical dimensions of the host structure.

| Material | Young's Modulus [GPa] | Shear Modulus [GPa] | Thickness [mm] | Width [mm] | Length [mm] |
|---|---|---|---|---|---|
| Aluminum 7075-T6 | 71.7 | 26.9 | 78 | 20 | 300 |

(A4) The strain transfer from the structure towards the fiber core depends only on the cable components surrounding the fiber under test. Therefore, referring to Figure 4.2.1 (a, c) only the left half of the two cables, where the strain sensing fiber is embedded, was considered in the development of the model.

(A5) In the second cable prototype the effect of the reinforced bar is neglected, since, as already said, it is mechanically decoupled from the surrounding cable jacket.

Based on the assumption (A4) only one half of the cable is considered, modelling its geometry as outlined in Figure 4.2.2.

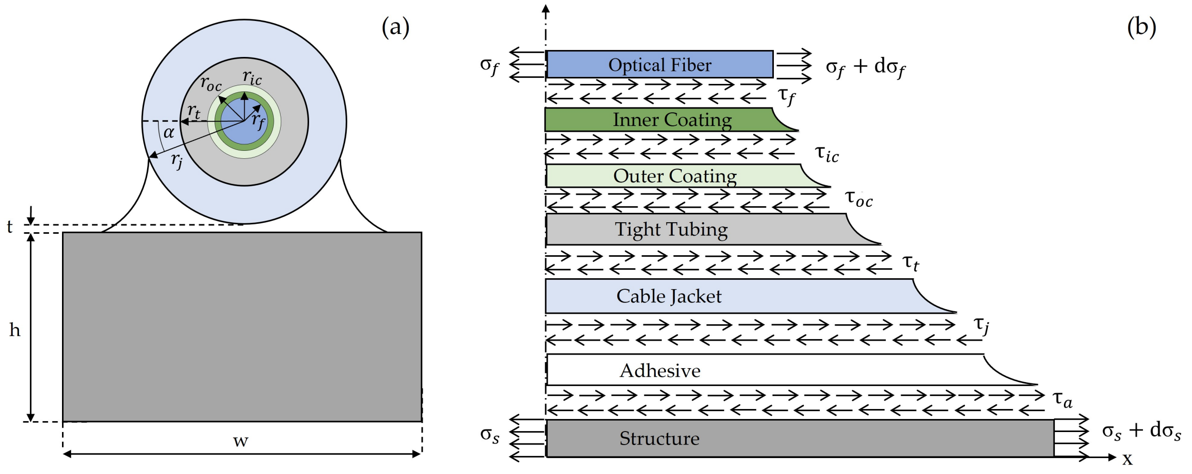

**Figure 4.2.2:** Multilayered model for the two cable prototypes. Cross section (a), free body diagram of an infinitely small cable segment (b)

The analysis was carried out using cylindrical coordinates. The axial direction, along the axis of the optical fiber, is denoted with x, the radial direction with r, whereas $\vartheta$ represents the azimuth. The analysis starts considering an infinitesimal fiber segment and imposing the equilibrium condition:

$$\left(\sigma_f + d\sigma_f\right)\pi\, r_f^2 - \sigma_f \pi\, r_f^2 + \int_0^{2\pi} \tau\left(x, r_f\right) r_f d\vartheta \cdot dx \; = 0 \qquad (4.1)$$

Where, referring to Figure 4.2.2, $r_f$ represents the optical fiber radius, $\sigma_f$ denotes the normal stress in the optical fiber and $\tau(x, rf)$ is the shear stress at the interface between the optical fiber and the inner coating. Then, it is possible to extract the shear stress at the optical fiber boundary as follows:

$$\tau\left(x, r_f\right) = -\frac{r_f}{2}\frac{d\sigma_f}{dx} \tag{4.2}$$

Recalling the assumption (A3), the equilibrium condition in the $x$ direction of the first layer surrounding the optical fiber, which is the inner fiber coating, leads to Equation 4.3:

$$\int_{\alpha}^{\pi-\alpha} \tau\left(x, r\right) r d\vartheta \cdot dx - \int_{0}^{2\pi} \tau\left(x, r_f\right) r d\vartheta \cdot dx = 0 \tag{4.3}$$

The first integral of Equation 4.3 is defined within the interval $[\alpha, \pi - \alpha]$, where $\alpha$ represents the angle between the horizontal direction and the line connecting the center of the optical fiber with the top point of the adhesive layer on the cable surface (see Figure 4.2.2). In the case of an embedded optical fiber the integration interval would be $[0, 2\pi]$ as is for the second term of Equation 4.3. However, for surface bonded optical cables the strain field is not axially symmetric. Hence, the shear stresses in the coating can be expressed as:

$$\tau\left(x, r\right) = \frac{2\pi}{\pi - 2\alpha}\frac{r_f}{r}\tau\left(x, r_f\right) \tag{4.4}$$

Substituting Equation 4.2 into Equation 4.4 one obtains:

$$\tau\left(x, r\right) = -\frac{\pi}{\pi - 2\alpha}\frac{r_f^2}{r}\frac{d\sigma_f}{dx} \tag{4.5}$$

Assumption (A1) allows to use Hooke's law, relating stresses to strains with the constitutive equations:

$$\begin{cases} \sigma = E\varepsilon \\ \tau = G\gamma \end{cases} \tag{4.6}$$

Where E, G, $\varepsilon$ and $\gamma$ represent, respectively, the Young's modulus the shear modulus, the normal strain and the shear strain of a generic layer of the sensing cable. Based on these parameters, Equation 4.5 can be rewritten as:

$$\gamma\left(x, r\right) = -\frac{1}{G_{ic}}\frac{\pi}{\pi - 2\alpha}\frac{r_f^2}{r}E_f\frac{d\varepsilon_f}{dx} \tag{4.7}$$

Where $G_{ic}$, $E_f$ and $\epsilon_f$ represent the shear modulus of the inner coating, the Young's modulus and the normal strain of the optical fiber, respectively.
The shear strain can be expressed under the assumption of small displacements:

$$\gamma\left(x, r\right) = \left(\frac{\partial u}{\partial r} + \frac{\partial w}{\partial x}\right) \tag{4.8}$$

The radial displacements, $w$, are negligible compared to the axial displacements

$u$. Indeed, the radial displacements are mainly induced by the Poisson contraction occurring in the coating and the displacements along the x axis are at least one order of magnitude higher than $w$. Hence, substituting Equation 4.8 into Equation 4.7 leads to:

$$\gamma\left(x,r\right) \cong \frac{\partial u}{\partial r} = -\frac{1}{G_{ic}}\frac{\pi}{\pi-2\alpha}\frac{r_f^2}{r}E_f\frac{d\varepsilon_f}{dx} \tag{4.9}$$

Then, integrating Equation 4.9 from the outer optical fiber radius, $r_f$, to the inner coating boundary, $r_{ic}$ one gets:

$$\int_{r_f}^{r_{ic}}\frac{\partial u}{\partial r}dr = \int_{r_f}^{r_{ic}} -\frac{1}{G_{ic}}\frac{\pi}{\pi-2\alpha}\frac{r_f^2}{r}E_f\frac{d\varepsilon_f}{dx}dr \tag{4.10}$$

The result of the integration is given by Equation 4.11, with $u_{ic}$ and $u_f$ being the axial displacements of the inner coating and the optical fiber, respectively:

$$u_{ic} - u_f = -\frac{1}{G_{ic}}\frac{\pi}{\pi-2\alpha}r_f^2E_f\frac{d\varepsilon_f}{dx}\ln\frac{r_{ic}}{r_f} \tag{4.11}$$

Performing the same operation for all the other layers leads to:

$$u_s - u_f = -\frac{\pi}{\pi-2\alpha}r_f^2E_f\frac{d\varepsilon_f}{dx}\left[\frac{1}{G_a}\ln\frac{t_a}{r_j}+\frac{1}{G_j}\ln\frac{r_j}{r_t}+\frac{1}{G_t}\ln\frac{r_t}{r_{oc}}+\frac{1}{G_{oc}}\ln\frac{r_{oc}}{r_{ic}}+\frac{1}{G_{ic}}\ln\frac{r_{ic}}{r_f}\right] \tag{4.12}$$

Where the axial displacement of the structure is denoted with $u_s$, whereas $G_a$, $G_j$, $G$t and $G_{oc}$ and $r_j$, $r_t$ and $r_{oc}$ are the shear moduli ($G$) and the radii ($r$) of the adhesive, cable jacket, tight tubing and outer coating, respectively. The thickness of the adhesive, $ta$, deserves additional considerations because it is a function of the azimuthal angle $\vartheta$ (see Figure 4.2.2). In Equation 4.12, ta is assumed equal to the average adhesive thickness and is calculated as outlined in the following expression:

$$t_a = \frac{1}{\pi-2\alpha}\int_{\alpha}^{\pi-\alpha}\left[r_j\left(1-\sin\alpha\right)+t\right]d\vartheta = r_j + t - \frac{2r_j\cos\alpha}{\pi-2\alpha} \tag{4.13}$$

Where $t$ is the minimum adhesive thickness (see Figure 4.2.2). Substituting Equation 4.13 into Equation 4.12, and introducing the shear lag parameter $k$, one gets:

$$u_s - u_f = -\frac{1}{k^2}\frac{d\varepsilon_f}{dx} \tag{4.14}$$

Where $k$ is defined by the following equation:

$$k = \sqrt{\frac{\pi-2\alpha}{\pi r_f^2E_f\left[\frac{1}{G_a}\ln\frac{t_a}{r_j}+\frac{1}{G_j}\ln\frac{r_j}{r_t}+\frac{1}{G_t}\ln\frac{r_t}{r_c}+\frac{1}{G_{oc}}\ln\frac{r_{oc}}{r_{ic}}+\frac{1}{G_{ic}}\ln\frac{r_{ic}}{r_f}\right]}} \tag{4.15}$$

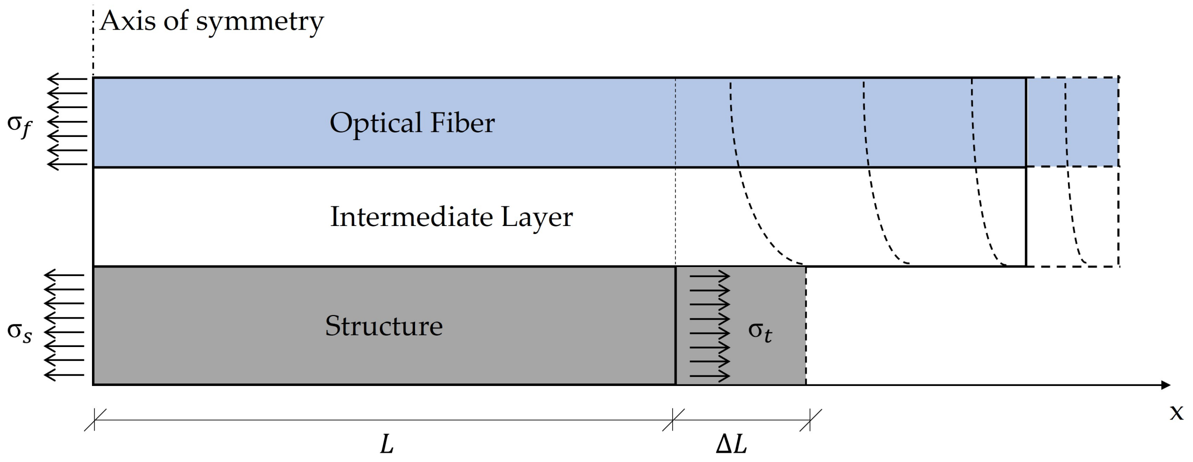

**Figure 4.2.3:** Optical cable response to a ΔL deformation of the structure.

Since the axial strain is defined as the derivative of the longitudinal displacement with respect to the $x$ variable, the differentiation of Equation 4.14 with respect to $x$ leads to:

$$\frac{d^2\varepsilon_f}{dx^2} - k^2\varepsilon_f = -k^2\varepsilon_s \tag{4.16}$$

With $\epsilon_s$ being the axial strain of the structure. Equation 4.16 is a second order linear non-homogeneous differential equation with constant coefficients. Adding up the homogeneous and the particular solutions, one obtains:

$$\varepsilon_f\left(x\right) = C_1e^{-kx} + C_2e^{kx} + \varepsilon_s \tag{4.17}$$

Where $C_1$ and $C_2$ represent the integration constants whose value can be computed imposing the corresponding BCs. Normally, the strain values at the optical fiber extremities are assumed equal to zero. However, this is not the case in real applications, where the strain does not suddenly reduce to zero, although the cable is not subjected to external loads. Figure 4.2.3 represents the actual situation.

Assuming a null strain level in the optical fiber at the two extremities of the bonding length generates a discontinuity in the first derivative of the strain profile which is unlikely to occur. In addition, since the fiber core stiffness is higher than that of the other cable components, the related deformation at the fiber boundaries is expected to be significantly lower with respect to the outer layers. Consequently, the fiber core prevents the cable jacket from stretching whereas the cable jacket tends to stretch the fiber core. This results in a self-equilibrating configuration where the fiber core experiences a tensile load whereas the other cable components undergo a compressive load. Such effect vanishes after few cable diameters (Figure 4.2.3) based on the De Saint Venant principle (stresses are free to redistribute along the structure). In addition, in a surface-bonded cable the two ends tend to bend upwards as a result of the shear strains acting in those sections. If the optical fiber core is not perfectly centered in the cable structure, the misalignment with the neutral axis produces an additional axial load. Based on these considerations, the BCs applied to Equation 4.17 are not null and assumed equal to:

$$\varepsilon_f\left(\pm L\right)=p\varepsilon_s \tag{4.18}$$

Where $L$ is half of the bonded length and the $p$ parameter symbolizes the percentage of residual strain in the optical fiber core, thus $p\in[0,1]$. Imposing the BCs defined in Equation 4.18, the integration constant $C1$ and $C2$ can be found to be:

$$C_1=C_2=\frac{(p-1)}{2}\varepsilon_s\,\mathrm{sech}\left(kL\right) \tag{4.19}$$

Then, the substitution of $C1$ and $C2$ into Equation 4.17 leads to an expression for the strain profile of the fiber core as a function of $x$:

$$\varepsilon_f\left(x\right)=\varepsilon_s\left[1+\left(p-1\right)\frac{\cosh\left(kx\right)}{\cosh\left(kL\right)}\right] \tag{4.20}$$

Equation 4.20 holds when $x\in[-L,L]$. For $x>L$ and $x<-L$, it is assumed that, in accordance with the De Saint Venant principle, the axial strain shows an exponential decay as follows:

$$\varepsilon_f\left(x\right)=ae^{-b|x|}=\begin{cases}ae^{+bx} & \text{for } x<0\\ ae^{-bx} & \text{for } x>0\end{cases} \tag{4.21}$$

Equation 4.21 represents an even function in line with the fact that the strain profile should be symmetric with respect to the sensing cable midpoint. The $a$, $b$, and $p$ parameters can be determined by fitting the experimental data. However, the authors propose the following methodology to assess their value without any prior test. The b parameter represents the exponential strain decay in the optical cable beyond the bonding length (i.e., $x>L\vee x<-L$). Hence, an estimate of b can be carried out using the same approach used to determine the shear lag parameter $k$. However, in this case the adhesive layer is not present and the first term of Equation 4.3 should be integrated from $0$ to $2\pi$ since the strain propagates with no preferential direction as in the case of a fully embedded optical fiber. These considerations lead to the following expression for $b$:

$$b=\sqrt{\frac{2}{r_f^2E_f\left[\frac{1}{G_j}ln\frac{r_j}{r_t}+\frac{1}{G_t}ln\frac{r_t}{r_c}+\frac{1}{G_{oc}}ln\frac{r_{oc}}{r_{ic}}+\frac{1}{G_{ic}}ln\frac{r_{ic}}{r_f}\right]}} \tag{4.22}$$

The other two parameters, $a$ and $p$, can be evaluated by imposing the continuity of the strain profile and its derivative at the two extremities, where $x = \pm L$. The derivative of the strain profile is estimated differentiating Equation 4.20 along the $x$ axis as follows:

$$\varepsilon_f'(x) = \varepsilon_h k (p-1) \frac{\sinh(kx)}{\cosh(kL)} \tag{4.23}$$

Considering for example the interval $x \in [L, +\infty]$ it is possible to write the following system of equations:

$$\begin{cases} \varepsilon_f(L) = ae^{-bL} = p\varepsilon_s \\ \varepsilon_f'(L) = -abe^{-bL} = \varepsilon_s k(p-1)\tanh(kL) \end{cases} \tag{4.24}$$

The system solved for $a$ and $b$ returns:

$$\begin{cases} a = \frac{e^{bL}\varepsilon_s \tanh(kL)}{b/k \tanh(kL)} \\ p = \frac{\tanh(kL)}{b/k \tanh(kL)} \end{cases} \tag{4.25}$$

Once every parameter of the model is determined and the corresponding strain profile is computed, it is convenient to introduce the so-called effective bonding length $L_{eff}$, which has been defined in the literature by several authors using various expressions [265], [279], [280]. In this study, $L_{eff}$ is defined as the minimum half fiber length to be bonded such that at the midpoint (i.e., $x = 0$) of the fiber core the strain level reaches $95\%$ of the strain present in the structure. Assuming $\varepsilon_f(0) = 0.95\varepsilon_s$, $L_{eff}$ can be obtained from Equation 4.20 as follows:

$$L_{eff} = \frac{1}{k}\cosh^{-1}\left(\frac{1-p}{0.05}\right) \tag{4.26}$$

Hence, the higher the shear lag parameter, the lower the corresponding effective bonding length. Moreover, since $p$ represents the percentage of strain in the fiber core at $x = \pm L$ with respect to the strain present in the structure, it can be stated that high values of $p$ entail lower values of $L_{eff}$. An alternative conservative approach would be to apply Equation 4.26 with $p = 0$.

### Cable-Specimen Interaction

It is worth to consider in the analysis the mutual interaction between the sensing cable and the structure if the former is particularly stiff with respect to the latter. Referring to Figure 4.2.3, it is possible to relate the theoretical strain in the structure with the actual strain, i.e., the result of the reciprocal interaction between the sensing cable and the structure. The equilibrium condition for the system is given by:

$$\sigma_t A_s = \sigma_s A_s + \sigma_f A_f \tag{4.27}$$

Where $\sigma_t$ is the true stress applied to the structure, $\sigma_s$ is the corresponding actual stress, $\sigma_f$ is the stress acting in the optical fiber, whereas $A_s$ and $A_f$ are the cross section of the structure and the optical fiber, respectively. Exploiting the Hooke's law and substituting the values of the relative cross sections one has:

$$E_s \varepsilon_t hw = E_s \varepsilon_s hw + E_f \varepsilon_f \pi r_f^2 \tag{4.28}$$

Where $h$ and $w$ are the two cross section dimensions of the structure (Figure 4.2.2), and $E_s$ is its modulus of elasticity. Solving for the actual longitudinal strain in the substrate structure, $\varepsilon_s$ , leads to:

$$\varepsilon_s = \varepsilon_t - \varepsilon_f \frac{E_f \pi r_f^2}{E_s hw} \tag{4.29}$$

Hence, when the cable stiffness is not negligible with respect the host structure, the mutual interaction must be considered.

### Interrogator Resolution

The interrogator resolution has an impact on the measured strain profile, $\varepsilon_m$. In [281] J.M. Henault et al., estimated the interrogator effect on the strain transfer mechanism by convolving the strain profile in the fiber core, $\varepsilon_f$, with a rectangular function $\Pi_i(x)$. The interval width of $\Pi_i(x)$ corresponds to the resolution of the measuring system. Hence, the filtering operation due to the interrogator can be expressed by:

$$\varepsilon_m(x) = \varepsilon_f(x) \otimes \Pi_i(x) \tag{4.30}$$

Where the symbol $\otimes$ denotes the convolution operator. For a consistent comparison between the analytical and the experimental data it is necessary to filter the analytical model results according to Equation 4.30.

## 4.2.2 Experimental Methodology

### Sensing Principle

The experimental activity was carried out at the Materials Structures Technologies Research Laboratory (MaSTeR Lab, University of Bologna, Bologna, Italy). A distributed fiber sensing technique was used in order to obtain pointwise data on the deformation occurring in the fiber core. In particular, the measurements were performed using a LUNA Optical Backscatter Reflectometer™ (OBR 4413). The working principle is

based on the Swept-Wavelength Interferometry (SWI) technique, and the interested reader can find additional information in several references [9], [253], [254].
Using the same mathematical description adopted for FBG sensors, a change in temperature, $\Delta T$, or mechanical strain, $\varepsilon$, entails a shift in the reflected wavelength, $\Delta\lambda_R$, or spectrum, $\Delta\nu_R$ , as follows:

$$\frac{\Delta\lambda_R}{\lambda_R} = \frac{\Delta\nu_R}{\nu_R} = K_T\Delta T + K_\varepsilon\varepsilon \tag{4.31}$$

Where $K_T$ and $K_\varepsilon$ denote the temperature and strain calibration coefficients, respectively. The strain transfer model developed in § 4.2.1 does not consider the effect of temperature. Consequently, the experiments were conducted at constant ambient temperature to make the term $K_T\Delta T$ negligible and filter any undesired thermal effect. The accuracy of the measurement depends on the level of accuracy of the strain calibration coefficient which in turns depends on the photo-elastic coefficient, $\rho_\varepsilon$:

$$K_\varepsilon = 1 - \rho_\varepsilon \tag{4.32}$$

The photo-elastic coefficient is defined as:

$$\rho_\varepsilon = \frac{n_{eff}^2}{2}\left[p_{12} - \nu\left(p_{11} + p_{12}\right)\right] \tag{4.33}$$

Where $\nu$ is Poisson's ratio of the fiber core and $p_{11}$ and $p_{12}$ are the components of the strain optic tensor [241]. All these parameters are affected by uncertainty depending on the concentration of the dopant species in the fiber core and the composition of the outer layers such as the cladding and the coating [282]. For standard silica fibers with germanium doped core it is common to approximate $\rho_\varepsilon$ to $0.22$ [5], [9]. Assuming a constant temperature, it is possible to derive the expression linking the strain and spectral shift:

$$\varepsilon = -\frac{\bar{\lambda}}{cK_\varepsilon}\Delta\nu_R = \alpha\Delta\nu_R \tag{4.34}$$

where $\bar{\lambda}$ is the scan centre wavelength ($\bar{\lambda} = 1306$ nm for the OBR 4413) and $\alpha$ denotes the static sensitivity of the measuring system. Considering the standard value of $0.22$ for the photo-elastic coefficient, leading to a value of $0.78$ for $K_\varepsilon$, and substituting the values of $\bar{\lambda}$ and $c$ into Equation 4.34, one obtains $\alpha = -5.59\,\mu\varepsilon/GHz$. However, in this study the authors decided to perform a preliminary calibration procedure in order to reduce the uncertainty associated with the estimation of $\alpha$ for a more accurate strain transfer analysis.

### Calibration

In order to perform the calibration of the two sensing cables, a specific test rig with a high-precision linear actuator was developed (see Figure 4.2.4).

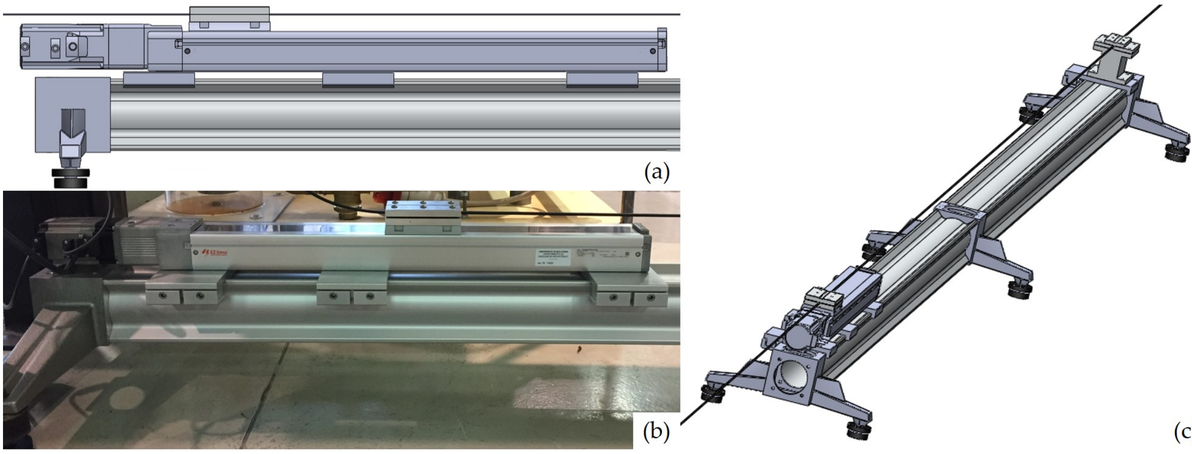

**Figure 4.2.4:** Linear actuator schematic (a) and picture (b); test rig assembly representation (c).

The test rig is composed of two rails with a length of 2 m each. They are connected and supported by 3 T-stand elements (max. load of 110 kg) to ensure stiffness, ground levelling and vibration insulation to the structure. The rails have a bending tolerance and a twisting tolerance of 0.8 mm/m and 0.75°/m, respectively. The linear actuator, with a travel range of 500 mm and a resolution of 0.02 mm, is mounted on one extremity of the test rig allowing to test an optical fiber cable with a length of 3.5 m. The displacement of the moving table surface is regulated using a closed loop controller that is connected to a laptop by means of an USB interface. The number of points, n, considered for the calibration was 80:40 in the forward path (increasing load) and 40 in the backward path (decreasing load). A maximum strain of 4000 $\mu\varepsilon$ was achieved with steps of 100 $\mu\varepsilon$ corresponding to a $\Delta L$ movement of the translation stage of 0.35 mm. This $\Delta L$ value is well above the resolution limit of the linear actuator (0.02 mm), which is key to obtain accurate data. As shown in Figure 4.2.5, the calibration results demonstrated a good linear relationship between the spectral shift and the strain, with a negligible hysteresis.

The experimental data were interpolated with a linear regression analysis and the slopes of the two lines were $-0.181 \pm 5.8 \cdot 10^{-4} GHz/\mu\varepsilon$ and $-0.179 \pm 7.4 \cdot 10^{-4} GHz/\mu\varepsilon$, respectively, with a confidence interval of three standard deviations. The corresponding static sensitivity coefficients for the first and second cable prototypes were found to be $\alpha_1 = -5.52 \pm 1.8 \cdot 10^{-2} \mu\varepsilon/GHz$ and $\alpha_2 = -5.59 \pm 2.3 \cdot 10^{-2} \mu\varepsilon/GHz$, respectively. Behind this calibration methodology there is the implicit assumption that the relation linking the strain and the spectral shift is linear. In principle non-linear effects can be present but, in this study, they were not considered. The effect of the quadratic term

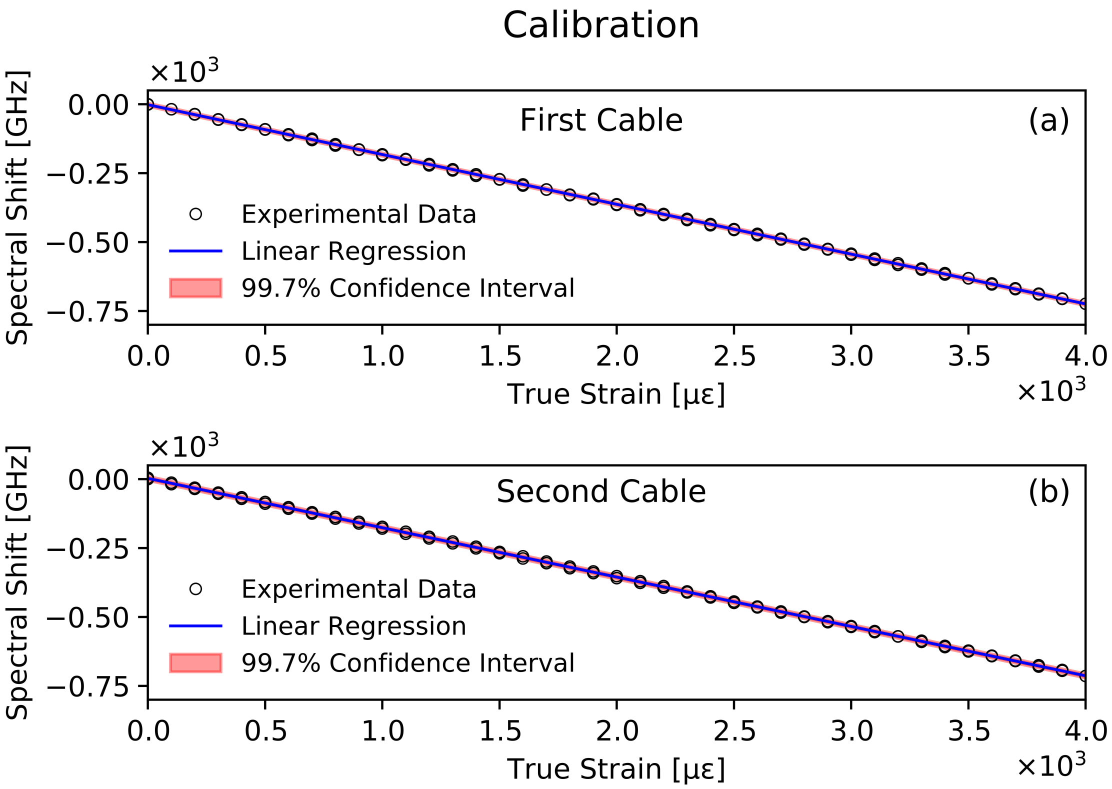

**Figure 4.2.5:** Calibration data for the first (a), and the second (b), cable prototypes.

on the determination of the static sensitivity coefficient, also known as the strain gage factor, is analyzed in [283]. If non-linearities are taken into account, the results show a deviation from the original definition of $0.55\%$. The quadratic term can therefore be reasonably neglected. The final step in the calibration procedure is to select a proper spatial shift resolution, $\Delta x$. In principle, the minimum spatial resolution achievable with the interrogator equipment can be computed as:

$$\Delta x_{min} = \frac{\lambda_1 \lambda_2}{n_{eff} \Delta\lambda} \tag{4.35}$$

Which, considering a wavelength scan ranging from 1299.03 nm to 1313.96 nm and an effective refractive index $n_{eff} = 1.4676$, leads to a value of 0.078 mm. However, this spatial resolution value is not feasible in practice for stable and accurate measurements. The choice of $\Delta x$ depends on two main considerations. First, the number of data points used to compute the Fourier transform and then the cross-correlation is proportional to $\Delta x$. If the number of points involved in the spectral shift computation is insufficient, the noise level increases. Second, the presence of significant variations of the local spectral shift (i.e., high strain gradients) can cause measurements instabilities because of the correlation peak broadening [253]. The best value of $\Delta x$ is therefore the result of a compromise between these two considerations. The method used in this study consisted in performing several measurements at constant strain, fixing the translation stage position, and gradually increasing the spectral shift spatial resolution. For each measurement, the standard deviation of the relative spectral shift was computed. A value of 20 mm for $\Delta x$ was found to be the best compromise.

### Experimental Setup

The two cable prototypes were bonded using an epoxy adhesive (LOCTITE® EA 9466™) on the surface of an aluminum specimen. The material and geometrical properties of the adhesive used for the two cables were reported in Table 4.2.1 and Table 4.2.2, whereas Table 4.2.3 summarizes the main characteristics of the specimen. Three different values of the bonding length $L$ were considered in the experiments, i.e., 210, 240, and 270 mm, for five applied loads F of 5, 10, 15, 20, and 25 kN. Besides the evaluation of the influence of these parameters on the strain transfer, this parametric analysis aims at assessing the presence of non-linear effects. In other words, the study also investigates whether the shear lag parameter depends on the applied load F, hence on the strain value in the structure. Figure 4.2.6(a) illustrates the experimental setup used for the experiments. Two electrical strain gauges, visible in Figure 4.2.6(b), were fixed on the specimen and used as a reference to estimate the longitudinal strain value. The two optical cables were bonded along the lateral side of the specimen to ensure smooth radii of curvature in the proximity of the specimen clamping areas. In fact, if the optical cables had been attached on the front sides of the specimen, a small curvature radius would have been required at the end of the bonded segment, before the clamps of the tensile test machine.

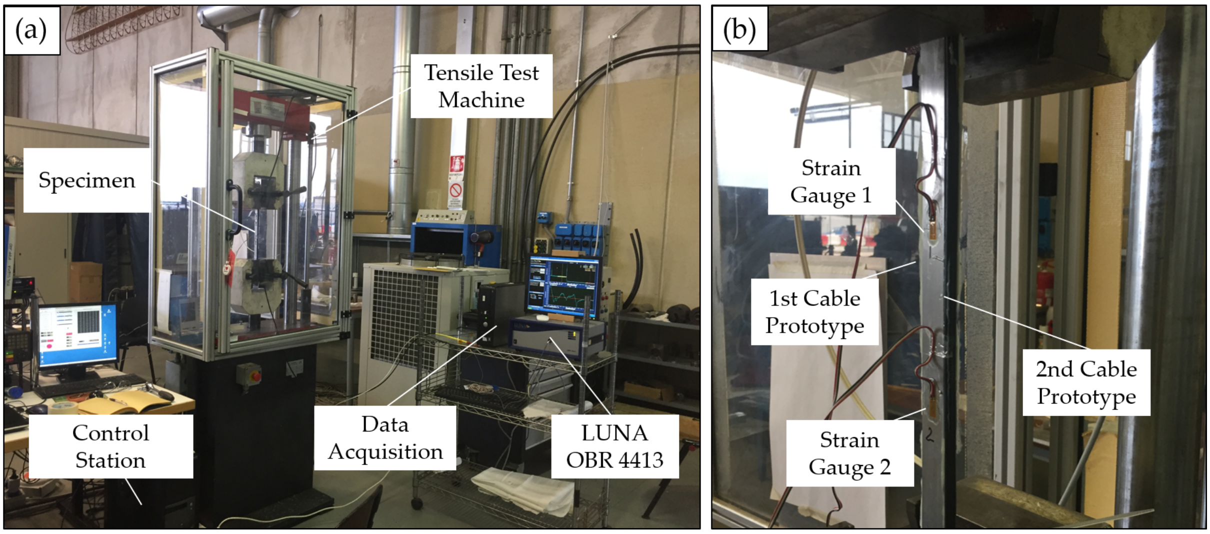

**Figure 4.2.6:** Experimental setup (a), and clamped specimen (b).

### 4.2.3 Numerical Model

The numerical model provides a third perspective to compare analytical and experimental data. Moreover, when the complexity of the geometry prevents the development of physics-based models and in the absence of experimental data, the numerical model can be a viable solution to obtain a first hint about the strain transfer characteristic of the sensing cable. The commercial software Abaqus/CAE$^{\text{TM}}$ was used to perform the numerical modeling. In particular, since strain transfer analysis can be considered a static problem, the solver Abaqus/Standard was chosen. All the model parts were meshed using the C3D8R element type. A preliminary analysis using a microscope was carried out to analyze the cross section of the two sensing cables and thus estimate their effective shape. The material properties and dimensions of the two cables and the specimen were defined according to Table 4.2.1, Table 4.2.2 and Table 4.2.3, respectively. Figure 4.2.7 shows the cable cross section of the two meshed models and the reference frame ($x$ axis pointing inward).

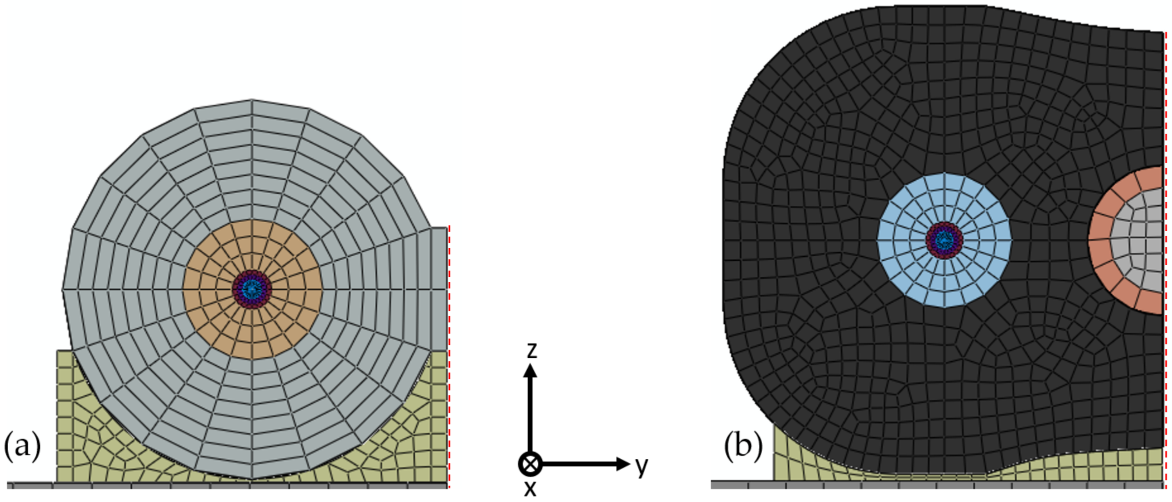

**Figure 4.2.7:** Meshed numerical models with a material-dependent mapping color. First cable prototype (a) and second cable prototype (b).

The analysis was performed applying two symmetry BCs to the two cables in order to simulate one quarter of the model, thus minimizing the computational cost. The first symmetry BC was applied to the cable cross section at the midpoint ($x = 0$). This condition is obtained by posing the displacement along the x direction equal to zero and fixing the rotation with respect to the other directions. The other symmetry BC was applied on the $x - z$ plane in correspondence of the dashed red lines in Figure 4.2.7, assuming a zero displacement along the $y$ direction and no rotation with respect the $x$ and $z$ axes. In both numerical models, the adhesive layer was connected to the structure and cable jacket using a tie constrain between the respective surfaces. In the second numerical model, shown in Figure 4.2.7(b), the reinforcing bar was coupled to the outer layer with a frictionless connection. Following the testing procedure outlined in § 4.2.2, six numerical models were generated. Due to the first symmetry BC, for each cable the simulations were carried out for L equal to 135 mm, 120 mm and 105 mm. In order to take into account the strain variation beyond the bonding length, in the numerical model the two cables were extended by 50 mm, which is more than 10 cable diameters in both cases. This choice is the result of a tradeoff between minimizing the computational cost of the simulation and avoiding any alteration of the strain transfer in the extended region, i.e., for $x > L$. The different strain levels were imposed applying a fixed displacement along the $x$ direction, $\Delta u$, in the specimen cross section at the end of the bonding length ($x = L$). The value of $\Delta u$ for the different load cases was obtained from the average strain values measured by the strain gauges, $SG_{avg}$, and the corresponding bonding lengths. Finally, in order to compare the results with the experiments, the computed strain profile along the fiber was convolved with the interrogator resolution according to Equation 4.30. The latter corresponds to the shift resolution, $\Delta x$, selected in the data processing area of the OBR 4413 system.

## 4.3 Results and Discussion

The experimental data were compared with the numerical results and those obtained from the analytical model. The comparison is shown in Figure 4.3.1, for the two cable prototypes at the three bonding lengths selected for the analysis. The horizontal lines in each diagram correspond to the average of the strain values measured by the two strain gauges mounted on the central part of the specimen, which is subjected to a constant axial strain. The vertical line indicates the point where the bonded region of the cable starts. Figure 4.3.1 shows only one half of the strain profile exploiting the symmetry with respect to the fiber midpoint.

As already illustrated, the analytical results for each subcase were obtained from Equation 4.30, whereas the parameters $a$, $b$ and $p$ were estimated following the methodology presented in § 4.2.1. The numerical data were also obtained from Equation 4.30 but using the deformation values computed along the fiber core in the FEM models. Referring to Figure 4.3.1, it is possible to observe a good qualitative agreement between the novel analytical model and the experimental and numerical data. The analytical model did not require any a priori knowledge on the shear lag parameter, k, or the percentage of residual strain in the optical fiber at the end of the bonding length, $p$, and the two constants $a$ and $b$, which describe the exponential decay of the longitudinal strain in the regions where the cables were not bonded to the structure. The input data in the model were just the mechanical properties and the geometrical characteristics of the two sensing cables. Nevertheless, if it is possible to perform a preliminary experimental campaign to characterize the cable, the different parameters can be tuned

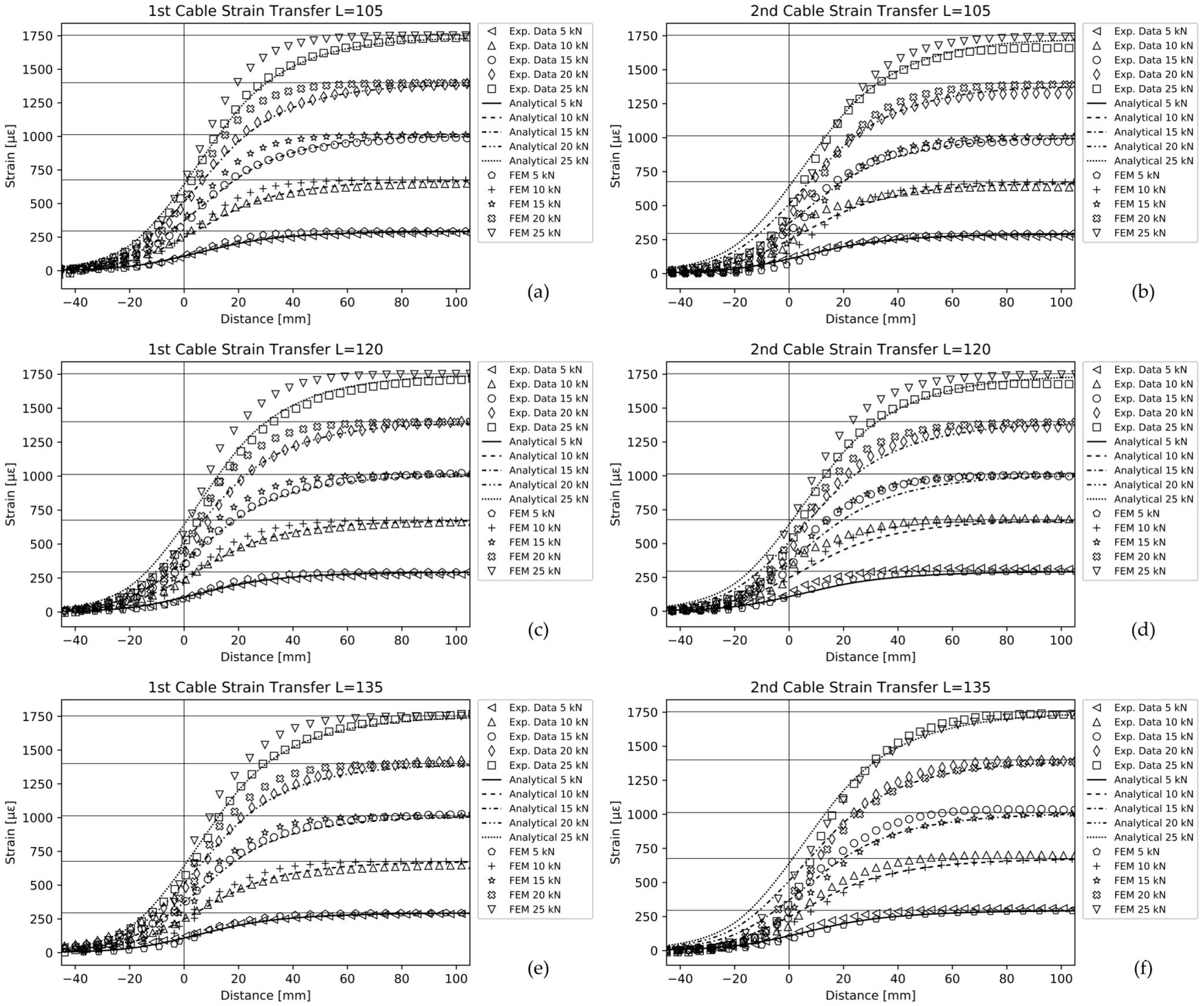

**Figure 4.3.1:** Comparison between experimental data, numerical results and analytical model.

for an optimal matching with real experimental data. Here, the authors discuss the result of the analytical model obtained without any a posteriori tuning, to assess its performance based on the deviation with respect to the numerical and experimental data. The computed shear lag parameters for the first and the second optical cables were found to be $k_1 = 0.049mm^{-1}$ and $k_2 = 0.039mm^{-1}$, respectively. Then, the application of Equation 4.26 led to $L_{eff1} = 66mm$ and $L_{eff2} = 85mm$. Considering the results obtained for the first cable prototype, it can be seen that there is a good agreement between the analytical model and the experimental data, in both regions, before and after the vertical line, at all the studied load cases. Regarding the numerical results, they tend to overestimate the strain profile in the bonding region. The numerical model seems to behave as if the cable was stiffer than the one used in the experiments. This discrepancy can be attributed to the uncertainty of the geometrical model used in the simulations, leading to a higher transfer rate. In particular, the adhesive shape plays a key role in the strain transfer mechanism. An inaccurate representation of its shape and thickness may cause a discrepancy between the analytical and experimental data. On the contrary, in the second cable prototype this effect is less evident and occurs only at the highest loads, which is instead a possible sign of nonlinearity in the behavior of the second cable. The modelling of the adhesive layer for the first cable (Figure 4.2.7(a)) is more complex if compared to the second (Figure 4.2.7(b)). In fact, in the first case the adhesive thickness varies significantly along the y direction, whereas in the second case is almost constant. The authors believe that this could be a possible explanation for such discrepancy. The predictions made for the second cable were also satisfactory from a qualitative point of view, but some considerations should be addressed. In the bonded region, there is a dependency of the results on the different load cases, most likely indicating a nonlinear behavior of the sensing cable. In particular, the analytical model tends to underestimate the strains compared to the experimental data, but not for the highest loads (20 and 25 kN). It seems, therefore, that the strain transfer efficiency of the real cable decreases as the load increases. The fact that the shear lag parameter, k, depends on the strain value in the structure, $\varepsilon$, can be attributed to the first assumption, (A1), made for the analytical model. In the second cable prototype the cable jacket is made of a plastic material (i.e., Ethylene-Propylene Diene Monomer) which may start to diverge form the linear behavior at high strain values. Moreover, in real applications there could be micro-slipping between the layer interfaces at the highest loads, leading to a reduction of the effective shear lag parameter. On the contrary, in the region before the bonded fiber segment, the analytical model predicts higher strain levels. In the authors' opinion, this effect can be attributed to the fifth assumption, (A5), in the analytical model development. The (A5) hypothesis was made to simplify the analysis which is already complex in nature. However, if the reinforced bar is not completely disconnected from the system, as it should be, it can bear a portion of axial load due to internal friction between the layers. Consequently, the composite reinforcing rod partially unloads the optical fiber core at the end of the bonded fiber segment. These considerations can also be used to interpret the comparison between the numerical and experimental data in this region. At the highest loads the cable experiences an increased contraction in the radial direction, which may cause possible grip between the rod and the cable jacket and therefore a likely nonlinearity. It is worth highlighting that all the experimental results are indeed different from zero at the starting point of the bonding region. This result indicates that the BCs of Equation 4.18 are well-posed. One could argue that the spreading of the strain profile beyond the bonded area is due to the resolution limit of the interrogator, acting as a filter. Since the convolution operation with a rectangular function extends the strain profile no further than half of the interrogator resolution, the strain should reduce to zero within 10 mm from the vertical line (Figure 4.3.1). However, all the strain values measured experimentally and reported in Figure 4.3.1 became null well after that value, thus confirming the validity of the approach. In addition, the numerical simulations showed that the results remain practically unchanged even if the resolution is assumed equal to an infinitely narrow window. Considering null strain values at the two bonded fiber ends produces therefore a wrong localization of the bonded region starting point. Referring to Figure 4.3.1, the starting point would be placed 40 mm before the actual one if it had to be the point where the strain is null. The proposed analytical model allows a different interpretation of the results, i.e., the starting point of the bonded region should coincide with the inflection point of the strain profile. The inflection point represents the real discontinuity in the system, and it can be useful when dealing, for example, with disbonding or cracks, to locate the exact damage position. The proposed analytical model was then compared with other analytical models related to previous studies (Figure 4.3.2).

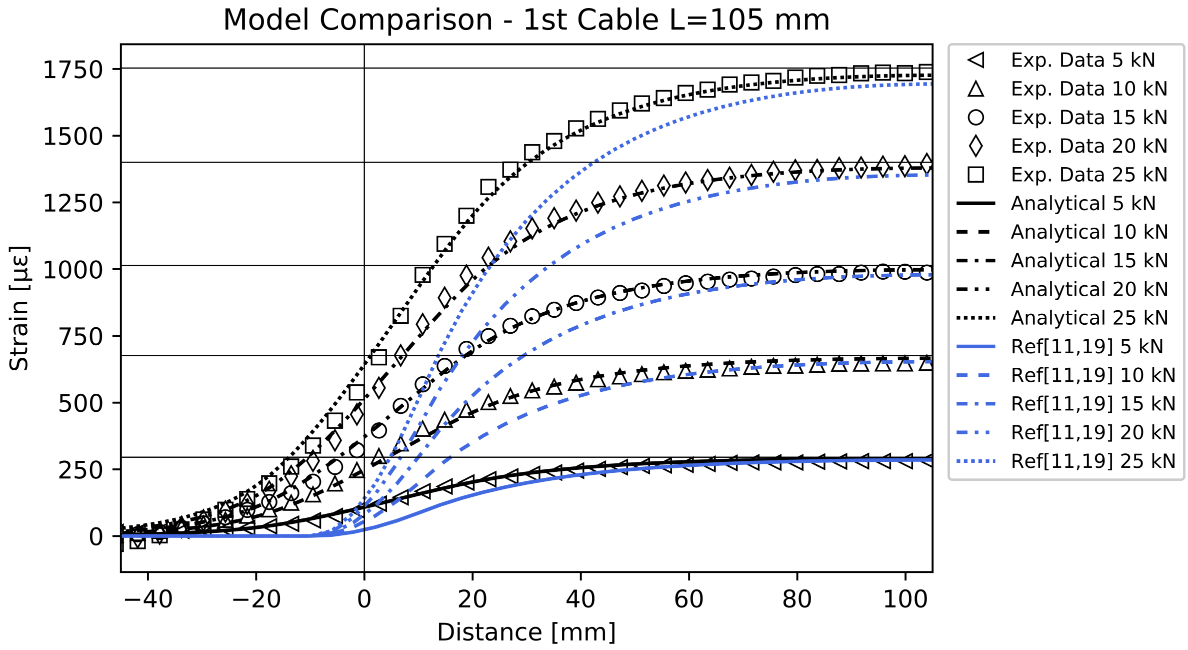

**Figure 4.3.2:** Comparison between the novel analytical model, experimental data and analytical models of references [265], [273] using $k = 0.049mm^{-1}$ and neglecting the reciprocal interaction with the specimen.

In particular, even though there are several strain transfer models available in the literature, they are governed by the same differential equations and differ from each other in the way they define the shear lag parameter and the reciprocal interaction with the structure. Thus, neglecting the reciprocal interaction with the structure (i.e., assuming that the structure stiffness is much higher than the cables stiffness), and using the k values obtained in this study for the two optical cables, it is possible to make a consistent comparison with previous studies. Here, the models of Li et al. [265] and Her and Huang [273] are considered. These models, under the previously stated conditions, are consistent with Equation 4.20 when $p = 0$. The comparison was made considering as a benchmark the experimental results related to the first cable prototype at a bonding length equal to 105 mm. The reason of this choice depends on two considerations. First, for a consistent comparison the first cable prototype is more suitable thanks to its quasi-linear response and relatively simple structure. Second, the shortest length between (105, 120, 135 mm) was chosen because it allows to focus more on the transient region. Indeed, all the models tend to converge for longer bonding lengths and the transient region becomes less visible. The interrogator resolution was taken into account in the previous models applying Equation 4.30 to their predicted strain profiles. It is evident from Figure 4.3.2 that the previous analytical models did not take into account the transient region, whereas the proposed model is able to predict it. As already stated, from a mathematical point of view the main difference lies in the $p$ parameter, which in turn depends on the "$b/k$" ratio (described in Equation 4.25). The b parameter was defined as the shear lag coefficient of the cable without the effect of the adhesive (because it is related to the free-bonding region). It is possible to infer that the higher the "$b/k$" ratio, the lower is p, for similar values of k and L. For bare optical fiber b increases. The k parameter also increases but less, since it takes into account the adhesive effect as well. As a result, for bare optical fiber the "$b/k$" ratio increases and p decreases. In this situation the proposed model behaves similarly to those available in the literature. Considering complex optical fiber cables, b decreases due to the additional layers. Accordingly, $k$ also decreases but again less, due to the adhesive terms in its definition. Consequently, "$b/k$" decreases leading to higher $p$ values. This is the reason why in this study, where complex optical fiber cables were considered, the discrepancies with respect the traditional models were evident. Since previous models were tested with standard optical fibers without a protective cable jacket, their predictions agreed better with experimental data.

## 4.4 Conclusions

The study focused on the development of a novel analytical model to study the strain transfer phenomenon in multilayered surface-bonded sensing cables. Two cable prototypes developed under the EU-funded PULSe project were investigated under different loading conditions at varying bonding lengths. SWI based on Rayleigh backscattering was adopted to measure the strain profile, allowing the determination of the strain profile shape even in presence of strain gradients at the ends of the sensing fiber segment. The model considered a complex cable structure with seven layers and non-null BCs at the end of the bonded area to reproduce the configuration found in real application cases. Successively, the analytical model was compared with both numerical and experimental data. The results confirmed its ability to predict the expected strain profile with superior performance compared with previous physics-based models available in the literature. The author also discussed the discrepancies arising from possible nonlinear effects, suggesting that further studies could improve understanding the strain transfer mechanism for surface-bonded optical fiber sensors.

This chapter lays the foundations to relate the damage detection performance of DOFSs using POD curves to the strain transfer effect.

# Chapter 5

# Qualifications of DOFS using POD curves

> *An experiment is a question which science poses to Nature, and a measurement is the recording of Nature's answer*
>
> *Max Planck*

## 5.1 Introduction

Chapter 5 presents a systematic experimental methodology based on the LaD method to qualify the damage detection performance of DOFS. The method is validated considering the use of DOFS for monitoring delamination in composite structures as a case study. Specifically, Step Index Single-Mode Optical Fiber Sensors (SISM-OFS) with ORMOCER® coating and Graded-Index Multimode Optical Fiber Sensors (GIM-OFS) with a dual acrylate coating are surface mounted onto CFRP DCB specimens under Mode I quasi-static and fatigue loading.

POD curves developed with the LaD method are used to evaluate the performance of the monitoring system of the two DOFS types in the two loading conditions. The results confirm that both strain transfer and loading conditions affect POD curves and prove that the proposed methodology can quantify the damage detection performance of DOFS in different scenarios.

Moreover, the authors introduce a practical approach to evaluating the required number of specimens based on the expected level of uncertainty. This method is twofold since it can also serve for comparing POD curves generated from different sample sizes introducing the concept of virtual specimens. This dual functionality might be of great help in real applications where it is rare having homogeneous datasets.

The final aim of this article is not to promote the use of specific DOFS for delamination detection, rather is to develop a comprehensive methodology to assess the performance of DOFS and show the implications of making a POD study in SHM using DOFS. The proposed methodology aims to provide the SHM community with a reference procedure required to deploy DOFS in composite aircraft structures.

Chapter 5 is organized as follows:  presents the method to estimate the required number of specimens and to compare POD curves produced from various sample sizes, and the experimental methodology employed in the study; § 5.3 presents the results of the research; § 5.4 discusses the results and highlights their implications; § 5.5 retraces the main stages of the study and suggests potential future research activities.

## 5.2 Materials and Methods

### 5.2.1 Required number of specimens

Usually, the number of specimens used in the experiments is arbitrarily chosen based on the researchers' expertise without a rigorous methodology. Therefore, it is interesting to develop a practical scheme to estimate the required number of specimens, $n$, required for the experimental campaign. Referring to the LaD method, see § 2.4.1, the strategy is to perform first a pilot study with few samples required to compute $\bar{x}_p$ and $s_p$, the mean and the standard deviation of the lengths at detection. Then, $\Delta = a_{90/95} - a_{90}$ is iteratively computed, leveraging the properties of the non-central t-distribution [284], and increasing the number of specimens, $n$, in each cycle. Once $\Delta$ exceeds the imposed tolerance value, the algorithm exits the while loop and returns the required number of specimens. Table 5.2.1 outlines the corresponding pseudo-code:

**Table 5.2.1:** Pseudo-code for estimated number of specimens.

```
$n = n_p$                                        Define the number of specimens used in the pilot test study
$lad_p = [lad_{p_0}, \cdots, lad_{p_n}]$         Lengths at detection vector
$\bar{x}_p = mean(lad)$                          Mean of lengths at detection vector
$s_p = std(lad)$                                 Standard deviation of lengths at detection vector
$\gamma = 0.95$                                  Confidence level on the lower bound of the POD
While $\Delta > tol$                             Imposing *guard condition*, Start While Loop
    $\delta = z_{90}\sqrt{n}$                    Non-centrality parameter of the non-central $t$ distribution
    $n = n + 1$                                  Increase the number of specimens by 1
    $k = t_{n-1,\gamma,\delta}/\sqrt{n}$         Computation of the tolerance factor $k$
    $a_{90/95} = \bar{x}_p + k \cdot s_p$        Updating $a_{90/95}$
    $\Delta = a_{90/95} - a_{90}$                Updating $\Delta$
End                                              End of the While Loop
```

Where $t_{n-1,\gamma,\delta}$ stands for the inverse of the $\gamma$ percentile of the non-central $t$ distribution with $n-1$ degrees of freedom and non-centrality parameter $\delta$.

### 5.2.2 Simulating the effect of virtual specimens on the lower bound

As the $a_{90/95}$ value reduces with $n$, in principle would only be possible to compare the POD curves obtained from equal sample sizes. This aspect is a limiting factor when acquiring data is particularly expensive and time-consuming. Therefore, in real applications, there is the need to consistently compare POD curves generated from a different number of test structures. The problem can be tackled by virtually augmenting the number of samples to a common value.

Table 5.2.2 summarizes the procedure to augment the number of specimens virtually. The algorithm is similar to the one shown in Table 5.2.1. The difference is that, in this case, the number of virtual specimens is arbitrarily chosen, and it is not determined based on a specific value of Delta.

**Table 5.2.2:** Pseudo-code for virtual specimens effect on the lower bound.

```
$n = n_e$                                        Number of specimens used in the experimental activity
$lad_e = [lad_{e_0}, \cdots, lad_{e_n}]$         Lengths at detection vector
$\bar{x}_e = mean(lad)$                          Mean of lengths at detection vector
$s_e = std(lad)$                                 Standard deviation of lengths at detection vector
$\gamma = 0.95$                                  Confidence level on the lower bound of the POD
For $n$ in Range $(n_e, n_v)$                    Imposing the number of virtual specimens ($n_v$) , Start For Loop
    $\delta = z_{90}\sqrt{n}$                    Non-centrality parameter of the non-central $t$ distribution
    $n = n + 1$                                  Increase the number of specimens by 1
    $k = t_{n-1,\gamma,\delta}/\sqrt{n}$         Computation of the tolerance factor $k$
    $a_{90/95} = \bar{x}_e + k \cdot s_e$        Updating $a_{90/95}$
    $\Delta = a_{90/95} - a_{90}$                Updating $\Delta$
End                                              End of the For Loop
```

The first step is to use the LaD method to compute the value of $\bar{x}_e$ and $s_e$. Then, assuming that the tested specimens correctly captured the primary variability sources affecting the experimental setup, it is possible to simulate the effect of an increasing number of specimens. Referring to the equations in Table 5.2.2, one can define the tolerance factor $k$ at different $n$ values but keeping the values of $\bar{x}_e$ and $s_e$ fixed. Introducing these *virtual* specimens shifts the lower bound toward the POD curve, potentially allowing for comparison of POD curves obtained from small datasets with others obtained from greater sample sizes.

For example, comparing POD curves obtained from different experiments, $n_v$ could be set equal to the number of samples of the larger dataset. It is possible to generalize the previous example to an $m$ number of POD curves obtained from $m$ different datasets. The i$^{\text{th}}$ dataset is composed of a number of elements equal to the length of the vector $lad_e^i$. Then, it is possible to define the vector $L_{lad}$ as:

$$L_{lad} = \left[length\left(lad_e^1\right), \cdots, length\left(lad_e^m\right)\right] \tag{5.1}$$

Therefore, it must be that $n_v$ is chosen such that it is greater or equal to the number of elements of the larger dataset:

$$n_v \geq max(L_{lad}) \tag{5.2}$$

The results of the proposed simulation must be taken cautiously, and based on the user expertise and the available previous knowledge, one can judge if the initial hypothesis that the original specimens properly capture the inherent variability of the experimental setup holds.

This statement can be clarified with the following example. Let us consider the scenario where two POD curves obtained with the LaD method from datasets with a different number of specimens must be compared. Temperature is the dominant source of variability, and this is known from previous experimental activities. Then, let us consider the two following cases:

(i) Both datasets were obtained by testing the specimens at different temperature levels evenly distributed in the range of temperatures under investigation;

(ii) The smaller dataset contains specimens tested only at the same temperature.

In the first case, it is reasonable to simulate the lower bound convergence of the POD by virtually augmenting the number of samples of the smaller dataset because it is likely that the variability in the system was correctly captured.

On the other hand, in the second case, the application of this procedure would lead to unconservative results. Therefore, this method must be seen as an additional tool to compare the lower bounds of POD curves originating from different datasets. Its applicability must be judged depending on the specific application and the available amount of information.

Another reason the engineers could be interested in this kind of analysis could be the following. Let us assume that, for a particular application, $a_{90/95}$ cannot exceed a certain value. After a certain amount of tested specimens, one obtains a value for $a_{90/95}$. It would be helpful to know whether additional testing will lower the $a_{90/95}$ enough. With the above-mentioned methodology, it is possible to answer this question assuming that the sample standard deviation and mean are kept constant. Suppose the simulated $a_{90/95}$ does not fulfill the requirement. In that case, the engineer has two options: testing more specimens if it is believed that $\bar{x}_e$ and $s_e$ were overestimated in the first place or redesigning the experiment to reduce the amount of variability in the system. Once again, the methodology provides a tool but the choice is based on engineering judgment.

### 5.2.3 Specimens manufacturing

The DCB coupons were manufactured following the guidelines described in the ASTM D5528 standard [285]. The AS4 HexPly 8552® unidirectional carbon prepreg [286] was employed to fabricate a $300\,\mathrm{mm}$ square panel with $[0_{24}]$ stacking sequence by hand layup. A Teflon™ film of $12\,\mu\mathrm{m}$ was placed during lamination at the panel mid-plane. This non-adhesive insert served as an initiation site for the delamination, providing an initial crack length of $50\,\mathrm{mm}$. Next, the specimens were cut from the panel utilizing an automated Proth® cutting machine, obtaining strips of $25\,\mathrm{mm}$. Ad hoc loading bocks of $25\,\mathrm{mm}$ were machined to match the width of the specimens. Before bonding, the loading block surface was sandblasted, whereas the bonding surface of the specimens was slightly scrubbed with traditional sandpaper. Impurities were removed with an alcoholic solution, and the 3M™ Scotch-Weld™ EC-9323 structural epoxy adhesive [287] was used for bonding.

### 5.2.4 Optical Fiber Sensors

Two types of DOFS were used in this study: SISM-OFS with ORMOCER® [288] coating, produced by FBGS Technologies GmbH (Jena, Germany), and GIM-OFS, produced by Plasma Optical Fibre (Eindhoven, The Netherlands). These were connected via LC/APC connectors to an ODiSI-B [255], developed by Luna Innovations Inc. (Roanoke, VA, USA). The interrogator uses coherent SWI (see § 3.3.2) to measure Rayleigh backscattering [9], [253], [254], which originates as a result of non-propagating material-density fluctuations [247]. The scattered light exhibits a repeatable profile that is sensitive to longitudinal strain ($\varepsilon$) and temperature ($T$) variations. By correlating the scattered light profile before (baseline) and after (testing) a particular perturbation, it is possible to compute the spectral shift ($\Delta\nu$) or the variation in the resonance wavelength ($\Delta\lambda$) of the scattered light according to Equation 3.21. This Equation 3.21 resembles the response of an FBG sensor. However, in this case, strain and temperature changes can be computed as a function of the fiber length with a specific spatial resolution ($\Delta X$) rather than just at the grating location. In this study, the interrogator was set up with a sampling frequency of $23.8\,\mathrm{Hz}$ and $\Delta X$ equal to $0.65\,\mathrm{mm}$.

### 5.2.5 Experimental setup

There is a considerable number of studies proposing analytical solutions for DCB specimens. The simplest analytical solution considers the DCB arms as cantilever beams clamped at the crack tip [289]. Both the Euler–Bernoulli beam theory and the Timoshenko beam theory can be used, with the latter providing more accurate results (Euler–Bernoulli-based solutions are a particular case of Timoshenko-based solutions if the shear stiffness becomes infinite) [290].

Figure 5.2.1 (a) shows a qualitative representation of the theoretical (Euler-Bernoulli theory) and experimentally measured strain profiles along the longitudinal direction (x-axis) of the DCB specimen. The scheme shown in Figure 5.2.1 (b) illustrates the specimen geometry and the positioning of the DOFS along the top surface. The labels, denoted as Seg. # 1, Seg. # 2, and Seg. # 3, indicate the three bonded segments present in each specimen. The configuration was chosen to minimize the bending radii of the DOFS, which is fundamental to reducing noise.

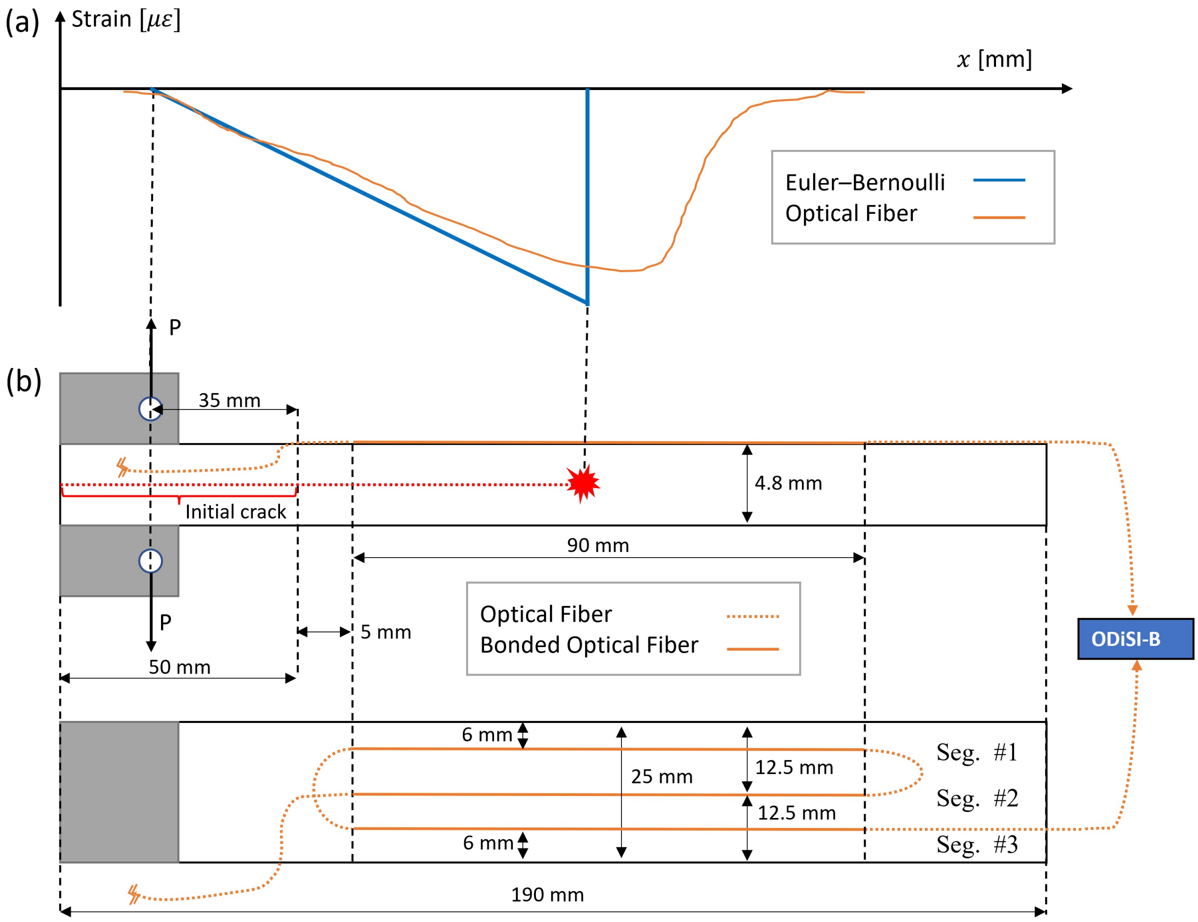

**Figure 5.2.1:** DCB specimen geometry and the optical fiber layout.

Figure 5.2.2 shows an example of a DCB specimen used in the fatigue test and the optical fiber positioned above its top surface, which was bonded using ThreeBond 1742® cyanoacrylate adhesive [291].

Before testing, one side of the DCB specimens was coated with a thin layer of white spray paint. After drying, vertical lines with 1 mm of spacing were drawn and used for visually estimating the crack length. An extra vertical mark is placed at the crack tip after the pre-cracking procedure explained in the D5528 standard [285]. Figure 5.2.3 shows a picture captured from a 9-Megapixel camera positioned in front of the specimen.

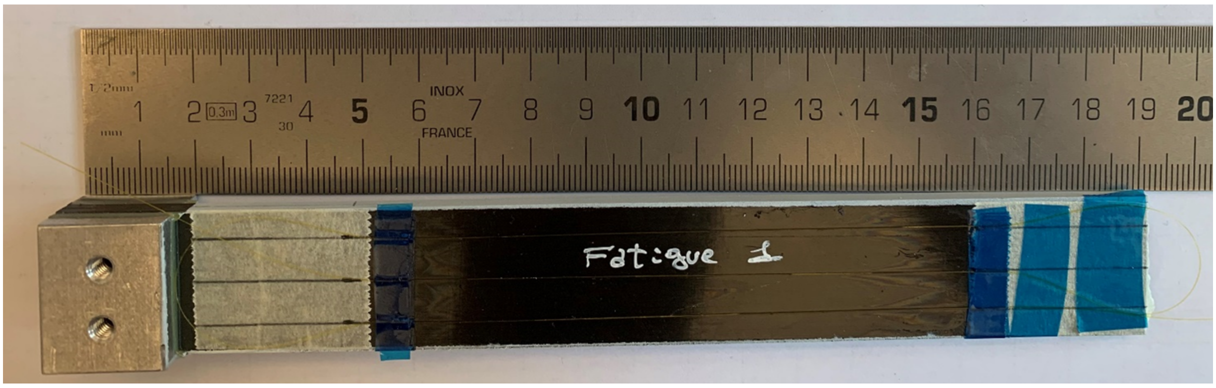

**Figure 5.2.2:** Example of the first specimen used in the fatigue test.

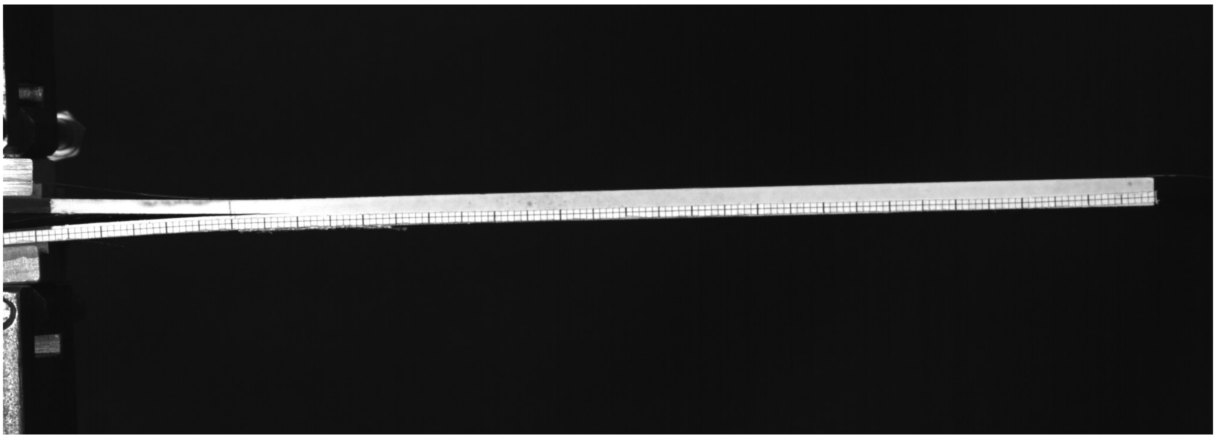

**Figure 5.2.3:** Side view of the DCB specimen captured from a 9-Megapixel camera used for crack length estimation.

The true crack length is estimated by exploiting its relationship with the compliance ($C$), defined as the ratio between the displacement at the load point ($\delta$) and the applied load ($P$) in the DCB specimen. As explained in the D5528 standard [285], and shown in Sans et al. [292], there is a linear relationship between the cube root of $C$ and the crack length, $a$:

$$\sqrt[3]{C} = \sqrt[3]{\frac{\delta}{P}} = c_1 a + c_2 \tag{5.3}$$

Where $c_1$ and $c_2$ in Equation 5.3 are the fitting parameters of the linear model. Once a sufficient number of observations is available, the linear model can be fitted, allowing the assessment of future crack length estimations from the $C$ values without visualizing hundreds of images.

For example, Figure 5.2.4 shows the linear regression obtained from the analysis of the fourth specimen, along with confidence and prediction intervals (see § 2.2.4 for confidence and prediction interval definitions). The zoomed view shows that data fall inside the prediction intervals.

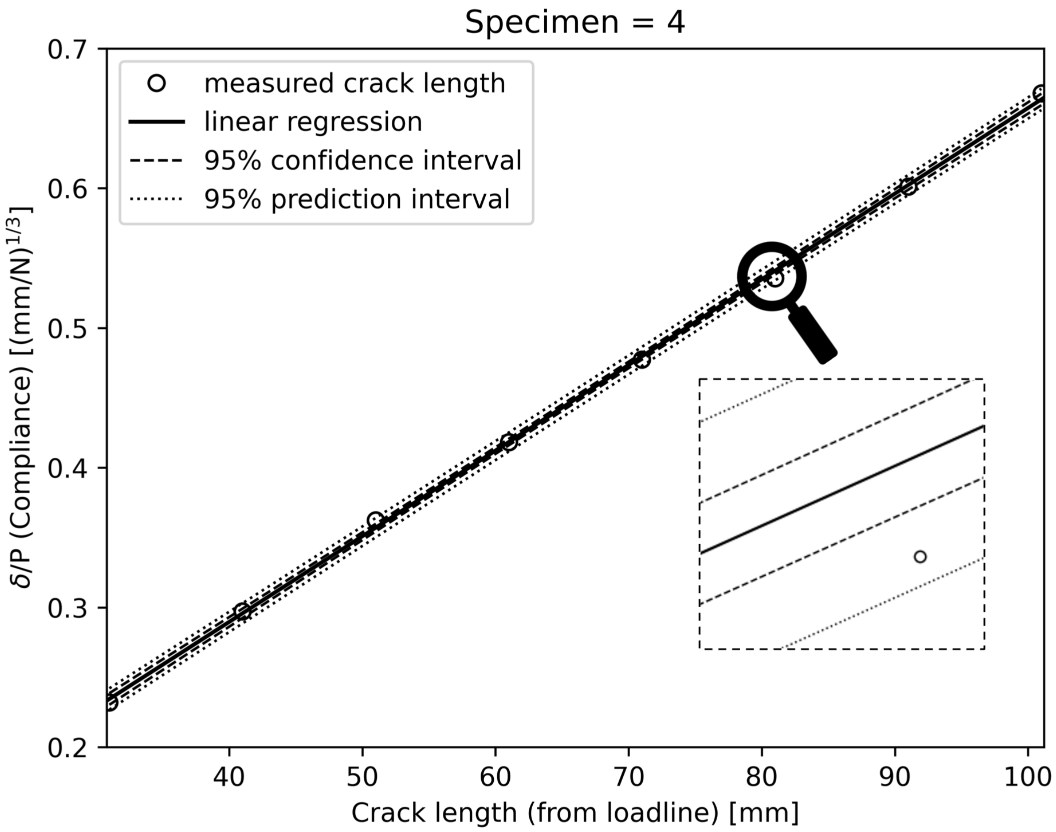

**Figure 5.2.4:** Linear regression between the cube root of $C$ and $a$.

### 5.2.6 Data structure

The acquired strain data related to the static and fatigue tests of the i<sup>th</sup> DOFS segment and j<sup>th</sup> specimen are organized in a matrix $\boldsymbol{S}_i^j$ as follows:

$$\boldsymbol{S}_i^j = \begin{bmatrix} \varepsilon_{t=0}^{x=0} & \cdots & \varepsilon_{t=0}^{x=n} \\ \vdots & \ddots & \vdots \\ \varepsilon_{t=T}^{x=0} & \cdots & \varepsilon_{t=T}^{x=n} \end{bmatrix} \tag{5.4}$$

Where $t$ and $x$ represent the time the measurement was taken and the location along the x-coordinate, respectively. The columns of $\boldsymbol{S}_i^j$ can be interpreted as the time history of a single sensing element. In contrast, each row represents the strain profile along the fiber segment at a particular moment.

Similarly, the crack lengths are organized in a vector $\boldsymbol{a}_c^j$, where the lower script, $c$, indicates that the crack has been estimated leveraging on the compliance value:

$$\boldsymbol{a}_c^j = \begin{bmatrix} a_{c,t=0}^j \\ \vdots \\ a_{c,t=T}^j \end{bmatrix} \tag{5.5}$$

### 5.2.7 Static tests

Figure 5.2.5 shows the Zwick - 20 kN tensile test machine utilized for static testing.

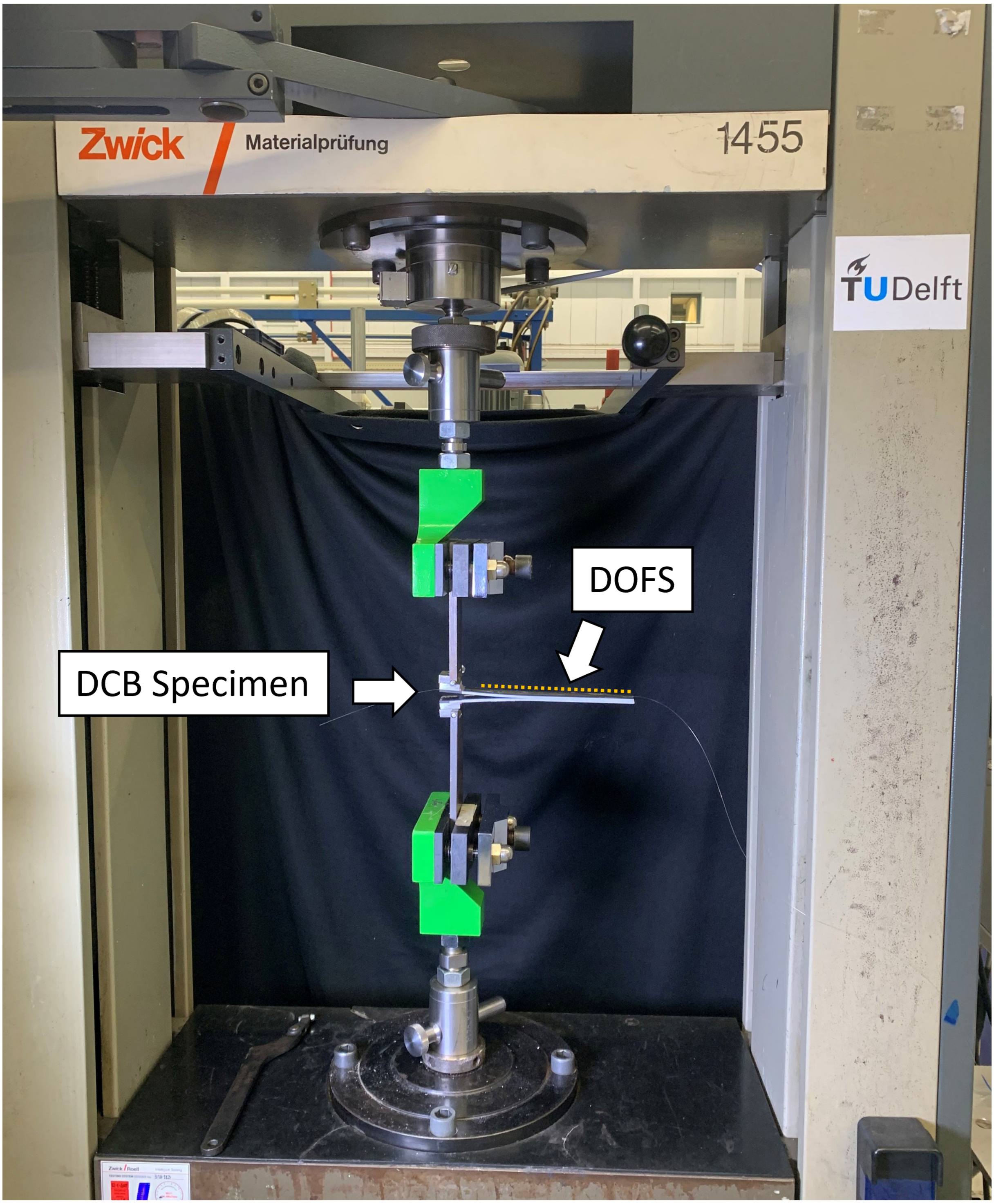

**Figure 5.2.5:** DCB specimen installed in the Zwick - 20 kN tensile test machine.

The Zwick software was set up to synchronize the LUNA interrogator unit and the camera. The tensile load was applied at a $1\,\mathrm{mm\,min^{-1}}$ displacement rate, and a sampling frequency of $0.5\,\mathrm{Hz}$ was used to collect data. The first experimental campaign used five DCB specimens equipped with SISM-OFS with ORMOCER® coating. Since three optical fiber segments are bonded onto each specimen, the number of linear regressions used to build POD curves can be multiplied by three.

The same methodology was applied in a second experimental campaign, where six specimens with GIM-OFS were tested. Preliminary results revealed that GIM-OFS are more sensitive to small bending radii. As a result of the repeated bending of the optical fiber, the configuration shown in Figure 5.2.1 would have resulted in an unsatisfactory signal-to-noise ratio. Therefore, in this case, only one central optical fiber segment was bonded in the specimen.

### 5.2.8 Fatigue test

An experimental fatigue test campaign was carried out on three specimens, where SISM-OFS with ORMOCER® coating were surface bonded using the scheme previously shown in Figure 5.2.1. The DCB specimens were mounted in an MTS - 10 kN Elastomer hydraulic test machine equipped with a 10 kN load cell. Figure 5.2.6 shows the whole experimental setup.

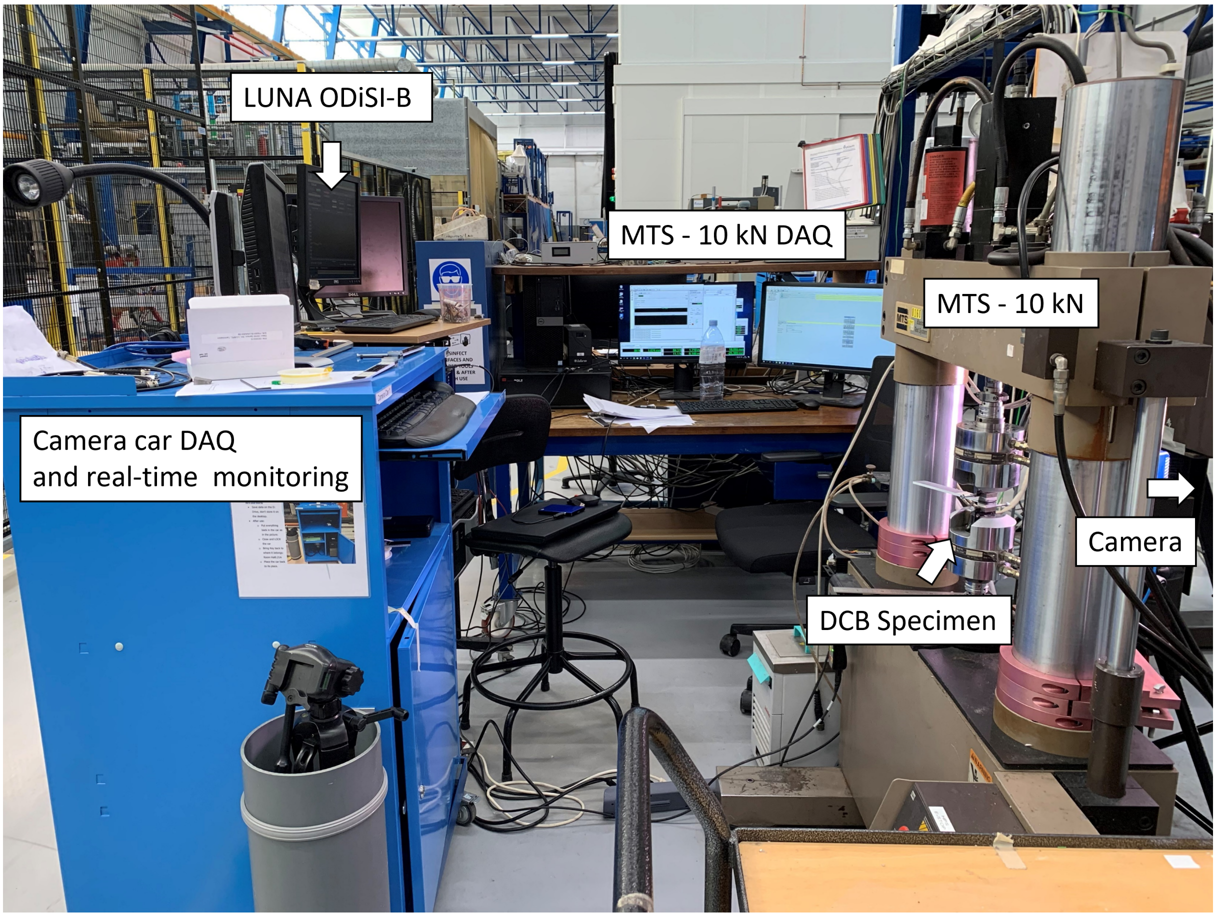

**Figure 5.2.6:** Fatigue test setup.

The fatigue tests were performed in load control. Figure 5.2.7 shows a schematic overview of how the cycling loading was applied to the DCB specimens. In addition, preliminary fatigue tests using DCB specimens manufactured from the same CFRP laminate were performed to assess the optimal load level for fatigue testing. This preliminary study found that 80% of the pre-cracking load was the optimum load level for delamination growth. Lower loads would have led to particularly slow delamination growth; in contrast, higher loads would have resulted in unstable delamination growth, which is unsuitable for developing POD curves.

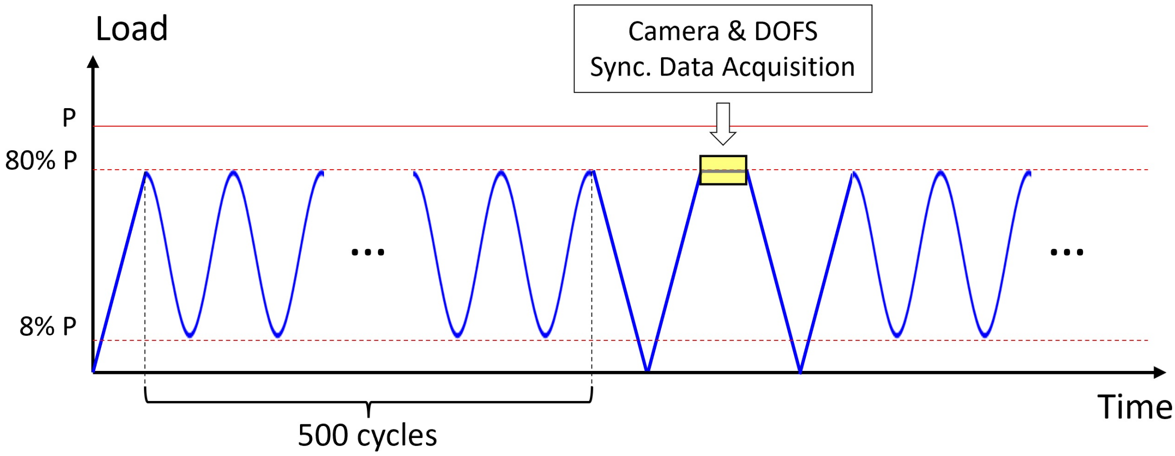

**Figure 5.2.7:** Fatigue test loading and measurement scheme.

The MTS software was programmed to reach $80\%$ of the pre-cracking load ($P$) with a ramp. Then, after every $500$ cycles at $5\,\mathrm{Hz}$ with a loading ratio ($R$) equal to $0.1$, the test is paused, and a trigger signal is sent to both the camera and the LUNA interrogator unit, allowing synchronized DOFS measurements and crack length estimation, respectively. This scheme was necessary because the DOFS signal-to-noise ratio degrades with vibrations, and acquiring clean data without interrupting the test is difficult. Moreover, this acquisition configuration guarantees that DOFS measurements are acquired under the same applied load on the specimens during the fatigue test. This is desirable since the damage index (defined in § 5.2.9) is load-dependent. Even if this choice brings difficulties because the crack propagation may become unstable, the damage index will depend only on the crack propagation and not on the applied load.

### 5.2.9 Damage index definition

Identifying a proper damage-sensitive feature represents the first step in developing POD curves. From theory, it is possible to predict that the stress field reaches its maximum compressive value at the crack tip. Thus, the strain value at the crack tip is a potential damage-sensitive feature. For a generic delamination value, and thus a generic time value $t$, it is possible to define a Damage Index (DI) as:

$$DI\,(t) = \left|\min\left(\varepsilon_t^{x=0}, \cdots, \varepsilon_t^{x=n}\right)\right| \tag{5.6}$$

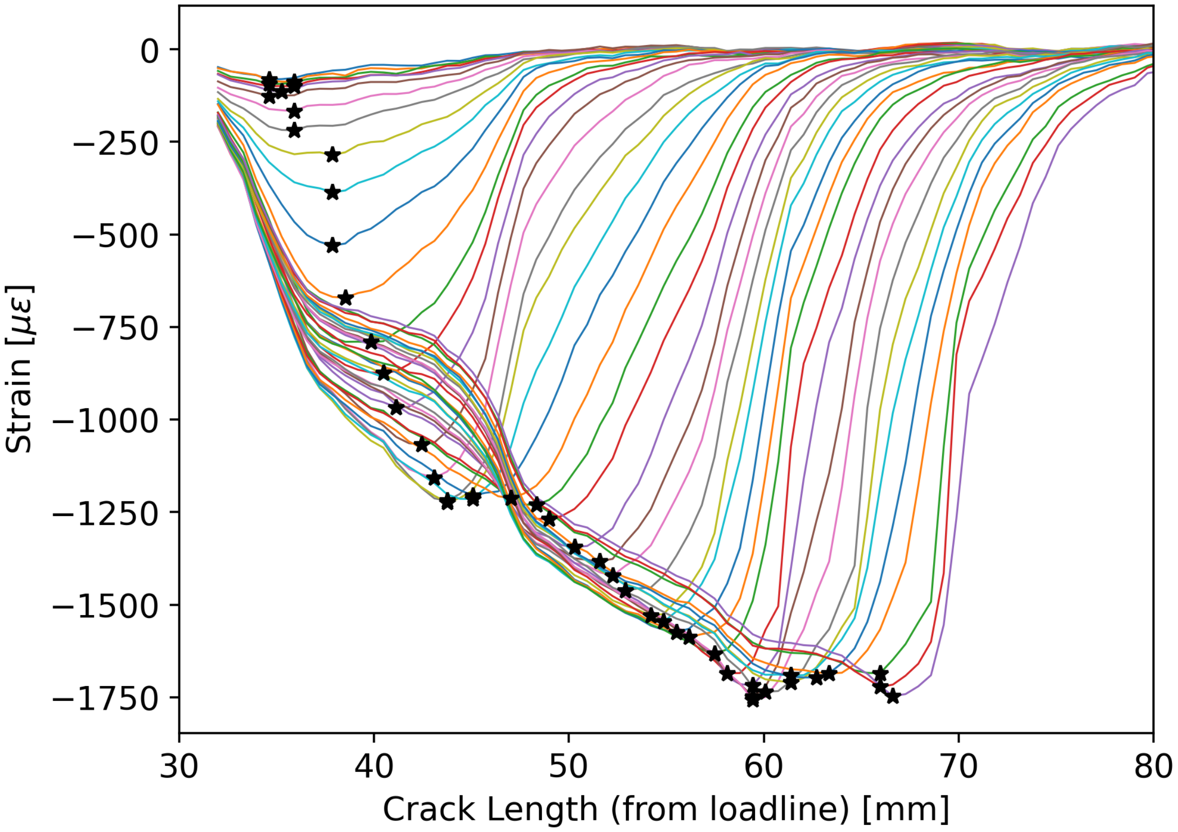

**Figure 5.2.8:** Example of strain profiles generated from DOFS during delamination growth.

Figure 5.2.8 shows an example of the strain profiles obtained using DOFS at different times in the static test profile. The black stars, placed in correspondence with the lower peak of each strain profile, highlight the estimated crack tip position and its relative propagation as delamination grows. The strain does not decrease linearly with the delamination length due to the non-linear strain transfer between the specimen and the optical fiber (see Chapter 4) and the distortion in the measured strain caused by the interrogator resolution. The linearity is restored by applying a logarithmic transformation to the DI. The new definition of DI at generic $t$ is given by Equation 5.7:

$$DI\,(t) = \ln\left|\min\left(\varepsilon_t^{x=0}, \cdots, \varepsilon_t^{x=n}\right)\right| \tag{5.7}$$

Accordingly, it is possible to define a DI vector $\boldsymbol{DI}_i^j$ (Equation 5.8) denoting the evolution over time of the damage index related to the i<sup>th</sup> DOFS segment and j<sup>th</sup> specimen:

$$\boldsymbol{DI}_i^j = \begin{bmatrix} DI_i^j\,(t=0) \\ \vdots \\ DI_i^j\,(t=T) \end{bmatrix} \tag{5.8}$$

## 5.3 Results

### 5.3.1 Static test

**Single-Mode (SM) Optical Fibers**

Figure 5.3.1 shows the application of the LaD method to SISM-OFS with ORMOCER® coating. The abovementioned DI behaves linearly with respect to the crack length, and linear regression is performed for every damage index vector $\boldsymbol{DI}_i^j$. Since every regression line has its own intercept and slope, the model is able to capture the between-segment and between-specimen variability.

In Figure 5.3.1, the abscissa assumes zero value at the onset of the bonding length of each DOFS segment. The threshold was chosen by quantifying the noise level in preliminary experiments. Precisely, three standard deviations related to noise data were summed to the highest intercept of the regression lines to avoid negative LaD values. Obtaining negative LaD values would be the equivalent of saying that the crack was detected before it reached the bonded region of the DOFS, which should not be possible in principle.

The normality assumption of the LaD method can be verified using the Anderson Darling test (Figure 5.3.2). The Null hypothesis ($H_0$) states that the data follow a normal distribution and can be rejected if, for a certain significance level $\alpha$ the Anderson-Darling statistics ($A^2$) is greater than the critical value. In the present case, considering $\alpha = 0.05$, and with a sample size $N = 13$, the critical value is equal to $0.679$ and $A^2$ resulted in being $0.298$. Therefore, since $A^2 = 0.298 < 0.679$, $H_0$ cannot be rejected, and the normality assumption holds.

Under the assumption that the LaD cracks, denoted as black squares in Figure 5.3.1, follow a normal distribution, it is possible to build a POD and its relative lower bound by applying Equation 2.12 and Equation 2.14, respectively. Figure 5.3.3 shows the corresponding POD curve obtained using this methodology.

The identified values for $a_{90}$ and $a_{90/95}$ in Figure 5.3.3 were $4.93\,\mathrm{mm}$ and $5.56\,\mathrm{mm}$, respectively. The symbol $\Delta$ denotes their difference.

**Graded-Index Multimode (GIM) Fibers**

The same methodology used for SISM-OFS in § 5.3.1 is now applied to the static test data obtained with GIM-OFS. Figure 5.3.4 shows the corresponding results. Although

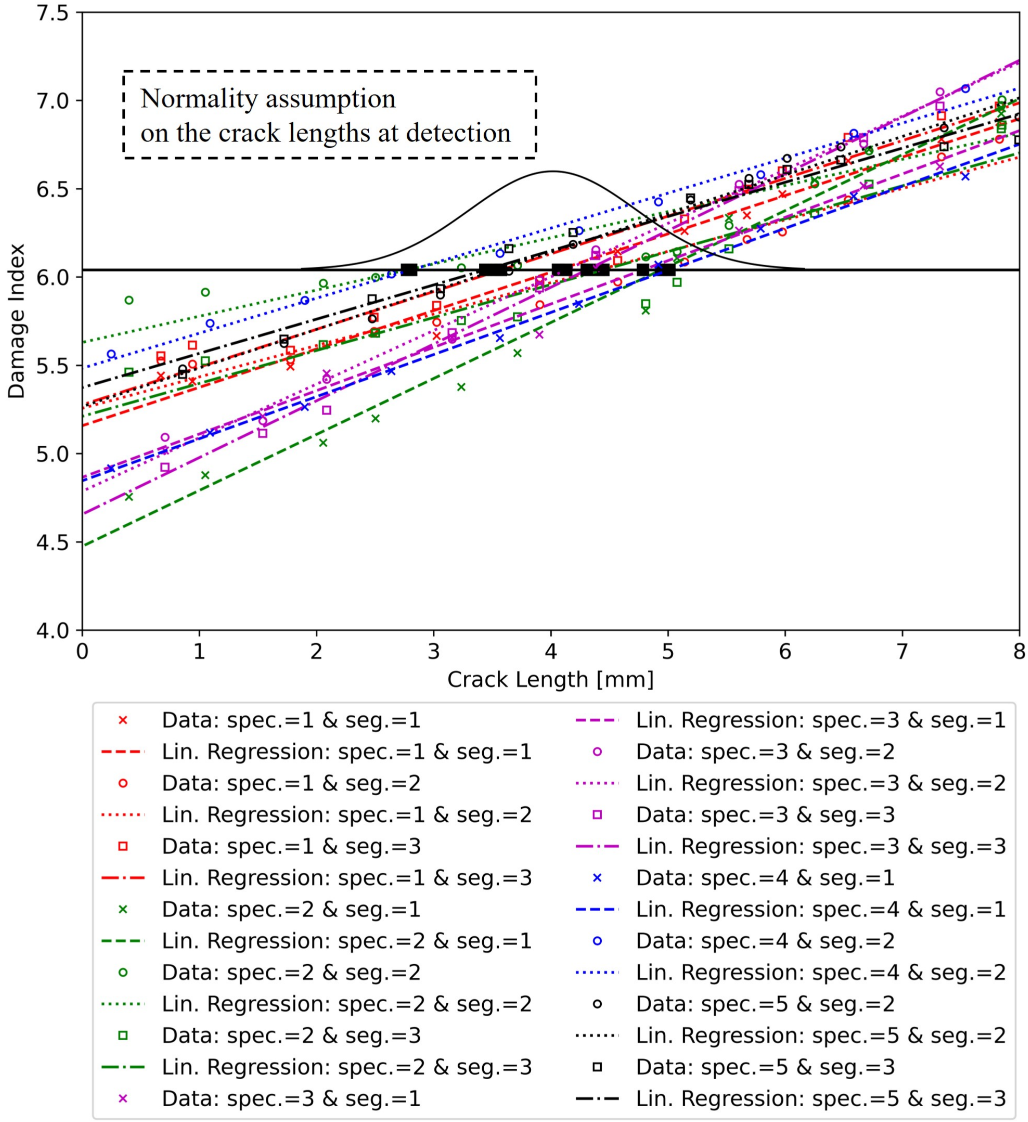

**Figure 5.3.1:** LaD method applied to SISM-OFS static test data for crack detection.

it is difficult to verify the normality assumption using the Anderson-Darling test due to the low number of samples, the collected data are enough to show how a different strain transfer performance affects the resulting POD curve. The GIM-OFS has a dual acrylate coating whose stiffness is lower than the ORMOCER® coating of SISM-OFS. This results in a lower strain transfer performance and a higher discrepancy between the real strain field (the one on the specimen surface) and the measured strain field (strain present in the fiber core).

Figure 5.3.5 displays the corresponding POD curve with $a_{90}$ and $a_{90/95}$ equal to $13.03\,\mathrm{mm}$ and $18.56\,\mathrm{mm}$, respectively. The poor performance in terms of strain transfer results in significantly higher $a_{90}$ and $a_{90/95}$ values compared to the previous static case.

Applying the methodology proposed in § 5.2.2, it is possible to show the convergence of the lower bound as the number of specimens increases (Figure 5.3.6). For

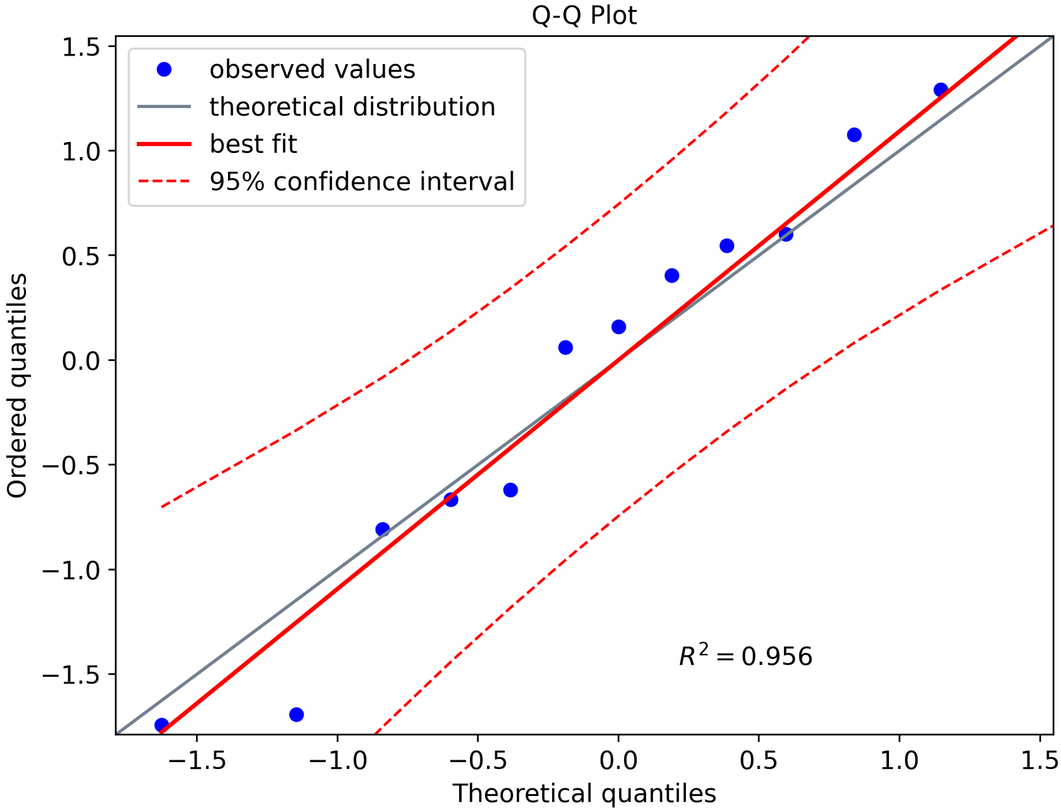

**Figure 5.3.2:** Darling-Anderson test.

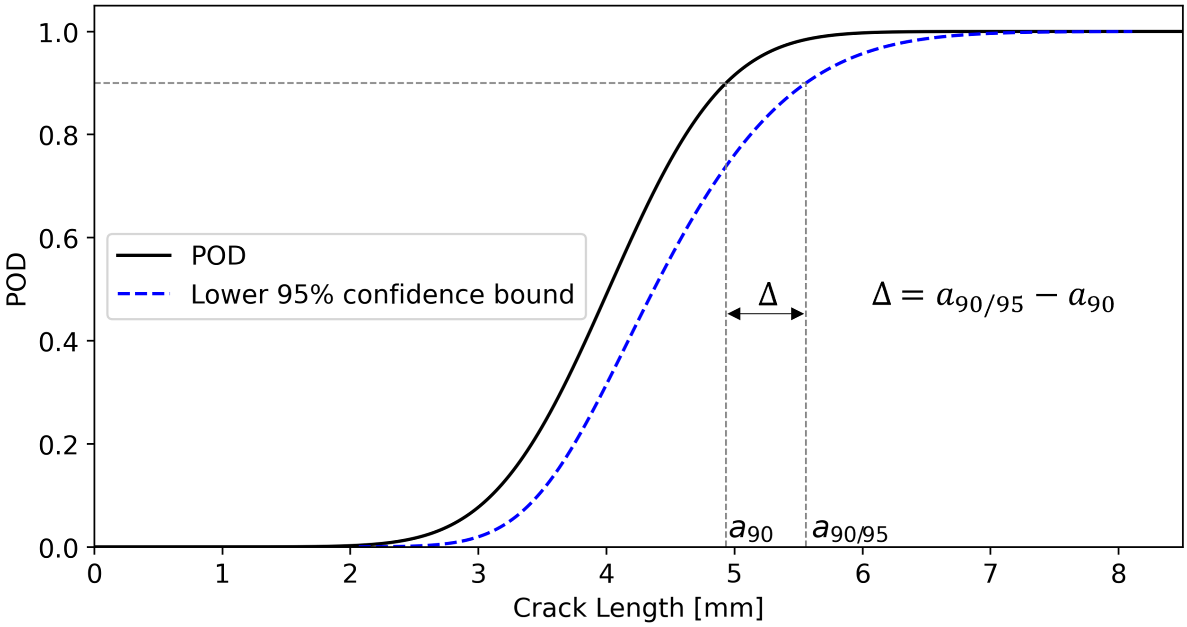

**Figure 5.3.3:** POD curve and its lower 95% confidence bound for SISM-OFS static test data.

instance, when the number of specimens equals 97, $a_{90/95}$ reaches 14.02 mm. This procedure helps compare experimental data collected from different samples. As will be

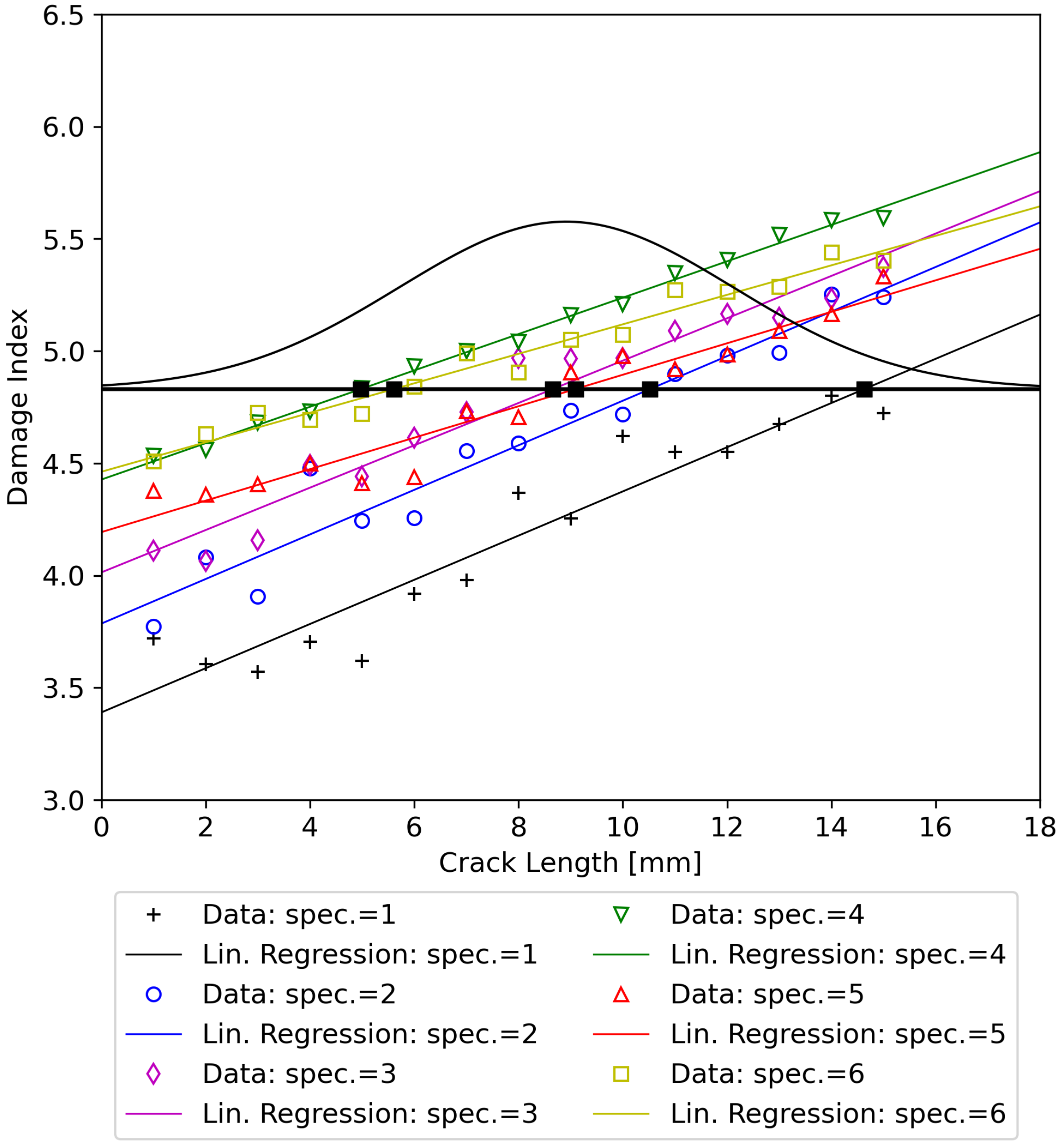

**Figure 5.3.4:** LaD method applied to GIM-OFS static test data for crack detection.

shown in § 5.4, to compare the $a_{90/95}$ values of different experimental setups, the number of samples is virtually augmented to $30$ in all scenarios.

## 5.3.2 Fatigue test

Figure 5.3.7 shows the LaD method applied to fatigue test data. The variability within segments belonging to the same specimens and between different specimens is more pronounced than for the static case, even if the same type of SISM-OFS was used (with ORMOCER® coating).

The corresponding POD curve is shown in Figure 5.3.8, with $a_{90}$ and $a_{90/95}$ equal to $5.88\,\mathrm{mm}$ and $7.82\,\mathrm{mm}$, respectively. The data highlight that both variability sources due

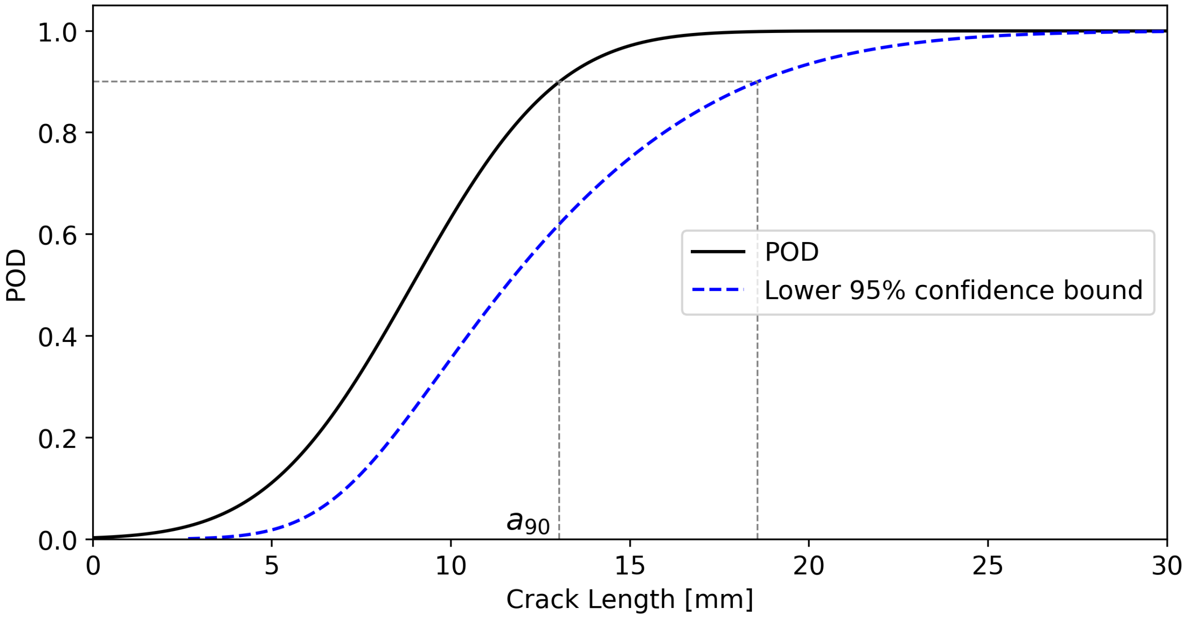

**Figure 5.3.5:** POD and its lower 95% confidence bound for GIM-OFS static test data.

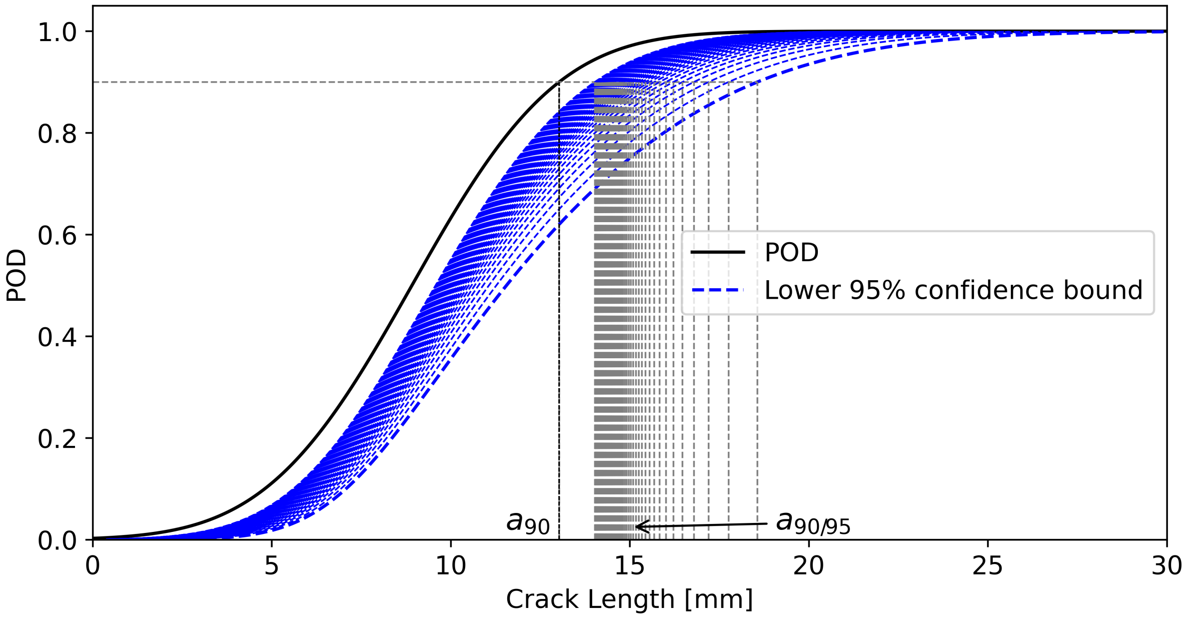

**Figure 5.3.6:** POD lower bound convergence as the number of specimens increases.

to between-specimens and within-specimen heterogeneity are present. The first two specimens (black and blue marker color in Figure 5.3.7) have more data points with respect to the static case because of the large number of samples (acquired every 500 cycles). On the other hand, the third specimen (magenta marker color in Figure 5.3.7) has few data points. This is because, in the third specimen, the crack propagated beyond the bonded region of the DOFS right after the application of the pre-cracking load and propagated faster than in the previous two cases. Compared to the static case, the measured strain is lower because the specimens were fatigue loaded at 80% of the pre-

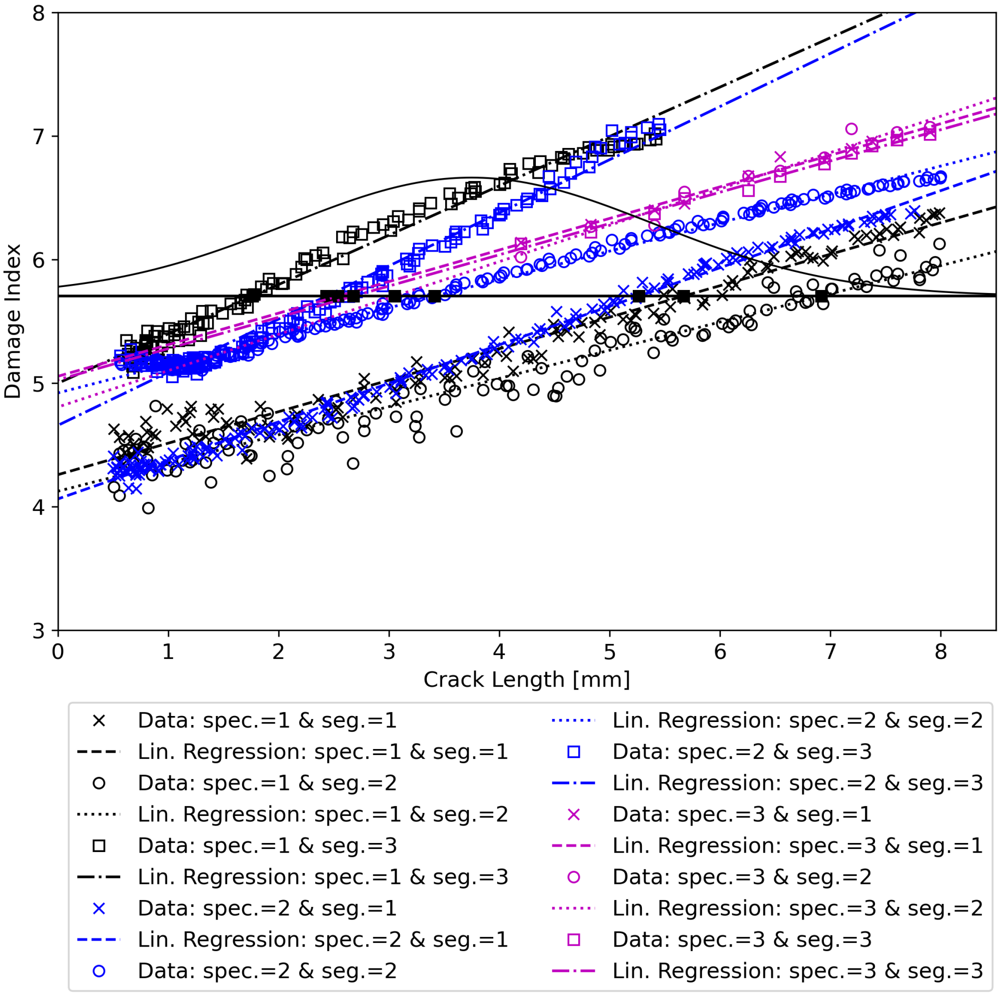

**Figure 5.3.7:** LaD method applied to SISM-OFS data in fatigue loading conditions for crack detection.

cracking load, $P$. A lower load implicates lower DI values and a lower signal-to-noise ratio, producing higher $a_{90}$ and $a_{90/95}$.

## 5.4 Discussion

### 5.4.1 Comparison of POD curves

Table 5.4.1 summarizes the results in terms of $a_{90}$, $a_{90/95}$ and $\Delta$ for the different case studies.

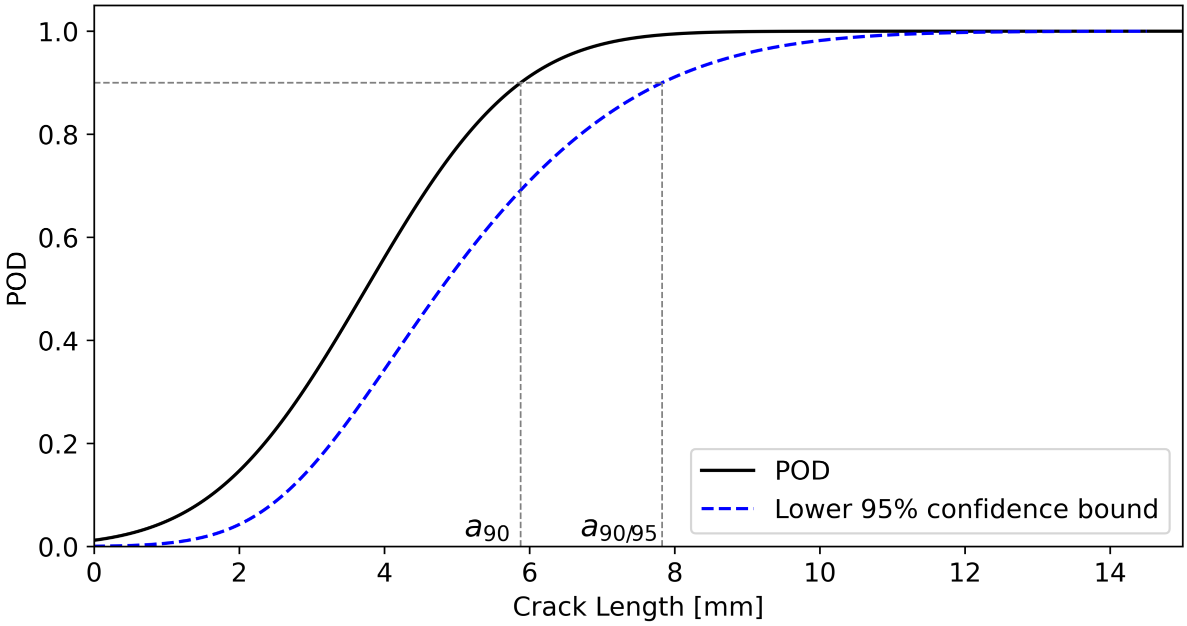

**Figure 5.3.8:** POD and its lower 95% confidence bound of SISM-OFS in fatigue loading conditions.

**Table 5.4.1:** Summary of $a_{90}$, $a_{90/95}$ and $\Delta$ values for the scenarios.

| | Static Testing | | Fatigue Testing |
|---|---|---|---|
| DOFS | SISM-OFS | GIM-OFS | SISM-OFS |
| Coating | ORMOCER® | Dual acrylate | ORMOCER® |
| $n$ | 13 | 6 | 9 |
| $a_{90}$ | $4.93\,\mathrm{mm}$ | $13.03\,\mathrm{mm}$ | $5.88\,\mathrm{mm}$ |
| $a_{90/95}$ | $5.56\,\mathrm{mm}$ | $18.56\,\mathrm{mm}$ | $7.82\,\mathrm{mm}$ |
| $\Delta$ | $0.63\,\mathrm{mm}$ | $5.53\,\mathrm{mm}$ | $1.94\,\mathrm{mm}$ |

Different optical fibers in the same loading configuration exhibit different $a_{90}$ values, as shown in Table 5.4.1. GIM-OFS with the dual acrylate coating have lower strain transfer performance than SISM-OFS with ORMOCER® coating, resulting in a higher $a_{90}$ value. Note that even the load plays a significant role even if the fiber type is kept the same, as shown in Table 5.4.1, comparing the first and the third columns. In fatigue loading, the POD curves are worse than the static case, with higher values of $a_{90}$.

### 5.4.2 Comparison of POD curves lower bounds with virtual samples

The value of $\Delta$ can be considered a measure of the variability sources involved in the experiments. Indeed, as shown in Equation 2.14, the distance of the lower confidence bound from the POD curve is a function of the standard deviation of the lengths at detection $s$.

In this study, the number of DOFS segments (samples) in each case differs. This situation is likely to occur in real applications due to the availability of different DOFS or, for example, a limited amount of time to perform fatigue tests compared to static tests.

As described in § 2.4.1 and Table 5.2.1, since $K$ decreases as $n$ increases, a higher number of samples shrinks the distance between the POD curve and its lower bound, thus decreasing $a_{90/95}$ and correspondingly $\Delta$. For example, Figure 5.3.6 shows how the number of samples affects the $a_{90/95}$ value using the strategy described in § 5.2.2. However, performing long and expensive experimental activities is not always possible. In such a case, the only solution to lower $a_{90/95}$ is redesigning the experimental setup and diminishing the associated variability sources to reduce $s$.

Nevertheless, it would be interesting to compare the results obtained in this research by having the same number of samples for each case study. Therefore, referring to the procedure outlined in § 5.2.2, the authors virtually augmented the number of samples, $n_v$, of the different case studies to $30$ units. Under the assumption that the experimental data correctly captured the variability sources involved in the experimental setup, this methodology allows a fair comparison between the different cases, eliminating a potential bias error due to the different sample sizes. Applying this procedure, one obtains the results in Table 5.4.2.

**Table 5.4.2:** Comparison of $a_{90}$ and $a_{90/95}$ values for the different case using a number of virtual samples equal to $30$.

| | Static Testing | | Fatigue Testing |
|---|---|---|---|
| DOFS | SISM-OFS | GIM-OFS | SISM-OFS |
| Coating | ORMOCER® | Dual acrylate | ORMOCER® |
| $n_v$ | $30$ | $30$ | $30$ |
| $a_{90}$ | $4.93\,\mathrm{mm}$ | $13.03\,\mathrm{mm}$ | $5.88\,\mathrm{mm}$ |
| $a_{90/95}$ | $5.29\,\mathrm{mm}$ | $14.62\,\mathrm{mm}$ | $6.70\,\mathrm{mm}$ |
| $\Delta$ | $0.35\,\mathrm{mm}$ | $1.59\,\mathrm{mm}$ | $0.82\,\mathrm{mm}$ |

The results confirm the results seen in Table 5.4.1, even if the differences within the case studies are less accentuated.

### 5.4.3 Interpretation and implications of the results

The DOFS type proved to be a determinant factor in the POD analysis, which can be directly correlated to their different strain transfer properties. On the other hand, the loading type is also shown to be a key variable since DOFS are sensitive to strain which depends on the applied load. The higher scattering in the fatigue data can be attributed to a lower Signal-to-Noise Ratio (SNR). First, the test involves a higher amount of noise due to vibrations. Second, the crack propagates at a lower load, thus further reducing the SNR. Moreover, the mechanisms involved in delamination growth differ in fatigue loading compared to quasi-static loading [2]. For example, a different amount of fiber bridging can affect the strain field in the process zone [293], thus affecting the damage index and the POD parameters.

This result suggests that also the loading mode could potentially lead to different POD curves. Indeed, the percentage of mixed Mode I/II delamination would affect the process zone and the strain profile, thus affecting the DI. In such a case, a novel and more appropriate DI should be developed because the strain at the crack tip may no longer be the best damage-sensitive feature.

Temperature variations are not considered in this study but are expected to be determinant in the POD analysis due to the relation between $\Delta T$ and $\Delta\lambda$ (see Chapter 3). In general, variation of EOCs, damage morphology, sensor drift due to degradation (sensor and coupling), and additional variability sources dependent on the specific application will certainly affect POD curves. Therefore, it is essential to raise awareness about the limitations of the results and perform sensitivity studies to address the influence of the most determinant parameters.

### 5.4.4 Upscaling POD curves

In real applications, it could be inconceivable to test a sufficiently high number of structures to perform a statistically consistent POD study for DOFS. Indeed, one should be able to produce and replicate a large number of identical complex structures, each equipped with an identical DOFS setup. Even though the proposed methodology was developed considering DOFS in laboratory case studies, it offers a framework for assessing POD curves in real applications in two different ways.

First, it is possible to use the same methodology as a basis to derive MAPOD for DOFS; this could be achieved by simulating the outcome of the LaD method given the noise level, the loading conditions, and the strain transfer properties of the DOFS-structure mechanical system. The variability sources can be modeled assigning a certain probability distribution to the most critical parameters.

Second, POD curves obtained at a coupon level could be transferred at a structure level for the monitoring of a specific damage type. The objective is to use the proposed methodology and build an experimental setup that mimics the local perturbation caused by damage in the strain field of a real structure. For example, in a hot spot monitoring scenario, where the structure is expected to fail due to mode-I delamination, the POD curves obtained from equivalent DCB specimens can provide an acceptable estimate of the damage detection performance of the system in the real application.

## 5.5 Conclusions

To the best of the author's knowledge, this is the first time an experimental POD study has been performed for DOFS based on the Rayleigh backscattering. The study proposed a methodology to develop POD curves using the LaD method focusing on delamination, which is one of the major causes of failure for composites. Mode I static and fatigue loading experiments were performed on DCB specimens with SISM-OFS with ORMOCER® coating and GIM-OFS with dual acrylate coating).

Probably, better POD curves could be obtained by using stiffer adhesives, redesigning the experimental setup to have lower noise, or using DOFS with higher strain transfer properties. However, the case studies that have been shown only serve as examples to show the implications of performing a POD study in SHM using DOFS. The goal is to develop an easily reproducible methodology to assess the performance of DOFS and to bring the attention of the SHM community to this topic which is often underestimated.

The following bullet points summarize the main finding of this research:

- Both loading conditions and DOFS type affect the performance in delamination detection.
- POD curves for DOFS can also be sensitive to different loading modes, damage types, and laminate stacking sequences, dramatically increasing the problem complexity compared to classical NDE applications.
- The LaD method proved effective in producing POD curves for DOFS, but the normality assumption is difficult to verify as the sample size decreases.
- Other POD models, such as the REM, do not require any normality assumption but are challenging to fit with small sample sizes.
- In many cases, the only feasible solution is to derive a MAPOD. The proposed framework, combined with preliminary knowledge regarding the most frequent damage modes in the structure, could be used to develop MAPOD for DOFS.
- The study provides a practical approach to estimating the required number of samples for the POD study.
- The same approach can be used to simulate the lower bound convergence, imposing a certain number of virtual samples, $n_v$, to compare POD curves obtained from different sample sizes. Caution must be taken in interpreting the results since the underlying assumption is that the available samples properly captured the variability.

- The presence of unexpected variability sources, which are not captured in the experiments, such as varying EOCs, leads to unconservative results.

Based on the finding of this work, further research is needed and should be devoted to the following aspects:

- Development of multi-dimensional POD curves varying the percentage of mixed Mode I/II delamination.
- Development of a MAPOD framework for DOFS.
- Link the concepts of strain transfer and POD curves;
- Development of compensation strategies for varying EOCs, sensor drift, and other variability sources potentially affecting POD curves.
- Analysis of upscaling potentialities and limitations of such methodology, from both structural complexity and loading complexity aspects.

The final aim of this work is to spark a constructive debate in the SHM community about developing the most appropriate methodologies to certify DOFS for damage detection using POD curves.

## 5.A Appendix: Strain-based delamination prediction in fatigue loaded CFRP coupon specimens by deep learning and static loading data

The experimental data acquired in Chapter 5 were also employed to develop a delamination prediction framework based on 1D and 2D CNNs. The main contents of this correlated research activity can be found in the following publication:

D. Cristiani, **F. Falcetelli**, N. Yue, C. Sbarufatti, R. Di Sante, D. Zarouchas and M. Giglio, "Strain-based delamination prediction in fatigue loaded CFRP coupon specimens by deep learning and static loading data," *Composites Part B: Engineering*, 2022. `https://doi.org/10.1016/j.compositesb.2022.110020`

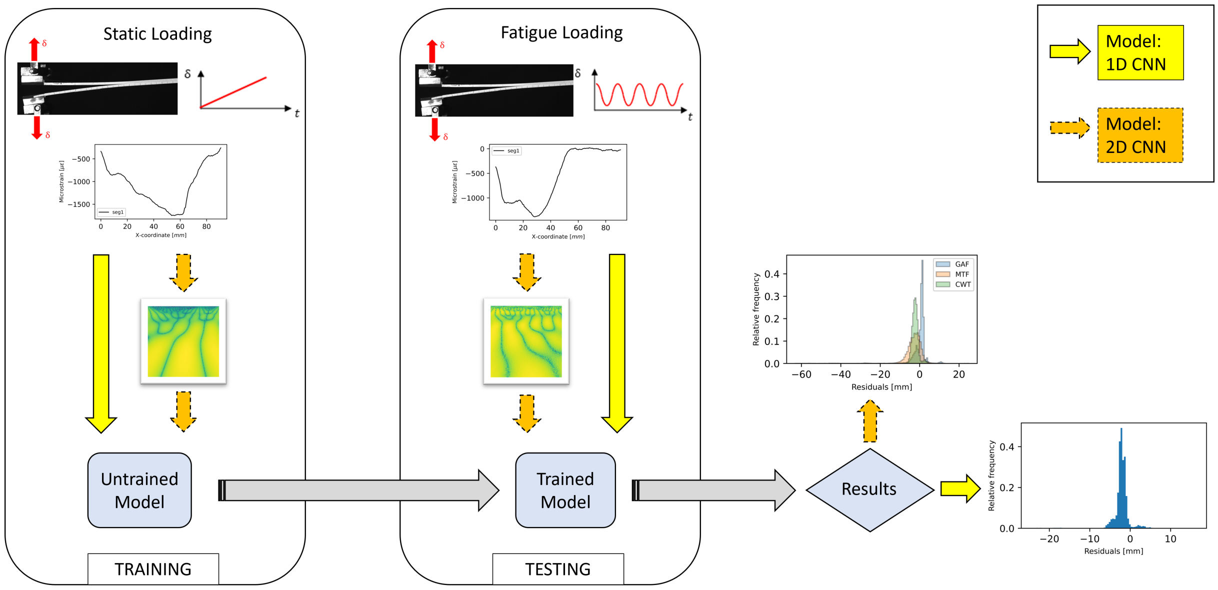

**Figure 5.A.1:** Graphical abstract of the research

# Chapter 6

# A MAPOD Framework for DOFS

> *All models are wrong, but some are useful*
>
> *George E. P. Box*

Chapter 6 introduces the preliminary results of a novel MAPOD approach for DOFS using the LaD method considering CFRP DCB specimens under quasi-static Mode I loading. Moreover, a parametric study is carried out to understand how different parameters can affect the detection performance of DOFS. The qualitative analysis of these preliminary results suggests that this framework can be used to model DOFS experimental setup.

## 6.1 Methodology

Several factors affect the performance of DOFS for damage detection (see Chapter 5): the structure geometry and type of loading, the human factor, the strain transfer from the structure to the fiber core, the interrogator resolution, and the SNR. Each one of these variables should be properly modeled in a MAPOD framework.

### 6.1.1 Structure geometry and loading

Delamination is one of the most common and dangerous damage mechanisms in composite structures, and DCBs are representative structures of many different components. Thanks to well-defined standards describing the experimental procedure [285], DCBs are relatively easy to manufacture and test, which is crucial to validate the MAPOD model.

Taking as reference the experimental setup described in § 5.2.5, the effect of delamination in CFRP DCB specimens under mode I loading is modeled following the, Euler-Bernoulli theory, as a triangular strain profile [294]. The schematic of the case study is shown in Figure 6.1.1.

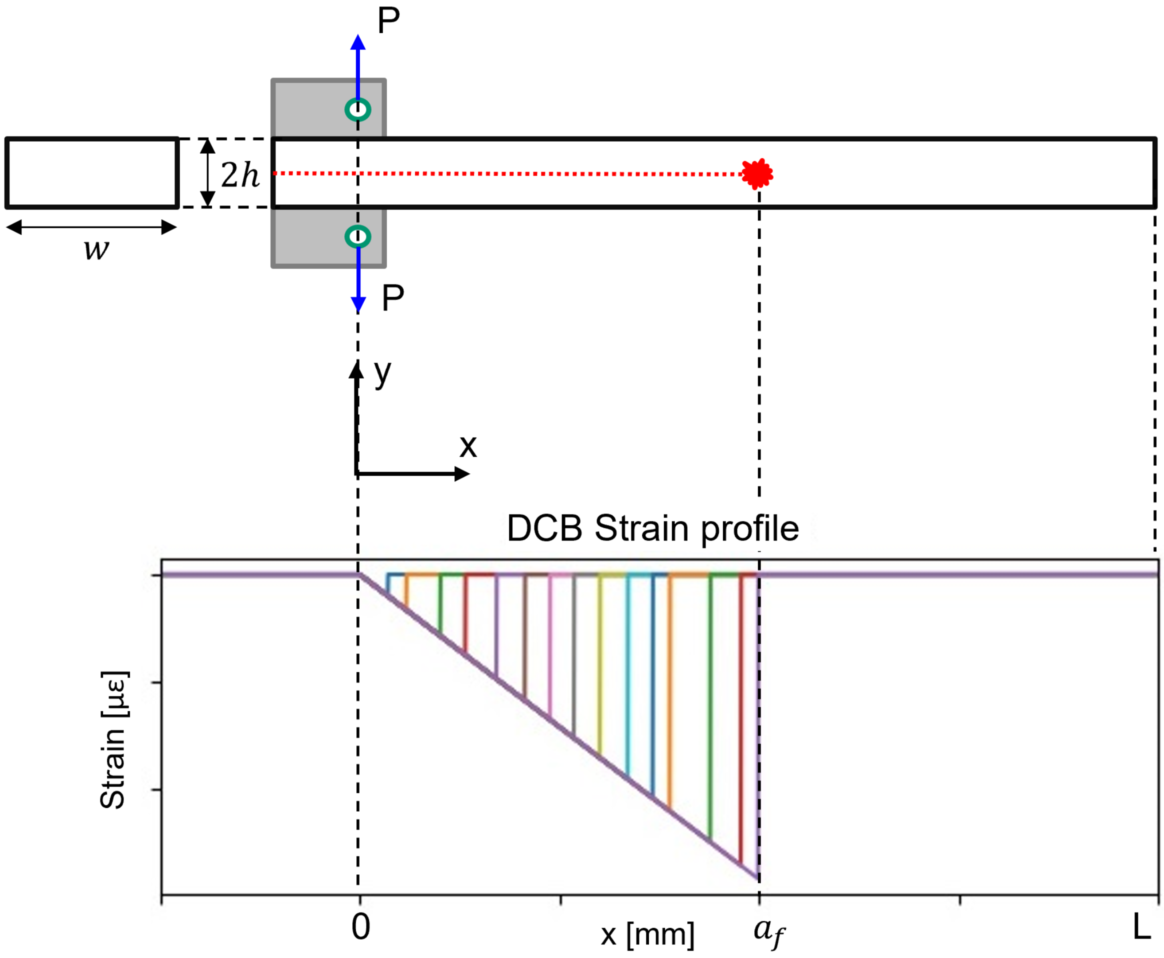

**Figure 6.1.1:** DCB specimen modeling and theoretical strain profiles.

Applying Navier's formula (Equation 6.1) to the case study shown in Figure 6.1.1, one can find the stress distribution along the x-axis ($\sigma_x$):

$$\sigma_x = \frac{M_z}{I_z} y \tag{6.1}$$

Where $M_z$ and $I_z$ denote the moment and moment of inertia about the z-axis (perpendicular to the paper pointing outward in Figure 6.1.1), respectively.

The moment ($M_z$) increase linearly with the distance from the applied load ($P$) as shown in Equation 6.2:

$$M_z = Px \tag{6.2}$$

Equation 6.2 holds for $x \in [0, a]$ since $M_z$ must be null after the crack tip at $x = a$, where $a$ is the crack length.

The applied load ($P$) decreases with the delamination length according to a function that can be determined experimentally or through FEM simulations [295]. In this case $P(a)$ was determined by a third degree polynomial regression (Equation 6.3) using the experimental static test data of the SISM-OFS with ORMOCER® coating. Moreover, was added a random component ($\epsilon_P$) to account for the impossibility to reproduce the exact loading condition across different specimens ($\epsilon_p \sim \mathcal{N}(0, \sigma_P)$). Where $\sigma_p$ represents the standard deviation of the normal distribution with mean equal to zero. Its value can be assessed from the analysis of previous experimental activity or based on the expected operational loading conditions for a given application.

$$P(a) = c_0 + c_1 a + c_2 a^2 + c_3 a^3 + \epsilon_p \tag{6.3}$$

Referring to Figure 6.1.1, the moment of inertia about the z-axis for the rectangular cross-section with width and height equal to $w$ and $h$, respectively, can be computed as follows:

$$I_z = \frac{wh^3}{12} \tag{6.4}$$

Moreover, the specimen width is assumed to vary across the different specimens to account for the cutting accuracy in the manufacturing process. Therefore the specimen width of the i$^{\text{th}}$ specimen is sampled from a normal distribution with $\mu_w$ mean and $\sigma_w$ standard deviation:

$$w_i \sim \mathcal{N}(\mu_w, \sigma_w) \tag{6.5}$$

The values of $\mu_w$ and $\sigma_w$ can be experimentally determined by measuring the specimens under test with a caliper.

Then, combining Hooke's law (Equation 6.6):

$$\sigma_x = E_x \varepsilon_x \tag{6.6}$$

With Equation 6.1, one can derive the strain distribution along the x-axis ($\varepsilon_x$) as shown in Equation 6.7:

$$\varepsilon_x = \frac{M_z}{E_x I_z} y \tag{6.7}$$

Where $E_x$ is the Young's modulus of the material in the fiber direction. Furthermore, Young's modulus variability across different specimens should be considered in the model due to possible inhomogeneities in the composite panel from where specimens are cut. Hence, it is assumed that the Young's modulus of the i$^{\text{th}}$ specimen is sampled from a normal distribution with $\mu_E$ mean and $\sigma_E$ standard deviation:

$$E_x^i \sim \mathcal{N}\left(\mu_E, \sigma_E\right) \tag{6.8}$$

One can estimate the value of $\mu_E$ and $\sigma_E$ by looking at the load-displacement curves of specimens cut from the same composite panel used to manufacture the specimens under test. These specimens do not require the installation of any sensor since they are used only to characterize the mechanical properties of the composite laminate.

Then, the expected strain distribution along the x-axis at the specimen surface is obtained posing $y = h/2$ in Equation 6.7.

The proposed MAPOD approach simulates delamination growth in a DCB specimen of length ($L$) for a user-defined number of cracks ($n_c$), starting from a user-defined initial crack length ($a_0$), to a user-defined final crack length ($a_f$). It is assumed that every crack length measurement is taken after a certain delamination length increment $\Delta a$. The true crack length ($a_{true}$) is usually visually estimated, thus introducing uncertainty in the model. Therefore, it is further assumed that $\Delta a$ is composed of a mean constant value ($\Delta a_m$) and a random error ($\varepsilon_a$):

$$\Delta a = \Delta a_m + \varepsilon_a \tag{6.9}$$

Where $\varepsilon_a \sim \mathcal{N}\left(0, \sigma_a\right)$ follows a normal probability distribution with zero mean and standard deviation $\sigma_a$. The $\sigma_a$ value is challenging to assess and depends on many factors, such as the loading type, the geometry, and the material properties. Therefore, the best option is to evaluate $\sigma_a$ using data from a pilot study experiment.

On the other hand, $\Delta a_m$ can be computed as:

$$\Delta a_m = \frac{a_f - a_0}{n_c - 1} \tag{6.10}$$

Then, the model generates a vector of crack lengths ($\boldsymbol{a}$), which is defined in Equation 6.11:

$$\boldsymbol{a} = \boldsymbol{a_m} + \boldsymbol{\varepsilon_a} \tag{6.11}$$

Where $\boldsymbol{a_m}$ and $\boldsymbol{\varepsilon_a}$ are the mean and random vectors of crack lengths defined in Equation 6.12 and Equation 6.13, respectively:

$$\boldsymbol{a_m} = [a_0, a_0 + \Delta a_m, \cdots, a_0 + n_c \Delta a_m = a_f] \tag{6.12}$$

$$\boldsymbol{\varepsilon_a} = [\varepsilon_{a1}, \cdots, \varepsilon_{an_c}] \tag{6.13}$$

The spatial domain, $x \in [0, L]$, is discretized with a user-defined spatial resolution $\Delta x$, which must be sufficiently smaller than the average delamination increment, thus

$\Delta x \ll \Delta a_m$. The spatial domain vector ($\boldsymbol{x}$) has $N+1$ elements ($N = \frac{L}{\Delta x}$) and is defined in Equation 6.14:

$$\boldsymbol{x} = [x_0, \cdots, x_N] \tag{6.14}$$

### 6.1.2 Human factor

The first step in DOFS experiments is to locate a certain spatial coordinate in the optical fiber. Indeed, one must correlate the spatial frame of reference in the interrogator software with specific physical points in the DOFS. This is usually done by applying the so-called *hot touch*, a concentrated heat source, and reading the coordinate of the induced peak in the strain profile in the software. Ideally, the heat source should be infinitely narrow, but in reality, it is not, thus introducing an error in the coordinate locations along the fiber.

It is also crucial to identify the start and the end of the bonded region in the DOFS. Here, an additional uncertainty source can be present, even assuming that a perfect *hot touch* procedure is accomplished. Indeed, bonding is never perfect, and the glue can infiltrate underneath the DOFS and thus extend the bonded region by a few millimeters. Moreover, this adhesive leakage, being an undesired effect, is often irregular, leading to unpredictable strain profiles in the transient region on the onset of bonding. Therefore, this uncertainty source must be incorporated into the model and strictly relates to the researcher's expertise and the available equipment.

In this preliminary stage of the MAPOD framework, this uncertainty source is incorporated into the model suing Equation 6.15, by shifting the $\boldsymbol{x}$ vector for each specimen by a quantity ($\epsilon_{ht}$), leading to a new translated spatial domain vector ($\boldsymbol{x'}$):

$$\boldsymbol{x'} = \boldsymbol{x} + \epsilon_{ht}\mathbf{1}_{\boldsymbol{n}} \tag{6.15}$$

Where $\epsilon_{ht} \sim \mathcal{N}(0, \sigma_{ht})$ is sampled from a normal distribution with zero mean and a user-defined standard deviation ($\sigma_{ht}$), and $\mathbf{1}_{\boldsymbol{N}}$ is a vector of length $N+1$ of ones (Equation 6.16):

$$\mathbf{1}_{\boldsymbol{N}} = [1_0, \cdots, 1_N] \tag{6.16}$$

The human factor uncertainty can dominate over the other uncertainty sources if the experimentalist cannot perform a satisfactory *hot touch* procedure. The validation of $\sigma_{ht}$ can be achieved by performing a series of *hot touches* in a segment of fiber not necessarily bonded in the specimen. Since the *hot touch* procedure is relatively easy and quick to be performed, one can easily take a sufficiently high number of measurements and obtain a good estimation of $\sigma_{ht}$.

### 6.1.3 Strain transfer

A flexible and practical solution to model the effect of the strain transfer from the DCB surface to the fiber core is to apply a convolution operation to the strain profile with a specific windowing function.

Referring to the second order linear non-homogeneous differential equation with constant coefficients Equation 4.16 and its solution Equation 4.17 (see Chapter 4), one can derive the coefficients $C_1$ and $C_2$ by considering as boundary conditions $\varepsilon_f\left(0\right) = 0$ and $\varepsilon_f\left(L \rightarrow +\infty\right) = \varepsilon_s$. The result, shown in Equation 6.17, can be interpreted as the optical fiber step response with strain equal to $\varepsilon_m$:

$$\varepsilon_f = \varepsilon_s\left(1 - e^{-kt}\right) \tag{6.17}$$

From Equation 6.17, exploiting the analogy with linear-time-invariant systems, it is possible to define the system transfer function ($\Gamma$) for $x > 0$ as:

$$\Gamma^+\left(x\right) = ke^{-kx} \tag{6.18}$$

Exploiting the symmetry that should have the transfer function (strain can propagates backwards), it is possible to extend $\Gamma$ to negative values, which after normalization leads to Equation 6.19:

$$\Gamma\left(x\right) = \frac{k}{2}e^{-k|x|} \tag{6.19}$$

This result coincides with the mechanical transfer function proposed by Billon et al., who modeled the strain profile response induced by a surface crack [275]. Then, it is possible to compute the strain field in the DOFS core with Equation 6.20:

$$\varepsilon_f\left(x\right) = \left(\Gamma \otimes \varepsilon_s\right)\left(x\right) \tag{6.20}$$

Moreover, the shear lag constant ($k$) is assumed to vary across the different specimens to take into account the inherent variability associated with the limited repeatability of the bonding process and the possible non-homogeneity of the DOFS coating. Therefore the shear lag constant of the i$^{\text{th}}$ specimen is sampled from a normal distribution with $\mu_k$ mean and $\sigma_k$ standard deviation:

$$k_i \sim \mathcal{N}\left(\mu_k, \sigma_k\right) \tag{6.21}$$

The $\mu_k$ value can be assessed with Equation 4.15. However, it is often unpractical to derive $\mu_k$ from Equation 4.15 since the material properties of the optical fiber might be unknown. In this case, one can assess the value of $\mu_k$ by performing a tensile test with the DOFS bonded in the specimen surface and fitting the analytical model expressed by Equation 4.20. Then, by repeating the procedure several times using different specimens, one can improve the accuracy of $\mu_k$ and assess $\sigma_k$, thus incorporating the variability associated with the bonding process in the model. It is also interesting to notice that in this MAPOD model, the shear lag constant is considered constant within the specimen, i.e., $k$ does not change along the fiber axis but only between different specimens. This assumption holds in such cases where the bonding or the embedding is homogeneous without particular geometrical variations along the fiber path. If the fiber is bonded along a longer path, it is reasonable to assume that changes in $k$ can also occur within the same specimen. Nevertheless, In this MAPOD study, it is hypothesized that $k$ does not change along the fiber length to keep the analysis as simple as possible.

### 6.1.4 Interrogator Resolution

The interrogator resolution, using an approach similar to the one used for the strain transfer phenomenon, can be considered by convolving a particular rectangular function (Equation 6.22) with the DOFS strain profile:

$$\Pi_i(x) = \begin{cases} \frac{1}{\Delta X} & \text{for } |x| \leqslant \frac{\Delta X}{2} \\ 0 & \text{elsewhere} \end{cases} \tag{6.22}$$

Where $\Pi_i$ is a rectangular function having unitary area and width equal to the interrogator resolution, $\Delta X$. Hence, the theoretical measured strain profile is given by Equation 6.23

$$\varepsilon_{mt}(x) = (\Pi_i \otimes \varepsilon_f)(x) \tag{6.23}$$

### 6.1.5 Environmental noise

Noise is modeled as a strain noise vector ($\boldsymbol{Z}$), whose i$^{\text{th}}$ element ($z_i$) is defined as:

$$z_i \sim \mathcal{N}(0, \sigma_z) \tag{6.24}$$

Where $\mathcal{N}(0, \sigma_z)$ denotes a normal distribution with zero mean and $\sigma_z$ standard deviation. One can assess $\sigma_z$ by performing a series of measurements with no load applied to the specimen.

Finally, the real measured strain ($\varepsilon_m$), that also takes into account the effect of noise, is obtained by simply superimposing the strain noise vector ($\boldsymbol{Z}$) to $\varepsilon_{mt}$, as outlined in Equation 6.25 and Equation 6.26:

$$\boldsymbol{Z} = [z_1, \cdots, z_N] \tag{6.25}$$

$$\varepsilon_m(x) = \varepsilon_{mt} + \boldsymbol{Z} \tag{6.26}$$

## 6.2 Results

Table 6.2.1 shows the parameters configuration for the following demonstrative example, classifying the sources of uncertainty into within- and between-specimen variability (if the parameters are just model settings, they belong to neither of the two classes).

**Table 6.2.1:** Example of parameters setting.

| Variable | Value | Within-specimen variability | Between-specimen variability |
|---|---|---|---|
| $n$ | 20 | No | No |
| $L$ | 135 mm | No | No |
| $\sigma_p$ | 3 N | No | Yes |
| $h$ | 2 mm | No | No |
| $\mu_w$ | 20 mm | No | No |
| $\sigma_w$ | 0.25 mm | No | Yes |
| $\mu_E$ | 141 GPa | No | No |
| $\sigma_E$ | 2 GPa | No | Yes |
| $n_c$ | 15 | No | No |
| $\Delta x$ | 0.01 mm | No | No |
| $a_0$ | 0 mm | No | No |
| $a_f$ | 10 mm | No | No |
| $\sigma_a$ | 0.1 mm | Yes | No |
| $\sigma_{ht}$ | 0.5 mm | No | Yes |
| $\mu_k$ | 0.6 $\text{mm}^{-1}$ | No | Yes |
| $\sigma_k$ | 0.06 $\text{mm}^{-1}$ | No | Yes |
| $\sigma_z$ | 5 µε | Yes | No |
| $\Delta X$ | 0.65 mm | No | No |

The corresponding strain profiles are shown in Figure 6.2.1:

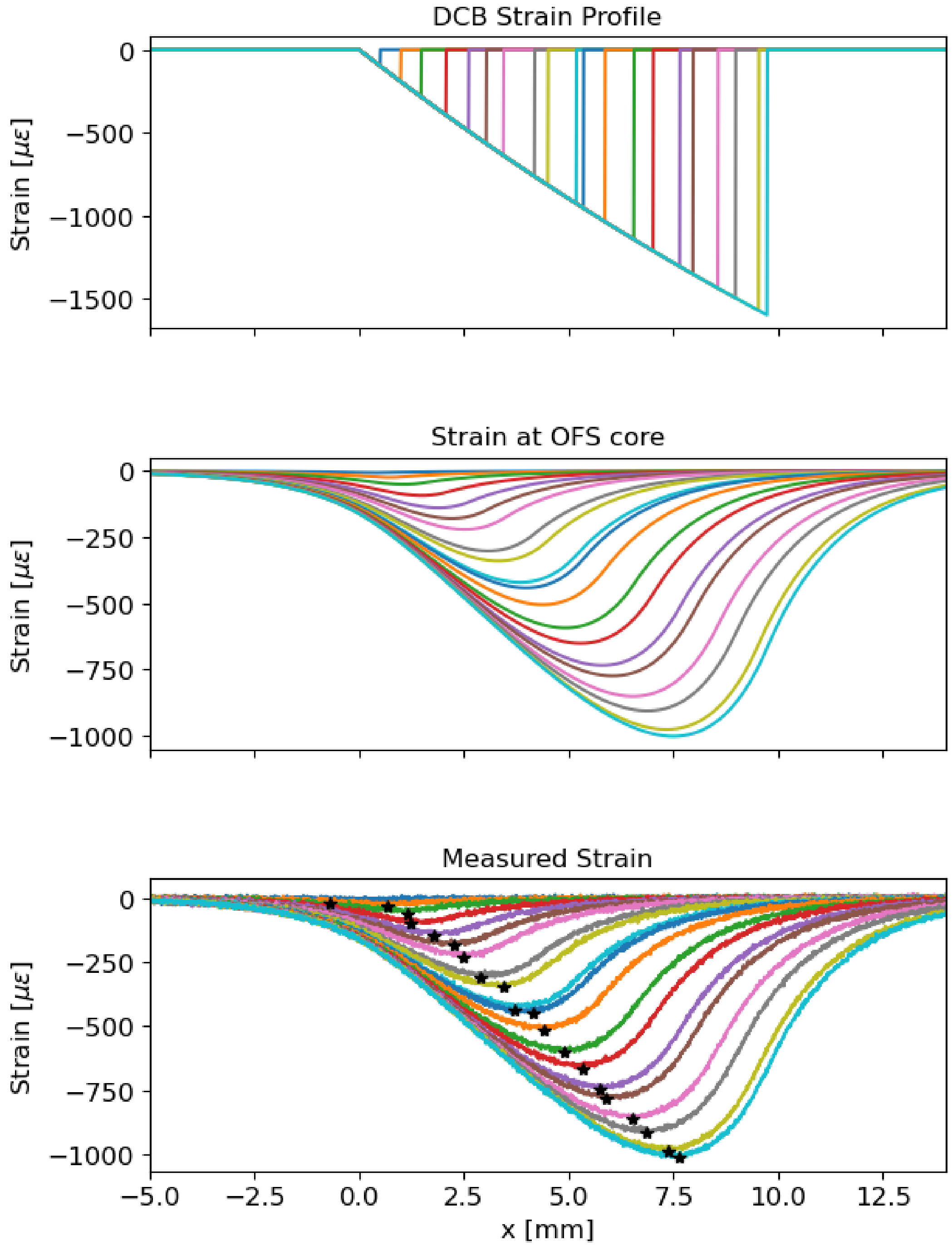

**Figure 6.2.1:** Strain profiles in the DCB specimen surface (top), strain profile in DOFS core showing the strain transfer effect (center), and expected measured strain profile showing the interrogator resolution and noise effects (bottom).

The Damage Index (DI) is defined according to Equation 5.6 (black stars in Figure 6.2.1). Figure 6.2.2 shows the application of the MAPOD methodology using the LaD method. Every regression line represents a different specimen. From a qualitative point of view, the numerical model is able to simulate both the within-specimen variability and the between-specimen variability. However, compared to the experimental data in Figure 5.3.1 the model shows less variability in the slopes.

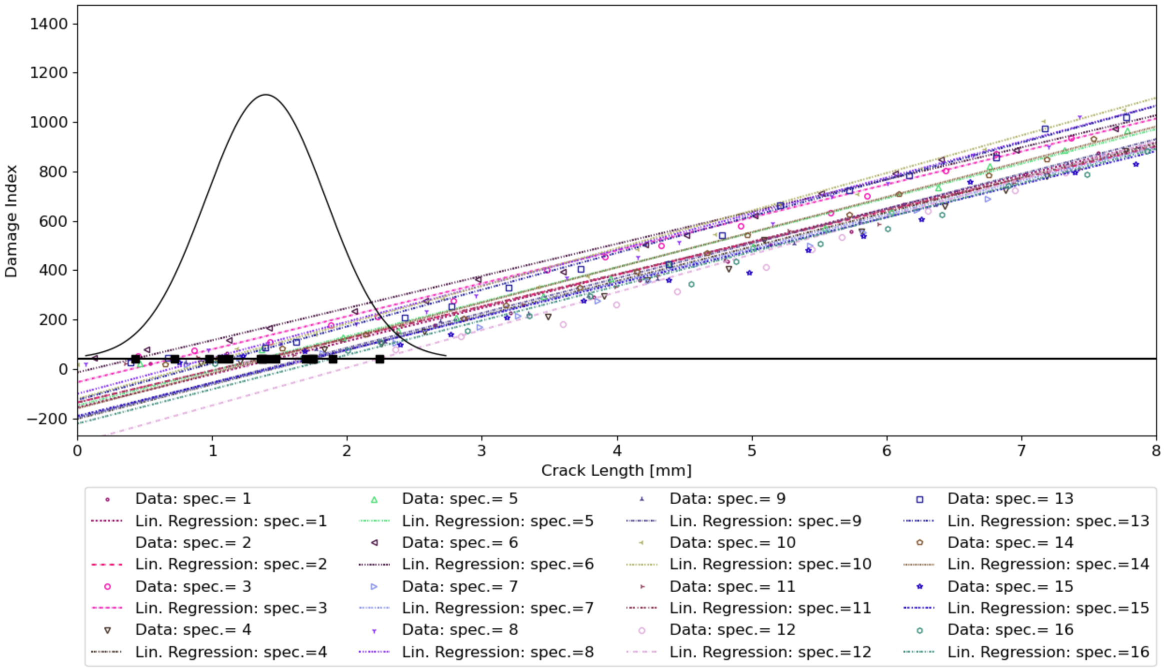

**Figure 6.2.2:** Model-Assisted LaD method applied to synthetic DOFS data for crack detection.

Computing the cumulative function of the LaD distribution it is possible to obtain the corresponding POD curve (see Figure 6.2.3). The distance of the lower 95% confidence bound (blue dashed line) from the POD curve (black solid line) reflects the uncertainty affecting the system. High uncertainty values in the model parameters will result in a lower 95% confidence bound far away from the original POD curve.

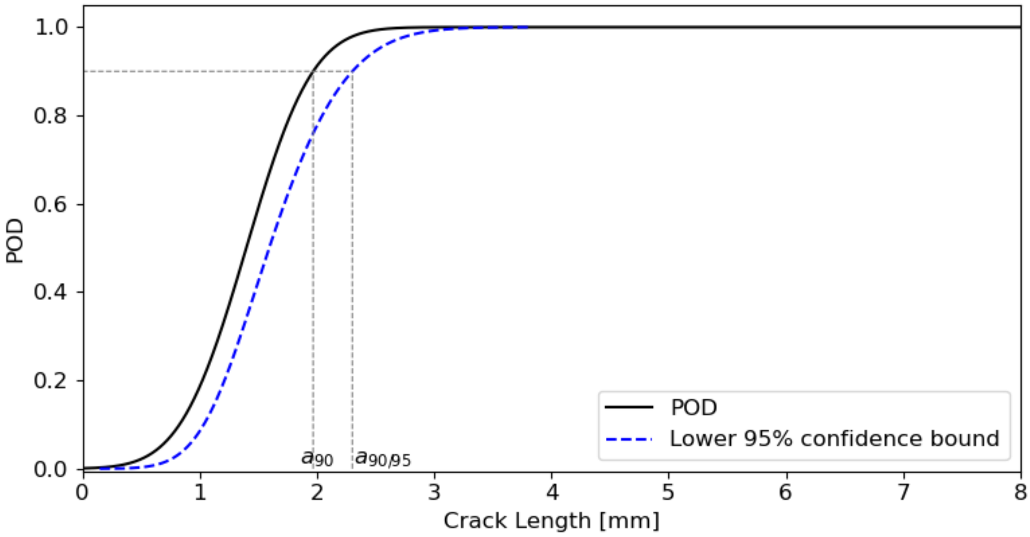

**Figure 6.2.3:** MAPOD curve and its lower confidence bound showing the $a_{90}$ and $a_{90/95}$values

### 6.2.1 Parametric study

The MAPOD framework allows the engineers not only to calculate the POD curve of a given DOFS system, but also to understand which are the most influencing parameters. In this study, the focus was posed on three parameters: the shear lag constant ($k$), the standard deviation of the noise ($\sigma_z$) superimposed to the theoretical measured strain ($\varepsilon_{mt}$), and the interrogator resolution ($\Delta X$).

Table 6.2.2 outlines the parameters setting in the three case studies. The wording ($\langle initial\ value\rangle, \langle final\ value\rangle, \langle number\ of\ elements\rangle$) symbolizes that the parameter is linearly swept from $\langle initial\ value\rangle$ to $\langle final\ value\rangle$ with spacing intervals equal to $(\langle initial\ value\rangle - \langle final\ value\rangle)\ /\ (\langle number\ of\ elements\rangle - 1)$.

**Table 6.2.2:** Parametric study definition.

| Variable | Case 1 | Case 2 | Case 3 |
|---|---|---|---|
| $n$ | 50 | 50 | 50 |
| $L$ | 135 mm | 135 mm | 135 mm |
| $\sigma_p$ | 3 N | 3 N | 3 N |
| $h$ | 2 mm | 2 mm | 2 mm |
| $\mu_w$ | 20 mm | 20 mm | 20 mm |
| $\sigma_w$ | 0.25 mm | 0.25 mm | 0.25 mm |
| $\mu_E$ | 141 GPa | 141 GPa | 141 GPa |
| $\sigma_E$ | 1 GPa | 1 GPa | 1 GPa |
| $n_c$ | 20 | 20 | 20 |
| $\Delta x$ | 0.01 mm | 0.01 mm | 0.01 mm |
| $a_0$ | 0 mm | 0 mm | 0 mm |
| $a_f$ | 10 mm | 10 mm | 10 mm |
| $\sigma_a$ | 0.1 mm | 0.1 mm | 0.1 mm |
| $\sigma_{ht}$ | 0.5 mm | 0.5 mm | 0.5 mm |
| $\mu_k$ | (0.05 $\mathrm{mm}^{-1}$, 1 $\mathrm{mm}^{-1}$, 100) | 0.6 $\mathrm{mm}^{-1}$ | 0.6 $\mathrm{mm}^{-1}$ |
| $\sigma_k$ | 0.06 $\mathrm{mm}^{-1}$ | 0.06 $\mathrm{mm}^{-1}$ | 0.06 $\mathrm{mm}^{-1}$ |
| $\sigma_z$ | 5 με | (0 με, 50 με, 100) | 5 με |
| $\Delta X$ | 0.65 mm | 0.65 mm | (0.1 mm, 30 mm, 100) |

#### Case 1: Shear lag effect

The shear lag constant effect on the detection capabilities is highlighted in Figure 6.2.4. When $k$ increases $a_{90}$ and $a_{90/95}$ decrease correspondingly after reaching a quasi-steady value around 6.5 mm. This means that stiffer DOFS with high $k$ values have better detection performance but the benefit is negligible after a certain value. Moreover, $a_{90}$ and $a_{90/95}$ are less scattered due to the fact that the lower bound is closer to the POD curve. The analysis can also be used to implement a degradation model of the DOFS coupling with the structure. Indeed, different values of $k$ can correspond to different adhesives but also subsequent moments in time of the same adhesive.

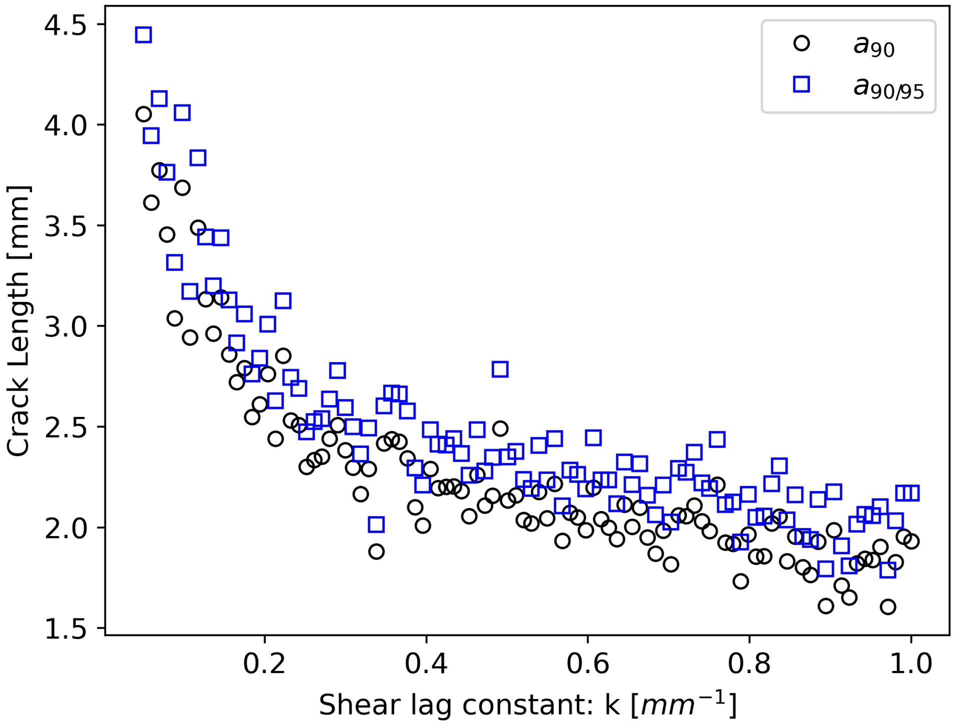

**Figure 6.2.4:** Shear lag constant effect on $a_{90}$ and $a_{90/95}$

### Case 2: Noise effect

The second parametric analysis is shown in Figure 6.2.5, where $a_{90}$ and $a_{90/95}$ are plotted against the standard deviation of the noise $\sigma_z$. As expected, noise has a detrimental effect on the detection performance. A first analysis suggests that there is a linear relationship between a $a_{90}$ and $a_{90/95}$ and $\sigma_z$. The simulation of the noise effect assumes a particular importance because it shows one example of simulating POD curves for varying EOCs.

### Case 3: Interrogator Resolution effect

In the last plot it is shown the effect of the interrogator resolution $\Delta x$. An ideal interrogator with infinite spatial resolution ($\Delta x \to 0$) offers the best performance. It is interesting to observe how $a_{90}$ and $a_{90/95}$ increase as $\Delta x$ increases. Moreover, as $\Delta x$ increases, the $a_{90/95}$ values are more scattered from the $a_{90}$ values, reflecting an higher amount of uncertainty present in the system. This kind of simulation can be beneficial to the engineer in selecting the right interrogator in the preliminary design phase of the SHM system. Indeed, considering all the available information about the other model parameters, the SHM system equipped with such an interrogator should satisfy specific requirements for $a_{90/95}$.

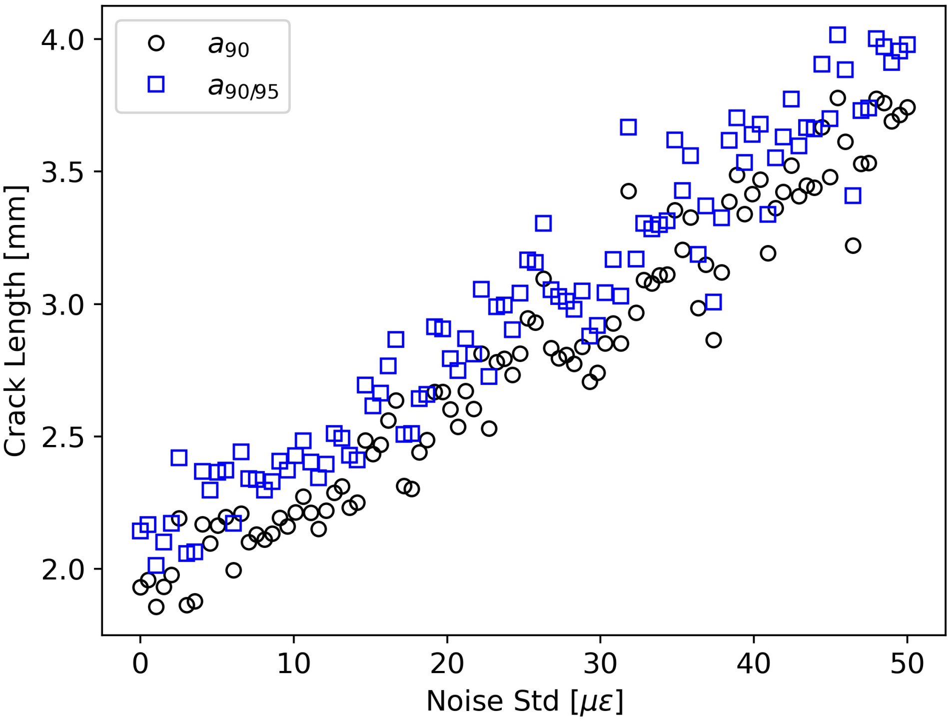

**Figure 6.2.5:** Effect of noise on $a_{90}$ and $a_{90/95}$

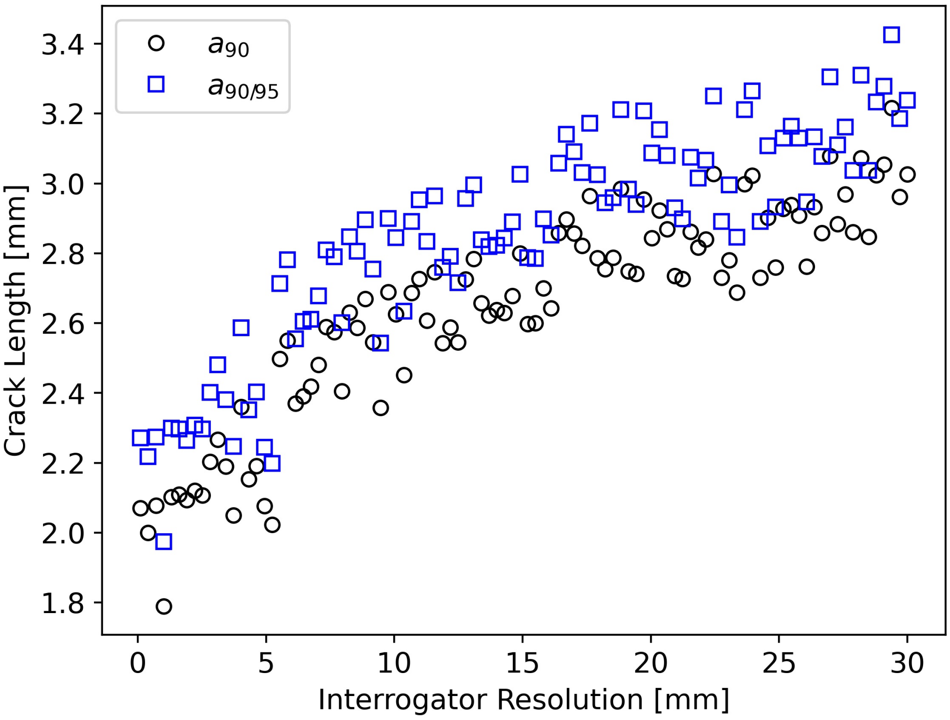

**Figure 6.2.6:** $a_{90}$ and $a_{90/95}$ trend for increasing interrogator resolution values.

### 6.2.2 Crack localization error

The focus of this study is damage detection. However, this MAPOD framework allows making some considerations not only for crack detection but also for crack localization, which is the second phase in the SHM paradigm. Indeed, the example shown in Figure 6.2.7 (parameter settings → Table 6.2.1) highlights an error in the estimated crack tip location (black stars) with respect the true crack tip location (red squares) due to the flattening of the strain profile. This bias in the crack tip position estimation was unknown in the experimental campaign and deserves to be considered in further studies.

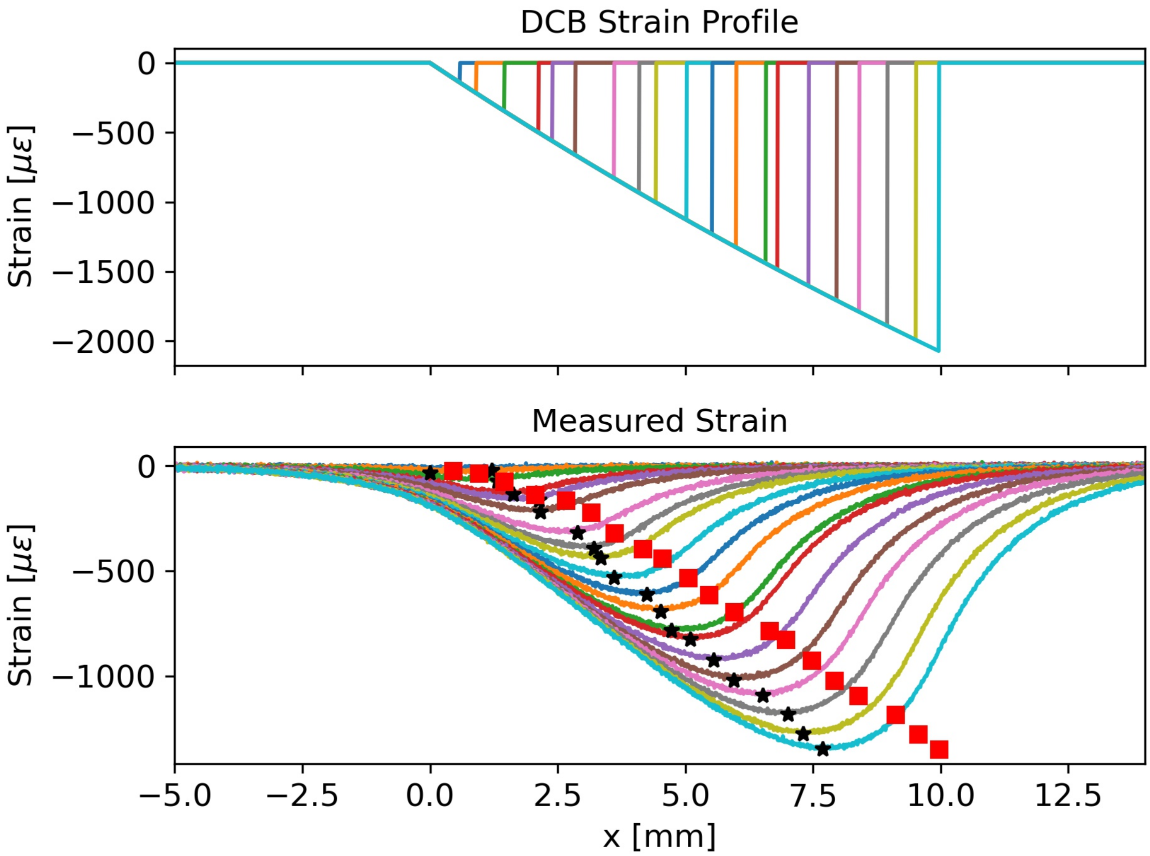

**Figure 6.2.7:** Qualitative example of crack localization error.

Moreover, Figure 6.2.8 highlights the trend of the localization error which seems to increase with the delamination length. This aspect deserves particular attention because the crack length is underestimated, thus leading to non-conservative results.

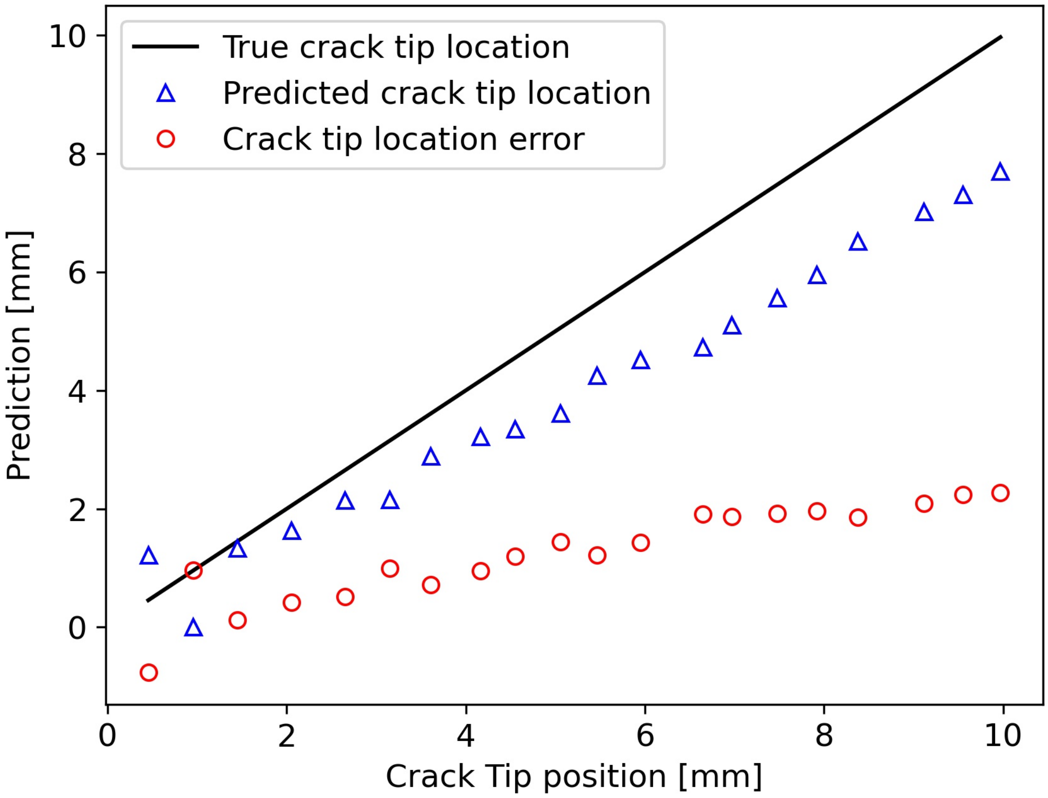

**Figure 6.2.8:** Localization error trend.

## 6.3 Conclusions

In this Chapter 6 a MAPOD framework for DOFS based on the LaD model was proposed. Preliminary MAPOD results are encouraging and shed some light on the most significant factors contributing to the level of uncertainty for crack detection. A parametric analysis was carried out showing how the shear lag parameter ($k$), the noise standard deviation ($\sigma_z$), and the interrogator resolution ($\Delta x$) affect the experimental results. The results are analyzed qualitatively and are strictly related to the specific case study. Nevertheless, the methodology is general and can be applied to structures experiencing more complex strain profiles and subjected to dynamic loading.

In § 5.2.1, the number of specimens was virtually augmented to simulate the lower bound convergence. However, this MAPOD approach is different because the new samples are generated by effectively performing a Monte Carlo simulation. Nevertheless, the central question is always the same: to what extent is it possible to populate the database given the *limited* available data? Therefore, it becomes fundamental that every parameter in the model reflects the right amount of variability.

In § 6.1, it is described how each uncertainty source can be determined. However, even when the assessment of these parameters is impossible to achieve, this methodology still offers a framework to study the effects of these variables on the POD curves. Moreover, unexpected phenomena might be noticed, as happened in § 6.2.2. with the observation of the localization error. Therefore this MAPOD approach can increase the understanding of SHM systems based on DOFSs.

This work paves the way for optimization studies aimed at improving the design of new DOFS based on the application of interest. This approach also offers a framework for the development of certifications standards for DOFSs, which are crucial for the transition of this technology from the academia toward the industry.

# Chapter 7

# Conclusions

> *The only true wisdom is in*
> *knowing you know nothing*
>
> *Socrates*

This final Chapter 7 retraces the main stages of this Ph.D. thesis, summarizing the main achievements and the ongoing challenges. The discussion is structured following as guiding light the four Scientific Research Sub-Questions (SRSQs), leading to the conclusive answer to the main Scientific Research Question (SRQ).

## 7.1 Answer to the scientific research sub-questions

### 7.1.1 First scientific research sub-question

SRSQ1: *"Which is the most appropriate statistical method to develop POD curves in SHM for DOFS?"*

The investigation to answer SRSQ1 represented the first step in this Ph.D. project. The amount of SHM literature produced in the last decades is overwhelming, and consequently, a huge amount of time was dedicated to reviewing the studies relevant to answer SRSQ1. The extensive analysis of the literature in Chapter 2 shows that the most common metrics used in NDE cannot be applied in SHM. The LaD and the REM are the two main statistical methodologies capable of handling spatial/time-correlated data. However, their use is still limited to a few case studies and, as also summarized in Table 2.A.3 (see § 2.A), no studies use these statistical methods to quantify the performance of DOFS.

In this thesis, the LaD method was preferred over the REM for its easy-to-use characteristics and because it is often difficult to fit the REM with few specimens. Nevertheless, the REM offers a more efficient use of data and is compatible with a Bayesian framework in the case prior knowledge is available. Therefore, leveraging the LaD method should be seen as a first step towards developing MAPOD for DOFSs rather than the optimal choice.

### 7.1.2 Second scientific research sub-question

SRSQ2: *"Is it possible to develop a novel strain transfer model to understand its underlying mechanism and unfold its critical parameters?"*

The strain transfer mechanism has been shown to be crucial for DOFSs detection performance. The analytical model, developed in Chapter 4, proved efficient in predicting the expected strain profile. In addition, the model predictions were consistent with both experimental data and FEM simulation results. The importance and the physical meaning of the shear lag constant ($k$) were properly discussed. Moreover, understanding the shear lag constant ($k$) role in DOFSs was fundamental to planning the subsequent experimental research activity and establishing a link between POD curves and strain transfer.

### 7.1.3 Third scientific research sub-question

SRSQ3: *"Is it possible to conduct an experimental POD study for DOFSs in composite laminates?"*

Chapter 5 proves that it is possible to develop an experimental POD methodology for DOFSs. Two types of DOFSs with different strain transfer properties were tested. POD curves produced with the lad method could capture the differences between the DOFSs and quantify the performance in terms of $a_{90}$ and $a_{90/95}$.

The intuition that the load type could also potentially affect the detection capabilities fostered the author to compare quasi-static and fatigue loading results with the same DOFS. The results confirm the intuition and pave the way for further investigations in this direction. Preliminary test on ongoing research seems to show that POD curves for delamination detection in mode II have higher $a_{90}$ and $a_{90/95}$ values compared to the POD obtained in this thesis.

### 7.1.4 Fourth scientific research sub-question

SRSQ4: *"Is it possible to develop a MAPOD framework for DOFSs?"*

SRSQ4 stems from the findings of Chapter 5, highlighting that many parameters can potentially affect POD curves. The curse of dimensionality would lead to a tremendous amount of tests with unbearable time and economic costs. Therefore, since it is unfeasible to develop such POD curves experimentally, it is clear that a numerical approach is the only way forward.

Chapter 6 provides the first MAPOD framework for DOFSs in a specific case study (the same as Chapter 5). The research is still in its infancy, and the results are preliminary. However, the study provides instructive insights into how the strain transfer is related to POD curves as well as other parameters, such as the noise and the interrogator resolution.

The model will be validated in future activities with experimental data available in Chapter 5. The main limitation at the moment is the knowledge of the DOFS mechanical properties required to assess the corresponding shear lag constant since manufacturers do not usually provide them. Current research is devoted to developing experimental methodologies for defining these properties through the analytical model developed in Chapter 4.

## 7.2 Answer to the main scientific research question

SRQ: *"Is it possible to develop a rigorous methodology to qualify the detection performance of DOFSs in composite laminates?"*

The focus was posed from the beginning on DOFSs, one of the most promising technologies of the contemporary age. However, their implementation in SHM systems depends on the ability to identify their performance in damage detection and possibly localization and sizing. State-of-the-art statistical methods were explored, highlighting a lack of methodologies to quantify the performance of DOFSs in SHM.

The development of such methodology started from understanding the physical working principle of DOFSs, passing through the comprehension of the strain transfer phenomenon. The results obtained in this first phase determined the selection of the proper case study for developing a novel and rigorous methodology to qualify the detection performance of DOFSs in composite laminates.

The experimental activities outlined how crucial it is to identify the variability sources to obtain reliable POD curves. These sources of uncertainty are likewise fundamental to obtaining MAPOD curves whose reliability depends on the quality of experimental data upon which the model is validated. Therefore, experimental and modeling procedures are both crucial to assess the detection performance of DOFSs.

In this regard, Bayesian statistics offers an interesting perspective to incorporate the previous knowledge in the model. The Bayesian framework could be implemented by employing the REM method. Therefore, in future research, the application of the REM method to MAPOD for DOFSs should be further investigated.

Moreover, future studies should establish whether the methodology can be extended to different damage modes in other types of composite laminates. In this regard, MAPOD curves might provide preliminary insights.

At this point, the novel research questions arising from this conclusion are:

- To which extent do the results hold in terms of upscaling?
- How is it possible to consider the effect of EOCs on POD curves over time?
- Given the results in section § 6.2.2, is it possible to develop POL curves for DOFSs applied to composite laminates?

One of the biggest challenges for future research is the capability to transfer POD curves obtained at a coupon level in a laboratory environment to a higher structural component. The upscaling problem is a clear scientific gap that requires additional research effort. In principle, the experimental methodology proposed in Chapter 5 and the MAPOD approach developed in Chapter 6 offer upscaling potentials for a hot spot monitoring scenario if the experimental setup and the numerical model mimic the geometry and the loading conditions of the real structural component in a localized region around the damaged location with sufficient accuracy.

Varying EOCs are another fundamental challenge preventing the full application of many SHM techniques. In this case, one solution could be to implement in MAPOD method a sensor degradation model and simulate the amount of time required to exceed a certain $a_{90/95}$ value. For instance, this can be easily done by decreasing the value of the shear lag constant ($k$), thus simulating the degradation of the mechanical coupling between the sensor and the structure. As also shown in Chapter 6, another possibility is to vary the the standard deviation of the noise $\sigma_z$. This is just one of the many parameters representing EOCs. Therefore, other variables, such as temperature, should be investigated in further studies.

Finally, the localization and sizing accuracy should also be addressed to provide full certification of the DOFS-based SHM system. Preliminary results obtained in this thesis shed some light on the potential correlation between damage size and localization error, which can be used as a starting point to develop POL curves or equivalent metrics.

Future studies should investigate these new questions to bridge further the gap separating DOFSs from their full certification and implementation in SHM.

# Bibliography

[1] M. Saeedifar and D. Zarouchas, “Damage characterization of laminated composites using acoustic emission: A review,” *Composites Part B: Engineering*, vol. 195, p. 108 039, Aug. 2020, ISSN: 13598368. DOI: `10.1016/j.compositesb.2020.108039`.

[2] J. Pascoe, R. Alderliesten, and R. Benedictus, “Methods for the prediction of fatigue delamination growth in composites and adhesive bonds – a critical review,” *Engineering Fracture Mechanics*, vol. 112-113, pp. 72–96, Nov. 2013, ISSN: 00137944. DOI: `10.1016/j.engfracmech.2013.10.003`.

[3] V. Giurgiutiu, *Structural health monitoring of aerospace composites*. Amsterdam: Elsevier, 2016, 457 pp., ISBN: 978-0-12-409605-9.

[4] I. Alj, M. Quiertant, A. Khadour, Q. Grando, and K. Benzarti, “Environmental durability of an optical fiber cable intended for distributed strain measurements in concrete structures,” *Sensors*, vol. 22, no. 1, p. 141, Dec. 26, 2021, ISSN: 1424-8220. DOI: `10.3390/s22010141`.

[5] R. Di Sante, “Fibre optic sensors for structural health monitoring of aircraft composite structures: Recent advances and applications,” *Sensors*, vol. 15, no. 8, pp. 18 666–18 713, Aug. 2015. DOI: `10.3390/s150818666`.

[6] F. Falcetelli, R. Di Sante, and E. Troiani, “Strategies for embedding optical fiber sensors in additive manufacturing structures,” in *European Workshop on Structural Health Monitoring*, P. Rizzo and A. Milazzo, Eds., vol. 128, Series Title: Lecture Notes in Civil Engineering, Cham: Springer International Publishing, 2021, pp. 362–371, ISBN: 978-3-030-64908-1. DOI: `10.1007/978-3-030-64908-1_34`.

[7] F. Falcetelli, A. Martini, R. Di Sante, and M. Troncossi, “Strain modal testing with fiber bragg gratings for automotive applications,” *Sensors*, vol. 22, no. 3, p. 946, Jan. 26, 2022, ISSN: 1424-8220. DOI: `10.3390/s22030946`.

[8] F. Bastianini, R. Di Sante, F. Falcetelli, D. Marini, and G. Bolognini, “Optical fiber sensing cables for brillouin-based distributed measurements,” *Sensors*, vol. 19, no. 23, p. 5172, Nov. 26, 2019, ISSN: 1424-8220. DOI: `10.3390/s19235172`.

[9] D. K. Gifford, S. T. Kreger, A. K. Sang, *et al.*, "Swept-wavelength interferometric interrogation of fiber rayleigh scatter for distributed sensing applications," in *Fiber Optic Sensors and Applications V*, vol. 6770, International Society for Optics and Photonics, Oct. 12, 2007, 67700F. DOI: `10.1117/12.734931`.

[10] C. R. Farrar and K. Worden, *Structural health monitoring: a machine learning perspective*. Chichester, West Sussex, U.K. ; Hoboken, N.J: Wiley, 2012, Medium: electronic resource, ISBN: 978-1-119-99433-6.

[11] F. Falcetelli, L. Rossi, R. Di Sante, and G. Bolognini, "Strain transfer in surface-bonded optical fiber sensors," *Sensors*, vol. 20, no. 11, p. 3100, May 30, 2020, ISSN: 1424-8220. DOI: `10.3390/s20113100`.

[12] *Department of Defense Handbook: Nondestructive Evaluation System Reliability Assessment*. Jul. 4, 2009.

[13] T. Fawcett, "An introduction to ROC analysis," *Pattern Recognition Letters*, vol. 27, no. 8, pp. 861–874, Jun. 2006, ISSN: 01678655. DOI: `10.1016/j.patrec.2005.10.010`.

[14] C. Haynes, M. D. Todd, E. Flynn, and A. Croxford, "Statistically-based damage detection in geometrically-complex structures using ultrasonic interrogation," *Structural Health Monitoring*, vol. 12, no. 2, pp. 141–152, Mar. 2013, ISSN: 1475-9217, 1741-3168. DOI: `10.1177/1475921712466756`.

[15] C. M. Schubert Kabban, B. M. Greenwell, M. P. DeSimio, and M. M. Derriso, "The probability of detection for structural health monitoring systems: Repeated measures data," *Structural Health Monitoring: An International Journal*, vol. 14, no. 3, pp. 252–264, May 2015, ISSN: 1475-9217, 1741-3168. DOI: `10.1177/1475921714566530`.

[16] W. Q. Meeker, D. Roach, and S. S. Kessler, "Statistical methods for probability of detection in structural health monitoring," in *Structural Health Monitoring 2019*, DEStech Publications, Inc., Nov. 15, 2019, ISBN: 978-1-60595-601-5. DOI: `10.12783/shm2019/32095`.

[17] D. Roach, "Real time crack detection using mountable comparative vacuum monitoring sensors," *Smart Structures and Systems*, vol. 5, no. 4, pp. 317–328, Jul. 25, 2009. DOI: `10.12989/SSS.2009.5.4.317`.

[18] S. S. Kessler, C. T. Dunn, P. Swindell, and W. Meeker, "Detection sensitivity analysis for a potential drop (PD) structural health monitoring (SHM) system," in *Proceedings of the 12th International Workshop on Structural Health Monitoring*, Stanford, CA, USA: DEStech Publications, Inc., Sep. 10, 2019, ISBN: 978-1-60595-601-5. DOI: `10.12783/shm2019/32219`.

[19] F. Foucher, R. Fernandez, S. Leberre, and P. Calmon, "New tools in CIVA for model assisted probability of detection (MAPOD) to support NDE reliability studies," presented at the NDE of Aerospace Materials & Structures, Jun. 5, 2018, p. 12.

[20] M. F. Foucher, S. Lonne, G. Toullelan, S. Mahaut, and S. Chatillon, "An overview of validation campaigns of the CIVA simulation software," p. 9,

[21] M. S. H. Leung and J. Corcoran, "Evaluating the probability of detection capability of permanently installed sensors using a structural integrity informed approach," *Journal of Nondestructive Evaluation*, vol. 40, no. 3, p. 82, Sep. 2021, ISSN: 0195-9298, 1573-4862. DOI: `10.1007/s10921-021-00806-5`.

[22] S. Mariani, Q. Rendu, M. Urbani, and C. Sbarufatti, "Causal dilated convolutional neural networks for automatic inspection of ultrasonic signals in non-destructive evaluation and structural health monitoring," *Mechanical Systems and Signal Processing*, vol. 157, p. 107 748, Aug. 2021, ISSN: 08883270. DOI: `10.1016/j.ymssp.2021.107748`.

[23] K. Tschoke, I. Mueller, V. Memmolo, *et al.*, "Feasibility of model-assisted probability of detection principles for structural health monitoring systems based on guided waves for fibre-reinforced composites," *IEEE Transactions on Ultrasonics, Ferroelectrics, and Frequency Control*, pp. 1–1, 2021, ISSN: 0885-3010, 1525-8955. DOI: `10.1109/TUFFC.2021.3084898`.

[24] S. Mariani and P. Cawley, "Change detection using the generalized likelihood ratio method to improve the sensitivity of guided wave structural health monitoring systems," *Structural Health Monitoring*, p. 147 592 172 098 183, Dec. 31, 2020, ISSN: 1475-9217, 1741-3168. DOI: `10.1177/1475921720981831`.

[25] N. Yue and M. Aliabadi, "Hierarchical approach for uncertainty quantification and reliability assessment of guided wave-based structural health monitoring," *Structural Health Monitoring*, p. 147 592 172 094 064, Aug. 28, 2020, ISSN: 1475-9217, 1741-3168. DOI: `10.1177/1475921720940642`.

[26] C. Liu, J. Dobson, and P. Cawley, "Efficient generation of receiver operating characteristics for the evaluation of damage detection in practical structural health monitoring applications," *Proceedings of the Royal Society A: Mathematical, Physical and Engineering Sciences*, vol. 473, no. 2199, p. 20 160 736, Mar. 2017, ISSN: 1364-5021, 1471-2946. DOI: `10.1098/rspa.2016.0736`.

[27] J. Moriot, N. Quaegebeur, A. Le Duff, and P. Masson, "A model-based approach for statistical assessment of detection and localization performance of guided wave–based imaging techniques," *Structural Health Monitoring*, vol. 17,

no. 6, pp. 1460–1472, Nov. 2018, ISSN: 1475-9217, 1741-3168. DOI: 10.1177/1475921717744679.

[28] A. Gianneo, M. Carboni, and M. Giglio, "Feasibility study of a multi-parameter probability of detection formulation for a lamb waves–based structural health monitoring approach to light alloy aeronautical plates," *Structural Health Monitoring: An International Journal*, vol. 16, no. 2, pp. 225–249, Mar. 2017, ISSN: 1475-9217, 1741-3168. DOI: 10.1177/1475921716670841.

[29] D. Roach, "Use of comparative vacuum monitoring sensors for automated, wireless health monitoring of bridges and infrastructure," in *Proceedings of the 9th International Conference on Bridge Maintenance, Safety and Management*, Jul. 2018.

[30] A. A. Pollock, D. O. Thompson, and D. E. Chimenti, "A POD MODEL FOR ACOUSTIC EMISSION—DISCUSSION AND STATUS," presented at the REVIEW OF PROGRESS IN QUANTITATIVE NONDESTRUCTIVE EVALUATION VOLUME 29, Kingston (Rhode Island), 2010, pp. 1927–1933. DOI: 10.1063/1.3362339.

[31] M. G. R. Sause, F. F. Linscheid, and M. Wiehler, "An experimentally accessible probability of detection model for acoustic emission measurements," *Journal of Nondestructive Evaluation*, vol. 37, no. 2, p. 17, Jun. 2018, ISSN: 0195-9298, 1573-4862. DOI: 10.1007/s10921-018-0474-4.

[32] F. P. Grooteman, "Damage detection and probability of detection for a SHM system based on optical fibres applied to a stiffened composite panel," in *Proceedings of the 25th International Conference on Noise and Vibration engineering, ISMA2012 in conjunction with the 4th International Conference on Uncertainty in Structural Dynamics, USD 2012*, vol. 4, Leuven, Belgium: Katholieke Universiteit Leuven, Sep. 17, 2012, pp. 3317–3330.

[33] C. Sbarufatti and M. Giglio, "Performance qualification of an on-board model-based diagnostic system for fatigue crack monitoring," *Journal of the American Helicopter Society*, vol. 62, no. 4, pp. 1–10, Oct. 1, 2017, ISSN: 2161-6027. DOI: 10.4050/JAHS.62.042008.

[34] W. D. Rummel, "Recommended practice for demonstration of nondestructive evaluation (NDE) reliability in aircraft parts," *Materials Evaluation*, vol. 40, pp. 922–932, 1982.

[35] S. International, "Aerospace recommended practice: Guidelines for implementation of structural health monitoring on fixed wing aircraft," ARP6461, Sep. 2013.

[36] P. J. Shull, Ed., *Nondestructive evaluation: theory, techniques, and applications*, Mechanical engineering 142, New York: M. Dekker, 2002, 841 pp., ISBN: 978-0-8247-8872-8.

[37] C. Hellier, *Handbook of nondestructive evaluation*, 2nd ed. New York: McGraw-Hill, 2013, 1 p., ISBN: 978-0-07-177714-8.

[38] B. I. of Non-Destructive Testing, *About NDT*.

[39] J. D. Achenbach, "Structural health monitoring – what is the prescription?" *Mechanics Research Communications*, vol. 36, no. 2, pp. 137–142, Mar. 2009, ISSN: 00936413. DOI: `10.1016/j.mechrescom.2008.08.011`.

[40] A. Oishi, K. Yamada, S. Yoshimura, and G. Yagawa, "Quantitative nondestructive evaluation with ultrasonic method using neural networks and computational mechanics," *Computational Mechanics*, vol. 15, no. 6, pp. 521–533, Mar. 1995, ISSN: 0178-7675, 1432-0924. DOI: `10.1007/BF00350265`.

[41] J. D. Achenbach, "Quantitative nondestructive evaluation," *International Journal of Solids and Structures*, vol. 37, no. 1, pp. 13–27, Jan. 2000. DOI: `10.1016/S0020-7683(99)00074-8`.

[42] J. D. Achenbach, "Modeling for quantitative non-destructive evaluation," *Ultrasonics*, vol. 40, no. 1, pp. 1–10, May 2002, ISSN: 0041624X. DOI: `10.1016/S0041-624X(02)00083-5`.

[43] M. M. Derriso, M. P. DeSimio, C. D. McCurry, C. M. Schubert Kabban, and S. E. Olson, "Industrial age non-destructive evaluation to information age structural health monitoring," *Structural Health Monitoring*, vol. 13, no. 6, pp. 591–600, Nov. 1, 2014, Publisher: SAGE Publications, ISSN: 1475-9217. DOI: `10.1177/1475921714546061`.

[44] C. R. Farrar and K. Worden, "An introduction to structural health monitoring," *Philosophical Transactions of the Royal Society A: Mathematical, Physical and Engineering Sciences*, vol. 365, no. 1851, pp. 303–315, Feb. 15, 2007, ISSN: 1364-503X, 1471-2962. DOI: `10.1098/rsta.2006.1928`.

[45] D. Balageas, C.-P. Fritzen, and A. Güemes, Eds., *Structural health monitoring*, OCLC: ocm62493224, London ; Newport Beach, CA: ISTE, 2006, 495 pp., ISBN: 978-1-905209-01-9.

[46] C. Boller, F.-K. Chang, and Y. Fujino, Eds., *Encyclopedia of structural health monitoring*, Chichester, West Sussex, U.K: John Wiley, 2009, ISBN: 978-0-470-06162-6.

[47] M. H. Aliabadi and Z. Sharif-Khodaei, Eds., *Structural health monitoring for advanced composite structures*, Computational and experimental methods in structures volume 8, New Jersey: World Scientific, 2017, 274 pp., ISBN: 978-1-78634-392-5.

[48] D. Roach, "Validation and verification processes to certify SHM solutions for commercial aircraft applications," Sandia National Labs, SAND2013-7867C, 2013.

[49] D. Roach, T. Rice, and P. Swindell, "Convergence of multiple statistical methods for calculating the probability of detection from SHM sensor networks," in *Structural Health Monitoring 2017*, DEStech Publications, Inc., Sep. 28, 2017, ISBN: 978-1-60595-330-4. DOI: `10.12783/shm2017/14209`.

[50] D. Roach and T. Rice, "Wide area monitoring of aircraft structures using acousto-ultrasonic sensor networks," presented at the International Symposium on Aircraft Health Management, Xiamen, China, Oct. 2016.

[51] D. Roach, "Does the maturity of structural health monitoring technology match user readiness?" In *In Proceedings of the International Workshop on SHM*, Stanford, CA, USA, Sep. 13, 2011.

[52] M. Seaver, A. Chattopadhyay, A. Papandreou-Suppapola, *et al.*, "Workshop on transitioning structural health monitoring technology to military platforms," *Journal of Intelligent Material Systems and Structures*, vol. 24, no. 17, pp. 2063–2073, Nov. 2013, ISSN: 1045-389X, 1530-8138. DOI: `10.1177/1045389X12440753`.

[53] P. Cawley, "Structural health monitoring: Closing the gap between research and industrial deployment," *Structural Health Monitoring*, vol. 17, no. 5, pp. 1225–1244, Sep. 2018, ISSN: 1475-9217, 1741-3168. DOI: `10.1177/1475921717750047`.

[54] P. Cawley, "A development strategy for structural health monitoring applications," *Journal of Nondestructive Evaluation, Diagnostics and Prognostics of Engineering Systems*, vol. 4, no. 4, p. 041 012, Nov. 1, 2021, ISSN: 2572-3901, 2572-3898. DOI: `10.1115/1.4051974`.

[55] E. A. Lindgren, C. F. Buynak, J. C. Aldrin, E. A. Medina, and M. M. Derriso, "Model-assisted methods for validation of structural health monitoring systems," in *Proceedings of the 7th International Workshop on Structural Health Monitoring*, Stanford, CA, Sep. 9, 2009, pp. 2188–2195.

[56] J. C. Aldrin, E. A. Medina, J. Santiago, E. A. Lindgren, C. F. Buynak, and J. S. Knopp, "Demonstration study for reliability assessment of SHM systems incorporating model-assisted probability of detection approach," presented at the REVIEW OF PROGRESS IN QUANTITATIVE NONDESTRUCTIVE EVALUATION: Volume 31, Burlington, VT, 2012, pp. 1543–1550. DOI: 10.1063/1.4716398.

[57] E. A. Lindgren and C. F. Buynak, "The need and requirements for validating damage detection capability," in *Proceedings of the 8th International Workshop on SHM*, DEStech Publications, Inc., 2011, pp. 2444–2451.

[58] F. K. Chang, "The need of SHM quantification for implementation," presented at the EWSHM - 7th European Workshop on Structural Health Monitoring, Jul. 8, 2014.

[59] A. Güemes, A. Fernandez-Lopez, A. R. Pozo, and J. Sierra-Pérez, "Structural health monitoring for advanced composite structures: A review," *Journal of Composites Science*, vol. 4, no. 1, p. 13, Jan. 27, 2020, ISSN: 2504-477X. DOI: 10.3390/jcs4010013.

[60] C. M. Kabban and M. M. Derriso, "Certification in structural health monitoring systems," in *Proceedings of the 8th International Workshop on SHM*, Stanford, CA, USA, 2011, pp. 2429–2436.

[61] J. C. Aldrin, E. A. Medina, E. A. Lindgren, C. Buynak, G. Steffes, and M. Derriso, "Model-assisted probabilistic reliability assessmnt for structural health monitoring systems," presented at the Review of Progress in QNDE, vol. 29, AIP, 2010, pp. 1965–1972. DOI: 10.1063/1.3362348.

[62] E. A. Medina and J. C. Aldrin, "Value assessment approaches for structural life management," in *Encyclopedia of Structural Health Monitoring*, C. Boller, F.-K. Chang, and Y. Fujino, Eds., Chichester, UK: John Wiley & Sons, Ltd, Jan. 26, 2008, shm189, ISBN: 978-0-470-06162-6. DOI: 10.1002/9780470061626.shm189.

[63] D. of Defense, "Procedures for performing a failure mode, effects, and criticality analysis," Washington, DC, MIL-STD-1629A, Nov. 24, 1980.

[64] J. C. Aldrin, E. A. Medina, E. A. Lindgren, C. F. Buynak, and J. S. Knopp, "Protocol for reliability assessment of structural health monitoring systems incorporating model-assisted probability of detection (MAPOD) approach," in *Proceedings of the 8th international workshop on structural health monitoring*, Stanford, Sep. 13, 2011, pp. 2452–2459.

[65] "Environmental conditions and test procedures for airborne equipment," Washington, DC, RTCA Paper No. 111-04/SC135-645, 2005.

[66] "Department of defense test method standard for environmental engineering considerations," Jan. 1, 2000.

[67] "Department of defense interface standard requirements for the control of electromagnetic interference characteristics of subsystems and equipment," Aug. 1999.

[68] S. S. Kessler, "Certifying a structural health monitoring system: Characterizing durability, reliability and longevity," in *Proceedings of the 1st International Forum on Integrated Systems Health Engineering and Management in Aerospace*, Napa, CA, Nov. 7, 2005.

[69] V. Janapati, F. Kopsaftopoulos, F. Li, S. J. Lee, and F.-K. Chang, "Damage detection sensitivity characterization of acousto-ultrasound-based structural health monitoring techniques," *Structural Health Monitoring: An International Journal*, vol. 15, no. 2, pp. 143–161, Mar. 2016, ISSN: 1475-9217, 1741-3168. DOI: `10.1177/1475921715627490`.

[70] A. Rytter, "Vibrational based inspection of civil engineering structures," Issue: 44 Series: Fracture and Dynamics, Ph.D. dissertation, Dept. of Building Technology and Structural Engineering, Aalborg University, Denmark, 1993.

[71] S. Doebling, C. Farrar, M. Prime, and D. Shevitz, "Damage identification and health monitoring of structural and mechanical systems from changes in their vibration characteristics: A literature review," LA–13070-MS, 249299, May 1, 1996, LA–13070–MS, 249 299. DOI: `10.2172/249299`.

[72] M. Derriso, C. McCurry, and C. Schubert Kabban, "A novel approach for implementing structural health monitoring systems for aerospace structures," in *Structural Health Monitoring (SHM) in Aerospace Structures*, Elsevier, 2016, pp. 33–56, ISBN: 978-0-08-100148-6. DOI: `10.1016/B978-0-08-100148-6.00002-0`.

[73] "Department of defense standard practice. aircraft structural integrity program (ASIP)," United States Air Force, MIL-STD-1530C, 2005.

[74] E. Monaco, V. Memmolo, F. Ricci, N. D. Boffa, and L. Maio, "Guided waves based SHM systems for composites structural elements: Statistical analyses finalized at probability of detection definition and assessment," presented at the SPIE Smart Structures and Materials + Nondestructive Evaluation and Health Monitoring, T. Kundu, Ed., San Diego, California, United States, Mar. 23, 2015, p. 94380M. DOI: `10.1117/12.2084334`.

[75] G. Casella and R. L. Berger, *Statistical inference*, 2nd ed. Australia ; Pacific Grove, CA: Thomson Learning, 2002, 660 pp., ISBN: 978-0-534-24312-8.

[76] C. Annis. "False positives," Statistical Engineering. (Jan. 1, 2018), [Online]. Available: `https://statistical-engineering.com/false-positives/` (visited on 12/22/2020).

[77] M. Wright, "How to implement a PoD into a highly effective inspection strategy," presented at the NDT in Canada 2016 & 6th International CANDU In-Service Inspection Workshop, Burlington, ON, Canada: NDT.net, Nov. 15, 2016.

[78] C. Petrin, C. Annis, and S. Vukelich, "A recommended methodology for quantifying NDE/NDI based on aircraft engine experience," AGARD LECTURE SERIES 190, Apr. 1993.

[79] A. P. Berens, "NDE reliability data analysis," in *Metals handbook Volume 17: Nondestructive evaluation and quality control*, 9th ed, Metals Park, Ohio: American Society for Metals, 1989, pp. 689–701.

[80] D. Kanzler and C. Müller, "How much information do we need? a reflection of the correct use of real defects in POD-evaluations," presented at the 42ND ANNUAL REVIEW OF PROGRESS IN QUANTITATIVE NONDESTRUCTIVE EVALUATION: Incorporating the 6th European-American Workshop on Reliability of NDE, Minneapolis, Minnesota, 2016, p. 200 008. DOI: `10.1063/1.4940652`.

[81] D. S. Forsyth, "On the independence of multiple inspections and the resulting probability of detection," in *AIP Conference Proceedings*, ISSN: 0094243X, vol. 509, Montreal (Canada): AIP, 2000, pp. 2159–2166. DOI: `10.1063/1.1291337`.

[82] J. C. Aldrin, C. Annis, H. A. Sabbagh, J. S. Knopp, and E. A. Lindgren, "Assessing the reliability of nondestructive evaluation methods for damage characterization," presented at the 40TH ANNUAL REVIEW OF PROGRESS IN QUANTITATIVE NONDESTRUCTIVE EVALUATION: Incorporating the 10th International Conference on Barkhausen Noise and Micromagnetic Testing, Baltimore, Maryland, USA, 2014, pp. 2071–2078. DOI: `10.1063/1.4865078`.

[83] W. Q. Meeker, "R. b. thompson's contributions to model assisted probability of detection," presented at the REVIEW OF PROGRESS IN QUANTITATIVE NONDESTRUCTIVE EVALUATION: Volume 31, Burlington, VT, 2012, pp. 83–94. DOI: `10.1063/1.4716215`.

[84] L. Gandossi and K. Simola, "Derivation and use of probability of detection curves in the nuclear industry," *Insight - Non-Destructive Testing and Condition Monitoring*, vol. 52, no. 12, pp. 657–663, Dec. 1, 2010, ISSN: 1354-2575. DOI: `10.1784/insi.2010.52.12.657`.

[85] D. Kanzler, C. Müller, and J. Pitkänen, "Combining of different data pools for calculating a reliable POD for real defects," presented at the 41ST ANNUAL REVIEW OF PROGRESS IN QUANTITATIVE NONDESTRUCTIVE EVALUATION: Volume 34, Boise, Idaho, 2015, pp. 1924–1932. DOI: `10.1063/1.4914819`.

[86] C. Annis, L. Gandossi, and O. Martin, "Optimal sample size for probability of detection curves," *Nuclear Engineering and Design*, vol. 262, pp. 98–105, Sep. 2013, ISSN: 00295493. DOI: `10.1016/j.nucengdes.2013.03.059`.

[87] L. Gandossi and C. Annis, "Influence of sample size and other factors on hit/miss probability of detection curves," Publications Office, Luxembourg, ENIQ report No. 47. 2012, OCLC: 870614852.

[88] C. Annis and L. Gandossi, "Probability of detection curves: Statistical best-practices," Publications Office of the European Union, Luxembourg, ENIQ report No 41, 2010.

[89] Y.-M. Koh and W. Q. Meeker, "Methods for planning a statistical POD study," presented at the REVIEW OF PROGRESS IN QUANTITATIVE NONDESTRUCTIVE EVALUATION: VOLUME 32, Denver, Colorado, USA, 2013, pp. 1725–1732. DOI: `10.1063/1.4789249`.

[90] C. Annis. "How hit/miss models work," Statistical Engineering. (Jan. 1, 2018), [Online]. Available: `https://statistical-engineering.com/how-hit-miss-models-work/` (visited on 12/14/2020).

[91] I. Virkkunen, T. Koskinen, S. Papula, T. Sarikka, and H. Hänninen, "Comparison of â versus a and hit/miss POD-estimation methods: A european viewpoint," *Journal of Nondestructive Evaluation*, vol. 38, no. 4, p. 89, Dec. 2019, ISSN: 0195-9298, 1573-4862. DOI: `10.1007/s10921-019-0628-z`.

[92] J. Knopp, R. Grandhi, L. Zeng, and J. Aldrin, "Considerations for statistical analysis of nondestructive evaluation data: Hit/miss analysis," *E-Journal of Advanced Maintenance*, vol. 4, no. 3, pp. 105–115, 2012.

[93] "Standard practice for probability of detection analysis for hit/miss data," ASTM E2862 - 18.

[94] C. A. Harding, "Statistical analysis of probability of detection hit/miss data for small data sets," in *AIP Conference Proceedings*, ISSN: 0094243X, vol. 657, Bellingham, Washington (USA): AIP, 2003, pp. 1838–1845. DOI: `10.1063/1.1570352`.

[95] C. Annis and J. Knopp, "Comparing the effectiveness of a90/95 calculations," in *AIP Conference Proceedings*, ISSN: 0094243X, vol. 894, Portland, Oregon (USA): AIP, 2007, pp. 1767–1774. DOI: `10.1063/1.2718177`.

[96] F. W. Spencer, "The calculation and use of confidence bounds in POD models," in *AIP Conference Proceedings*, ISSN: 0094243X, vol. 894, Portland, Oregon (USA): AIP, 2007, pp. 1791–1798. DOI: `10.1063/1.2718181`.

[97] R. C. H. Cheng and T. C. Iles, "Confidence bands for cumulative distribution functions of continuous random variables," *Technometrics*, vol. 25, no. 1, pp. 77–86, Feb. 1983, ISSN: 0040-1706, 1537-2723. DOI: `10.1080/00401706.1983.10487822`.

[98] R. C. H. Cheng and T. C. lies, "One-sided confidence bands for cumulative distribution functions," *Technometrics*, vol. 30, no. 2, pp. 155–159, May 1988, ISSN: 0040-1706, 1537-2723. DOI: `10.1080/00401706.1988.10488362`.

[99] J. C. Aldrin, C. Annis, H. A. Sabbagh, and E. A. Lindgren, "Best practices for evaluating the capability of nondestructive evaluation (NDE) and structural health monitoring (SHM) techniques for damage characterization," presented at the 42ND ANNUAL REVIEW OF PROGRESS IN QUANTITATIVE NONDESTRUCTIVE EVALUATION: Incorporating the 6th European-American Workshop on Reliability of NDE, Minneapolis, Minnesota, 2016. DOI: `10.1063/1.4940646`.

[100] C. Annis, J. C. Aldrin, and H. A. Sabbagh, "What is missing in nondestructive testing capability evaluation?" *Materials Evaluation*, vol. 73, no. 1, Jan. 1, 2015.

[101] D. A. Ameyaw, S. Rothe, and D. Söffker, "A novel feature-based probability of detection assessment and fusion approach for reliability evaluation of vibration-based diagnosis systems," *Structural Health Monitoring*, vol. 19, no. 3, pp. 649–660, May 2020, ISSN: 1475-9217, 1741-3168. DOI: `10.1177/1475921719856274`.

[102] J. Swets, "Measuring the accuracy of diagnostic systems," *Science*, vol. 240, no. 4857, pp. 1285–1293, Jun. 3, 1988. DOI: `10.1126/science.3287615`.

[103] A. Rouhan and F. Schoefs, "Probabilistic modeling of inspection results for offshore structures," *Structural Safety*, vol. 25, no. 4, pp. 379–399, Oct. 2003, ISSN: 01674730. DOI: `10.1016/S0167-4730(03)00016-X`.

[104] F. Schoefs, A. Clément, and A. Nouy, "Assessment of ROC curves for inspection of random fields," *Structural Safety*, vol. 31, no. 5, pp. 409–419, Sep. 2009, ISSN: 01674730. DOI: `10.1016/j.strusafe.2009.01.004`.

[105] T. Fawcett, "ROC graphs: Notes and practical considerations for data mining researchers," HP Laboratories, Palo Alto, CA, Technical Report HPL-2003–4, 2003.

[106] W. Q. Meeker, S.-L. Jeng, C.-P. Chiou, and R. B. Thompson, "Improved methodology for predicting POD of detecting synthetic hard alpha inclusions in titanium," in *Review of Progress in Quantitative Nondestructive Evaluation*, D. O. Thompson and D. E. Chimenti, Eds., Boston, MA: Springer US, 1997, pp. 2021–2028, ISBN: 978-1-4615-5947-4. DOI: 10.1007/978-1-4615-5947-4_264.

[107] C. Cox, "Delta method," in *Encyclopedia of Biostatistics*, P. Armitage and T. Colton, Eds., Chichester, UK: John Wiley & Sons, Ltd, Jul. 15, 2005, b2a15029, ISBN: 978-0-470-01181-2. DOI: 10.1002/0470011815.b2a15029.

[108] G. W. Oehlert, "A note on the delta method," *The American Statistician*, vol. 46, no. 1, pp. 27–29, Feb. 1992, ISSN: 0003-1305, 1537-2731. DOI: 10.1080/00031305.1992.10475842.

[109] M. Li, F. W. Spencer, and W. Q. Meeker, "Distinguishing between uncertainty and variability in nondestructive evaluation," presented at the REVIEW OF PROGRESS IN QUANTITATIVE NONDESTRUCTIVE EVALUATION: Volume 31, Burlington, VT, 2012, pp. 1725–1732. DOI: 10.1063/1.4716420.

[110] M. Li, W. Q. Meeker, R. B. Thompson, D. O. Thompson, and D. E. Chimenti, "Physical model assisted probability of detection in nondestructive evaluation," presented at the REVIEW OF PROGRESS IN QUANTITATIVE NONDESTRUCTIVE EVALUATION: Volume 30A; Volume 30B, San Diego, California, (USA), 2011, pp. 1541–1548. DOI: 10.1063/1.3592113.

[111] A. Berens and P. Hovey, "Statistical methods for estimating crack detection probabilities," in *Probabilistic Fracture Mechanics and Fatigue Methods: Applications for Structural Design and Maintenance*, J. Bloom and J. Ekvall, Eds., 100 Barr Harbor Drive, PO Box C700, West Conshohocken, PA 19428-2959: ASTM International, Jan. 1, 1983, pp. 79–79–16, ISBN: 978-0-8031-0242-2. DOI: 10.1520/STP33213S.

[112] D. S. Forsyth, "Structural health monitoring and probability of detection estimation," presented at the 42ND ANNUAL REVIEW OF PROGRESS IN QUANTITATIVE NONDESTRUCTIVE EVALUATION: Incorporating the 6th European-American Workshop on Reliability of NDE, Minneapolis, Minnesota, 2016, p. 200 004. DOI: 10.1063/1.4940648.

[113] I. Müller, V. Janapati, S. Banerjee, K. Lonkar, S. Roy, and F.-K. Chang, "On the performance quantification of active sensing SHM systems using model-assisted POD methods," in *Proceedings of the 8th international workshop on structural health monitoring*, vol. 2, Stanford, CA, USA: DEStech Publications, Inc., Sep. 13, 2011, pp. 2417–2428.

[114] V. Janapati, F. Kopsaftopoulos, S. Roy, *et al.*, "Sensor network configuration effect on detection sensitivity of an AcoustoUltrasound- based active SHM system," in *Proceedings of the 9th International Workshop on Structural Health Monitoring*, Stanford, CA, USA: DEStech Publ, 2013, pp. 2147–2156.

[115] L. Pado, J.-B. Ihn, and J. Dunne, "Understanding probability of detection (POD) in structure health monitoring systems," in *Proceedings of the 9th International Workshop on Structural Health Monitoring*, vol. 2, Stanford, CA, USA: DEStech Publications, Inc., Sep. 10, 2013, pp. 2107–2114.

[116] T. Hayo, B. Frankenstein, C. Boller, and C. Bockenheimer, "Approach to the technical qualification of a SHM system in terms of damage detection in aerospace industry," in *Proceedings of the International Workshop Smart Materials, Structures & NDT in Aerospace*, Montreal, Quebec, Canada, Nov. 2, 2011.

[117] A. Gianneo, M. Carboni, and M. Giglio, "A preliminary study of multi-parameter POD curves for a guided waves based SHM approach to lightweight materials," presented at the 42ND ANNUAL REVIEW OF PROGRESS IN QUANTITATIVE NONDESTRUCTIVE EVALUATION: Incorporating the 6th European-American Workshop on Reliability of NDE, Minneapolis, Minnesota, 2016, p. 030 018. DOI: 10.1063/1.4940490.

[118] H. Sohn, "Effects of environmental and operational variability on structural health monitoring," *Philosophical Transactions of the Royal Society A: Mathematical, Physical and Engineering Sciences*, vol. 365, no. 1851, pp. 539–560, Feb. 15, 2007, ISSN: 1364-503X, 1471-2962. DOI: 10.1098/rsta.2006.1935.

[119] C. Mandache, M. Genest, M. Khan, and N. Mrad, "Considerations on structural health monitoring reliability," Montreal, Quebec, Canada: Proceedings of the International Workshop Smart Materials, Structures & NDT in Aerospace, Nov. 2, 2011.

[120] R. Howard and F. Cegla, "Detectability of corrosion damage with circumferential guided waves in reflection and transmission," *NDT & E International*, vol. 91, pp. 108–119, Oct. 2017, ISSN: 09638695. DOI: 10.1016/j.ndteint.2017.07.004.

[121] Y. Tan and L. Zhang, "Computational methodologies for optimal sensor placement in structural health monitoring: A review," *Structural Health Monitoring*, vol. 19, no. 4, pp. 1287–1308, Jul. 2020, ISSN: 1475-9217, 1741-3168. DOI: 10.1177/1475921719877579.

[122] E. B. Flynn and M. D. Todd, "A bayesian approach to optimal sensor placement for structural health monitoring with application to active sensing," *Mechanical Systems and Signal Processing*, vol. 24, no. 4, pp. 891–903, May 2010, ISSN: 08883270. DOI: `10.1016/j.ymssp.2009.09.003`.

[123] M. Azarbayejani, A. I. El-Osery, K. K. Choi, and M. M. Reda Taha, "A probabilistic approach for optimal sensor allocation in structural health monitoring," *Smart Materials and Structures*, vol. 17, no. 5, p. 055 019, Oct. 1, 2008, ISSN: 0964-1726, 1361-665X. DOI: `10.1088/0964-1726/17/5/055019`.

[124] J. F. C. Markmiller and F.-K. Chang, "Sensor network optimization for a passive sensing impact detection technique," *Structural Health Monitoring*, vol. 9, no. 1, pp. 25–39, Jan. 2010, ISSN: 1475-9217, 1741-3168. DOI: `10.1177/1475921709349673`.

[125] V. Mallardo, Z. Sharif Khodaei, and F. Aliabadi, "A bayesian approach for sensor optimisation in impact identification," *Materials*, vol. 9, no. 11, p. 946, Nov. 22, 2016, ISSN: 1996-1944. DOI: `10.3390/ma9110946`.

[126] V. Mallardo, M. H. Aliabadi, and Z. S. Khodaei, "Optimal sensor positioning for impact localization in smart composite panels," *Journal of Intelligent Material Systems and Structures*, vol. 24, no. 5, pp. 559–573, Mar. 2013, ISSN: 1045-389X, 1530-8138. DOI: `10.1177/1045389X12464280`.

[127] J. Yan, S. Laflamme, and L. Leifsson, "Computational framework for dense sensor network evaluation based on model-assisted probability of detection," *Materials Evaluation*, vol. 78, no. 5, pp. 573–583, May 1, 2020, ISSN: 00255327. DOI: `10.32548/2020.me-04111`.

[128] C.-D. Chen, Y.-C. Chiu, Y.-H. Huang, P.-H. Wang, and R.-D. Chien, "Assessments of structural health monitoring for fatigue cracks in metallic structures by using lamb waves driven by piezoelectric transducers," *Journal of Aerospace Engineering*, vol. 34, no. 1, p. 04 020 091, Jan. 2021, ISSN: 0893-1321, 1943-5525. DOI: `10.1061/(ASCE)AS.1943-5525.0001212`.

[129] J. L. Tabjula, S. Kanakambaran, S. Kalyani, P. Rajagopal, and B. Srinivasan, "Outlier analysis for defect detection using sparse sampling in guided wave structural health monitoring," *Structural Control and Health Monitoring*, vol. 28, no. 3, Mar. 2021, ISSN: 1545-2255, 1545-2263. DOI: `10.1002/stc.2690`.

[130] B. Liu and F.-K. Chang, "Generating damage probability-of-detection curves in structural health monitoring transducer networks," U.S. Patent 8069011B2.

[131] K. Worden, G. Manson, and N. Fieller, "Damage detection using outlier analysis," *Journal of Sound and Vibration*, vol. 229, no. 3, pp. 647–667, Jan. 2000, ISSN: 0022460X. DOI: `10.1006/jsvi.1999.2514`.

[132] S. J. Roberts, "Novelty detection using extreme value statistics," *IEE Proceedings - Vision, Image and Signal Processing*, vol. 146, no. 3, pp. 124–129, Jun. 1999. DOI: 10.1049/ip-vis:19990428.

[133] M. Markou and S. Singh, "Novelty detection: A review—part 1: Statistical approaches," *Signal Processing*, vol. 83, no. 12, pp. 2481–2497, Dec. 2003, ISSN: 01651684. DOI: 10.1016/j.sigpro.2003.07.018.

[134] M. Markou and S. Singh, "Novelty detection: A review—part 2: Neural network based approaches," *Signal Processing*, vol. 83, no. 12, pp. 2499–2521, Dec. 1, 2003, ISSN: 0165-1684. DOI: 10.1016/j.sigpro.2003.07.019.

[135] A. C. Cobb, J. Fisher, and J. E. Michaels, "Model-assisted probability of detection for ultrasonic structural health monitoring," in *th European-American Workshop on Reliability of NDE*, Berlin, Germany, Jun. 2009.

[136] V. Memmolo, L. Maio, N. D. Boffa, E. Monaco, and F. Ricci, "Damage detection tomography based on guided waves in composite structures using a distributed sensor network," *Optical Engineering*, vol. 55, no. 1, p. 011 007, Oct. 20, 2015, ISSN: 0091-3286. DOI: 10.1117/1.OE.55.1.011007.

[137] N. Yue, Z. S. Khodaei, and M. H. Aliabadi, "Damage detection in large composite stiffened panels based on a novel SHM building block philosophy," *Smart Materials and Structures*, vol. 30, no. 4, p. 045 004, Apr. 1, 2021, ISSN: 0964-1726, 1361-665X. DOI: 10.1088/1361-665X/abe4b4.

[138] S. Mariani, S. Heinlein, and P. Cawley, "Compensation for temperature-dependent phase and velocity of guided wave signals in baseline subtraction for structural health monitoring," *Structural Health Monitoring*, vol. 19, no. 1, pp. 26–47, Jan. 2020, ISSN: 1475-9217, 1741-3168. DOI: 10.1177/1475921719835155.

[139] A. Raghavan and C. E. Cesnik, "Effects of elevated temperature on guided-wave structural health monitoring," *Journal of Intelligent Material Systems and Structures*, vol. 19, no. 12, pp. 1383–1398, Dec. 2008, ISSN: 1045-389X, 1530-8138. DOI: 10.1177/1045389X07086691.

[140] T. Clarke, F. Simonetti, and P. Cawley, "Guided wave health monitoring of complex structures by sparse array systems: Influence of temperature changes on performance," *Journal of Sound and Vibration*, vol. 329, no. 12, pp. 2306–2322, Jun. 2010, ISSN: 0022460X. DOI: 10.1016/j.jsv.2009.01.052.

[141] Y. Lu and J. E. Michaels, "A methodology for structural health monitoring with diffuse ultrasonic waves in the presence of temperature variations," *Ultrasonics*, vol. 43, no. 9, pp. 717–731, Oct. 2005, ISSN: 0041624X. DOI: 10.1016/j.ultras.2005.05.001.

[142] A. Croxford, P. Wilcox, B. Drinkwater, and G. Konstantinidis, "Strategies for guided-wave structural health monitoring," *Proceedings of the Royal Society A: Mathematical, Physical and Engineering Sciences*, vol. 463, no. 2087, pp. 2961–2981, Nov. 8, 2007, ISSN: 1364-5021, 1471-2946. DOI: `10.1098/rspa.2007.0048`.

[143] J. E. Michaels, "Detection, localization and characterization of damage in plates with an *in situ* array of spatially distributed ultrasonic sensors," *Smart Materials and Structures*, vol. 17, no. 3, p. 035 035, Jun. 1, 2008, ISSN: 0964-1726, 1361-665X. DOI: `10.1088/0964-1726/17/3/035035`.

[144] J. B. Harley and J. M. F. Moura, "Scale transform signal processing for optimal ultrasonic temperature compensation," *IEEE Transactions on Ultrasonics, Ferroelectrics and Frequency Control*, vol. 59, no. 10, p. 6 327 494, Oct. 2012, ISSN: 0885-3010. DOI: `10.1109/TUFFC.2012.2448`.

[145] C. Fendzi, M. Rébillat, N. Mechbal, M. Guskov, and G. Coffignal, "A data-driven temperature compensation approach for structural health monitoring using lamb waves," *Structural Health Monitoring*, vol. 15, no. 5, pp. 525–540, Sep. 2016, ISSN: 1475-9217, 1741-3168. DOI: `10.1177/1475921716650997`.

[146] N. Yue and M. Aliabadi, "A scalable data-driven approach to temperature baseline reconstruction for guided wave structural health monitoring of anisotropic carbon-fibre-reinforced polymer structures," *Structural Health Monitoring*, vol. 19, no. 5, pp. 1487–1506, Sep. 2020, ISSN: 1475-9217, 1741-3168. DOI: `10.1177/1475921719887109`.

[147] S. Mariani, S. Heinlein, and P. Cawley, "Location specific temperature compensation of guided wave signals in structural health monitoring," *IEEE Transactions on Ultrasonics, Ferroelectrics, and Frequency Control*, vol. 67, no. 1, pp. 146–157, Jan. 2020, ISSN: 0885-3010, 1525-8955. DOI: `10.1109/TUFFC.2019.2940451`.

[148] *Guided ultrasonics ltd.*

[149] S. Mariani, "Signal processing," pat. WO2020058663.

[150] T. L. Lai, "Sequential analysis: Some classical problems and new challenges," *Statistica Sinica*, vol. 11, no. 2, pp. 303–351, 2001, Publisher: Institute of Statistical Science, Academia Sinica, ISSN: 1017-0405.

[151] S. Mariani, Y. Liu, and P. Cawley, "Improving sensitivity and coverage of structural health monitoring using bulk ultrasonic waves," *Structural Health Monitoring*, p. 147 592 172 096 512, Oct. 16, 2020, ISSN: 1475-9217, 1741-3168. DOI: `10.1177/1475921720965121`.

[152] A. v. d. Oord, S. Dieleman, H. Zen, *et al.*, "WaveNet: A generative model for raw audio," *arXiv:1609.03499 [cs]*, Sep. 19, 2016. arXiv: `1609.03499`.

[153] B. Shook, H. Millwater, M. Enright, S. Hudak, and W. Francis, "Simulation of recurring automated inspections on probability-of-fracture estimates," *Structural Health Monitoring: An International Journal*, vol. 7, no. 4, pp. 293–307, Dec. 2008, ISSN: 1475-9217, 1741-3168. DOI: `10.1177/1475921708091169`.

[154] D. Roach, K. Rackow, W. DeLong, S. Yepez, D. Reedy, and S. White, "Use of composite materials, health monitoring, and self-healing concepts to refurbish our civil and military infrastructure," Department of Energy - Sandia National Laboratories, Albuquerque, New Mexico 87185 and Livermore, California 94550, SAND2007-5547, Sep. 2007.

[155] C. Sbarufatti, M. Corbetta, J. San Millan, M. Frovel, M. Stefaniuk, and M. Giglio, "Model-assisted performance qualification of a distributed SHM system for fatigue crack detection on a helicopter tail boom," in *EWSHM 2016*, Bilbao, Spain, Jul. 5, 2016.

[156] D. Roach, T. Rice, S. Neidigk, D. Piotrowski, and J. Linn, "Establishing the reliability of SHM systems through the extrapolation of NDI probability of detection principles," in *Structural Health Monitoring 2015*, Destech Publications, 2015. DOI: `10.12783/SHM2015/330`.

[157] T. W. Anderson and D. A. Darling, "A test of goodness of fit," *Journal of the American Statistical Association*, vol. 49, no. 268, pp. 765–769, Dec. 1954, ISSN: 0162-1459, 1537-274X. DOI: `10.1080/01621459.1954.10501232`.

[158] W. Q. Meeker, G. J. Hahn, and L. A. Escobar, *Statistical intervals: a guide for practitioners and researchers* (Wiley series in probability and statistics), Second edition. Hoboken, New Jersey: Wiley, 2017, 592 pp., ISBN: 978-0-471-68717-7.

[159] D. Roach, "Calculating probability of detection for SHM systems using one-sided tolerance intervals – applications & limitations," Sandia National Labs, SAND2015-3998PE, 2015.

[160] D. Roach and P. Swindell, "Generating viable data to accurately quantify the performance of SHM systems," in *Structural Health Monitoring 2019*, DEStech Publications, Inc., Nov. 15, 2019, ISBN: 978-1-60595-601-5. DOI: `10.12783/shm2019/32220`.

[161] K. Krishnamoorthy and T. Mathew, *Statistical tolerance regions: theory, applications, and computation* (Wiley series in probability and statistics). Hoboken, N.J: Wiley, 2009, 461 pp., OCLC: 602593273, ISBN: 978-0-470-38026-0.

[162] A. C. Aitken, "IV.—on least squares and linear combination of observations," *Proceedings of the Royal Society of Edinburgh*, vol. 55, pp. 42–48, 1936, Publisher: Royal Society of Edinburgh Scotland Foundation, ISSN: 0370-1646. DOI: `10.1017/S0370164600014346`.

[163] P. Swindell, J. Doyle, and D. Roach, "Integration of structural health monitoring solutions onto commercial aircraft via the federal aviation administration structural health monitoring research program," presented at the 43RD ANNUAL REVIEW OF PROGRESS IN QUANTITATIVE NONDESTRUCTIVE EVALUATION, VOLUME 36, Atlanta, Georgia, USA, 2017, p. 070 001. DOI: `10.1063/1.4974616`.

[164] E. O'Connor, "Quantifying method differences in predicting the probability of detection for structural health monitoring applications," Master of Science (MS) in Statistics, Iowa State University, 2019.

[165] S. Kessler, G. Thomas, M. Borgen, and C. Dunn, "Carbon nanotube appliques for fatigue crack diagnostics," in *Structural Health Monitoring 2015*, Destech Publications, 2015. DOI: `10.12783/SHM2015/207`.

[166] S. Mishra, S. K. Yadav, and F.-K. Chang, "Reliability of probability of detection (POD) of fatigue cracks for built-in acousto-ultrasound technique as "in-situ" NDE," in *Structural Health Monitoring 2019*, DEStech Publications, Inc., Nov. 15, 2019, ISBN: 978-1-60595-601-5. DOI: `10.12783/shm2019/32506`.

[167] M. D. Bode, D. Ashbaugh, K. Boyce, and F. W. Spencer, "Corrosion structured experiment," in *AIP Conference Proceedings*, ISSN: 0094243X, vol. 615, Brunswick, Maine (USA): AIP, 2002, pp. 1779–1786. DOI: `10.1063/1.1473008`.

[168] J. B. Lee, J. H. Park, H. D. Kim, and H. S. Chung, "Evaluation of ECT reliability for axial ODSCC in steam generator tubes," *International Journal of Pressure Vessels and Piping*, vol. 87, no. 1, pp. 46–51, Jan. 2010, ISSN: 03080161. DOI: `10.1016/j.ijpvp.2009.11.005`.

[169] W. C. Hoppe, "A parametric study of eddy current response for probability of detection estimation," presented at the REVIEW OF PROGRESS IN QUANTITATIVE NONDESTRUCTIVE EVALUATION VOLUME 29, Kingston (Rhode Island), 2010, pp. 1895–1902. DOI: `10.1063/1.3362330`.

[170] J. C. Aldrin, H. A. Sabbagh, R. K. Murphy, *et al.*, "Demonstration of model-assisted probability of detection evaluation methodology for eddy current nondestructive evaluation," presented at the REVIEW OF PROGRESS IN QUANTITATIVE NONDESTRUCTIVE EVALUATION: Volume 31, Burlington, VT, 2012, pp. 1733–1740. DOI: `10.1063/1.4716421`.

[171] J. C. Aldrin, J. S. Knopp, E. A. Lindgren, K. V. Jata, D. O. Thompson, and D. E. Chimenti, "Model-assisted probability of detection evaluation for eddy current inspection of fastener sites," in *AIP Conference Proceedings*, Chicago (Illinois): AIP, 2009, pp. 1784–1791. DOI: `10.1063/1.3114175`.

[172] J. C. Aldrin, J. S. Knopp, and H. A. Sabbagh, "Bayesian methods in probability of detection estimation and model-assisted probability of detection evaluation," presented at the REVIEW OF PROGRESS IN QUANTITATIVE NONDESTRUCTIVE EVALUATION: VOLUME 32, Denver, Colorado, USA, 2013, pp. 1733–1740. DOI: `10.1063/1.4789250`.

[173] M. Pavlović, K. Takahashi, and C. Müller, "Probability of detection as a function of multiple influencing parameters," *Insight - Non-Destructive Testing and Condition Monitoring*, vol. 54, no. 11, pp. 606–611, Nov. 1, 2012, ISSN: 1354-2575. DOI: `10.1784/insi.2012.54.11.606`.

[174] N. Yusa and J. S. Knopp, "Evaluation of probability of detection (POD) studies with multiple explanatory variables," *Journal of Nuclear Science and Technology*, vol. 53, no. 4, pp. 574–579, Apr. 2, 2016, ISSN: 0022-3131, 1881-1248. DOI: `10.1080/00223131.2015.1064332`.

[175] C. Gao, W. Q. Meeker, and D. Mayton, "Detecting cracks in aircraft engine fan blades using vibrothermography nondestructive evaluation," *Reliability Engineering & System Safety*, vol. 131, pp. 229–235, Nov. 2014, ISSN: 09518320. DOI: `10.1016/j.ress.2014.05.009`.

[176] RM Meyer, JP Lareau, SL Crawford, and MT Anderson, "Review of literature for model assisted probability of detection," US Department of Energy, PNNL-23714.

[177] *Model-assisted POD working group*.

[178] R. B. Thompson, D. O. Thompson, and D. E. Chimenti, "A unified approach to the model-assisted determination of probability of detection," in *AIP Conference Proceedings*, ISSN: 0094243X, vol. 975, Golden (Colorado): AIP, 2008, pp. 1685–1692. DOI: `10.1063/1.2902639`.

[179] K. D. Smith, "POD transfer function approach," Palm Springs, California, USA, MAPOD Working Group meeting, Feb. 4, 2005.

[180] R. B. Thompson, L. Brasche, D. Forsyth, E. A. Lindgren, P. Swindell, and W. Winfree, "Recent advances in model-assisted probability of detection," presented at the 4th European-American Workshop on Reliability of NDE, Berlin, Germany: NDT.net, Jun. 2009.

[181] A. Gallina, P. Paćko, and Ł. Ambroziński, "Model assisted probability of detection in structural health monitoring," in *Advanced Structural Damage Detection: From Theory to Engineering Applications*, 1st ed., Wiley, Jun. 17, 2013, pp. 57–72, ISBN: 978-1-118-53614-8. DOI: `10.1002/9781118536148`.

[182] R. Austin, P. Ziehl, J. Yu, and D. Forsyth, “Development and validation of acoustic emission structural health monitoring for aerospace structures,” in *Proceedings of the 9th International Workshop on Structural Health Monitoring*, vol. 2, Stanford, CA, USA: DEStech Publications, Inc., Sep. 10, 2013, pp. 2123–2129.

[183] V. Memmolo, F. Ricci, L. Maio, N. D. Boffa, and E. Monaco, “Model assisted probability of detection for a guided waves based SHM technique,” presented at the SPIE Smart Structures and Materials + Nondestructive Evaluation and Health Monitoring, T. Kundu, Ed., Las Vegas, Nevada, United States, Apr. 1, 2016, p. 980 504. DOI: `10.1117/12.2219306`.

[184] “CIVA.” (2021), [Online]. Available: `https://www.extende.com/` (visited on 10/06/2021).

[185] F. W. Spencer, D. O. Thompson, and D. E. Chimenti, “Nonparametric POD estimation for hit/miss data: A goodness of fit comparison for parametric models,” presented at the Review of Progress in Quantitative Nondestructive Evaluation, vol. 30a; 30b, San Diego, California, (USA), 2011, pp. 1557–1564. DOI: `10.1063/1.3592115`.

[186] R. Miorelli, X. Artusi, A. B. Abdessalem, and C. Reboud, “Database generation and exploitation for efficient and intensive simulation studies,” presented at the 42ND ANNUAL REVIEW OF PROGRESS IN QUANTITATIVE NONDESTRUCTIVE EVALUATION: Incorporating the 6th European-American Workshop on Reliability of NDE, Minneapolis, Minnesota, 2016, p. 180 002. DOI: `10.1063/1.4940632`.

[187] N. Dominguez, C. Reboud, A. Dubois, and F. Jenson, “A new approach of confidence in POD determination using simulation,” presented at the Review Of Progress In Quantitative Nondestructive Evaluation, vol. 32, Denver, Colorado, USA, 2013, pp. 1749–1756. DOI: `10.1063/1.4789252`.

[188] S. Mahadevan and R. Rebba, “Validation of reliability computational models using bayes networks,” *Reliability Engineering & System Safety*, vol. 87, no. 2, pp. 223–232, Feb. 2005, ISSN: 09518320. DOI: `10.1016/j.ress.2004.05.001`.

[189] W. Q. Meeker and L. A. Escobar, “Introduction to the use of bayesian methods for reliability data,” in *Statistical methods for reliability data*, ser. Wiley series in probability and statistics. Applied probability and statistics section, New York: Wiley, 1998, pp. 343–368, ISBN: 978-0-471-14328-4.

[190] R. B. Thompson, "NDE simulations: Critical tools in the integration of NDE and SHM," presented at the SPIE Smart Structures and Materials + Nondestructive Evaluation and Health Monitoring, H. F. Wu, A. A. Diaz, P. J. Shull, and D. W. Vogel, Eds., San Diego, California, USA, Mar. 26, 2009, p. 729 402. DOI: `10.1117/12.824474`.

[191] F. Jenson, N. Dominguez, P. Willaume, and T. Yalamas, "A bayesian approach for the determination of POD curves from empirical data merged with simulation results," presented at the REVIEW OF PROGRESS IN QUANTITATIVE NONDESTRUCTIVE EVALUATION: VOLUME 32, Denver, Colorado, USA, 2013, pp. 1741–1748. DOI: `10.1063/1.4789251`.

[192] M. S. Syed Akbar Ali, A. Kumar, P. B. Rao, J. Tammana, K. Balasubramaniam, and P. Rajagopal, "Bayesian synthesis for simulation-based generation of probability of detection (PoD) curves," *Ultrasonics*, vol. 84, pp. 210–222, Mar. 2018, ISSN: 0041624X. DOI: `10.1016/j.ultras.2017.11.004`.

[193] D. Forsyth and D. V. Leemans, "Bayesian approaches to using FIeld inspection data in determining the probability of detection," *Materials Evaluation*, vol. 62, no. 8, Aug. 1, 2004.

[194] D. Kanzler, C. Mueller, U. Ewert, and J. Pitkänen, "Bayesian approach for the evaluation of the reliability of non-destructive testing methods," in *18th World Conference on Nondestructive Testing*, Durban, South Africa: NDT.net, Apr. 16, 2012, p. 6.

[195] R. B. Thompson, D. O. Thompson, and D. E. Chimenti, "A bayesian approach to the inversion of NDE and SHM data," presented at the REVIEW OF PROGRESS IN QUANTITATIVE NONDESTRUCTIVE EVALUATION VOLUME 29, Kingston (Rhode Island), 2010, pp. 679–686. DOI: `10.1063/1.3362460`.

[196] D. A. Ameyaw, S. Rothe, and D. Söffker, "Probability of detection (POD)-oriented view to fault diagnosis for reliability assessment of FDI approaches," in *Volume 8: 30th Conference on Mechanical Vibration and Noise*, Quebec City, Quebec, Canada: American Society of Mechanical Engineers, Aug. 26, 2018, V008T10A041, ISBN: 978-0-7918-5185-2. DOI: `10.1115/DETC2018-85554`.

[197] D. A. Ameyaw, S. Rothe, and D. Söffker, "Adaptation and implementation of probability of detection (POD)-based fault diagnosis in elastic structures through vibration-based SHM approach," in *9th European Workshop on Structural Health Monitoring*, Manchester, UK: NDT.net, Jul. 10, 2018.

[198] D. Hall and J. Llinas, "An introduction to multisensor data fusion," *Proceedings of the IEEE*, vol. 85, no. 1, pp. 6–23, Jan. 1997, ISSN: 00189219. DOI: `10.1109/5.554205`.

[199] C. Kralovec and M. Schagerl, "Review of structural health monitoring methods regarding a multi-sensor approach for damage assessment of metal and composite structures," *Sensors*, vol. 20, no. 3, p. 826, Feb. 4, 2020, ISSN: 1424-8220. DOI: `10.3390/s20030826`.

[200] N. Eleftheroglou, D. Zarouchas, T. Loutas, R. Alderliesten, and R. Benedictus, "Structural health monitoring data fusion for in-situ life prognosis of composite structures," *Reliability Engineering & System Safety*, vol. 178, pp. 40–54, Oct. 2018, ISSN: 09518320. DOI: `10.1016/j.ress.2018.04.031`.

[201] D. Gagar, P. E. Irving, I. K. Jennions, P. Foote, I. Read, and J. McFeat, "Development of probability of detection data for structural health monitoring damage detection techniques based on acoustic emission," in *Proceedings of the 8th International Workshop on Structural Heath Monitoring*, Stanford, CA, USA, Sep. 13, 2011, pp. 1391–1398.

[202] E. B. Flynn, M. D. Todd, P. D. Wilcox, B. W. Drinkwater, and A. J. Croxford, "Maximum-likelihood estimation of damage location in guided-wave structural health monitoring," *Proceedings of the Royal Society A: Mathematical, Physical and Engineering Sciences*, vol. 467, no. 2133, pp. 2575–2596, Sep. 8, 2011, ISSN: 1364-5021, 1471-2946. DOI: `10.1098/rspa.2011.0095`.

[203] J. Moriot, N. Quaegebeur, A. Le Duff, and P. Masson, "Characterization of the robustness of SHM imaging techniques using the absolute error of localization," in *Proceedings of the 8th European workshop on structural health monitoring*, Bilbao, Jul. 5, 2016.

[204] *ISO 5725-1:1994 accuracy (trueness and precision) of measurement methods and results — part 1: General principles and definitions*, 1994.

[205] *ISO 5725-2:2019 accuracy (trueness and precision) of measurement methods and results — part 2: Basic method for the determination of repeatability and reproducibility of a standard measurement method*, 2019.

[206] W. Visser, Great Britain, and Health and Safety Executive, *POD/POS curves for non-destructive examination*. Sudbury: HSE Books, 2002, OCLC: 49832768, ISBN: 978-0-7176-2297-9.

[207] O. Førli, "Nordtest report," Nordtest Report, NT TECHN REPORT 394, Apr. 1998.

[208] P. Ducharme, S. Rigault, I. Strijdonk, *et al.*, "Automated ultrasonic phased array inspection of fatigue sensitive riser girth welds with a weld overlay layer of corrosive resistant alloy," *NDT.net*, Sep. 2012.

[209] R. Spencer, E. Todorov, P. White, N. Porter, and M. Lozev, "Advanced technologies and methodology for automated ultrasonic testing systems quantification," U.S. Department of Transportation Pipeline and Hazardous Materials Safety Administration, Washington, DC, EWI Project No. 50454GTH, Apr. 29, 2011.

[210] S. Nath, K. Balasubramaniam, C. Krishnamurthy, and B. Narayana, "Reliability assessment of manual ultrasonic time of flight diffraction (TOFD) inspection for complex geometry components," *NDT & E International*, vol. 43, no. 2, pp. 152–162, Mar. 2010, ISSN: 09638695. DOI: `10.1016/j.ndteint.2009.10.007`.

[211] S. Nath, "Effect of variation in signal amplitude and transit time on reliability analysis of ultrasonic time of flight diffraction characterization of vertical and inclined cracks," *Ultrasonics*, vol. 54, no. 3, pp. 938–952, Mar. 2014, ISSN: 0041624X. DOI: `10.1016/j.ultras.2013.11.007`.

[212] A. Barrett, R. Smith, and M. Modarres, "A multivariate model to assess the probability of detection and sizing of defects in aluminum panels using eddy current inspections," *Engineering Failure Analysis*, vol. 94, pp. 182–194, Dec. 2018, ISSN: 13506307. DOI: `10.1016/j.engfailanal.2018.07.028`.

[213] C. R. A. Schneider and J. R. Rudlin, "Review of statistical methods used in quantifying NDT reliability," *Insight - Non-Destructive Testing and Condition Monitoring*, vol. 46, no. 2, pp. 77–79, Feb. 2004, ISSN: 1354-2575. DOI: `10.1784/insi.46.2.77.55549`.

[214] E. Ginzel, R. Ginzel, and W. Kanters, "Ermolov sizing equations revisited," *NDT.net*, vol. 7, no. 1, 2002.

[215] I. Ermolov, "The reflection of ultrasonic waves from targets of simple geometry," *Non-Destructive Testing*, vol. 5, no. 2, pp. 87–91, Apr. 1972, ISSN: 00291021. DOI: `10.1016/0029-1021(72)90100-4`.

[216] S. K. Nath, "Estimates of probability of detection and sizing of flaws in ultrasonic time of flight diffraction inspections for complex geometry components with grooved surfaces," *Journal of Nondestructive Evaluation, Diagnostics and Prognostics of Engineering Systems*, vol. 4, no. 2, p. 021 003, May 1, 2021, ISSN: 2572-3901, 2572-3898. DOI: `10.1115/1.4048381`.

[217] S. Beard, C.-C. Liu, and F.-K. Chang, "Design of a robust SHM system for composite structures," presented at the The 14th International Symposium on: Smart Structures and Materials & Nondestructive Evaluation and Health Monitoring, L. P. Davis, B. K. Henderson, and M. B. McMickell, Eds., San Diego, California, Apr. 6, 2007, p. 652 709. DOI: 10.1117/12.717319.

[218] F. Brennan and B. de Leeuw, "The use of inspection and monitoring reliability information in criticality and defect assessments of ship and offshore structures," in *Volume 2: Structures, Safety and Reliability*, Estoril, Portugal: ASMEDC, Jan. 1, 2008, pp. 921–925, ISBN: 978-0-7918-4819-7. DOI: 10.1115/OMAE2008-57934.

[219] J. C. Aldrin, C. Annis, H. A. Sabbagh, E. B. Shell, J. Knopp, and E. A. Lindgren, "Case study on NDE characterization metrics for optimization, validation and quality control," presented at the 41ST ANNUAL REVIEW OF PROGRESS IN QUANTITATIVE NONDESTRUCTIVE EVALUATION: Volume 34, Boise, Idaho, 2015, pp. 845–855. DOI: 10.1063/1.4914688.

[220] P. Servais, C. Ibarra-Castenado, X. Maldague, Y. Gélébart, and Y. Duan, "Probability of detection for in field thermal non destructive testing of aircraft composite structures," in *Proceedings of the 2010 International Conference on Quantitative InfraRed Thermography*, QIRT Council, 2010, ISBN: 978-2-9809199-1-6. DOI: 10.21611/qirt.2010.124.

[221] Y. Duan, P. Servais, M. Genest, C. Ibarra-Castanedo, and X. P. V. Maldague, "ThermoPoD: A reliability study on active infrared thermography for the inspection of composite materials," *Journal of Mechanical Science and Technology*, vol. 26, no. 7, pp. 1985–1991, Jul. 2012, ISSN: 1738-494X, 1976-3824. DOI: 10.1007/s12206-012-0510-8.

[222] J. H. Kurz, A. Jüngert, S. Dugan, G. Dobmann, and C. Boller, "Reliability considerations of NDT by probability of detection (POD) determination using ultrasound phased array," *Engineering Failure Analysis*, vol. 35, pp. 609–617, Dec. 2013, ISSN: 13506307. DOI: 10.1016/j.engfailanal.2013.06.008.

[223] L. Junyan, L. Yang, W. Fei, and W. Yang, "Study on probability of detection (POD) determination using lock-in thermography for nondestructive inspection (NDI) of CFRP composite materials," *Infrared Physics & Technology*, vol. 71, pp. 448–456, Jul. 2015, ISSN: 13504495. DOI: 10.1016/j.infrared.2015.06.007.

[224] S. Heinlein, P. Cawley, and T. Vogt, "Validation of a procedure for the evaluation of the performance of an installed structural health monitoring system," *Struc-*

*tural Health Monitoring*, vol. 18, no. 5, pp. 1557–1568, Nov. 2019, ISSN: 1475-9217, 1741-3168. DOI: `10.1177/1475921718798567`.

[225] P. Calmon, B. Chapuis, F. Jenson, and E. Sjerve, "The use of simulation in POD curves estimation: An overview of the IIW best practices proposal," p. 7,

[226] P. Huthwaite, "Accelerated finite element elastodynamic simulations using the GPU," *Journal of Computational Physics*, vol. 257, pp. 687–707, Jan. 2014, ISSN: 00219991. DOI: `10.1016/j.jcp.2013.10.017`.

[227] G. Keiser, *Optical fiber communications*, 4th ed. New York, NY: McGraw-Hill Companies, 2011, 654 pp., OCLC: ocn496964420, ISBN: 978-0-07-338071-1.

[228] B. H. Lee, Y. H. Kim, K. S. Park, *et al.*, "Interferometric fiber optic sensors," *Sensors*, vol. 12, no. 3, pp. 2467–2486, Feb. 23, 2012, ISSN: 1424-8220. DOI: `10.3390/s120302467`.

[229] F. Chiavaioli, C. Gouveia, P. Jorge, and F. Baldini, "Towards a uniform metrological assessment of grating-based optical fiber sensors: From refractometers to biosensors," *Biosensors*, vol. 7, no. 4, p. 23, Jun. 21, 2017, ISSN: 2079-6374. DOI: `10.3390/bios7020023`.

[230] K. O. Hill, Y. Fujii, D. C. Johnson, and B. S. Kawasaki, "Photosensitivity in optical fiber waveguides: Application to reflection filter fabrication," *Applied Physics Letters*, vol. 32, no. 10, pp. 647–649, May 15, 1978, ISSN: 0003-6951, 1077-3118. DOI: `10.1063/1.89881`.

[231] G. Meltz, W. W. Morey, and W. H. Glenn, "Formation of bragg gratings in optical fibers by a transverse holographic method," *Optics Letters*, vol. 14, no. 15, p. 823, Aug. 1, 1989, ISSN: 0146-9592, 1539-4794. DOI: `10.1364/OL.14.000823`.

[232] S. A. Slattery, D. N. Nikogosyan, and G. Brambilla, "Fiber bragg grating inscription by high-intensity femtosecond UV laser light: Comparison with other existing methods of fabrication," *Journal of the Optical Society of America B*, vol. 22, no. 2, p. 354, Feb. 1, 2005, ISSN: 0740-3224, 1520-8540. DOI: `10.1364/JOSAB.22.000354`.

[233] A. Cusano, A. Cutolo, and J. Albert, Eds., *Fiber Bragg Grating Sensors: Recent Advancements, Industrial Applications and Market Exploitation*, BENTHAM SCIENCE PUBLISHERS, Mar. 20, 2012, ISBN: 978-1-60805-084-0. DOI: `10.2174/97816080508401110101`.

[234] R. Kashyap, *Fiber Bragg gratings*, 2nd ed. Burlington, MA: Academic Press, 2010, 614 pp., OCLC: ocn233544011, ISBN: 978-0-12-372579-0.

[235] M. M. Werneck, R. C. S. B. Allil, B. A. Ribeiro, and F. V. B. de Nazaré, "A guide to fiber bragg grating sensors," in *Current Trends in Short- and Long-period Fiber Gratings*, C. Cuadrado-Laborde, Ed., InTech, May 15, 2013, ISBN: 978-953-51-1131-3. DOI: 10.5772/54682.

[236] I. Ashry, A. Elrashidi, A. Mahros, M. Alhaddad, and K. Elleithy, "Investigating the performance of apodized fiber bragg gratings for sensing applications," in *Proceedings of the 2014 Zone 1 Conference of the American Society for Engineering Education*, Bridgeport, CT, USA: IEEE, Apr. 2014, pp. 1–5, ISBN: 978-1-4799-5233-5 978-1-4799-5232-8. DOI: 10.1109/ASEEZone1.2014.6820640.

[237] P. V. R. Shekar, D. M. Latha, K. Kumari, and V. G. K. M. Pisipati, "Optimal parameters for fiber bragg gratings for sensing applications: A spectral study," *SN Applied Sciences*, vol. 3, no. 6, p. 666, Jun. 2021, ISSN: 2523-3963, 2523-3971. DOI: 10.1007/s42452-021-04650-0.

[238] K. S. Khalid, M. Zafrullah, S. M. Bilal, and M. A. Mirza, "Simulation and analysis of gaussian apodized fiber bragg grating strain sensor," *Journal of Optical Technology*, vol. 79, no. 10, p. 667, Oct. 31, 2012, ISSN: 1070-9762. DOI: 10.1364/JOT.79.000667.

[239] A. Othonos, K. Kalli, D. Pureur, and A. Mugnier, "Fibre bragg gratings," in *Wavelength Filters in Fibre Optics*, H. Venghaus, Ed., vol. 123, Series Title: Springer Series in Optical Sciences, Springer Berlin Heidelberg, 2006, pp. 189–269, ISBN: 978-3-540-31769-2. DOI: 10.1007/3-540-31770-8_6.

[240] J. Albert, L.-Y. Shao, and C. Caucheteur, "Tilted fiber bragg grating sensors: Tilted fiber bragg grating sensors," *Laser & Photonics Reviews*, vol. 7, no. 1, pp. 83–108, Jan. 2013, ISSN: 18638880. DOI: 10.1002/lpor.201100039.

[241] Y. Rao, "Fiber bragg grating sensors: Principles and applications," in *Optical Fiber Sensor Technology*, K. T. V. Grattan and B. T. Meggitt, Eds., Boston, MA: Springer US, 1998, pp. 355–379, ISBN: 978-1-4615-5787-6. DOI: 10.1007/978-1-4615-5787-6_11.

[242] W. W. Morey, G. Meltz, and W. H. Glenn, "Fiber optic bragg grating sensors," presented at the OE/FIBERS '89, R. P. DePaula and E. Udd, Eds., Boston, Feb. 13, 1990, p. 98. DOI: 10.1117/12.963022.

[243] A. Othonos, "Fiber bragg gratings," *Review of Scientific Instruments*, vol. 68, no. 12, pp. 4309–4341, Dec. 1997, ISSN: 0034-6748, 1089-7623. DOI: 10.1063/1.1148392.

[244] C. Campanella, A. Cuccovillo, C. Campanella, A. Yurt, and V. Passaro, "Fibre bragg grating based strain sensors: Review of technology and applications," *Sensors*, vol. 18, no. 9, p. 3115, Sep. 15, 2018, ISSN: 1424-8220. DOI: 10.3390/s18093115.

[245] A. Kersey, M. Davis, H. Patrick, *et al.*, "Fiber grating sensors," *Journal of Lightwave Technology*, vol. 15, no. 8, pp. 1442–1463, Aug. 1997, ISSN: 07338724. DOI: 10.1109/50.618377.

[246] M. G. Xu, J.-L. Archambault, L. Reekie, and J. P. Dakin, "Discrimination between strain and temperature effects using dual-wavelength fibre grating sensors," *Electronics Letters*, vol. 30, no. 13, pp. 1085–1087, Jun. 23, 1994, Publisher: IET Digital Library, ISSN: 1350-911X. DOI: 10.1049/el:19940746.

[247] P. Lu, N. Lalam, M. Badar, *et al.*, "Distributed optical fiber sensing: Review and perspective," *Applied Physics Reviews*, vol. 6, no. 4, p. 041 302, Sep. 2019, ISSN: 1931-9401. DOI: 10.1063/1.5113955.

[248] P. Oberson, B. Huttner, and N. Gisin, "Frequency modulation via the doppler effect in optical fibers," *Optics Letters*, vol. 24, no. 7, p. 451, Apr. 1, 1999, ISSN: 0146-9592, 1539-4794. DOI: 10.1364/OL.24.000451.

[249] G. P. Agrawal, *Nonlinear fiber optics*, Fifth edition. Amsterdam: Elsevier/Academic Press, 2013, 629 pp., ISBN: 978-0-12-397023-7.

[250] Z. Ding, C. Wang, K. Liu, *et al.*, "Distributed optical fiber sensors based on optical frequency domain reflectometry: A review," *Sensors*, vol. 18, no. 4, p. 1072, Apr. 3, 2018, ISSN: 1424-8220. DOI: 10.3390/s18041072.

[251] W. Eickhoff and R. Ulrich, "Optical frequency domain reflectometry in single-mode fiber," *Applied Physics Letters*, vol. 39, no. 9, pp. 693–695, Nov. 1981, ISSN: 0003-6951, 1077-3118. DOI: 10.1063/1.92872.

[252] M. Froggatt and J. Moore, "High-spatial-resolution distributed strain measurement in optical fiber with rayleigh scatter," *Applied Optics*, vol. 37, no. 10, p. 1735, Apr. 1, 1998, ISSN: 0003-6935, 1539-4522. DOI: 10.1364/AO.37.001735.

[253] S. T. Kreger, D. K. Gifford, M. E. Froggatt, B. J. Soller, and M. S. Wolfe, "High resolution distributed strain or temperature measurements in single- and multi-mode fiber using swept-wavelength interferometry," in *Optical Fiber Sensors*, Cancún, Mexico: OSA, 2006, ThE42, ISBN: 978-1-55752-817-9. DOI: 10.1364/OFS.2006.ThE42.

[254] B. J. Soller, M. S. Wolfe, and M. E. Froggatt, "Polarization resolved measurement of rayleigh backscatter in fiber-optic components," in *OFC Technical Digest*, OSA Publishing, 2005.

[255] L. I. Inc., "Optical distributed sensor interrogator model ODiSI-b: User's guide," Roanoke, VA, USA, 2017.

[256] T.-J. Ahn, J. Y. Lee, and D. Y. Kim, "Suppression of nonlinear frequency sweep in an optical frequency-domain reflectometer by use of hilbert transformation," *Applied Optics*, vol. 44, no. 35, p. 7630, Dec. 10, 2005, ISSN: 0003-6935, 1539-4522. DOI: `10.1364/AO.44.007630`.

[257] K. Tsuji, K. Shimizu, T. Horiguchi, and Y. Koyamada, "Coherent optical frequency domain reflectometry using phase-decorrelated reflected and reference lightwaves," *Journal of Lightwave Technology*, vol. 15, no. 7, pp. 1102–1109, Jul. 1997, ISSN: 07338724. DOI: `10.1109/50.596955`.

[258] L. Schenato, L. Palmieri, M. Camporese, *et al.*, "Distributed optical fibre sensing for early detection of shallow landslides triggering," *Scientific Reports*, vol. 7, no. 1, p. 14 686, Dec. 2017, ISSN: 2045-2322. DOI: `10.1038/s41598-017-12610-1`.

[259] S. Cola, L. Schenato, L. Brezzi, F. C. Tchamaleu Pangop, L. Palmieri, and A. Bisson, "Composite anchors for slope stabilisation: Monitoring of their in-situ behaviour with optical fibre," *Geosciences*, vol. 9, no. 5, p. 240, May 25, 2019, ISSN: 2076-3263. DOI: `10.3390/geosciences9050240`.

[260] H. L. Cox, "The elasticity and strength of paper and other fibrous materials," *British Journal of Applied Physics*, vol. 3, no. 3, p. 72, Mar. 1952, Publisher: IOP Publishing, ISSN: 0508-3443. DOI: `10.1088/0508-3443/3/3/302`.

[261] R. O. Claus, K. D. Bennett, A. M. Vengsarkar, and K. A. Murphy, "Embedded optical fiber sensors for materials evaluation," *Journal of Nondestructive Evaluation*, vol. 8, no. 2, pp. 135–145, Jun. 1989, ISSN: 0195-9298, 1573-4862. DOI: `10.1007/BF00565637`.

[262] A. Nanni, C. C. Yang, K. Pan, J. S. Wang, and R. R. Michael, "Fiber-optic sensors for concrete strain/stress measurement," *ACI Materials Journal*, vol. 88, no. 3, pp. 257–264, May 1, 1991, Publisher: American Concrete Institute, ISSN: 0889-325X.

[263] Y. E. Pak, "Longitudinal shear transfer in fiber optic sensors," *Smart Materials and Structures*, vol. 1, no. 1, pp. 57–62, Mar. 1, 1992, ISSN: 0964-1726, 1361-665X. DOI: `10.1088/0964-1726/1/1/008`.

[264] F. Ansari and Y. Libo, "Mechanics of bond and interface shear transfer in optical fiber sensors," *Journal of Engineering Mechanics*, vol. 124, no. 4, pp. 385–394, Apr. 1998, ISSN: 0733-9399, 1943-7889. DOI: `10.1061/(ASCE)0733-9399(1998)124:4(385)`.

[265] Dong-Sheng Li, Hongnan Li Sr., Liang Ren, and Gangbing Song, "Strain transferring analysis of fiber bragg grating sensors," *Optical Engineering*, vol. 45, no. 2, pp. 1–8, Feb. 1, 2006. DOI: `10.1117/1.2173659`.

[266] H.-N. Li, G.-D. Zhou, L. Ren, and D.-S. Li, "Strain transfer coefficient analyses for embedded fiber bragg grating sensors in different host materials," *Journal of Engineering Mechanics*, vol. 135, no. 12, pp. 1343–1353, Dec. 2009, ISSN: 0733-9399, 1943-7889. DOI: `10.1061/(ASCE)0733-9399(2009)135:12(1343)`.

[267] M. LeBlanc, A. Guemes, A. Othonos, S. Y. Huang, M. Ohn, and R. M. Measures, "Distributed strain measurement based on a fiber bragg grating and its reflection spectrum analysis," *Optics Letters*, vol. 21, no. 17, p. 1405, Sep. 1, 1996, ISSN: 0146-9592, 1539-4794. DOI: `10.1364/OL.21.001405`.

[268] J. Guemes and J. Menéndez, "Response of bragg grating fiber-optic sensors when embedded in composite laminates," *Composites Science and Technology*, vol. 62, no. 7, pp. 959–966, Jun. 2002, ISSN: 02663538. DOI: `10.1016/S0266-3538(02)00010-6`.

[269] H. Wang and P. Xiang, "Strain transfer analysis of optical fiber based sensors embedded in an asphalt pavement structure," *Measurement Science and Technology*, vol. 27, no. 7, p. 075 106, Jul. 1, 2016, ISSN: 0957-0233, 1361-6501. DOI: `10.1088/0957-0233/27/7/075106`.

[270] D. Li, L. Ren, and H. Li, "Mechanical property and strain transferring mechanism in optical fiber sensors," in *Fiber Optic Sensors*, M. Yasin, Ed., InTech, Feb. 22, 2012, ISBN: 978-953-307-922-6. DOI: `10.5772/27731`.

[271] K. T. Wan, C. K. Y. Leung, and N. G. Olson, "Investigation of the strain transfer for surface-attached optical fiber strain sensors," *Smart Materials and Structures*, vol. 17, no. 3, p. 035 037, Jun. 1, 2008, ISSN: 0964-1726, 1361-665X. DOI: `10.1088/0964-1726/17/3/035037`.

[272] W. Li, C. Cheng, and Y. Lo, "Investigation of strain transmission of surface-bonded FBGs used as strain sensors," *Sensors and Actuators A: Physical*, vol. 149, no. 2, pp. 201–207, Feb. 2009, ISSN: 09244247. DOI: `10.1016/j.sna.2008.11.011`.

[273] S.-C. Her and C.-Y. Huang, "Effect of coating on the strain transfer of optical fiber sensors," *Sensors*, vol. 11, no. 7, pp. 6926–6941, Jul. 1, 2011, ISSN: 1424-8220. DOI: `10.3390/s110706926`.

[274] X. Feng, J. Zhou, C. Sun, X. Zhang, and F. Ansari, "Theoretical and experimental investigations into crack detection with BOTDR-distributed fiber optic sensors," *Journal of Engineering Mechanics*, vol. 139, no. 12, pp. 1797–1807, Dec. 2013, ISSN: 0733-9399, 1943-7889. DOI: `10.1061/(ASCE)EM.1943-7889.0000622`.

[275] A. Billon, J.-M. Hénault, M. Quiertant, *et al.*, "Qualification of a distributed optical fiber sensor bonded to the surface of a concrete structure: A methodology to obtain quantitative strain measurements," *Smart Materials and Structures*, vol. 24, no. 11, p. 115 001, Nov. 1, 2015, ISSN: 0964-1726, 1361-665X. DOI: 10.1088/0964-1726/24/11/115001.

[276] PULSe. "Pervasive ubiquitous lightwave sensor." (2017), [Online]. Available: https://cordis.europa.eu/project/id/737801 (visited on 06/03/2020).

[277] M. A. Soto, P. K. Sahu, S. Faralli, *et al.*, "High performance and highly reliable raman-based distributed temperature sensors based on correlation-coded OTDR and multimode graded-index fibers," presented at the Third European Workshop on Optical Fibre Sensors, Napoli, Italy, Jul. 4, 2007, 66193B. DOI: 10.1117/12.738902.

[278] D. Marini, M. Iuliano, F. Bastianini, and G. Bolognini, "BOTDA sensing employing a modified brillouin fiber laser probe source," *Journal of Lightwave Technology*, vol. 36, no. 4, pp. 1131–1137, Feb. 15, 2018, ISSN: 0733-8724, 1558-2213. DOI: 10.1109/JLT.2017.2772326.

[279] H. Yuan, "Improved theoretical solutions of FRP-to-concrete interfaces," in *Proceedings of the International Symposium on Bond Behaviour of FRP in Structures*, Hong Kong, China, Dec. 7, 2005, pp. 97–102.

[280] U. Ben-Simon, S. Shoham, Y. Ofir, *et al.*, "Choosing the right optical fiber coating to meet individual fiber-optic strain measurement application," in *Structural Health Monitoring 2019*, DEStech Publications, Inc., Nov. 15, 2019, ISBN: 978-1-60595-601-5. DOI: 10.12783/shm2019/32259.

[281] J. Henault, J. Salin, G. Moreau, *et al.*, "Analysis of the strain transfer mechanism between a truly distributed optical fiber sensor and the surrounding medium," in *Concrete Repair, Rehabilitation and Retrofitting III*, Cape Town, South Africa, Sep. 2012, pp. 733–739.

[282] L. Technologies, *Optical backscatter reflectometer user guide*, 2009.

[283] L. Technologies, "ODiSI-b sensor strain gage factor uncertainty," Technical Note EN-FY1602, Nov. 30, 2016.

[284] D. B. Owen, "A survey of properties and applications of the noncentral t-distribution," *Technometrics*, vol. 10, no. 3, p. 445, Aug. 1968, ISSN: 00401706. DOI: 10.2307/1267101.

[285] D30 Committee, "Test method for mode i interlaminar fracture toughness of unidirectional fiber-reinforced polymer matrix composites," ASTM International, D5528 - 13. DOI: 10.1520/D5528-13.

[286] Hexcel. "HexPly® 8552 UD carbon prepregs." (), [Online]. Available: `https://www.hexcel.com/user_area/content_media/raw/HexPly_8552_eu_DataSheet.pdf` (visited on 02/03/2022).

[287] "3m™ scotch-weld™ structural epoxy adhesive EC-9323 b/a, 1 l, redorange." Archive Location: GB Layout: Luxury. (), [Online]. Available: `https://www.3m.co.uk/3M/en_GB/p/d/b40066445/` (visited on 02/04/2022).

[288] F. T. GmbH. "ORMOCER® coating." (), [Online]. Available: `https://fbgs.com/technology/ormocer-coating/` (visited on 02/04/2022).

[289] E. J. Ripling, S. Mostovoy, and H. T. Corten, "Fracture mechanics: A tool for evaluating structural adhesives," *The Journal of Adhesion*, vol. 3, no. 2, pp. 107–123, Nov. 1971, ISSN: 0021-8464, 1545-5823. DOI: `10.1080/00218467108081158`.

[290] L. Škec, G. Alfano, and G. Jelenić, "Complete analytical solutions for double cantilever beam specimens with bi-linear quasi-brittle and brittle interfaces," *International Journal of Fracture*, vol. 215, no. 1, pp. 1–37, Jan. 2019, ISSN: 0376-9429, 1573-2673. DOI: `10.1007/s10704-018-0324-5`.

[291] "Product information - TB1742," ThreeBond. (), [Online]. Available: `https://threebond-europe.com/products/tb1742/` (visited on 02/04/2022).

[292] D. Sans, J. Renart, J. Costa, N. Gascons, and J. Mayugo, "Assessment of the influence of the crack monitoring method in interlaminar fatigue tests using fiber bragg grating sensors," *Composites Science and Technology*, vol. 84, pp. 44–50, Jul. 2013, ISSN: 02663538. DOI: `10.1016/j.compscitech.2013.04.022`.

[293] S. Stutz, J. Cugnoni, and J. Botsis, "Studies of mode i delamination in monotonic and fatigue loading using FBG wavelength multiplexing and numerical analysis," *Composites Science and Technology*, vol. 71, no. 4, pp. 443–449, Feb. 28, 2011, ISSN: 02663538. DOI: `10.1016/j.compscitech.2010.12.016`.

[294] L. Škec, G. Alfano, and G. Jelenić, "Enhanced simple beam theory for characterising mode-i fracture resistance via a double cantilever beam test," *Composites Part B: Engineering*, vol. 167, pp. 250–262, Jun. 2019, ISSN: 13598368. DOI: `10.1016/j.compositesb.2018.11.099`.

[295] D. Cristiani, C. Sbarufatti, and M. Giglio, "Damage diagnosis and prognosis in composite double cantilever beam coupons by particle filtering and surrogate modelling," *Structural Health Monitoring*, vol. 20, no. 3, pp. 1030–1050, May 2021, ISSN: 1475-9217, 1741-3168. DOI: `10.1177/1475921720960067`.